

UNITED KINGDOM • CHINA • MALAYSIA

Division of Molecular Therapeutics and Formulation

Amino Acid-Modified Ultrafine Superparamagnetic Iron Oxide Nanoparticles: Fabrication, Size Characterisation and Potential Cytotoxicity and Cell Interaction

Muqdam Alali

Thesis submitted to the University of Nottingham for the degree of Doctor of Philosophy

February 2018

Acknowledgements

My greatest special thanks is to my sponsor Higher Committee for Education Development in Iraq (HCED) for funding and providing me the opportunity to study my PhD at the University of Nottingham.

I would also like to express my deepest gratefulness to my principal supervisor, Dr. Snow Stolnik, in addition to Dr. Gareth Cave, whose office doors were always open to me, for their guidance from the very early stage of this research and who went far beyond what was required of them to help me. I always admire their patience, scientific rigor and providing me with an excellent atmosphere for doing research. I thank them for believing in me and improving my abilities and their extending supports. It was a great pleasure to be able to work on this project and share your great knowledge in the field of advanced drug delivery.

I would like to thank Vincenzo, Rob, Abdullah, Rosa, Ali, Ibtisam, vijender Alejandro, Waleed, Mohammed, Eman, emanuela and Ammar for all the wonderful, pleasant and memorable moments that we shared and for all their help during my stay at Nottingham.

I extend my thanks and acknowledge Nottingham University's senior lab technician Christy Grainger-Boultby and Paul Cooling for their expert advice and assistance on instruments, laboratory protocols and for ensuring the department's safety at all times.

My thanks also go to my parents where I have been extremely fortunate to have them, Mr. Mahdi and Mrs. Masoumeh. They have presented me unflagged love and support throughout my life. My deep appreciation and gratitude to my sister,

Fadak, and brothers, Nasek and Ghiath, for their wonderful support especially when I am far away from my home country.

Finally, I would like to send my heartfelt gratefulness to my wife, Zahraa Alali, for her support, encouragement, prayers, tolerance and patience. The woman who has made all the differences in life. I will never forget my little daughters for adding taste to this scientific journey.

Dedication

Every challenging work need self-efforts as well as guidance of elders especially those who are very close to my heart

I dedicate this humble effort to my sweet and loving

Mother & Wife,

Whose affection, love, encouragement and prays of day and night make me able to get such success and honor

Along with all hard working and respected

Supervisors

Abstract

The potential applications of transition metals-based nanoparticles are expanding in the biomedical field. Oxides of iron are the matter of investigation in this study where various preparations of ultrafine superparamagnetic iron oxide nanoparticles (USPIONs) were fabricated using flow injection technology with spinning disc reactor. Basically, two types of preparation parameters were examined; first, instrument-related (physical) parameters and, second, chemistry-related parameters. USPIONs fabricated by this instrument showed fine-tuning size adjustment. Subsequent surface modification of these nanoparticles produced hydrophobic, hydrophilic and neutral amino acids modified surface, whereby aminoacid 'monomers', rather than polymeric materials were used. Transmission electron microscopy (TEM), dynamic light scattering (DLS), zeta potential measurements, thermogravimetric analysis (TGA) and fourier-transform infrared-attenuated total reflection spectroscopy (FTIR-ATR) were employed to characterise the coated nanoparticles. The data show that ultrafine, 4-9 nm sized coated nanoparticles show good dispersion upon TEM imaging. Measurement of number of monomers molecules effectively associated with USPIONs suggest formation of multilayer of amino acid adsorbed on nanoparticles (NPs). Prediction of NPs- amino acid association mechanism by FTIR-ATR study reveals presence of either monodentate or bidentate molecular adsorption on the surface of USPIONs.

In the second stage of the project, interactions of differently modified USPIONs with epithelial cell layer (model of intestinal epithelium) are now investigated. An intestinal adenocarcinoma cell line (Caco-2) is used for performing the *in vitro* studies. The toxicity of three types of USPIONs (Asp-, His-, and Phe-

USPIONs) reveals that these particles have potential toxic effect on biological system. Relatively long term exposure to these particles (24 hours) with high concentration 250 µg/ml and more was found to enhance apoptotic mode of cell death. Cell-NPs interaction study displayed presence of different forms of cellular interaction which are supposed to be related to USPIONs surface chemistry. While some of Phe-USPIONs are found internalised and accumulated inside some cells, Asp-USPIONs exhibit different interaction mode where the cell membrane of most cells is covered with thin layer of NPs without significant cell penetration. This gives an indication that metal oxide NPs (USPIONs) that are associated by their surface with small molecules could render these NPs with aggravated toxicity and cell-NPs interaction and hence long term effect.

List of Contents

Acknowledgements ..... **I**

Abstract ..... **IV**

List of figures ..... **XVII**

List of tables ..... **XXII**

List of abbreviation ..... **XXIII**

Chapter 1: Literature review **1**

1.1 Introduction 1

1.2 Routes of SPIONs fabrication 1

1.2.1 Chemical route for SPIONs fabrication 1

1.2.1.1 Co-precipitation method 2

1.2.1.2 Microemulsion (ME) method 2

1.2.1.3 Sol-gel and polyol methods 4

1.2.1.4 Hydrothermal/solvothermal method 5

1.2.1.5 Sonochemical method 6

1.2.1.6 Electrochemical synthesis 7

1.2.2 Physical route for SPIONs fabrication 8

1.2.3 Biological route for SPIONs fabrication 9

1.3 Surface modification of iron oxide NPs 10

1.3.1 Surface modification by organic materials 10

1.3.1.1 Small molecules and surfactants 11

1.3.1.2 Large molecules or polymers 12
1.3.1.2.1 Polymers deployed in modifying iron oxide NPs 12
1.3.1.2.1.1 Polyethylene glycol (PEG) 12
1.3.1.2.1.2 Polyvinyl alcohol (PVA) 13
1.3.1.2.1.3 Dextran 13
1.3.1.2.1.4 Chitosan 13
1.3.1.2.2 Techniques followed to prepare NPs-polymer composite 14
1.3.1.3 Biomolecules 15
1.3.2 Surface modification by inorganic materials 16
1.3.2.1 Silica 16
1.3.2.2 Carbon 17
1.3.2.3 Metals 18
1.3.3 Microstructure of surface-modified iron oxide NPs 18
1.4 Behaviour of metal and metal oxide in biological environment 18
1.4.1 An overview 18
1.4.2 The entry of iron oxide NPs into natural surroundings 20
1.4.3 Exposure of iron oxide NPs to human 21
1.4.4 NPs-biological system interaction following injection route 21
1.4.5 Metal oxide NPs – protein interaction (protein corona) 22
1.4.6 Protein corona formation and composition 22
1.4.6.1 Exposure to complex solutions 22

1.4.6.1.1 Cell culture media 22
1.4.6.1.2 Protein concentration effect 23
1.4.6.1.3 Exposure time 23
1.4.6.1.4 Stationary and flow conditions 24
1.4.6.1.5 Temperature 24
1.4.6.1.6 Biological media pH 25
1.4.6.2 NPs-related parameters 25
1.4.6.2.1 NPs size 25
1.4.6.2.2 NPs shape 25
1.4.6.2.3 NPs surface properties 26
1.4.6.2.3.1 Effect of surface charge 26
1.4.6.2.3.2 Surface roughness/smoothness 26
1.4.6.2.3.3 Surface hydrophilicity/hydrophobicity 26
1.4.6.2.3.4 Surface functionalisation and coating 27
1.4.7 The noxious response to metal oxide NPs 27
1.4.7.1 ROS-mediated cytotoxicity of metal oxide NPs 29
1.4.7.1.1 Parameters affecting ROS liberation 29
1.4.7.1.1.1 NPs-related parameters of ROS liberation 29
1.4.7.1.1.1.1 Chemical composition 29
1.4.7.1.1.1.2 Particles size 30
1.4.7.1.1.1.3 Degree of crystallinity 30

1.4.7.1.1.2 Bio-microenvironment related parameters of ROS generation ……31

1.4.7.1.1.2.1 pH effect 31

1.4.7.1.1.2.2 Reducing agents effect 31

1.4.7.1.1.2.3 Other effects 32

1.4.7.2 Oxidative stress 32

1.4.7.2.1 Effect of oxidative stress on DNA 33

1.4.7.2.2 Effect of oxidative stress on lipids 33

1.4.7.2.3 Effect of oxidative stress on proteins 33

1.4.7.3 ROS and apoptosis 34

1.4.7.3.1 Apoptosis 34

1.4.7.3.2 Mechanism of apoptotic cell death 34

1.4.7.3.3 The role of ROS in cells apoptosis 36

1.5 USPIONs bio-applications 38

1.6 Project aims 39

1.7 References: 40

Chapter 2: USPIONs preparation and size characterisation 71

2.1 Introduction 71

2.2 Materials and Methods 74

2.2.1 Materials 74

2.2.2 Methods 74

2.2.2.1 Reactant solution preparation 74

2.2.2.2 Production of USPIONs using Spinning Disc Reactor (SDR)75

2.2.2.3 USPIONs preparations under different conditions 78

2.2.2.4 Infrared analysis of USPIONs.....80

2.2.2.5 Transmission electron microscopy (TEM) 80

2.2.2.6 Dynamic light scattering (DLS).....81

2.2.2.7 Statistical analysis.....81

2.3 Results 82

2.3.1 Preparation of USPIONs.....82

2.3.2 Particle morphology and size analyses by TEM.....83

2.3.3 Factors affecting USPIONs size and morphology.....84

2.3.3.1 Effect of BISS flowrate.....84

2.3.3.1.1 Size and degree of circularity distribution 84

2.3.3.1.2 Comparison of TEM and DLS average particle sizes 86

2.3.3.1.3 Average of the fabricated USPIONs circularity.....88

2.3.3.2 Effect of spin disc rotational speed.....89

2.3.3.2.1 Size and degree of circularity distribution 89

2.3.3.2.2 Comparison of TEM and DLS average particle sizes 93

2.3.3.2.3 Extent of the fabricated USPIONs circularity.....95

2.3.3.3 Effect of spinning disc size.....96

2.3.3.3.1 Size and degree of circularity distribution 96

2.3.3.3.2 TEM and DLS average particle sizes.....100

2.3.3.3.3 Extent of the fabricated USPIONs circularity.....102

2.3.3.4 Effect of BISS concentration 104

2.3.3.4.1 Size and degree of circularity distribution 104

2.3.3.4.2 Comparison of TEM and DLS average particle size.....108

2.3.3.4.3 Effect on USPIONs circularity.....111

2.3.3.5 Effect of changing Fe^{2+}/Fe^{3+} ratio.....111

2.3.3.5.1 Size and degree of circularity distribution 111

2.3.3.5.2 Comparing TEM and DLS average particle size.....115

2.3.3.5.3 Effect on USPIONs circularity.....117

2.3.3.6 Effect of reducing the basicity of the alkaline 118

2.3.3.6.1 Size and degree of circularity distribution 118

2.3.3.6.2 TEM and DLS average particle sizes.....120

2.3.3.6.3 Extent of the fabricated USPIONs circularity.....122

2.4 Discussion.....124

2.4.1 Mechanism of iron oxide network formation.....124

2.4.2 Control over particles nucleation and growth.....125

2.4.3 Reactant injection into confined zone of nucleation.....131

2.4.4 The role of SDR as a space for NPs growth.....135

2.4.5 Effect of BISS flowrate on particles size, size distribution, polydispersity and circularity 138

2.4.6 The effect of SDR rotational speed on the particles size, size distribution, polydispersity and circularity.....140

2.4.7 The effect of SDR size on the particles size, size distribution, polydispersity and circularity. 145

2.4.8 The effect of total iron amount (TIA) in the BISS on the particle size, size distribution, polydispersity and circularity.....147

2.4.9 The effect of Fe^{+2}/Fe^{+3} ratio on the particles size, size distribution, polydispersity and circularity 150

2.4.10 The effect of reducing alkaline medium strength on the particle size, size distribution, polydispersity and circularity.....153

2.5 Conclusions 155

2.6 References.....158

Chapter 3: Surface Modification of USPIONs with Different Amino acids: Preparation and Characterisation. 168

3.1 Introduction.....168

3.2 Materials and Methods 171

3.2.1 Materials 171

3.2.2 Methods 171

3.2.2.1 USPIONs surface modification.....171

3.2.2.2 Purification of amino acid-modified USPIONs.....173

3.2.2.3 Detection Iron oxide amount 173

3.2.2.4 USPIONs- associated aminoacid detection 174

3.2.2.5 TEM imaging and hydrodynamic size measurement.....175

3.2.2.6 Infrared analysis of USPIONs.....176

3.2.2.7 Thermogravimetric analysis (TGA).....176

3.2.2.8 Colloidal dispersion stability of the aminoacid-modified USPIONs as a function of pH.....176

3.2.2.9 Statistical analysis.....177

3.3 Results.....177

3.3.1 Yield of aminoacid-modified USPIONs.....177

3.3.2 Aminoacid-modified USPIONs size and TEM images.....182

3.3.3 TGA of amino acids associated with USPIONs.....185

3.3.4 The mass and number of molecules of the adsorbed amino acids on USPIONs surfaces.....194

3.3.5 Colloidal properties of dispersion of aminoacid-modified USPIONs.....201

3.3.6 FTIR analysis.....204

3.3.6.1 Assignments of lysine IR spectra.....205

3.3.6.2 Assignments for aspartic acid IR spectra.....206

3.3.6.3 Assignment of glutamic acid IR spectra.....207

3.3.6.4 Assignments for histidine IR spectra.....208

3.3.6.5 Assignment of threonine IR spectra.....210

3.3.6.6 Assignment of leucine IR spectra.....211

3.3.6.7 Assignments of methionine IR spectra.....212

3.3.6.8 Assignment of phenylalanine IR spectra.....213

3.3.6.9 Assignment of glycine IR spectra.....214

3.4 Discussion.....219

3.4.1 Aminoacid-USPIONs binding mechanism.....224

3.4.1.1 Lysine salt and Lys-USPIONs.....225

3.4.1.2 Aspartic acid HCl salt association with USPIONs.....226

3.4.1.3 Glutamic acid HCl association with USPIONs.....228

3.4.1.4 Histidine 2HCl association with USPIONs.....229

3.4.1.5 Threonine HCl association with USPIONs.....230

3.4.1.6 Leucine HCl association with USPIONs.....231

3.4.1.7 Methionine HCl association with USPIONs.....232

3.4.1.8 Phenylalanine HCl association with USPIONs.....233

3.4.1.9 Glycine HCl association with USPIONs.....234

3.5 Conclusions.....235

3.6 References.....237

Chapter 4: Biological Assessment of Aminoacid-modified USPIONs in *in vitro* culture model.....245

4.1 Introduction.....245

4.2 Materials and Methods.....247

4.2.1 Materials.....247

4.2.1.1 Cells and Cell Culture Consumables.....247

4.2.1.2 Plasticware and Glassware.....247

4.2.1.3 Chemical and Biological Reagents.....248

4.2.2 Methods.....248

4.2.2.1 Maintenance of cells 248
4.2.2.1.1 Routine maintenance and culture of cells 248
4.2.2.1.2 Cells Culture of in transwells 250
4.2.2.2 Cytotoxicity of three USPIONs colloidal systems 250
4.2.2.2.1 MTT Cell metabolic activity assay 250
4.2.2.2.2 LDH release assay 251
4.2.2.2.3 Accumulation of ROS measurement 253
4.2.2.2.4 Assessment of Caspase-3/7 activation 254
4.2.2.2.5 Hoechst / Propidium iodide double staining of nuclei 255
4.2.2.3 Modified USPIONs-cell interaction 257
4.2.2.3.1 Well plate processing 257
4.2.2.3.2 Iron amount quantification (ICP-MS analysis) 258
4.2.2.3.3 Light scattering measurement (Flow cytometry study) 259
4.2.2.3.4 TEM imaging (Samples preparation) 259
4.2.2.3.4.1 Cell fixation 259
4.2.2.3.4.2 Embedding resin preparation 260
4.2.2.3.4.3 Cell dehydration and resin embedding 260
4.2.2.3.4.4 Resin blocks sectioning 261
4.2.2.4 Statistical analysis 261
4.3 Results 261
4.3.1 Colloidal stability of aminoacid modified USPIONs in cell culture media 261

4.3.2 Cytotoxicity assessment of aminoacid modified USPIONs 262

4.3.2.1 Effect on cell metabolic activity 262

4.3.2.2 Effect of the modified USPIONs on the cell membrane integrity (LDH assay) 264

4.3.2.3 Reactive oxidative stress 266

4.3.2.4 Effect of USPIONs on cell mitochondria 269

4.3.2.5 Effect on effector caspase activation 270

4.3.2.6 Hoechst 33342 / Propidium iodide double staining 271

4.3.3 Aminoacid modified USPIONs-cell association 273

4.3.3.1 Quantitative analysis of USPIONs associated with Caco-2 cells 273

4.3.3.2 Flow cytometry 276

4.3.3.3 TEM analysis 279

4.4 Discussion 288

4.5 Conclusion and summary 296

4.6 References 298

Chapter5: General discussion and future directions 305

5.1 General discussion 305

5.2 Future directions 310

5.3 References 313

List of figures

Figure 1-1: Schematic illustration of NPs behaviour in environment. 19

Figure 1-2: Schematic diagram of metal oxide NPs toxicity.....28

Figure 1-3: Schematic representation of apoptosis-related pathways. 36

Figure 2-1: Schematic representation of the developed instrument for preparation of USPIONs.....77

Figure 2-2: Schematic illustration of the six procedures used in preparation of USPIONs 78

Figure 2-3: FTIR spectrum of USPOINs as dry powder 83

Figure 2-4: TEM micrographs with distribution histograms of USPIONs prepared using different flowrates 85

Figure 2-5: Particles diameter obtinaed from A) TEM images and B) DLS measurments 87

Figure 2-6: Average of circularity values of four USPIONs batches prepared at each 30, 40, 50 and 60 ml/min flowrates.....89

Figure 2-7: TEM micrographs with distribution histograms of USPIONs prepared using different rotational speeds. 92

Figure 2-8: Line graphs represent the plot of particles average diameter extracted from TEM images and DLS measurements versus different SDR rotational speed.....94

Figure 2-9: Average of circularity values of two different USPIONs sets prepared at various rotational speed 96

Figure 2-10: TEM micrographs with distribution histograms of USPIONs prepared using two different disc sizes.....99

Figure 2-11: 3D bar graphs represent values of particles average diameter extracted from TEM images and DLS measurements upon using different spinning disc sizes 101

Figure 2-12: Average of circularity values of different USPIONs sets prepared using various rotational speed and flowrates.....103

Figure 2-13: TEM micrographs with distribution histograms of USPIONs prepared using different iron amounts.....107

Figure 2-14: Line graphs represent the plot of particles average diameter extracted from A) TEM images and B) DLS measurements versus different total iron amount used. 109

Figure 2-15: Average of circularity values of two different USPIONs sets prepared using various BISS concentration.....111

Figure 2-16: TEM micrographs with frequency distribution histograms of USPIONs prepared using two different Fe^{+2}/Fe^{+3} ratios 114

Figure 2-17: 3D bar graphs represent values of particles average diameter extracted from TEM images and DLS measurements upon using different Fe^{+2}/Fe^{+3} ratio 116

Figure 2-18: Average of circularity of different USPIONs sets prepared using various rotational speed and BISS with two Fe^{+2}/Fe^{+3} ratios. 118

Figure 2-19: TEM micrographs with frequency distribution histograms of USPIONs prepared using different concentrations of alkaline solution.....119

Figure 2-20: Bar graphs represent values of particles average diameter extracted from TEM images and DLS measurements upon using different NH_4OH concentrations 121

Figure 2-21: Average of circularity values of different USPIONs prepared using two total iron amounts. Red bar graphs represent results of 35% NH_4OH, while pink bars represent readings of 18% NH_4OH.....123

Figure 2-22: the mechanism of iron oxide network formation.....125

Figure 2-23: Schematic illustration of NPs nucleation and growth.....130

Figure 2-24: Schematic of injection flow synthesis. 134

Figure 2-25: Cross sectional view of spinning disc reactor (SDR) with different designs.....137

Figure 2-26: Schematic illustration of dual effect of reactant flowrate and rotational speed of SDR on NPs size.....144

Figure 3-1: Illustrative photographs of filtering aminoacid-modified USPIONs prepared using dry mixing method with applied mechanical pressure.....172

Figure 3-2: A photograph of Eppendorf tubes shows small pellets of pure modified USPIONs deposited at the bottom after centrifugation.....173

Figure 3-3: A bar graph showing the yields of aminoacid-modified USPIONs prepared using two different methods. 180

Figure 3-4: Yield of aminoacid-modified, colloidally stable USPIONs versus different quantities of amino acids monomers.....181

Figure 3-5: Morphology (TEM micrographs) and particle size distribution histograms for aminoacid-modified USPIONs.....185

Figure 3-6: TGA of bare and USPIONs modified with selected amino acids. 191

Figure 3-7: Thermal stability analysis of free amino acids and corresponding USPIONs-coordinated. 194

Figure 3-8: USPIONs surface modification at increasing aminoacids' amounts 198

Figure 3-9: Amount of USPIONs associated amino acid as a function of time. 199

Figure 3-10: Zeta potential (green line) and hydrodynamic size (red line) of bare USPIONs and the corresponding aminoacid-modified USPIONs as a function of pH.....204

Figure 3-11: FTIR spectra for free amino acid and aminoacid modified USPIONs 217

Figure 3-12: FTIR spectra for free amino acid and aminoacid modified USPIONs 218

Figure 4-1: Hydrodynamic particle size of amino acid modified USPIONs in culture media in the presence and absence of FBS as a function of time.....262

Figure 4-2: Caco-2 cell metabolic activity following exposure to Asp-, His-, and Phe-USPIONs for different time intervals. 263

Figure 4-3: Normalised activity of LDH after 8 hours exposure to aminoacid modified USPIONs in solution. 264

Figure 4-4: Normalised activity of LDH as following Caco-2 exposure to different aminoacids modified USPIONs systems. 265

Figure 4-5: Effects of a short term exposure of Caco-2 cells to aminoacid modified USPIONs on ROS production. 267

Figure 4-6: Effects of a longer term exposure of Caco-2 cells to aminoacid modified USPIONs on ROS production. 268

Figure 4-7: TEM micrographs morphology of cell mitochondria after 24 hrs of Caco-2 cells exposure to different USPIONs system 269

Figure 4-8: Effect of aminoacid modified SPIONs on the activation of Caspase-3/7 in Caco-2 cells. 270

Figure 4-9: Hoechst 33342 / Propridium Iodide (Ho/PI) double staining in Caco-2 cells. 272

Figure 4-10: Amount of cell associated modified USPIONs (in terms of picogram elemental iron per individual cell). 274

Figure 4-11: Amount of cell associated modified USPIONs (in terms of picogram elemental iron per individual cell). 275

Figure 4-12: Fold change of side scattering in flow cytometry analysis for exposure of Caco-2 cells to modified USPIONs. 277

Figure 4-13: Fold change of side scattering in flow cytometry analysis for exposure of Caco-2 cells to modified USPIONs. 278

Figure 4-14: TEM micrographs of Caco-2 cells following exposure to modified USPIONs 285

Figure 4-15: TEM micrographs of Caco-2 cells following exposure to modified USPIONs 287

List of tables

Table 2-1: PDI of particles size for USPIONs batches produced at different flowrates as detected by TEM image analysis.....88

Table 2-2: PDI of particles size USPIONs produced at different rotational speed and detected by TEM.....95

Table 2-3: PDI of particles size USPIONs at different spinning discs sizes and detected by TEM.....102

Table 2-4: PDI of particles size produced using different total iron amounts and detected by TEM.....110

Table 2-5: PDI of particles size fabricated at different Fe^{+2}/Fe^{+3} ratios and detected from TEM images 117

Table 2-6: PDI of particles size produced using different amonium hydroxide solution and detected by TEM.....122

Table 3-1: The yield of colloidally stable USPIONs using either amino acids as base or HCl salts.....179

Table 3-2: Amounts of USPIONs associated amino acid following two different NPs modification methods.....200

List of abbreviation

USPIONs	Ultrafine superparamagnetic iron oxide nanoparticles
SPIONs	Superparamagnetic iron oxide nanoparticles
TEM	Transmission electron microscopy
TGA	Thermogravimetric analysis
DLS	Dynamic light scattering
FTIR	Fourier-transform infrared
ATR	Attenuated total reflectance
NPs	Nanoparticles
Caco-2	Human intestinal adenocarcinoma cell line
ANOVA	Analysis of variance
aa	Amino acid
Asp	Aspartic acid
His	Histidine
Phe	Phenylalanine
Leu	Leucine
Lys	Lysine
Glu	Glutamic acid
Gly	Glycine
Met	Methionine
Thr	Threonine
VDW	Van der Waals
FBS	Foetal Bovine Serum
ROS	Reactive oxygen species
NADPH	Nicotinamide adenine dinucleotide phosphate
DNA	Deoxyribonucleic acid
MDA	Malondialdehyde
4-HNE	4-hydroxynonenal
SDR	Spinning disc reactor
IR	Infrared
BISS	Binary iron salt solution

LSDR	Larger spinning disc reactor
SSDR	Smaller spinning disc reactor
PDI	Polydispersity Index
Cs	Lower solubility limits
LRTD	Local residence time distribution
DLVO	Derjaguin Landau Verwey Overbeek
TIA	Total iron amount
IEP	Isoelectric point
ν	Stretching vibration
δas	Antisymmetric deformation (bending) vibration
δs	Symmetric deformation (bending) vibration
δ	Bending mode of vibration
EMEM	Eagle's Minimum Essential Medium
PBS	Phosphate buffered saline
LDH	Lactate dehydrogenase
H_2DCFDA	2′,7′-Dichlorodihydrofluorescein diacetate
HEPES	4-(2-hydroxyethyl)-1-piperazineethanesulfonic acid
HBSS	HBSS (Hank's Balanced Salt Solution
SERS	Surface-enhanced Raman scatterin

Chapter1: Literature review

1.1 Introduction

The emergence of nanomedicine field, together with the advances in the last two decades in fabrication and characterisation of iron oxide NPs, have focused work of chemists, biologists, physicists, and engineers' preparing iron oxide NPs with characteristics desirable for diverse applications [1-3]. In this regard, particles size and morphology of USPIONs are thought to be the key features that determine their usefulness in different applications, whereby their properties can be custom-tailored, depending upon synthesis methods adopted [4,5]. In this framework, understanding and control over the fabrication parameters of a selected preparation procedure are critical prerequisite in tailoring of USPIONs attributes [6]. In general, there are three major procedures comprising chemical, physical and biological routes for superparamagnetic iron oxide nanoparticles (SPIONs) production. Up to the present time, the chemical route dominates, where around 90% of the exploited protocols in preparation of SPIONs adopt this route [4]. In the following paragraphs some of the major synthesis protocols will be discussed.

1.2 Routes of SPIONs fabrication

1.2.1 Chemical route for SPIONs fabrication

There are various protocols of SPIONs fabrication by chemical reaction route. The most popular techniques, which have been widely employed, comprise co-precipitation, microemulsion, sol-gel, hydrothermal, polyol,

electrochemical deposition under oxidised condition, sono-chemical and thermal decomposition [7].

1.2.1.1 Co-precipitation method

Massart, in 1981, was the first to describe a controlled precipitation of SPIONs upon exposure of iron (III) and (II) salts to an alkaline (also named 'liquid phase method') [8]. The simplicity, cost effectiveness, shape homogeneity, high productivity and a fabrication of SPIONs in a good state of 'cleanliness' (owing to the lack of organic and surfactant impurities) are highlighted by most of the later researchers as advantageous features of this 'basic' method [9-12]. Both types of iron oxide NPs (magnetite and maghemite) could be produced by applying this method. Although being the most convenient method, a poor crystallinity and wide particle size distribution are the major limitations associated with SPIONs produced by this method. This could be partially attributed to an inadequate understanding about the mechanism(s) of a new solid-phase-generation occurring during the process, as well as the mass deposition mechanism that freshly formed particles may follow to acquire their characteristics. Therefore, new different strategies of NPs fabrication were proposed by many researchers[13-16].

1.2.1.2 Microemulsion (ME) method

In general, the use of micro-emulsions in different fields evolved dramatically from initial studies in 1943 by Hoar and Schulman [17,18]. Given the need to improve the drawbacks of the classical co-precipitation technique, several fabrication approaches with employing microemulsions (in which SPIONs could be synthesised within nano-dimensional 'reactors') have been introduced to fabricate USPIONs with more uniform characteristics. There are numerous

key materials that were employed to function as a 'nano-reactor confinement'. They often include the following: amphiphilic surfactants [19-25], apoferritin protein cages [26-29], dendrimers [30], cyclodextrins [31,32], and phospholipid membranes [33,34]. Depending on the micro-emulsion nature, the restricted nano-reactor is represented in the formation of nano-sized liquid vesicles or droplets which could be either aqueous or non-aqueous. In the case of aqueous nano-reactor approach, a reverse water-in-oil micro-emulsion is prepared, otherwise oil-in-water micro-emulsions are normally used. Interestingly, both types of micro-emulsions have been used in fabrication of SPIONs [35-37]. In addition, different emulsifying agents were used to produce micro-emulsions[38-44]. It is important to mention that the pioneering attempt to prepare magnetic nanoparticles in micelles was done by Inouye *et al* [45].

This technology offers a key advantage in the process of fabricating SPIONs which includes the ability to produce a fine-tuned narrow size range that, consequently produces NPs with uniform physical properties. This takes the advantage of the capability to control the size of formed nano-sized droplets (that may be falling in the rage of 1-100 nm [46]). For instance, researchers successfully synthesised SPIONs with size range between 2 and 10 nm. By controlling micro-emulsion conditions, these NPs showed enhanced magnetic properties and protein binding affinity, making them suitable for certain advanced applications [47]. Moreover, manipulating the nature and amount of surfactant and co-surfactant, in addition to the other 'basic' parameters (alkali and initial total iron precursor concentration, and reaction temperature) have shown to have a major influence on varying the sizes and shapes of resultant

SPIONs [48]. For example, cubic magnetite NPs were fabricated when aforementioned fabrication conditions were appropriately adjusted [49].

In contrast to single-phase method (co-precipitation), the two-phase (microemulsion) method was found to have two main issues. Firstly, it is extremely challenging to yield large quantities of NPs (at a gram scale) which is an important issue for industrial scale of production. Secondly, the presence of unwanted (potentially toxic) surfactant and organic solvent residues in the final product increases both time and cost required to purify the end product. This normally makes micro-emulsion based process unfeasible for biomedical applications [6,7]. However, many SPIONs are being fabricated *via* adopting this strategy [40,50-52].

1.2.1.3 Sol-gel and polyol methods

Sol-gel method is another SPIONs fabrication strategy [53-55] which involves four subsequent steps. Concisely, an initial hydrolysis and condensation of mineral salts (in form of alkoxides) triggers the dispersion of metal oxide primary particles to form a sol state. Afterwards, an additional condensation (an inorganic polymerisation) occurs to induce a three dimensional network generation (a step of wet gel state formation). The third step involves enabling the wet gel to dry. Finally, the required crystalline structure could be obtained through treating the dried gel at an elevated temperature. As described, the sol-gel method is characterised by implementing more than one step in order to gain the final product. Nevertheless, substantial alterations in the above-mentioned procedure have been introduced [56] to make this method easier to adopt and make it convenient for those applications that demand fabrication of large amounts of USPIONs without a significant aggregation [57-61].

Interestingly, one of the most significant modifications introduced involves utilizing the polyols (e.g., ethylene glycol, and di, tri, and tetraethylene glycol) to act as solvents, thereby this increases the capacity for inorganic compound dissolution [62]. Furthermore, as a result of a relatively increased boiling point that polyols possess, a wide spectrum of operating temperature (from ambient temperature to their boiling point) could be used to improve and control the crystalline structure of SPIONs [63-65]. Owing to their properties, polyols offer additional advantages in controlling the NPs growth, to result in a stable monodisperse colloidal dispersion of USPIONs[66-70]. It should be mentioned that unwanted oxidation was not observed [71]. Furthermore, by following this method, polyols can suspend and remove the unreacted precursors. Therefore, an increased purity of fabricated SPIONs would be expected making them more suitable for biomedical applications [72].

1.2.1.4 Hydrothermal/solvothermal method

Another promising technique is called 'hydrothermal method' in which a new factor is introduced, that is 'pressure' [38,73,74]. This is normally performed *via* operating the production process in a sealed housing vessel, such as an autoclave, as a reactor. Herein, the notion of 'enhancing the solubility of inorganic precursors in water at elevated pressure (more than 2000 psi) and temperature (above 200°C)' was exploited as the principle condition [75]. Subsequent hydrolysis and dehydration steps should be accomplished in order to perform the required SPIONs crystallisation [38,76]. While taking advantage of that the reaction is achieved in an aqueous medium (hence no introduction of possible further toxicity), the very low solubility of iron oxide in water presents a highly beneficial factor in constructing of SPIONs by this method[77-79]. Similar

to other methods, manipulating several reaction conditions, such as iron precursors, temperature and reaction time, have decisive impacts on the particle size and shape of the resulting USPIONs[80-82]. Accordingly, iron oxide nanotubes have been fabricated by this method *via* controlling the iron concentration and reaction time [83]. Another study showed that reaction temperature, time, and pH value played a crucial role in fabricating USPIONs of variable NPs sizes and morphologies [84].

Using precursor solution other than water [75] in the hydrothermal method results in a different procedure which preserves advantages of both hydrothermal and sol-gel fabrication method. This modified procedure is called 'solvothermal method'. It was found that following solvothermal fabrication method enables a strict control over particles shape, size distribution, and crystallinity. These features could be fine-tuned by adjusting common variables [85,86]. Moreover, solvothermal method is also well-known for fabricating hollow iron oxide NPs of spherical shape with sizes larger than 80 nm [87,88]. Despite of the unique size-tuning characteristics, the long reaction time required is so far considered as a major shortcoming making this technique of limited use. Nevertheless, recent successful improvements have addressed this problem, making the method applicable for scaling-up [89].

1.2.1.5 Sonochemical method

The required energy for SPIONs preparation might be supplied *via* different source. To this end, it was discovered that a powerful ultrasound radiation (20 kHz–10 MHz) has a potential capacity to drive a chemical reaction of molecules [90]. In this technology, liquids chosen to be exposed to a high intensity ultrasound will exhibit acoustic cavitation (the physical phenomenon that become

accountable for chemical effects owing to formation, enlargement and implosive collapsing of a bubble) [91,92], where transient hot spots have a temperature of 5000–25,000 K and pressure of ~1800 atm and are 'instantly born and die' (collapsed) within nanosecond lifespan [93]. Accordingly, these extreme environmental conditions at the rate of 10^{11} Ks^{-1} [94,95] are optimum for generation of amorphous nanoparticles [96-98]. Monodisperse nano-sized USPIONs could be prepared as a consequence of a shear effect of vortexes generated in a sonicated media[99-101]. Moreover, sonochemical synthesis technique was found to be highly energy efficient - capable of saving ~90% of energy in comparison with those methods that utilize conventional energy sources for NPs fabrication [102]. Herein, the sonication time, power and frequency play significant roles in the particles consistency (in size and shape) [101,103,104] and the rate of production of the ultimate product [105].

1.2.1.6 Electrochemical synthesis

Since it was launched by Reetz *et al* [106], the electrochemical synthesis method has been widely reported as one of the most effectual technique for fabrication of mineral nano-clusters with numerous non-spherical nanostructures, such as nanowires [107,108], nanorods [109-111], nanoflakes [112,113], and nanosheets [114]. The fundamental principle of this method includes an electrolyte cell with a anode and a cathode [115]. Referring to its cost-effectiveness, low operational temperature and simplicity, electrochemical deposition has also been used to prepare different iron oxide NPs[116-118]. Likewise, a group of researcher have recently published a novel modification of the method for preparation and *in situ* surface modification of SPIONs in 'one pot' protocol [115,119-124]. Apart from several attempts at controlling the particle size of generated USPIONs

[125,126], it is however difficult to achieve monodispersed and ordered products by following this approach [64].

1.2.2 Physical route for SPIONs fabrication

Although introducing a "matrix" providing a restricted zone of reaction – used as the main principle in producing NPs with narrow size distribution in microemulsion, sol-gel and polyol methods – the production of NPs with narrow particle size distribution with surface free from either chemically or physically bound material (surfactants, polymers, and complexing agents) is in fact extremely challenging [127]. To this end, a physical 'reaction confinement' could function as an alternative option to achieve fine-tuning of particles construction in which other (potentially toxic) materials were excluded. To achieve this, the method adopted in the current work uses the experimental set up where the reactants were streamed through a separate carrier tubing system which meets at Y-shaped 'connector' (a particular point designed to force the reaction precursors streams to meet) to initiate nanoparticles formation. The major advantage obtained by this is the ability to control particles growth within a well-defined tubular reactor they are flowing in. In similar works in the literature, a different flow systems have been tested in which, for instance, an injection valve could be positioned at the junction unit[128-130]. With the intention to achieve both a reduction in reaction time and improvement in particle homogeneity, the principle of 'flow-injection analysis', suggested by Ruzicka *et al* [131], was developed to successfully fabricate mineral NPs with controlled morphology [132].

Various strategies such as laser induced pyrolysis which is recognised as gas-phase method [133-137], pulsed laser ablation [138-140], and high-energy ball milling [141-144] were also employed in construction of different inorganic

nanocrystals, including SPIONs [145,146]. A considerable cost demand has been noted in operating these methods, due to the expensive equipment used.

Regarding pulsed laser ablation, a standard model of the system, as presented by Wang *et al* [147], comprises of vacuum chamber housing a furnace and connected from both sides to the laser beam source and NPs collector. According to Wang *et al*, spherical iron oxide NPs with a size range of 5 to 90 nm were successfully fabricated by this method. It was found that the diameter of fabricated SPIONs is strongly related to both laser power density and carrier gas pressure [147]. Another study demonstrated a fabrication of gold and magnetite composite NPs through exploiting a unique laser processes in water. In this case, the researchers used a modified pulsed laser ablation technique in liquid for NPs fabrication [148].

1.2.3 Biological route for SPIONs fabrication

The adoption of green chemistry principle for the production of SPIONs has been on increase. Since the first discovery around 40 years ago [149], certain magnetotactic microorganisms are recognised to synthesise iron oxide NPs through intra and extracellular mineralisation processes [150-152]. In 2008, more detailed information including development of functional biomineralised magnetite NPs was reviewed [153]. Given that biologically generated iron oxide NPs possess well-defined morphology and crystallinity along with high biocompatibility [154-157], these are the intrinsic advantages of the method. Some limitation were however noticed, such as substantially slow and uncontrolled rate of production. Therefore, the concept of 'bioinspired' or 'biosynthesis' processes for iron oxide NPs fabrication is increasingly studied and improved. [158-165].

1.3 Surface modification of iron oxide NPs

Bare iron oxide NPs are characterised by possessing large active surface area which is hydrophobic in nature. Therefore, after NPs have been dispersed in an aqueous solution, hydrophobic interactions among NPs continue to function until large agglomerates start to develop [166-170]. The obtained aggregates undergo further clustering under the effect of an additional force which is magnetic dipole-dipole interaction. Finally, all dispersed NPs would precipitate in their solution [171]. In this regard, NPs surface modification with a suitable material is becoming indispensable step for preserving the colloidal stability of iron oxide NPs for further applications.

Basically, both modified iron oxide NPs structures and materials used in modification process will be reviewed in the following sections.

1.3.1 Surface modification by organic materials

There are several types and categories of organic chemical substances could work to modify and functionalise iron oxide NPs surfaces. Various biological areas have exploited the advantages that organic modifying agents may offer. For instance, kinetically, improved blood circulation and half-life could be achieved using this kind of materials. In addition, NPs-associated layers of organic substances will endow more active functionalities that, in turn, could be considered as platform for further modifications. Here, other organic or inorganic materials such as therapeutic and targeting agents are potential candidate for the second stage surfaces modification [172-174].

1.3.1.1 Small molecules and surfactants

Attachment of various small molecules and surfactants could be easily allowed *via* an option of presence of numerous hydroxyl group directly associated with the surface of iron oxide NP. In addition, small molecules- and surfactant-modified iron oxide NPs are known for maintaining small hydrodynamic diameter with considerable magnetic properties compared to the bare counterparts.

Researchers have extensively exploited iron oxide NPs bound surfactant in controlling the growth of NPs during synthesis stage and preventing them from being aggregated. As an example, citrate-stabilised iron oxide NPs provide extremely stable colloidal dispersion in water [175]. Moreover, numerous conventional surfactant were engaged in protecting iron oxide NPs against aggregation during preparation process, such as sodium dodecyl sulfate [176], cetyltrimethyl ammonium bromide (CTAB) [177], alkyl benzenesulfonate (ABS) [178], and long-chain thiols [179]. The widely used fatty acid molecules, like oleic acid, oleylamine, and octadecylene, were successfully involved in providing monofunctional stabilised iron oxide NPs prepared by thermal decomposition methods [180,181].

Silane is another group of small molecules that can be covalently linked with the surficial iron oxide moieties. These molecules are vulnerable to further events in which a crosslinking reaction among them could render the NPs core tightly surrounded by a thin inorganic silica layer. Several members of silane were used to add different functionalities (such as amine, thiol, and carboxyl) to the surface of bare iron oxide NPs [182,183]. Likewise, it was found that dopamine can function as a stable anchor in order to present more functional groups on the surface of

iron oxide NPs [184,185]. As a result, dopamine-modified iron oxide NPs have engaged in more diverse fields of application[186-188].

1.3.1.2 Large molecules or polymers

For most of applications that are related to biomedicine, polymer-modified iron oxide NPs are strongly favoured over small molecules or surfactant-modified counterparts. There are two main reasons for this preference including: (i) enhanced stability due to increased repulsive forces that, in turn, work to balance both magnetic interaction and Van der Waal (VDW) attractive forces, (ii) improved blood circulation time, stability, and biocompatibility [189].

1.3.1.2.1 Polymers deployed in modifying iron oxide NPs

Polymers employed in preparing functionalised iron oxide NPs are either naturally occurring or synthetic. In contrast to the synthetic polymers, natural polymers are considered as water-based materials and thus could render the functionalised NPs with highest degree of biocompatibility. Starch, chitosan, dextran, gelatin, cellulose, and proteins are natural type of polymers and have all been investigated with iron oxide NPs [190,191], while others like poly (ethylene glycol) (PEG), poly(methyl methacrylate) (PMMA), polyethyleneimine (PEI), and poly(vinyl alcohol) (PVA) were fabricated in laboratory.

1.3.1.2.1.1 Polyethylene glycol (PEG)

Polyethylene glycol (PEG) is one of the most hydrophilic polymer involved in biomedicine-related formulas as a result of several key features it has[192-195]. Importantly, the capacity of PEG to conjugate different biological moieties allow it to play a crucial role in improving *in vivo* usage of biomolecules. It was also noticed that a prolonged circulation time has been recorded after treating

PEG with NPs which indicate enhanced biocompatibility and reduced immune system recognition [196,197].

1.3.1.2.1.2 Polyvinyl alcohol (PVA)

PVA is another widely used synthetic polymer. Hydrophilicity, biocompatibility, and capability to improve NPs size uniformity and dispersion stability are the main features that this polymer could offer upon modifying SPIONs surfaces [198,199]. Accordingly, PVA-modified SPIONs are found to be good candidate in drug delivery applications[200-202].

1.3.1.2.1.3 Dextran

Dextran is a naturally occurring polysaccharide polymer. Similar to previous polymers, it is neutral, water soluble, biocompatible, and biodegradable. In addition, it is well-known to modify iron oxide NPs [203,204] and, therefore, considered a promising multipurpose platform for targeted molecular imaging, diagnostics, and therapy [190]. Dextran adsorption layers are suitable for further functionalised and bio-conjugation with additional targeting biomolecules such as genes, proteins and enzymes [190,205], Moreover, the added active ligand could render dextran-SPIONs with improved pharmacokinetics such as blood circulation time [206].

1.3.1.2.1.4 Chitosan

Comparable to dextran as a natural occurring polymer, chitosan is hydrophilic, biocompatible, and biodegradable, however, it has alkaline nature. Several studies showed effective encapsulation of iron oxide NPs with chitosan polymer to produce highly useful system for different biomedical applications[207-209]. Interestingly, chitosan coated SPIONs was found to function as an effective antimicrobial agents [210].

1.3.1.2.2 Techniques followed to prepare NPs-polymer composite

Workers in this field have recognised several approaches that were investigated to allow combining different polymer with iron oxide NPs. In this review, the most known strategies were summarised in two main categories depending on the nature of interaction existed between core (iron oxide NPs) and coat (polymer), whether they are physical or chemical [189,211].

For the physical adsorption approach, there is two main techniques followed. The first is a process depending upon electronic structure of polymer-related functionalities that is barely perturbed over adsorption where the fundamental driving force is VDW forces. In this regard, copolymers are good candidate to stabilise and coat NPs either during or after the fabrication of iron oxide NPs. With diblock copolymers, it is seems understandable that one block could function to enable surface adhesion (usually called anchoring block) while the other block would be responsible for rendering iron oxide NPs thermodynamically stable in aqueous media. By manipulating the block component of copolymers, researchers have successfully prepared wide variety of magnetic NPs structures [212,213].

The second technique of this approach include enabling of either self-assembly or self-association of block copolymers in aqueous media (depending on the polymer chemistry) to form modified iron oxide NPs. In self-assembly of a highly stable core/shell micellar NP, the hydrophobic terminals of an amphiphilic copolymer directed towards iron oxide core leaving the hydrophilic tails to face the continuous media thereby rendering NPs stability [214-218]. On the other hand, self-association process include ionic interaction of a copolymer having both anionic and cationic blocks with iron oxide NPs. In this case, media

pH could control and determine which block of the copolymer will interact with the solid surfaces resulting in association required [219]. With similar principle, a good progress in preparing various photosensitive and pH-sensitive composites with iron oxide NPs has been achieved [220-223].

1.3.1.3 Biomolecules

Iron oxide NPs that are surface-engineered using biomolecules (such as proteins, antibodies, polypeptide and enzymes) show superior biocompatibility in comparison with surfactant and polymers engineered counterparts [224-226].

In this case, physical adsorption-related techniques are often adopted for preparing such kind of modified NPs. For instance applying ultrasound energy by sonicating the aqueous solution of both iron oxide NPs and bovine serum albumin result in fabricating protein-coated magnetite NPs [227]. Another method of functionalisation has been performed via simply transferring iron oxide NPs into a culture media containing different amount of fetal bovine serum (FBS) [228]. However, poor conjugation effectiveness to iron oxide NPs has been noticed as a main limitation relating to the involvement of biomolecules for biomedical application. This gives rise to a problem of cost effectiveness as more of these expensive material should be used to overcome the existed obstacles (low NPs binding affinity). Two steps were followed to avoid these problems, first, modifying bare NPs first with small or large molecules and second, performing attachment of biomolecule of interest with active functionalities of the already modified NPs [229-231]. For instance, antibody-decorated iron oxide NPs have been successfully exploited to capture and separate human breast cancer cells from fresh whole blood [232].

1.3.2 Surface modification by inorganic materials

Although using organic materials to modify and functionalise iron oxide NPs has achieved a considerable progress, the ultimate shape, stability, and compatibility along with surface structure and magnetic properties remains to be controlled. As a second choice, modifying iron oxide NPs with inorganic materials offer a good opportunity for more effective control of these properties. In addition, using this kind of surface modifying agents render iron oxide NPs a suitable candidate for further multi-functionalisation stage. Here, more application fields such as catalysis, biolabelling and bioseparation can obtain substantial benefit from involving this kind of NPs.

1.3.2.1 Silica

Silicon dioxide was found to be a good candidate for coating and modifying iron oxide NPs [233-236]. In addition to the inert characteristics that silica coating may offer, it is also known for providing an excellent separation barrier between biological environment coming into a contact with active material 'core', hence reducing USPIONs toxicity [237,238].

There are few different methods that have been adopted by researchers to fabricate iron oxide NPs covered by a layer of silica. The well-known Stöber synthesis is the first strategy used. The process includes a deposition of silicon dioxide on the surface of iron oxide NPs to form a uniform core-shell Fe_3O_4 - SiO_2 structure. The *in situ* generation of silicon dioxide occurs *via* hydrolysis and condensation of a precursor, such as tetraethyl orthosilicate (TEOS) [239-241]. The second method is based on the deposition of silicon dioxide from a precursor solution containing silicic acid [242-244]. Works applying this method have shown

that this, silicic method, may be more efficient in modifying iron oxide NPs surfaces than the TEOS method [243]. Furthermore, a wide spectrum of NPs size could be fabricated with a controlled tuning.

The third method of preparing Fe_3O_4-SiO_2 composites uses the principle of microemulsion in which both iron oxide NPs (core) and silicon dioxide (shell) undergo *in situ* seeding and salinisation processes inside emulsion droplets. Differently from the previous techniques, choosing a proper surfactant is a key factor influencing this preparation process [245,246]. Fine tuning of particles size can be achieved *via* controlling droplets size [247].

1.3.2.2 Carbon

Silica-coated iron oxide NPs showed improved colloidal stabilisation improving surface functionality and biocompatibility of USPIONs, compared to the above mentioned surfactant-coated counterparts, while the main carbon coating's advantage is a remarkable stability in environments of extreme conditions, in term of acidity or basicity, high temperature, or pressure [248].

There are numerous approaches using different sources or precursors of carbon, whereby glucose was the first material exploited. Once dissolved in aqueous solution, glucose could form carbon capsule *via* a so called hydrothermal treatment [249-252]. Sodium acetate is also used in some protocols [253]. An interesting alternative method includes using a polymer as a replacement for the glucose monomers. In this case, a step of preparing iron oxide-polymer composite NPs is followed by an annealing stage to 'transfer' polymer to carbon layer [254].

1.3.2.3 Metals

Covering iron oxide NPs with metal has numerous potential advantages where the core iron material could be effectively protected against environmental oxidation, particularly, as an example, for long-term storage. In this regard, noble metals are of particular interest, also due to their potential for further functionalisation with different types of materials, such as ligands [255], polymers [256] or other small molecular weight functionalities [257]. Gold and silver [258,259] are of the most metals have been used to modify the surface iron oxide NPs.

1.3.3 Microstructure of surface-modified iron oxide NPs

Depending on the orientation of both core and shell (coat) materials, different structures have been created for modified iron oxide NPs. Major types simply include: (i) core-shell and reverse core-shell structures [260,261], (ii) multicore-shell structures, where the core material is dispersed within a matrix of shell forming material [262,263] and (iii) yolk-shell structures, a hybrid of core-shell and hollow structures that could be described as core-void-shell configuration [264-266].

1.4 Behaviour of metal and metal oxide in biological environment

1.4.1 An overview

With the potential of a widespread use of nanoparticles not only in medicine [267], but also in many other industries and for many other applications, it is important to consider their behaviour in the biological environment and their potential safety issues [268,269]. Following metal and metal oxide NPs fabrication (Figure 1.1), they will undergo several cycles of aggregation and disaggregation and a 'pollutant' adsorption and desorption from different biological environments [270,271]. The metal and metal oxide NPs can enter a human body by different

routes, including exposure via inhalation, or via oral route through e.g. consumption of food and water in which these NPs are present [272,273]. Depending on the entry route, NPs will interact with the surrounding biological environment and will cause a biological response [274,275]. It is important to notice that environment-borne metal nanoparticles with adsorbed organic material on their surfaces (e.g. car exhaust particles) possess a great potential to amplify the toxic effect of both particle (core) and adsorbed (coat) material [276-279].

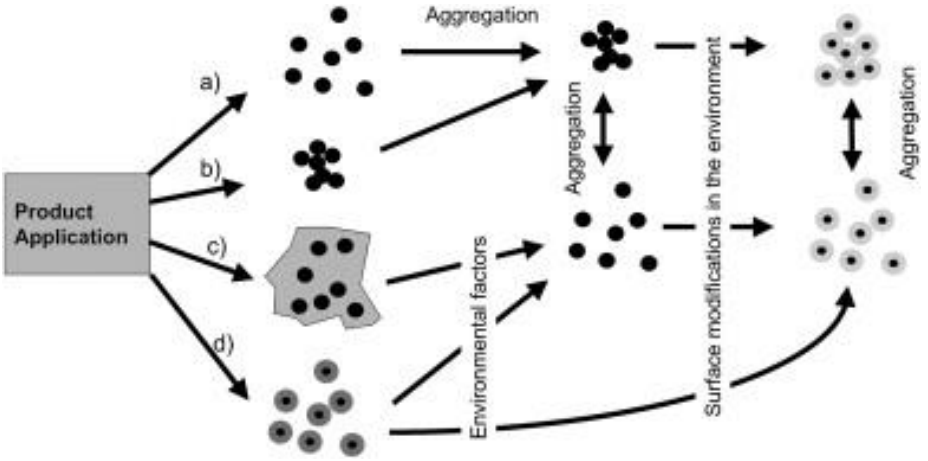


Figure 0-1: Schematic illustration of NPs potential behaviour in environment.

(a) and (b) direct release of individual and aggregated NPs, respectively. (c) and (d) liberation of embedded and functionalised NPs, respectively. In case of (c) and (d) environmental factors (for example. sunlight or microorganism) trigger a release of free NPs which in turn experience aggregation-disaggregation behaviour. Ultimately organic material (pollutant) is adsorbed onto NPs resulting in colloidally more stable nano-objects.

1.4.2 The entry of iron oxide NPs (USPIONs) into natural surroundings

The following section discusses the reasons for an increasing abundance of iron oxide NPs (USPIONs) in human environment and potentially functioning as a source of accumulated toxicity.

Different natural events (such as volcanoes and fires) routinely produce and emit different forms of iron oxide NPs in nano-sized crystals forms [280], that cause a serious hazard. However these events occur in limited locations, and with limited frequency [281]. On the contrary a rapid and widespread proliferation of nanotechnology-related applications [282], as noted above, is a cause for the deep concern about metal oxide nanoparticles effect on the ecosystem. Being a metal-based objects, iron oxide NPs (e.g. USPIONs) retain certain characteristics, including strong magnetic [283,284] and reducing properties, and high adsorption capacity [285]. These features make USPIONs attractive material in various applications, including environmental remediation [286,287] (such as decontamination of wastewater [288,289] *via* sorption of both heavy metals [290-294] and organic contaminants [295,296]), biomedicine (e.g. therapeutic drug delivery, cell labelling [297-299], and MRI contrast agents) [189,298,300-303], health care (such as nanoscale biosensors [304-308], nanocarrier for vaccination [309,310], and antimicrobial activities [210,311-313]), agriculture and food (for tackling plant diseases propagation and improve crop yield) [314-317], energy (as in fuel cells and batteries) [249,318,319], defence and aerospace [320,321], construction (iron oxide-based pigments could be extensively utilised for colouring concrete, brick, tile, and other construction materials) [322-324] , and finally electronics [320,325]. Therefore, with such a

widespread use / potential use ‘emission’ of these NPs into human environment needs to be considered with great attention.

1.4.3 Exposure of iron oxide NPs to human

Human contact with fine/micron-sized iron or iron oxide particulates has been assessed. Historically particularly for those working in mines and certain industries, a permissible exposure limits were established. This is ~ 5-14 mg/m^3 of fine iron oxide dust in atmosphere over the course of an 8 hours work day [326]. However, this limit does not provide an accurate safety assessment of iron oxide NPs exposure for all the potential exposures, as mentioned above. For instance, a study on the effect of prolonged exposure to iron oxide aerosol with diameter less than 100 nm has revealed dramatic discrepancies in the limit that is triggering a hazardous response. This study claims that even 0.083 mg/m^3 or 66,800 particles / cm^3 is sufficient to produce significant elevation in oxidative stress and inflammatory biomarkers in exhaled breath condensate (EBC) and urine [327].

Upon swallowing or inhalation, ingested nanoparticulates approach normal biological barriers – e.g. lung or gut epithelial tissue. At this stage, a possible interaction of the nanoparticles with biological structures at these locations will occur.

1.4.4 NPs-biological system interaction following injection route

If nanoparticles are used for therapeutic purpose, with normally be injected via a parenteral route. In this case their first interaction occurs with biological molecules and structures in systemic circulation and extracellular fluid [328].

Formation of a layer of adsorbed proteins and other biological molecules on NPs currently usually referred to as 'protein corona' [329], as will be discussed below.

1.4.5 Metal oxide NPs – protein interaction (protein corona)

Once present in the physiological environment, an immediate adsorption of a number of proteins occur to form a dynamic corona ('soft corona') [330]. A few minutes later, protein rearrangement occurs governed by a competition between NPs-protein and protein-protein interactions to form a 'long-lived' adsorptive layer called 'hard corona' [331,332]. Several hundreds of distinct protein have been identified in human blood plasma [333]. Therefore the constituents of protein corona is complex and is also unique to each NPs system (material) where it was found that both NPs nature and physiological environments related parameters play significant roles in constructing the corona [334]. These parameters been extensively reviewed by various groups of researchers [330,335-337].

1.4.6 Protein corona formation and composition

1.4.6.1 Exposure to complex solutions

1.4.6.1.1 Cell culture media

When NPs are tested in *in vitro* cell culture models, they are exposed to the 'complex solutions' i.e. media used for the cells to grow. Studies have shown that the presence of FBS, as a usual supplement in different cell growth media, results in the formation of 'corona' on the NPs surface [338]. However, for different serum sources used, the corona's properties may change due to variations in the serum protein compositions [339 340].

1.4.6.1.2 Protein concentration effect

The protein corona's composition and properties are found to be significantly affected by the initial concentration of plasma proteins in a medium [341]. Upon testing silica NPs against three concentrations of plasma, 3%, 20%, and 80%, different protein patterns were found associated with the NPs. This phenomenon was explained by different surface activities of proteins; those with higher concentration and diffusion will adsorb initially while those with present in small quantities but with high affinity (e.g immunoglobulins) will adsorb at later stages and replace initially adsorbed material (so called Vroman effect) [342]. Another study showed that, for magnetite NPs, increasing human serum concentration in a buffer will gradually increase the relative abundance of some constituents of protein corona compared to others [343]. However, the modification in protein corona composition did not produce significant effects on the phagocytosis of NPs, unless the abundance of the 'recognisable' protein is placed onto the surface of the NPs [344].

1.4.6.1.3 Exposure time

As mention above, the interaction between NPs and plasma proteins occur instantaneously where, within first 30 second of interaction, around 300 distinct proteins attached to NPs have been detected [332]. Nonetheless, prolonged exposure to biological media was found to enhance the variety of proteins adsorbed [338]. Although the adsorbed proteins continue to exchange with those present in the environment, due to differences in the binding affinities and molecular weights (lower molecular weight protein are favourable in the interaction process), after some period of time the overall composition of protein corona remains similar [338].

1.4.6.1.4 Stationary and flow conditions

The effect of static or flow state is thought to be important parameter on the quantity of protein adsorbed and the corona composition. Once in human body, NPs will face different shear stresses in different hydrodynamic conditions. For instance, the velocities of blood stream in blood vessels are: 0.03, 15, and 40 cm/sec in capillaries, superior and inferior vena cava and aorta, respectively [345,346]. For example, it was found that polyethylene glycol (PEG)-coated liposomes acquired more negative charge under a dynamic flow state of 40 cm/sec, compared to their 'static' counterparts – despite of their similar size and other physicochemical properties. Furthermore, higher diversity of adsorbed proteins in corona formed under flow conditions was observed [347].

1.4.6.1.5 Temperature

The role of temperature on the corona formation has obviously attracted less attention as *per* limited range of human body temperature [348,349]. However, it was noticed that the slight change in media temperature resulted in significant variations of protein corona composition after incubation with FBS. As an examples, dextran-coated SPIONs with different surface chemistries showed maximum protein adsorption around 40°C for positively charged particles, similar protein peaks have been seen (but to less intensity) for neutral and negative surfaces at 43°C and 37°C respectively [350]. Another study has revealed that the quantity of adsorbed protein on copper NPs increased proportionally with incubation temperature from 15°C, 27°C, and 37°C to 42°C [351]. This highlights the importance of the experimental conditions used when designing such studies.

1.4.6.1.6 Biological media pH

The NPs can be exposed to biological environment of different pH values when applied e.g. for therapeutic purpose, depending on the route of applications and a subsequent biodistribution in human body [352,353]. For example, intracellularly present lysosomes have pH in the ~6.8 and 4.5 range [354], cancer or tumour mass is also considered more acidic [355,356].

1.4.6.2 NPs-related parameters

1.4.6.2.1 NPs size

It was found that the curvature of NPs surface, which is an intrinsic reflection of their sizes [357], can play a significant role in the process of surface-adsorption. The extent of surface curvature has a great influence on the conformational changes that proteinaceous adsorbed materials may undergo [335,336,358]. In this regard, a study was designed to investigate the adsorption of some blood proteins onto gold NPs with different particle sizes (i.e., 5, 10, 20, 30, 60, 80, and 100 nm) [359]. It revealed that the rate of protein binding is directly proportional to NPs size until a certain limit (< 60 nm), beyond which irregular relationship was observed. This observation has been attributed to the difference in conformational flexibility that various proteins may have at the surface with different curvature. Similar was observed in the later studies [360-362]. Moreover, it was reported that corona thickness was increased for smaller size NPs, and that the adsorbed proteins experience less conformational modification [363-365]

1.4.6.2.2 NPs shape

Interestingly, by using two geometries of gold NPs (nanosphere and nanorod), it was found that NPs morphology exerts a considerable effect on the amount of protein adsorption, whereby protein analysis results revealed that gold nanorods

have higher protein surface density compared to gold nanosphere counterparts [366].

1.4.6.2.3 NPs surface properties

1.4.6.2.3.1 Effect of surface charge

The nature and extend of particles surface charge was found the play a crucial role in determining the composition of the formed protein adsorption layer and hence, their subsequent biodistribution. As an example, the early work on elimination of positively charged NPs by reticuloendothelial systems revealed a positive charge has a significant limitation on the application of these NPs [4,367]. It has been proposed that NPs surface charge functions to effect denature the adsorbed protein, and that this occurs at higher rate for charged relative to uncharged counterparts - which in turn makes the circulating NPs recognisable by the human immune system [340]. High binding affinity for protein adsorption was reported for both anionic liposomes and cationic lipid-vesicles, when exposed to plasma proteins [368,369]. In this context, an extensive body of literature reports on the studies with PEGylated surface, the areas that has be extensively reviewed elsewhere [370].

1.4.6.2.3.2 Surface roughness/smoothness

A number of recent studies reported on the effect of the presence of nanoscale local features have an important effect on the protein adsorption whereby protein adsorption can be, for instance, enhanced due to reduced repulsion forces [371,372].

1.4.6.2.3.3 Surface hydrophilicity/hydrophobicity

Hydrophobic surfaces are found to bind more protein in comparison with their hydrophilic counterparts [361,373,374] with an increased extent of structural changes of adsorbed protein molecules [375]. An extensive protein denaturation results in

enhanced effect on immune system [376-378]. It is very important to mention that NPs at their isoelectric point (PI) undergo minimum surface charge, which leads to the hydrophobic interaction to dominate protein binding and hence maximum protein denaturation would occur [379,380].

1.4.6.2.3.4 Surface functionalisation and coating

Controlling protein corona formation, and possibly composition, can be achieved *via* NPs surface functionalisation with a suitable material. In this context, Poloxamine 908 surface modified polystyrene NPs and Pluronic F127 surface modified carbon nanotubes and silicone dioxide NPs resulted in a significant reduction in serum protein adsorption [381,382]. A summary of the role of various coating materials on different NPs in term of protein species bound and biodistribution was reviewed by Aggarwal *et al.* [377].

Other parameters that are less studied but could still be important players in the corona formation involve protein to NPs ratio [335], electron transfer capacity [371], and NPs crystallinity [383].

1.4.7 The noxious response to metal oxide NPs

The main cytotoxic effect observed for metal oxide NPs (including USPIONs) is typically mediated *via* a generation of reactive oxygen species (ROS) [274,384]. Upon ROS overload, the subsequent cellular responses to oxidative stress are induced and, if 'repair' process fails, the cell apoptosis normally starts [385-387]. However, a non-ROS-mediated toxicities have been also described for metal oxide NPs. Here, an excessive accumulation of NPs associated with the cell membrane [388-391], ion release from NPs [391-394], and direct interaction of metal oxide NPs with 'death receptors' [395,396] were attributed to be the reasons of non-

ROS induced cytotoxicity, as illustrated in Figure 0-2. As the NPs in the current work are iron oxide NPs, the following sections will focus on toxic mechanisms reported for this type of NPs.

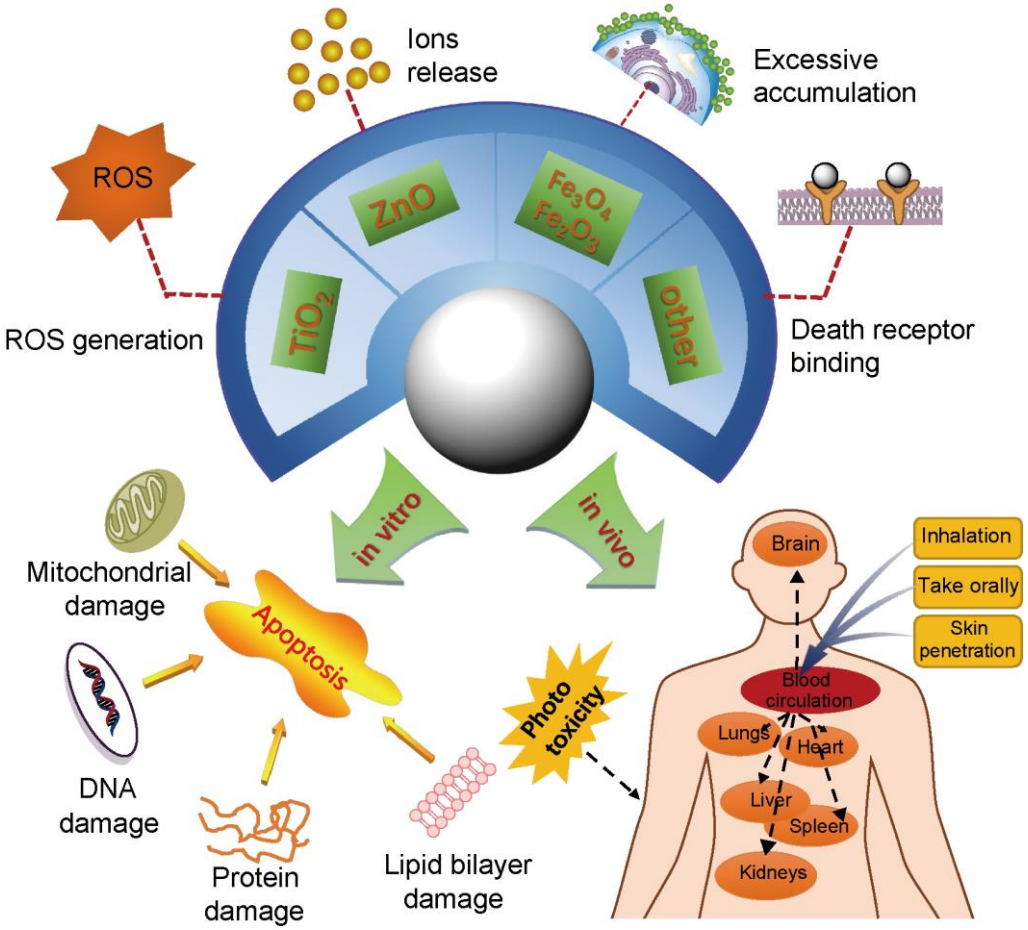


Figure 0-2: Schematic diagram of metal oxide NPs toxicity.

The damage of phospholipid bilayer of cell organelles, particularly mitochondria, and protein and DNA injury is the main 'cell level' toxicity of the NPs. Both ROS and non-ROS toxicity pathways are illustrated. The non-ROS mechanism is triggered by ion release (detachment) from NPs, excessive accumulation of NPs on the cell surface, and association of NPs with specific' death receptors'. In vivo toxicity results from entry of NPs into human body through e.g. inhalation, oral, and dermal routes and their subsequent biodistribution.

1.4.7.1 ROS-mediated cytotoxicity of metal oxide NPs

As mentioned above, most research to date has proposed that ROS production and subsequent oxidative stress is the major cytotoxic pathway induced when cells are exposed to metal oxide NPs [397-399]. There are few main factors that induce the process of ROS production by NPs. First, pro-oxidant functional species exist in the vicinity/at the NPs-bioenvironment interface. Second, intrinsic properties of NPs material and surface structure (such as redox reaction of transition metal NPs). Third, direct interactions/contacts between NPs and cellular compartments [397,400,401]. These will be in more details discussed in the following paragraphs.

1.4.7.1.1 Parameters affecting ROS liberation

1.4.7.1.1.1 NPs-related parameters of ROS liberation

In studying the variables that control NPs 'efficiency' in triggering the production of ROS, iron oxide NPs will be mainly discussed, as type of NPs used the current work.

1.4.7.1.1.1.1 Chemical composition

A cycle of two reactions, called Haber-Weiss and Fenton, function to regulate the process of hydroxyl radical production (the most hazardous ROS) [402,403] relying on the reducing capability of ferrous iron in USPIONs. In addition, ferrous iron has an ability to directly reduce molecular oxygen dissolved in culture medium to produce ROS. In this regard, two kinds of iron ions are working simultaneously, the dissolved and NPs surfaces-bound iron species. Considering the ratio of ferrous to ferric iron several literature findings suggest that: (i) increasing ferrous ion within the structure of NPs leads to their enhanced reactivity i.e. more ROS production [404,405], and (ii) under the same condition of

NPs surface area and volume, magnetite has higher effectiveness in generating hydroxyl radical than its maghemite counterparts [406].

1.4.7.1.1.1.2 Particles size

Particles size reduction has direct effect on increasing iron oxide solubility due to higher surface free energy [407]. Therefore, an increased amounts of highly reactive iron ions will be dissolved in the dispersion medium and can be expected to promote ROS production – arising now form both dissolved and solid surfaces-associated ions [408]. It was determined that the reduction reaction rates of iron increase proportionally to the surface area [409-411]. For instance, 10 - 100 times higher surface area normalised reduction rate constant was calculated after increasing the specific surface area from 0.9 m^2/g to 33.5 m^2/g [412]. Similar trend was reported by another group [413-415]. In addition, the catalytic efficiency in hydrogen peroxide decomposition has been found to be increasing after increasing specific surface area [416].

1.4.7.1.1.1.3 Degree of crystallinity

Iron oxide could be present in different crystalline phases where these phases show varied capability to initiate ROS. An inverse relationship was suggested between thermodynamic stabilities of crystalline phases and the solubility of ferric iron, i.e. the rate of reductive iron dissolution seems to follow the order of ferrihydrite > lepidocrocite > maghemite > goethite > hematite where ferrihydrite has least ordered molecules in comparison with hematite [407,417,418]. This relationship has been strongly supported in the literature [419-422]. In addition, the recorded Gibbs free energy for less thermodynamically stable iron oxide NPs is higher than that of more crystalline structure with equivalent dimensions. This may play an important role in enhancing iron dissolution and a consequent ROS

induced toxicity. Interestingly however, it was found that higher ROS generation rate was associated with an increased crystalline structure [423-425].

1.4.7.1.1.2 Bio-microenvironment related parameters of ROS generation

1.4.7.1.1.2.1 pH effect

It is important to notice that oxidant species produced in the redox reaction of iron ions are significantly affected by pH. At low bio-microenvironment pH, hydroxyl radicals were detected as the dominant oxidants, while neutral or alkaline conditions appear to support the production of ferryl-oxo complexes as main oxidant [426,427]. In this regard, it is essential to mention that hydroxyl radical has superior power, as a one-electron oxidant, compared to ferryl-oxo complexes [428]. Moreover, an interesting study has reported that the rate constant, and hence the efficiency, of hydrogen peroxide decomposition to more harmful species increased from 0.019 to 0.067 M^{-1} s^{-1} after changing media condition form acidic to alkaline in presence goethite [411]. An additional study has confirmed these results [429].

1.4.7.1.1.2.2 Reducing agents effect

Various intracellular and extracellular reducing agents (such as Nicotinamide adenine dinucleotide phosphate (NADPH), glutathione, cysteine, succinate, ubiquinol, retinol, tocopherol, and ascorbic acid) function to maintain a reducing environment of biological fluids [430]. As a result, an increase in the reductive dissolution of iron oxide NPs will inevitably occur and lead to a growth in the damaging ROS related to the dissolved iron [423]. Similar situation happens inside endosomes and lysosomes that would contain iron oxide NPs, causing severe cell damage [431-433].

1.4.7.1.1.2.3 Other effects

In biological fluids, a very wide range of organic substances with miscellaneous biological functionalities and chemical groups (such as carboxylate, phenolate, thiol, and amines) are found to be ubiquitous. These organic substances have a potential capacity to interfere and modify the scavenging ability of reactive intermediates of the redox reaction. This mechanism is mediated by their interaction or complexation with ferrous iron, thereby allowing an increased production of hazardous oxidant to initiate the toxic effect of iron oxide NPs [434]. In this regard, humic acid and other organic acid (including quinolinic acid, picolinic acid, and fusaric acid) have been shown to increase the yield of oxidant generation [435-438].

1.4.7.2 Oxidative stress

The oxidative stress describes a process damaging to the normal biological responses; disruption of a balance between biological system's ability to efficiently detoxify the reactive intermediates and accumulation of ROS. As a cell attempts to overcome this situation, the activation of both enzymatic and non-enzymatic antioxidant systems is initiated with the aim to restore the redox balance [439]. Usually, at mild oxidative stress, an activation of phase II antioxidant enzymes is capable to detoxify present oxidative species [440]. However, higher levels of oxidative stress will trigger a series of toxic cellular event which cause mitochondrial membrane damage and electron chain dysfunction, triggering cell death. Overproduction of noxious free radicals can cause an adverse effect on cell components including Deoxyribonucleic acid (DNA), lipids, and proteins [441].

1.4.7.2.1 Effect of oxidative stress on DNA

ROS cause damaging effects on DNA structure and function. 'Repairing' of DNA bases principally occurs as a result of their exposure to ROS, whereby guanine is the most vulnerable base to undergo oxidation [442]. Here, formation of a mutagenic 8-hydroxyguanine is the best-known DNA modification and a 'damage product' that could be used as a potential biomarker for ROS-related carcinogenesis [443,444]. An additional oxidative DNA damages affecting structure integrity include; DNA strand break, inter- and intra-strand crosslinks and DNA–protein crosslinks may cause significant DNA injury which are found to be involved in downstream conditions, such as carcinogenesis, neurodegenerative, cardiovascular and autoimmune diseases [445,446]

1.4.7.2.2 Effect of oxidative stress on lipids

ROS could target the carbon-carbon double bonds of lipids component of biological membranes in a process called 'lipid peroxidation' that ends with disruption of membrane integrity. As a result, an inactivation of membrane-bound receptors and enzymes, along with an increase in tissue permeability would be normally expected to occur [447]. In addition, the two extremely noxious lipid peroxidation products, malondialdehyde (MDA), and 4-hydroxynonenal (4-HNE) [448] are found to be capable of inactivating many cellular proteins by crosslinking them [449-451]. Moreover 4-HNE play an important role in intracellular glutathione depletion and in induction of peroxide production which cause serious deterioration in cell condition [452,453].

1.4.7.2.3 Effect of oxidative stress on proteins

The increased vulnerability of proteins to the proteolytic effect of specific proteases arises from several activities that could be mediated by ROS. A

peptide chain fragmentation [454], alteration of electrical charge of proteins, and protein crosslinking are the main outcomes of free radical species interactions with a proteinaceous material [455]. In addition, oxidation of specific amino acids residues in proteins (cysteine and methionine) can contribute towards conformational changes, protein unfolding and, ultimately, degradation [456-458]

1.4.7.3 ROS and apoptosis

1.4.7.3.1 Apoptosis

The term apoptosis simply refers to termination of cell life by following a specific cellular 'death program', hence another term often use is 'programmed cell death' [459]. Here, the dying cell undergoes biologically anticipated changes in order to diminish its death influence on the neighbouring cells and to avoid an uncontrolled immune response. Morphologically, events of cell shrinking and condensation (as a result of cytoskeleton collapse), and nuclear envelope dismantling mediate a formation self-enclosed bodies (called blebs) which function to prevent cellular components from being released into the extracellular medium [460].

1.4.7.3.2 Mechanism of apoptotic cell death

A detailed description of apoptosis process is beyond the scope of this thesis, and this section is only aiming to provide a brief introduction to the topic. Recent research suggests presence of two major apoptotic pathways through which an energy-dependant cascade of intracellular events occur, as illustrated in Figure 1-3. These pathways include the extrinsic or death receptor pathway and the intrinsic or mitochondrial pathway. However, a connection between the two pathways at a particular point was reported [461]. In addition, a third proposed pathway involves cytotoxic T-cells and perforin-granzyme-dependant cell

killing. This route can stimulate apoptosis *via* either granzyme A or granzyme B. Caspase 3-activation presents the convergence point at which the extrinsic, intrinsic, and granzyme B pathways merge. The activation of caspase-3 (a protease for different substrates) leads to subsequent events of DNA fragmentation, degradation of cytoskeletal and nuclear proteins, cross-linking of proteins. Finally, the formation of apoptotic bodies occurs which have specific ligands to be recognised by phagocytic cell receptors. The phagocytosis process then functions to remove the dying cell remnants without induction of uncontrolled immune- response. It is important to mention that granzyme A triggers a parallel, caspase-independent cell death route *via* damaging the single stranded DNA [462].

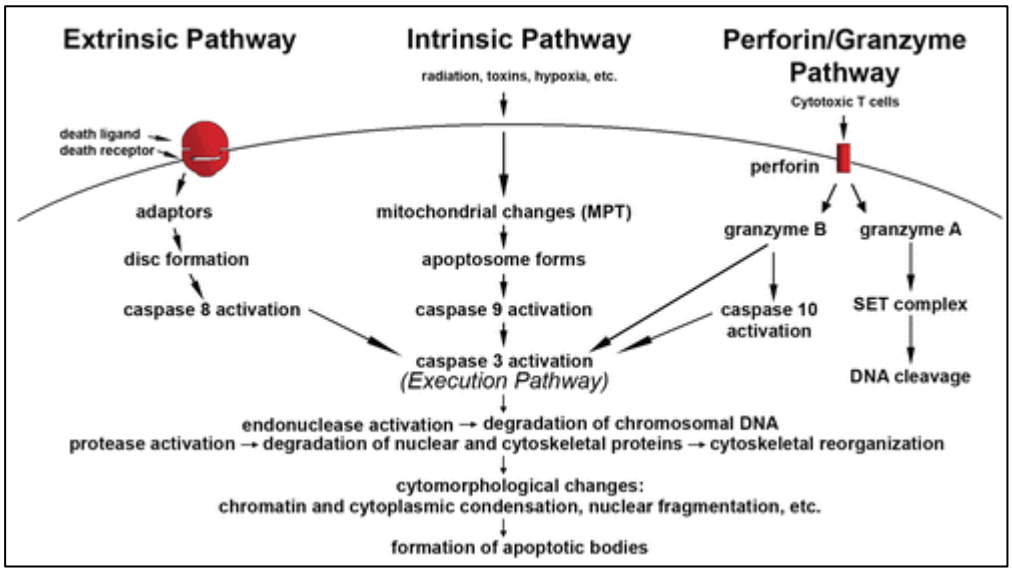


***Figure 0-3**: Schematic representation of apoptosis-related pathways.*

The extrinsic and intrinsic pathways are the major routes of triggering cell apoptosis. An additional perforin/granzyme pathway has also been identified. In order to initiate an energy-dependent cascade of molecular events, every path demands triggering of particular signals. Each separate path is able to activate particular initiator caspase (8, 9, and 10). All of the pathways will activate the common executioner, caspase-3, resulting in one execution pathway. The next stage includes complex processes of cell shrinkage, chromatin condensation, formation of cytoplasmic blebs and apoptotic bodies.

1.4.7.3.3 The role of ROS in cells apoptosis

When presents in low amount, ROS has been identified as useful/wanted species that are required for managing cell survival response, however cell death-related processes are a result of overloading cells with ROS [463]. There is an important ROS-activated protein called 'tumour suppressor protein p53' which has a pivotal role in orchestrating cellular responses with respect to ROS content in the biological environment [463]. Accordingly, either cell cycle arrest for supporting DNA repair and survival or cell death by apoptosis will be triggered [464]. Normally, p53 is a short-lived protein which regularly undergo proteasomal

degradation by the effect of Mouse double minute 2 homolog (Mdm2) so as to maintain it at low level [464].

Once a DNA damage has occurred as a result of mild ROS cellular accumulation, p53 will escape the proteasomal degradation to start repairing DNA strands (after cell cycle arrest). However, if DNA injury is severe, p53 can transcriptionally orchestrate the apoptosis process. A state of inhibition and reduction of pro-survival proteins, such as Bcl-2, Bcl-XL, IAPs and surviving, occurs with simultaneous upregulation of pro-apoptotic members [464]. In this regard, p53 will work to activate the transcription of pro-apoptotic genes related to the intrinsic apoptotic pathway, such as Bax, Bid, Puma, Noxa and Apaf-1, along with extrinsic pro-apoptotic factors such as Fas, FasL, DR-4 and DR-5. Similar to its former role, p53 can translocate to mitochondria in response to the mitochondrial DNA (mtDNA) oxidative damage where it is capable to interact with both anti-apoptotic and pro-apoptotic proteins resulting in leakage of more pro-apoptotic factors and hence apoptosis will proceed [465].

The activity of caspases (cysteine-aspartic proteases) can be regulated by redox action, whereby the catalytic site of these enzymes is susceptible to oxidation. Interestingly, while caspases can be activated by oxidants [466,467], oxidants itself are also able to irreversibly inactivate their enzymatic action [468]. Furthermore, S-glutathiolation process can regulate caspase-3 activity. In this regard, cellular glutathione has an ability to diminish the proteolytic cleavage of caspases causing cell resistance to apoptosis [469].

1.5 USPIONs bio-applications

USPIONs have several key features making them attractive for application in medicine. In addition, USPIONs show high flexibility to tailor these features for optimum application outcomes. For example, biocompatibility, long half-life in biological media, long-lived stability against aggregation, and immunological inertness could all be modified after controlling the physicochemical properties of NPs surfaces *via* selecting the suitable ligand and functional moiety for a particular application.

Interestingly, for biomedical healthcare application, USPIONs can be used for both diagnostic and therapeutic purposes, in which cell therapies can be monitored exploiting the dual capability of these NPs to function as a magnetic resonance imaging (MRI) contrast agent and to accumulate in tumours as potential therapeutic agent [470-472]. In addition to magnetic hyperthermia and thermoablation therapies [473-475], multi-decorated USPIONs in combination with multimodal therapy are considered as one of the most promising treatments in a personalised cancer management [476-478]. Moreover, biotechnological applications including food analysis, protein/enzyme immobilization, protein purification, and water treatment along with bioengineering applications such as biosensor, and tissue engineering worked to increase the USPIONs importance in the new emerging sciences [479].

1.6 Project aims

This project aims to investigate:

i. Preparation of iron oxide NPs (USPIONs) using a novel design of spinning disc reactor (SDR) combined with flow injection technology.

ii. Define design space with respect to nucleation and growth theory of inorganic particles formation

iii. Investigate the design-related (reactant flowrate, rotation speed, and SDR size) and some chemical (iron reactant amount, Fe^{+2}/Fe^{+3} ratio change, and alkaline reactant concentration) parameters influence on particles size and morphology features of fabricated USPIONs.

iv. Modify the produced NPs surfaces with simple aminoacid 'monomers', rather than polymeric materials, having different molecular structure and amino acid classes using an invented dry mixing process with applied shear force.

v. Provide an insight understanding of the surface interactions of these monomers with USPIONs, *via* studying the infrared (IR) spectroscopy, thermal behaviour, and outer surface charges of the aminoacid-modified USPIONs and, hence, assess their biophysical properties.

vi. Assess interactions of modified USPIONs owning different surface chemistries with epithelial cells in the cell culture model of intestinal epithelium, and cellular uptake.

vii. Explore the cytotoxic effect of these USPIONs in terms of the death pathway that these cell follow.

1.7 References:

1 Duncan, R. & Gaspar, R. Nanomedicine (s) under the microscope. *Molecular pharmaceutics* **8**, 2101-2141 (2011).

2 Boyer, C., Whittaker, M. R., Bulmus, V., Liu, J. & Davis, T. P. The design and utility of polymer-stabilized iron-oxide nanoparticles for nanomedicine applications. *NPG Asia Materials* **2**, 23-30 (2010).

3 Wahajuddin, S. A. Superparamagnetic iron oxide nanoparticles: magnetic nanoplatforms as drug carriers. *International journal of nanomedicine* **7**, 3445 (2012).

4 Mahmoudi, M., Sant, S., Wang, B., Laurent, S. & Sen, T. Superparamagnetic iron oxide nanoparticles (SPIONs): development, surface modification and applications in chemotherapy. *Advanced drug delivery reviews* **63**, 24-46 (2011).

5 Azam, A. *et al.* Antimicrobial activity of metal oxide nanoparticles against Gram-positive and Gram-negative bacteria: a comparative study. *International journal of nanomedicine* **7**, 6003 (2012).

6 Mahmoudi, M., Stroeve, P., Milani, A. S. & Arbab, A. S. *Superparamagnetic iron oxide nanoparticles: synthesis, surface engineering, cytotoxicity and biomedical applications.* (Nova Science Publishers, Inc., 2011).

7 F Hasany, S., H Abdurahman, N., R Sunarti, A. & Jose, R. Magnetic iron oxide nanoparticles: chemical synthesis and applications review. *Current nanoscience* **9**, 561-575 (2013).

8 Massart, R. Preparation of aqueous magnetic liquids in alkaline and acidic media. *IEEE transactions on magnetics* **17**, 1247-1248 (1981).

9 Li, Y.-S., Church, J. S., Woodhead, A. L. & Moussa, F. Preparation and characterization of silica coated iron oxide magnetic nano-particles. *Spectrochimica Acta Part A: Molecular and Biomolecular Spectroscopy* **76**, 484-489 (2010).

10 Majewski, P. & Thierry, B. Functionalized magnetite nanoparticles—synthesis, properties, and bio-applications. *Critical Reviews in Solid State and Materials Sciences* **32**, 203-215 (2007).

11 Sugimoto, T. *Fine particles: synthesis, characterization, and mechanisms of growth*. Vol. 92 (CRC Press, 2000).

12 Tang, B., Yuan, L., Shi, T., Yu, L. & Zhu, Y. Preparation of nano-sized magnetic particles from spent pickling liquors by ultrasonic-assisted chemical co-precipitation. *Journal of hazardous materials* **163**, 1173-1178 (2009).

13 Schwarzer, H. C. & Peukert, W. Combined experimental/numerical study on the precipitation of nanoparticles. *AIChE Journal* **50**, 3234-3247 (2004).

14 Morales, M. d. P. *et al.* Surface and internal spin canting in γ-Fe2O3 nanoparticles. *Chemistry of Materials* **11**, 3058-3064 (1999).

15 Mahmoudi, M., Milani, A. & Stroeve, P. Surface architecture of superparamagnetic iron oxide nanoparticles for application in drug delivery and their biological response: a review. *Int J Biomed Nanosci Nanotechnol* **1**, 3 (2010).

16 Yang, X.-C. *et al.* Synthesis of monodisperse Iron oxide nanoparticles without surfactants. *Journal of Nanomaterials* **2014**, 231 (2014).

17 Hoar, T. & Schulman, J. Transparent water-in-oil dispersions: the oleopathic hydro-micelle. *Nature* **152**, 102 (1943).
18 Bagwe, R., Kanicky, J., Palla, B., Patanjali, P. & Shah, D. Improved drug delivery using microemulsions: rationale, recent progress, and new horizons. *Critical reviews in therapeutic drug carrier systems* **18**, 77 (2001).
19 Lee, K., Sorensen, C., Klabunde, K. & Hadjipanayis, G. Synthesis and characterization of stable colloidal Fe/sub 3/O/sub 4/particles in water-in-oil microemulsions. *IEEE transactions on magnetics* **28**, 3180-3182 (1992).
20 Dresco, P. A., Zaitsev, V. S., Gambino, R. J. & Chu, B. Preparation and properties of magnetite and polymer magnetite nanoparticles. *Langmuir* **15**, 1945-1951 (1999).
21 O'connor, C. J. *et al.* Nanophase magnetic materials: synthesis and properties. *Molecular Crystals and Liquid Crystals* **335**, 423-442 (1999).
22 Lopez-Perez, J., Lopez-Quintela, M., Mira, J. & Rivas, J. Preparation of magnetic fluids with particles obtained in microemulsions. *IEEE Transactions on Magnetics* **33**, 4359-4362 (1997).
23 Santra, S. *et al.* Synthesis and characterization of silica-coated iron oxide nanoparticles in microemulsion: the effect of nonionic surfactants. *Langmuir* **17**, 2900-2906 (2001).
24 Gobe, M., Kon-No, K., Kandori, K. & Kitahara, A. Preparation and characterization of monodisperse magnetite sols in WO microemulsion. *Journal of Colloid and Interface Science* **93**, 293-295 (1983).
25 Liz, L., Quintela, M. L., Mira, J. & Rivas, J. Preparation of colloidal Fe3O4 ultrafine particles in microemulsions. *Journal of Materials Science* **29**, 3797-3801 (1994).
26 Meldrum, F. C., Heywood, B. R. & Mann, S. Magnetoferritin: in vitro synthesis of a novel magnetic protein. *Science* **257**, 522-524 (1992).
27 Dickson, D., Walton, S., Mann, S. & Wong, K. Properties of magnetoferritin: a novel biomagnetic nanoparticle. *NanoStructured materials* **9**, 595-598 (1997).
28 Wong, K. K., Douglas, T., Gider, S., Awschalom, D. D. & Mann, S. Biomimetic synthesis and characterization of magnetic proteins (magnetoferritin). *Chemistry of materials* **10**, 279-285 (1998).
29 Uchida, M. *et al.* Targeting of cancer cells with ferrimagnetic ferritin cage nanoparticles. *Journal of the American Chemical Society* **128**, 16626-16633 (2006).
30 Strable, E. *et al.* Synthesis and characterization of soluble iron oxide−dendrimer composites. *Chemistry of materials* **13**, 2201-2209 (2001).
31 Bonacchi, D. *et al.* Nanosized iron oxide particles entrapped in pseudo-single crystals of γ-cyclodextrin. *Chemistry of materials* **16**, 2016-2020 (2004).
32 Hou, Y. *et al.* Inorganic nanocrystal self-assembly via the inclusion interaction of β-cyclodextrins: toward 3D spherical magnetite. *The Journal of Physical Chemistry B* **109**, 4845-4852 (2005).
33 Sangregorio, C., Wiemann, J. K., O'Connor, C. J. & Rosenzweig, Z. A new method for the synthesis of magnetoliposomes. *Journal of applied physics* **85**, 5699-5701 (1999).

34 De Cuyper, M. & Joniau, M. Mechanistic aspects of the adsorption of phospholipids onto lauric acid stabilized magnetite nanocolloids. *Langmuir* **7**, 647-652 (1991).
35 Hao, J. *et al.* Synthesis of superparamagnetic Fe3O4 nanocrystals in reverse microemulsion at room temperature. *Materials Research Innovations* **14**, 324-326 (2010).
36 Okoli, C., Boutonnet, M., Mariey, L., Järås, S. & Rajarao, G. Application of magnetic iron oxide nanoparticles prepared from microemulsions for protein purification. *Journal of Chemical Technology and Biotechnology* **86**, 1386-1393 (2011).
37 Zhang, G., Liao, Y. & Baker, I. Surface engineering of core/shell iron/iron oxide nanoparticles from microemulsions for hyperthermia. *Materials Science and Engineering: C* **30**, 92-97 (2010).
38 Tavakoli, A., Sohrabi, M. & Kargari, A. A review of methods for synthesis of nanostructured metals with emphasis on iron compounds. *chemical papers* **61**, 151-170 (2007).
39 Pang, Y.-X. & Bao, X. Aluminium oxide nanoparticles prepared by water-in-oil microemulsions. *Journal of Materials Chemistry* **12**, 3699-3704 (2002).
40 Pillai, V., Kumar, P., Hou, M., Ayyub, P. & Shah, D. Preparation of nanoparticles of silver halides, superconductors and magnetic materials using water-in-oil microemulsions as nano-reactors. *Advances in Colloid and Interface Science* **55**, 241-269 (1995).
41 Tartaj, P. & De Jonghe, L. C. Preparation of nanospherical amorphous zircon powders by a microemulsion-mediated process. *Journal of Materials Chemistry* **10**, 2786-2790 (2000).
42 Capek, I. Preparation of metal nanoparticles in water-in-oil (w/o) microemulsions. *Advances in colloid and interface science* **110**, 49-74 (2004).
43 Li, F., Vipulanandan, C. & Mohanty, K. K. Microemulsion and solution approaches to nanoparticle iron production for degradation of trichloroethylene. *Colloids and Surfaces A: Physicochemical and Engineering Aspects* **223**, 103-112 (2003).
44 Wang, C.-C., Chen, D.-H. & Huang, T.-C. Synthesis of palladium nanoparticles in water-in-oil microemulsions. *Colloids and Surfaces A: Physicochemical and Engineering Aspects* **189**, 145-154 (2001).
45 Inouye, K. *et al.* Oxygenation of ferrous ions in reversed micelle and reversed microemulsion. *The Journal of Physical Chemistry* **86**, 1465-1469 (1982).
46 Pileni, M.-P. & Duxin, N. Micelle technology for magnetic nanosized alloys and composites. *Chemtech* **30**, 25-33 (2000).
47 Okoli, C. *et al.* Comparison and functionalization study of microemulsion-prepared magnetic iron oxide nanoparticles. *Langmuir* **28**, 8479-8485 (2012).
48 Munshi, N., De, T. K. & Maitra, A. Size modulation of polymeric nanoparticles under controlled dynamics of microemulsion droplets. *Journal of colloid and interface science* **190**, 387-391 (1997).
49 Liang, X., Jia, X., Cao, L., Sun, J. & Yang, Y. Microemulsion synthesis and characterization of nano-Fe3O4 particles and Fe3O4

nanocrystalline. *Journal of Dispersion Science and Technology* **31**, 1043-1049 (2010).

50 Gupta, A. K. & Wells, S. Surface-modified superparamagnetic nanoparticles for drug delivery: preparation, characterization, and cytotoxicity studies. *IEEE transactions on nanobioscience* **3**, 66-73 (2004).

51 Deng, Y., Wang, L., Yang, W., Fu, S. & Elaıssari, A. Preparation of magnetic polymeric particles via inverse microemulsion polymerization process. *Journal of Magnetism and Magnetic Materials* **257**, 69-78 (2003).

52 Seip, C. T., Carpenter, E. E., O'Connor, C. J., John, V. T. & Li, S. Magnetic properties of a series of ferrite nanoparticles synthesized in reverse micelles. *IEEE transactions on magnetics* **34**, 1111-1113 (1998).

53 Durães, L., Costa, B., Vasques, J., Campos, J. & Portugal, A. Phase investigation of as-prepared iron oxide/hydroxide produced by sol–gel synthesis. *Materials Letters* **59**, 859-863 (2005).

54 Ismail, A. A. Synthesis and characterization of Y 2 O 3/Fe 2 O 3/TiO 2 nanoparticles by sol–gel method. *Applied Catalysis B: Environmental* **58**, 115-121 (2005).

55 Carbajal-Franco, G., Eastman, M. & Ramana, C. Structure and optical properties of iron oxide films prepared by a modified wet-chemical method. *Ceramics International* **39**, 4581-4587 (2013).

56 Cui, H., Liu, Y. & Ren, W. Structure switch between α-Fe2O3, γ-Fe2O3 and Fe3O4 during the large scale and low temperature sol–gel synthesis of nearly monodispersed iron oxide nanoparticles. *Advanced Powder Technology* **24**, 93-97 (2013).

57 Xu, J. *et al.* Preparation and magnetic properties of magnetite nanoparticles by sol–gel method. *Journal of Magnetism and magnetic Materials* **309**, 307-311 (2007).

58 Cui, H. & Ren, W. Low temperature and size controlled synthesis of monodispersed γ-Fe2O3 nanoparticles by an epoxide assisted sol–gel route. *Journal of Sol-Gel Science and Technology* **47**, 81-84 (2008).

59 Qi, H., Yan, B., Lu, W., Li, C. & Yang, Y. A non-alkoxide sol-gel method for the preparation of magnetite (Fe3O4) nanoparticles. *Current Nanoscience* **7**, 381-388 (2011).

60 Sangermano, M. *et al.* Photo-Cured Epoxy Networks Functionalized With Fe3O4 Generated by Non-hydrolytic Sol–Gel Process. *Macromolecular Chemistry and Physics* **214**, 508-516 (2013).

61 Cui, H., Liu, Y. & Ren, W. Structure switch between a-Fe2O3, c-Fe2O3 and Fe3O4 during the large scale and low temperature sol–gel synthesis of nearly monodispersed iron oxide nanoparticles. *Adv Powder Technol* **24**, 93-97 (2013).

62 Fievet, F., Lagier, J., Blin, B., Beaudoin, B. & Figlarz, M. Homogeneous and heterogeneous nucleations in the polyol process for the preparation of micron and submicron size metal particles. *Solid State Ionics* **32**, 198-205 (1989).

63 Laurent, S. *et al.* Magnetic iron oxide nanoparticles: synthesis, stabilization, vectorization, physicochemical characterizations, and biological applications. *Chemical reviews* **108**, 2064-2110 (2008).

64 Wu, W., Jiang, C. Z. & Roy, V. A. Designed synthesis and surface engineering strategies of magnetic iron oxide nanoparticles for biomedical applications. *Nanoscale* **8**, 19421-19474 (2016).
65 Jézéquel, D., Guenot, J., Jouini, N. & Fiévet, F. Submicrometer zinc oxide particles: Elaboration in polyol medium and morphological characteristics. *Journal of Materials Research* **10**, 77-83 (1995).
66 Jiang, P. *et al.* Facile synthesis of water-soluble and superparamagnetic Fe3O4 dots through a polyol-hydrolysis route. *Journal of Materials Science* **48**, 2365-2369 (2013).
67 Caruntu, D., Caruntu, G. & O'Connor, C. J. Magnetic properties of variable-sized Fe3O4 nanoparticles synthesized from non-aqueous homogeneous solutions of polyols. *Journal of Physics D: Applied Physics* **40**, 5801 (2007).
68 Liu, H.-L. *et al.* One-pot polyol synthesis of monosize PVP-coated sub-5nm Fe 3 O 4 nanoparticles for biomedical applications. *Journal of Magnetism and Magnetic Materials* **310**, e815-e817 (2007).
69 Günay, M., Baykal, A. & Sözeri, H. Structural and magnetic properties of triethylene glycol stabilized monodisperse Fe3O4 nanoparticles. *Journal of superconductivity and novel magnetism* **25**, 2415-2420 (2012).
70 Hemery, G. *et al.* Tuning sizes, morphologies, and magnetic properties of mono-vs. multi-core iron oxide nanoparticles through control of added water in the polyol synthesis. *arXiv preprint arXiv:1701.05858* (2017).
71 Joseyphus, R. J. *et al.* Role of polyol in the synthesis of Fe particles. *Journal of Magnetism and Magnetic Materials* **310**, 2393-2395 (2007).
72 Wan, J., Cai, W., Meng, X. & Liu, E. Monodisperse water-soluble magnetite nanoparticles prepared by polyol process for high-performance magnetic resonance imaging. *Chemical Communications*, 5004-5006 (2007).
73 Mao, B. *et al.* Synthesis of magnetite octahedrons from iron powders through a mild hydrothermal method. *Materials Research Bulletin* **41**, 2226-2231 (2006).
74 Xu, C. & Teja, A. S. Continuous hydrothermal synthesis of iron oxide and PVA-protected iron oxide nanoparticles. *The Journal of Supercritical Fluids* **44**, 85-91 (2008).
75 Burda, C., Chen, X., Narayanan, R. & El-Sayed, M. A. Chemistry and properties of nanocrystals of different shapes. *Chemical reviews* **105**, 1025-1102 (2005).
76 Eckert, C. A., Knutson, B. L. & Debenedetti, P. G. Supercritical fluids as solvents for chemical and materials processing. *Nature* **383**, 313 (1996).
77 Hao, Y. & Teja, A. S. Continuous hydrothermal crystallization of α–Fe2O3 and Co3O4 nanoparticles. *Journal of Materials Research* **18**, 415-422 (2003).
78 Cabañas, A., Darr, J. A., Lester, E. & Poliakoff, M. Continuous hydrothermal synthesis of inorganic materials in a near-critical water flow reactor; the one-step synthesis of nano-particulate Ce1− xZrxO2 (x= 0–1) solid solutionsElectronic supplementary information (ESI) available: microanalysis results, FT-IR spectra.

org/suppdata/jm/b0/b008095k. *Journal of Materials Chemistry* **11**, 561-568 (2001).
79 Sue, K. *et al.* Size-controlled synthesis of metal oxide nanoparticles with a flow-through supercritical water method. *Green Chemistry* **8**, 634-638 (2006).
80 Xu, C., Lee, J. & Teja, A. S. Continuous hydrothermal synthesis of lithium iron phosphate particles in subcritical and supercritical water. *The Journal of Supercritical Fluids* **44**, 92-97 (2008).
81 Zargar, T. & Kermanpur, A. Effects of hydrothermal process parameters on the physical, magnetic and thermal properties of Zn 0.3 Fe 2.7 O 4 nanoparticles for magnetic hyperthermia applications. *Ceramics International* **43**, 5794-5804 (2017).
82 Wang, J., Sun, J., Sun, Q. & Chen, Q. One-step hydrothermal process to prepare highly crystalline Fe 3 O 4 nanoparticles with improved magnetic properties. *Materials research bulletin* **38**, 1113-1118 (2003).
83 Wu, W. *et al.* Large-scale and controlled synthesis of iron oxide magnetic short nanotubes: shape evolution, growth mechanism, and magnetic properties. *The Journal of Physical Chemistry C* **114**, 16092-16103 (2010).
84 Li, H. *et al.* Hydrothermal Synthesis and Properties of Controlled α-Fe2O3 Nanostructures in HEPES Solution. *Chemistry–An Asian Journal* **6**, 2320-2331 (2011).
85 Gao, J. *et al.* One-step solvothermal synthesis of highly water-soluble, negatively charged superparamagnetic Fe 3 O 4 colloidal nanocrystal clusters. *Nanoscale* **5**, 7026-7033 (2013).
86 Liu, J., Wang, L., Wang, J. & Zhang, L. Simple solvothermal synthesis of hydrophobic magnetic monodispersed Fe3O4 nanoparticles. *Materials Research Bulletin* **48**, 416-421 (2013).
87 Zhu, L.-P., Xiao, H.-M., Zhang, W.-D., Yang, G. & Fu, S.-Y. One-pot template-free synthesis of monodisperse and single-crystal magnetite hollow spheres by a simple solvothermal route. *Crystal Growth and Design* **8**, 957-963 (2008).
88 Xu, H.-L., Bi, H. & Yang, R.-B. Enhanced microwave absorption property of bowl-like Fe3O4 hollow spheres/reduced graphene oxide composites. *Journal of Applied Physics* **111**, 07A522 (2012).
89 Darr, J. A., Zhang, J., Makwana, N. M. & Weng, X. Continuous Hydrothermal Synthesis of Inorganic Nanoparticles: Applications and Future Directions. *Chemical Reviews* (2017).
90 Suslick, K. S. & Choe, S.-B. Sonochemical synthesis of amorphous iron. *nature* **353**, 414 (1991).
91 Suslick, K. S. Applications of ultrasound to materials chemistry. *Mrs Bulletin* **20**, 29-34 (1995).
92 Suslick, K., Fang, M., Hyeon, T. & Mdleleni, M. in *Sonochemistry and sonoluminescence* 291-320 (Springer, 1999).
93 Flint, E. B. & Suslick, K. S. The temperature of cavitation. *Science* **253**, 1397-1399 (1991).
94 Hiller, R., Putterman, S. J. & Barber, B. P. Spectrum of synchronous picosecond sonoluminescence. *Physical Review Letters* **69**, 1182 (1992).
95 Barber, B. P. & Putterman, S. J. Observation of synchronous picosecond sonoluminescence. *Nature* **352**, 318 (1991).

96 Shafi, K. V. *et al.* Sonochemical synthesis of functionalized amorphous iron oxide nanoparticles. *Langmuir* **17**, 5093-5097 (2001).
97 Gedanken, A. Using sonochemistry for the fabrication of nanomaterials. *Ultrasonics sonochemistry* **11**, 47-55 (2004).
98 Suslick, K. S., Hyeon, T., Fang, M. & Cichowlas, A. A. Sonochemical synthesis of nanostructured catalysts. *Materials Science and Engineering: A* **204**, 186-192 (1995).
99 Morel, A. *et al.* C. and Chevalier, G. *Deleris, C. Petibois, A. Brisson, and M. Simonoff: Sonochemical approach to the synthesis of Fe3O4@ SiO2 core-shell nanoparticles with tunable properties. ACS Nano* **2**, 847-856 (2008).
100 Islam, M. N., Jeong, J.-R. & Kim, C. A facile route to sonochemical synthesis of magnetic iron oxide (Fe 3 O 4) nanoparticles. *Thin Solid Films* **519**, 8277-8279 (2011).
101 Zhang, S., Zhang, Y., Wang, Y., Liu, S. & Deng, Y. Sonochemical formation of iron oxide nanoparticles in ionic liquids for magnetic liquid marble. *Physical Chemistry Chemical Physics* **14**, 5132-5138 (2012).
102 Pinjari, D. V. & Pandit, A. B. Room temperature synthesis of crystalline CeO 2 nanopowder: advantage of sonochemical method over conventional method. *Ultrasonics sonochemistry* **18**, 1118-1123 (2011).
103 Mandel, K., Kolb, C., Straßer, M., Dembski, S. & Sextl, G. Size controlled iron oxide nano octahedra obtained via sonochemistry and natural ageing. *Colloids and Surfaces A: Physicochemical and Engineering Aspects* **457**, 27-32 (2014).
104 Abbas, M., Takahashi, M. & Kim, C. Facile sonochemical synthesis of high-moment magnetite (Fe3O4) nanocube. *Journal of nanoparticle research* **15**, 1354 (2013).
105 Dolores, R., Raquel, S. & Adianez, G.-L. Sonochemical synthesis of iron oxide nanoparticles loaded with folate and cisplatin: effect of ultrasonic frequency. *Ultrasonics sonochemistry* **23**, 391-398 (2015).
106 Reetz, M. T., Helbig, W. & Quaiser, S. A. Electrochemical methods in the synthesis of nanostructured transition metal clusters. *Active Metals: Preparation, Characterization, Applications*, 279-297 (1996).
107 Lu, X. *et al.* WO3–x@ Au@ MnO2 Core–Shell Nanowires on Carbon Fabric for High-Performance Flexible Supercapacitors. *Advanced materials* **24**, 938-944 (2012).
108 Izaki, M., Komori, J., Shimizu, K., Koyama, T. & Shinagawa, T. Room temperature ultraviolet light-emitting ZnO vertical nanowires prepared by electrochemical growth. *physica status solidi (a)* **214** (2017).
109 He, Y.-B., Li, G.-R., Wang, Z.-L., Ou, Y.-N. & Tong, Y.-X. Pt nanorods aggregates with enhanced electrocatalytic activity toward methanol oxidation. *The Journal of Physical Chemistry C* **114**, 19175-19181 (2010).
110 Nouri, A., Beniaiche, A., Soucase, B. M., Guessas, H. & Azizi, A. Photoluminescence study of Eu+ 3 doped ZnO nanocolumns prepared by electrodeposition method. *Optik-International Journal for Light and Electron Optics* **139**, 104-110 (2017).
111 Jing, C. *et al.* New insights into electrocatalysis based on plasmon resonance for the real-time monitoring of catalytic events on single gold nanorods. *Analytical chemistry* **86**, 5513-5518 (2014).

112 Saadat, S. *et al.* Template-free electrochemical deposition of interconnected ZnSb nanoflakes for li-ion battery anodes. *Chemistry of Materials* **23**, 1032-1038 (2011).
113 Qian, X., Xu, Q., Hang, T., Shanmugam, S. & Li, M. Electrochemical deposition of Fe 3 O 4 nanoparticles and flower-like hierarchical porous nanoflakes on 3D Cu-cone arrays for rechargeable lithium battery anodes. *Materials & Design* **121**, 321-334 (2017).
114 Yin, J. *et al.* Honeycomb-like NiCo2S4 nanosheets prepared by rapid electrodeposition as a counter electrode for dye-sensitized solar cells. *Nanotechnology* **28**, 345403 (2017).
115 Karimzadeh, I., Aghazadeh, M., Doroudi, T., Ganjali, M. R. & Kolivand, P. H. Superparamagnetic Iron Oxide (Fe3O4) Nanoparticles Coated with PEG/PEI for Biomedical Applications: A Facile and Scalable Preparation Route Based on the Cathodic Electrochemical Deposition Method. *Advances in Physical Chemistry* **2017** (2017).
116 Cabrera, L., Gutierrez, S., Menendez, N., Morales, M. & Herrasti, P. Magnetite nanoparticles: electrochemical synthesis and characterization. *Electrochimica Acta* **53**, 3436-3441 (2008).
117 Mazario, E. *et al.* One-pot electrochemical synthesis of polydopamine coated magnetite nanoparticles. *RSC Advances* **4**, 48353-48361 (2014).
118 Ramimoghadam, D., Bagheri, S. & Hamid, S. B. A. Progress in electrochemical synthesis of magnetic iron oxide nanoparticles. *Journal of Magnetism and Magnetic Materials* **368**, 207-229 (2014).
119 Karimzadeh, I., Aghazadeh, M., Doroudi, T., Ganjali, M. R. & Kolivand, P. H. Electrochemical preparation and characterization of chitosan-coated superparamagnetic iron oxide (Fe3O4) nanoparticles. *Materials Research Innovations*, 1-9 (2017).
120 Karimzadeh, I. *et al.* Saccharide-coated superparamagnetic Fe 3 O 4 nanoparticles (SPIONs) for biomedical applications: an efficient and scalable route for preparation and in situ surface coating through cathodic electrochemical deposition (CED). *Materials Letters* **189**, 290-294 (2017).
121 Karimzadeh, I. *et al.* A novel method for preparation of bare and poly (vinylpyrrolidone) coated superparamagnetic iron oxide nanoparticles for biomedical applications. *Materials Letters* **179**, 5-8 (2016).
122 Aghazadeh, M., Karimzadeh, I., Ganjali, M. R. & Morad, M. M. A novel preparation method for surface coated superparamagnetic Fe 3 O 4 nanoparticles with vitamin C and sucrose. *Materials Letters* **196**, 392-395 (2017).
123 Aghazadeh, M., Karimzadeh, I. & Ganjali, M. R. Ethylenediaminetetraacetic acid capped superparamagnetic iron oxide (Fe 3 O 4) nanoparticles: A novel preparation method and characterization. *Journal of Magnetism and Magnetic Materials* **439**, 312-319 (2017).
124 Karimzadeh, I., Aghazadeh, M., Ganjali, M. R., Doroudi, T. & Kolivand, P. H. Preparation and characterization of iron oxide (Fe 3 O 4) nanoparticles coated with polyvinylpyrrolidone/polyethylenimine through a facile one-pot deposition route. *Journal of Magnetism and Magnetic Materials* **433**, 148-154 (2017).

125 Franger, S., Berthet, P. & Berthon, J. Electrochemical synthesis of Fe3O4 nanoparticles in alkaline aqueous solutions containing complexing agents. *Journal of Solid State Electrochemistry* **8**, 218-223 (2004).
126 Starowicz, M. *et al.* Electrochemical synthesis of magnetic iron oxide nanoparticles with controlled size. *Journal of Nanoparticle Research* **13**, 7167-7176 (2011).
127 Stein, A. & Schroden, R. C. Colloidal crystal templating of three-dimensionally ordered macroporous solids: materials for photonics and beyond. *Current Opinion in Solid State and Materials Science* **5**, 553-564 (2001).
128 Jongen, N. *et al.* Development of a Continuous Segmented Flow Tubular Reactor and the "Scale-out" Concept–In Search of Perfect Powders. *Chemical engineering & technology* **26**, 303-305 (2003).
129 Donnet, M., Jongen, N., Lemaitre, J. & Bowen, P. New morphology of calcium oxalate trihydrate precipitated in a segmented flow tubular reactor. *Journal of materials science letters* **19**, 749-750 (2000).
130 Harries, N., Burns, J., Barrow, D. & Ramshaw, C. A numerical model for segmented flow in a microreactor. *International journal of heat and mass transfer* **46**, 3313-3322 (2003).
131 Růžička, J. & Hansen, E. Flow-injection analysis and its early history. *Talanta* **29**, 157 (1982).
132 Wang, L. & Muhammed, M. Synthesis of zinc oxide nanoparticles with controlled morphology. *Journal of Materials Chemistry* **9**, 2871-2878 (1999).
133 Dumitrache, F. *et al.* Highly magnetic Fe 2 O 3 nanoparticles synthesized by laser pyrolysis used for biological and heat transfer applications. *Applied Surface Science* **336**, 297-303 (2015).
134 Malumbres, A. *et al.* Continuous production of iron-based nanocrystals by laser pyrolysis. Effect of operating variables on size, composition and magnetic response. *Nanotechnology* **24**, 325603 (2013).
135 Bomatí-Miguel, O., Mazeina, L., Navrotsky, A. & Veintemillas-Verdaguer, S. Calorimetric study of maghemite nanoparticles synthesized by laser-induced pyrolysis. *Chemistry of Materials* **20**, 591-598 (2008).
136 Marcu, A. *et al.* Magnetic iron oxide nanoparticles as drug delivery system in breast cancer. *Applied Surface Science* **281**, 60-65 (2013).
137 Morjan, I. *et al.* Iron oxide-based nanoparticles with different mean sizes obtained by the laser pyrolysis: structural and magnetic properties. *Journal of nanoscience and nanotechnology* **10**, 1223-1234 (2010).
138 Barshutina, M. & Barchanski, A. Pulsed Laser Ablation for Obtaining Contrast Agents Based on Dysprosium Oxide (Dy2O3) Nanoparticles. *Measurement Techniques* **60**, 216-219 (2017).
139 Svetlichnyi, V., Shabalina, A. & Lapin, I. Structure and Properties of Nanocrystalline Iron Oxide Powder Prepared by the Method of Pulsed Laser Ablation. *Russian Physics Journal* **59**, 2012-2016 (2017).
140 Kanitz, A. *et al.* Synthesis of magnetic nanoparticles by ultrashort pulsed laser ablation of iron in different liquids. *ChemPhysChem* **18**, 1155-1164 (2017).

141 De Carvalho, J., de Medeiros, S., Morales, M., Dantas, A. & Carriço, A. Synthesis of magnetite nanoparticles by high energy ball milling. *Applied Surface Science* **275**, 84-87 (2013).
142 Burnham, P., Dollahon, N., Li, C., Viescas, A. & Papaefthymiou, G. Magnetization and Specific Absorption Rate Studies of Ball-Milled Iron Oxide Nanoparticles for Biomedicine. *Journal of Nanoparticles* **2013** (2013).
143 Radhika Devi, A. *et al.* Generation of drugs coated iron nanoparticles through high energy ball milling. *Journal of Applied Physics* **115**, 124906 (2014).
144 Bajorek, A. *et al.* HoFe 3 magnetic nanopowders fabricated by high energy ball milling. *Materials Characterization* **126**, 42-56 (2017).
145 Morales, M. *et al.* Contrast agents for MRI based on iron oxide nanoparticles prepared by laser pyrolysis. *Journal of Magnetism and Magnetic Materials* **266**, 102-109 (2003).
146 Veintemillas-Verdaguer, S. *et al.* Colloidal dispersions of maghemite nanoparticles produced by laser pyrolysis with application as NMR contrast agents. *Journal of Physics D: Applied Physics* **37**, 2054 (2004).
147 Wang, Z., Liu, Y. & Zeng, X. One-step synthesis of γ-Fe2O3 nanoparticles by laser ablation. *Powder technology* **161**, 65-68 (2006).
148 Kawaguchi, K., Jaworski, J., Ishikawa, Y., Sasaki, T. & Koshizaki, N. Preparation of gold/iron-oxide composite nanoparticles by a unique laser process in water. *Journal of Magnetism and Magnetic Materials* **310**, 2369-2371 (2007).
149 Bazylinski, D. A. & Frankel, R. B. Magnetosome formation in prokaryotes. *Nature Reviews Microbiology* **2**, 217-230 (2004).
150 Blakemore, R. P. Magnetotactic bacteria. *Annual Reviews in Microbiology* **36**, 217-238 (1982).
151 Matsunaga, T. & Kamiya, S. Use of magnetic particles isolated from magnetotactic bacteria for enzyme immobilization. *Applied Microbiology and Biotechnology* **26**, 328-332 (1987).
152 Devouard, B. *et al.* Magnetite from magnetotactic bacteria: Size distributions and twinning. *American Mineralogist* **83**, 1387-1398 (1998).
153 Arakaki, A., Nakazawa, H., Nemoto, M., Mori, T. & Matsunaga, T. Formation of magnetite by bacteria and its application. *Journal of the Royal Society interface* **5**, 977-999 (2008).
154 Baumgartner, J. *et al.* Magnetotactic bacteria form magnetite from a phosphate-rich ferric hydroxide via nanometric ferric (oxyhydr) oxide intermediates. *Proceedings of the National Academy of Sciences* **110**, 14883-14888 (2013).
155 Arakaki, A., Yamagishi, A., Fukuyo, A., Tanaka, M. & Matsunaga, T. Co-ordinated functions of Mms proteins define the surface structure of cubo-octahedral magnetite crystals in magnetotactic bacteria. *Molecular microbiology* **93**, 554-567 (2014).
156 Lefevre, C. T. *et al.* Novel magnetite-producing magnetotactic bacteria belonging to the Gammaproteobacteria. *The ISME journal* **6**, 440 (2012).
157 Sarkar, J., Mollick, M. M. R., Chattopadhyay, D. & Acharya, K. An eco-friendly route of γ-Fe2O3 nanoparticles formation and investigation of

the mechanical properties of the HPMC-γ-Fe2O3 nanocomposites. *Bioprocess and biosystems engineering* **40**, 351-359 (2017).

158 Amemiya, Y., Arakaki, A., Staniland, S. S., Tanaka, T. & Matsunaga, T. Controlled formation of magnetite crystal by partial oxidation of ferrous hydroxide in the presence of recombinant magnetotactic bacterial protein Mms6. *Biomaterials* **28**, 5381-5389 (2007).

159 Kanazawa, A. *et al.* Biologically synthesized or bioinspired process-derived iron oxides as catalysts for living cationic polymerization of a vinyl ether. *Chemical Communications* **48**, 10904-10906 (2012).

160 Lopez-Moreno, R. *et al.* Magnetite nanoparticles biomineralization in the presence of the magnetosome membrane protein MamC: Effect of protein aggregation and protein structure on magnetite formation. *Crystal Growth & Design* **17**, 1620-1629 (2017).

161 Prasad, C. *et al.* Bio-inspired green synthesis of RGO/Fe3O4 magnetic nanoparticles using Murrayakoenigii leaves extract and its application for removal of Pb (II) from aqueous solution. *Journal of Environmental Chemical Engineering* (2017).

162 Prasad, C., Sreenivasulu, K., Gangadhara, S. & Venkateswarlu, P. Bio inspired green synthesis of Ni/Fe 3 O 4 magnetic nanoparticles using Moringa oleifera leaves extract: A magnetically recoverable catalyst for organic dye degradation in aqueous solution. *Journal of Alloys and Compounds* **700**, 252-258 (2017).

163 Venkateswarlu, S., Kumar, B. N., Prasad, C., Venkateswarlu, P. & Jyothi, N. Bio-inspired green synthesis of Fe 3 O 4 spherical magnetic nanoparticles using Syzygium cumini seed extract. *Physica B: Condensed Matter* **449**, 67-71 (2014).

164 Lenders, J. J. *et al.* A bioinspired coprecipitation method for the controlled synthesis of magnetite nanoparticles. *Crystal Growth & Design* **14**, 5561-5568 (2014).

165 Lenders, J. J. *et al.* Bioinspired magnetite crystallization directed by random copolypeptides. *Advanced Functional Materials* **25**, 711-719 (2015).

166 Pratt, L. R. & Chandler, D. Theory of the hydrophobic effect. *The Journal of Chemical Physics* **67**, 3683-3704 (1977).

167 Hummer, G., Garde, S., Garcia, A. E., Pohorille, A. & Pratt, L. R. An information theory model of hydrophobic interactions. *Proceedings of the National Academy of Sciences* **93**, 8951-8955 (1996).

168 Scheraga, H. A. Theory of hydrophobic interactions. *Journal of Biomolecular Structure and Dynamics* **16**, 447-460 (1998).

169 Ben-Naim, A. Y. *Hydrophobic interactions*. (Springer Science & Business Media, 2012).

170 Huang, D. M. & Chandler, D. The hydrophobic effect and the influence of solute− solvent attractions. *The Journal of Physical Chemistry B* **106**, 2047-2053 (2002).

171 Hamley, I. Nanotechnology with soft materials. *Angewandte Chemie International Edition* **42**, 1692-1712 (2003).

172 Wang, S. H. *et al.* Dendrimer-Functionalized Iron Oxide Nanoparticles for Specific Targeting and Imaging of Cancer Cells. *Advanced Functional Materials* **17**, 3043-3050 (2007).

173 Hadjipanayis, C. G. *et al.* EGFRvIII antibody–conjugated iron oxide nanoparticles for magnetic resonance imaging–guided convection-enhanced delivery and targeted therapy of glioblastoma. *Cancer research* **70**, 6303-6312 (2010).
174 Yang, H. *et al.* Targeted dual-contrast T1-and T2-weighted magnetic resonance imaging of tumors using multifunctional gadolinium-labeled superparamagnetic iron oxide nanoparticles. *Biomaterials* **32**, 4584-4593 (2011).
175 Hui, C. *et al.* Large-scale Fe 3O 4 nanoparticles soluble in water synthesized by a facile method. *The Journal of Physical Chemistry C* **112**, 11336-11339 (2008).
176 Shariati, S., Faraji, M., Yamini, Y. & Rajabi, A. A. Fe3O4 magnetic nanoparticles modified with sodium dodecyl sulfate for removal of safranin O dye from aqueous solutions. *Desalination* **270**, 160-165 (2011).
177 Jin, Y., Liu, F., Tong, M. & Hou, Y. Removal of arsenate by cetyltrimethylammonium bromide modified magnetic nanoparticles. *Journal of hazardous materials* **227**, 461-468 (2012).
178 Cui, S., Lin, B., Fan, M. & Shen, X. Interaction Mechanism between Fe3O4 nanoparticles and sodium 2-dodecylbenzenesulfonate. *Current Nanoscience* **7**, 366-370 (2011).
179 Katz, E., Baron, R. & Willner, I. Magnetoswitchable electrochemistry gated by alkyl-chain-functionalized magnetic nanoparticles: Control of diffusional and surface-confined electrochemical processes. *Journal of the American Chemical Society* **127**, 4060-4070 (2005).
180 Zhang, L., He, R. & Gu, H.-C. Oleic acid coating on the monodisperse magnetite nanoparticles. *Applied Surface Science* **253**, 2611-2617 (2006).
181 Sun, S. & Zeng, H. Size-controlled synthesis of magnetite nanoparticles. *Journal of the American Chemical Society* **124**, 8204-8205 (2002).
182 Wu, W., He, Q. & Chen, H. in *Bioinformatics and Biomedical Engineering, 2007. ICBBE 2007. The 1st International Conference on.* 76-79 (IEEE).
183 Zhang, S. *et al.* Size effects of Ag nanoparticles on plasmon-induced enhancement of photocatalysis of Ag-α-Fe2O3 nanocomposites. *Journal of colloid and interface science* **427**, 29-34 (2014).
184 Shultz, M. D., Reveles, J. U., Khanna, S. N. & Carpenter, E. E. Reactive nature of dopamine as a surface functionalization agent in iron oxide nanoparticles. *Journal of the American Chemical Society* **129**, 2482-2487 (2007).
185 Xu, C. *et al.* Dopamine as a robust anchor to immobilize functional molecules on the iron oxide shell of magnetic nanoparticles. *Journal of the American Chemical Society* **126**, 9938-9939 (2004).
186 Losic, D. *et al.* Surface functionalisation of diatoms with dopamine modified iron-oxide nanoparticles: toward magnetically guided drug microcarriers with biologically derived morphologies. *Chemical Communications* **46**, 6323-6325 (2010).
187 Yang, X. *et al.* cRGD-functionalized, DOX-conjugated, and 64Cu-labeled superparamagnetic iron oxide nanoparticles for targeted

anticancer drug delivery and PET/MR imaging. *Biomaterials* **32**, 4151-4160 (2011).

188 Kemikli, N., Kavas, H., Kazan, S., Baykal, A. & Ozturk, R. Synthesis of protoporphyrin coated superparamagnetic iron oxide nanoparticles via dopamine anchor. *Journal of Alloys and Compounds* **502**, 439-444 (2010).

189 Boyer, C., Whittaker, M. R., Bulmus, V., Liu, J. & Davis, T. P. The design and utility of polymer-stabilized iron-oxide nanoparticles for nanomedicine applications. *NPG Asia Materials* **2**, 23 (2010).

190 Tassa, C., Shaw, S. Y. & Weissleder, R. Dextran-coated iron oxide nanoparticles: a versatile platform for targeted molecular imaging, molecular diagnostics, and therapy. *Accounts of chemical research* **44**, 842-852 (2011).

191 Chang, P. R., Yu, J., Ma, X. & Anderson, D. P. Polysaccharides as stabilizers for the synthesis of magnetic nanoparticles. *Carbohydrate polymers* **83**, 640-644 (2011).

192 Shultz, M. D., Calvin, S., Fatouros, P. P., Morrison, S. A. & Carpenter, E. E. Enhanced ferrite nanoparticles as MRI contrast agents. *Journal of Magnetism and Magnetic Materials* **311**, 464-468 (2007).

193 Butterworth, M., Illum, L. & Davis, S. Preparation of ultrafine silica-and PEG-coated magnetite particles. *Colloids and Surfaces A: Physicochemical and Engineering Aspects* **179**, 93-102 (2001).

194 Kohler, N., Fryxell, G. E. & Zhang, M. A bifunctional poly (ethylene glycol) silane immobilized on metallic oxide-based nanoparticles for conjugation with cell targeting agents. *Journal of the American Chemical Society* **126**, 7206-7211 (2004).

195 Zhang, Y., Kohler, N. & Zhang, M. Surface modification of superparamagnetic magnetite nanoparticles and their intracellular uptake. *Biomaterials* **23**, 1553-1561 (2002).

196 Tiefenauer, L., Tschirky, A., Kühne, G. & Andres, R. In vivo evaluation of magnetite nanoparticles for use as a tumor contrast agent in MRI. *Magnetic resonance imaging* **14**, 391-402 (1996).

197 Moghimi, S. M., Hunter, A. C. & Murray, J. C. Long-circulating and target-specific nanoparticles: theory to practice. *Pharmacological reviews* **53**, 283-318 (2001).

198 Yokoi, H. & Kantoh, T. Thermal decomposition of the iron (III) hydroxide and magnetite composites of poly (vinyl alcohol). Preparation of magnetite and metallic iron particles. *Bulletin of the Chemical Society of Japan* **66**, 1536-1541 (1993).

199 Sairam, M., Naidu, B. V. K., Nataraj, S. K., Sreedhar, B. & Aminabhavi, T. M. Poly (vinyl alcohol)-iron oxide nanocomposite membranes for pervaporation dehydration of isopropanol, 1, 4-dioxane and tetrahydrofuran. *Journal of membrane science* **283**, 65-73 (2006).

200 Schöpf, B. *et al.* Methodology description for detection of cellular uptake of PVA coated superparamagnetic iron oxide nanoparticles (SPION) in synovial cells of sheep. *Journal of magnetism and magnetic materials* **293**, 411-418 (2005).

201 Petri-Fink, A., Chastellain, M., Juillerat-Jeanneret, L., Ferrari, A. & Hofmann, H. Development of functionalized superparamagnetic iron

oxide nanoparticles for interaction with human cancer cells. *Biomaterials* **26**, 2685-2694 (2005).

202 Kayal, S. & Ramanujan, R. Doxorubicin loaded PVA coated iron oxide nanoparticles for targeted drug delivery. *Materials Science and Engineering: C* **30**, 484-490 (2010).

203 Moore, A., Marecos, E., Bogdanov Jr, A. & Weissleder, R. Tumoral distribution of long-circulating dextran-coated iron oxide nanoparticles in a rodent model. *Radiology* **214**, 568-574 (2000).

204 Can, H. K., Kavlak, S., ParviziKhosroshahi, S. & Güner, A. Preparation, characterization and dynamical mechanical properties of dextran-coated iron oxide nanoparticles (DIONPs). *Artificial cells, nanomedicine, and biotechnology*, 1-11 (2017).

205 Bi, F., Zhang, J., Su, Y., Tang, Y.-C. & Liu, J.-N. Chemical conjugation of urokinase to magnetic nanoparticles for targeted thrombolysis. *Biomaterials* **30**, 5125-5130 (2009).

206 Abdollah, M. R. *et al.* Fucoidan Prolongs the Circulation Time of Dextran-Coated Iron Oxide Nanoparticles. *ACS nano* (2018).

207 Zhi, J., Wang, Y., Lu, Y., Ma, J. & Luo, G. In situ preparation of magnetic chitosan/Fe3O4 composite nanoparticles in tiny pools of water-in-oil microemulsion. *Reactive and Functional Polymers* **66**, 1552-1558 (2006).

208 Kim, E. H., Ahn, Y. & Lee, H. S. Biomedical applications of superparamagnetic iron oxide nanoparticles encapsulated within chitosan. *Journal of Alloys and Compounds* **434**, 633-636 (2007).

209 Kim, E. H., Lee, H. S., Kwak, B. K. & Kim, B.-K. Synthesis of ferrofluid with magnetic nanoparticles by sonochemical method for MRI contrast agent. *Journal of Magnetism and Magnetic Materials* **289**, 328-330 (2005).

210 Nehra, P., Chauhan, R., Garg, N. & Verma, K. Antibacterial and antifungal activity of chitosan coated iron oxide nanoparticles. *British journal of biomedical science* **75**, 13-18 (2018).

211 Oh, J. K. & Park, J. M. Iron oxide-based superparamagnetic polymeric nanomaterials: design, preparation, and biomedical application. *Progress in Polymer Science* **36**, 168-189 (2011).

212 Kim, B.-S., Qiu, J.-M., Wang, J.-P. & Taton, T. A. Magnetomicelles: composite nanostructures from magnetic nanoparticles and cross-linked amphiphilic block copolymers. *Nano letters* **5**, 1987-1991 (2005).

213 Hong, G.-b., Zhou, J.-x. & Yuan, R.-x. Folate-targeted polymeric micelles loaded with ultrasmall superparamagnetic iron oxide: combined small size and high MRI sensitivity. *International journal of nanomedicine* **7**, 2863 (2012).

214 Tong, S., Hou, S., Ren, B., Zheng, Z. & Bao, G. Self-assembly of phospholipid–PEG coating on nanoparticles through dual solvent exchange. *Nano letters* **11**, 3720-3726 (2011).

215 Su, H. *et al.* Amphiphilic starlike dextran wrapped superparamagnetic iron oxide nanoparticle clsuters as effective magnetic resonance imaging probes. *Biomaterials* **34**, 1193-1203 (2013).

216 Huang, J. *et al.* Fluxible nanoclusters of Fe3O4 nanocrystal-embedded polyaniline by macromolecule-induced self-assembly. *Langmuir* **29**, 10223-10228 (2013).

217 Rocha, N. *et al.* Novel nanoaggregates with peripheric superparamagnetic iron oxide nanoparticles and organic cores through self-assembly of tailor-made block copolymers. *RSC Advances* **4**, 24428-24432 (2014).
218 Pizarro, G. d. C., Marambio, O. G., Jeria-Orell, M., Sánchez, J. & Oyarzún, D. P. Nanocomposites based on self-assembly poly (hydroxypropyl metha crylate)-block-poly (N-phenylmaleimide) and Fe 3 O 4-NPs. Thermal stability, morphological characterization and optical properties. *Chemical Physics Letters* (2018).
219 Katagiri, K. *et al.* Templated nucleation of hybrid iron oxide nanoparticles on polysaccharide nanogels. *Colloid and Polymer Science* **291**, 1375-1380 (2013).
220 Ghamkhari, A., Agbolaghi, S., Poorgholy, N. & Massoumi, B. pH-responsive magnetic nanocomposites based on poly (2-succinyloxyethyl methacrylate-co-methylmethacrylate) for anticancer doxorubicin delivery applications. *Journal of Polymer Research* **25**, 37 (2018).
221 Suter, M. *et al.* Superparamagnetic photocurable nanocomposite for the fabrication of microcantilevers. *Journal of Micromechanics and Microengineering* **21**, 025023 (2011).
222 Liu, G., Wang, H. & Yang, X. Synthesis of pH-sensitive hollow polymer microspheres with movable magnetic core. *Polymer* **50**, 2578-2586 (2009).
223 Yu, S. *et al.* Magnetic and pH-sensitive nanoparticles for antitumor drug delivery. *Colloids and Surfaces B: Biointerfaces* **103**, 15-22 (2013).
224 Landgraf, L. *et al.* A plasma protein corona enhances the biocompatibility of Au@ Fe3O4 Janus particles. *Biomaterials* **68**, 77-88 (2015).
225 Spicer, C. D., Jumeaux, C., Gupta, B. & Stevens, M. M. Peptide and protein nanoparticle conjugates: versatile platforms for biomedical applications. *Chemical Society Reviews* (2018).
226 Lee, S.-J. *et al.* Intracellular translocation of superparamagnetic iron oxide nanoparticles encapsulated with peptide-conjugated poly (D, L lactide-co-glycolide). *Journal of applied physics* **97**, 10Q913 (2005).
227 Samanta, B. *et al.* Protein-passivated Fe 3 O 4 nanoparticles: low toxicity and rapid heating for thermal therapy. *Journal of materials chemistry* **18**, 1204-1208 (2008).
228 Wiogo, H. T., Lim, M., Bulmus, V., Yun, J. & Amal, R. Stabilization of magnetic iron oxide nanoparticles in biological media by fetal bovine serum (FBS). *Langmuir* **27**, 843-850 (2010).
229 Yang, Q., Liang, J. & Han, H. Probing the interaction of magnetic iron oxide nanoparticles with bovine serum albumin by spectroscopic techniques. *The Journal of Physical Chemistry B* **113**, 10454-10458 (2009).
230 Yang, H.-M. *et al.* HER2/neu antibody conjugated poly (amino acid)-coated iron oxide nanoparticles for breast cancer MR imaging. *Biomacromolecules* **11**, 2866-2872 (2010).
231 Ren, Y. *et al.* Facile, high efficiency immobilization of lipase enzyme on magnetic iron oxide nanoparticles via a biomimetic coating. *BMC biotechnology* **11**, 63 (2011).

232 Xu, H. *et al.* Antibody conjugated magnetic iron oxide nanoparticles for cancer cell separation in fresh whole blood. *Biomaterials* **32**, 9758-9765 (2011).
233 Alcalá, M. & Real, C. Synthesis based on the wet impregnation method and characterization of iron and iron oxide-silica nanocomposites. *Solid State Ionics* **177**, 955-960 (2006).
234 Woo, K., Hong, J. & Ahn, J.-P. Synthesis and surface modification of hydrophobic magnetite to processible magnetite@ silica-propylamine. *Journal of magnetism and magnetic materials* **293**, 177-181 (2005).
235 Bruce, I. J. *et al.* Synthesis, characterisation and application of silica-magnetite nanocomposites. *Journal of Magnetism and Magnetic Materials* **284**, 145-160 (2004).
236 Yu, J.-H., Lee, C.-W., Im, S.-S. & Lee, J.-S. Structure and magnetic properties of SiO 2 coated Fe 2 O 3 nanoparticles synthesized by chemical vapor condensation process. (2003).
237 Duanmu, C. *Expanding applications of iron oxide nanoparticles by surface functionalization: From magnetic resonance imaging to nano-catalysis*. (Southern Illinois University at Carbondale, 2009).
238 Sun, Y. *et al.* An improved way to prepare superparamagnetic magnetite-silica core-shell nanoparticles for possible biological application. *Journal of Magnetism and Magnetic Materials* **285**, 65-70 (2005).
239 Fang, C.-L. *et al.* Monodisperse α-Fe2O3@ SiO2@ Au core/shell nanocomposite spheres: synthesis, characterization and properties. *Nanotechnology* **19**, 125601 (2008).
240 Sun, X., Liu, F., Sun, L., Wang, Q. & Ding, Y. Well-dispersed Fe 3 O 4/SiO 2 nanoparticles synthesized by a mechanical stirring and ultrasonication assisted Stöber method. *Journal of Inorganic and Organometallic Polymers and Materials* **22**, 311-315 (2012).
241 Liu, Y.-L., Zhang, J.-L., Cheng, G., Hong, G.-Y. & Ni, J.-Z. A facile fabrication of spherical and beanpod-like magnetic-fluorescent particles with targeting functionalities. *Nanotechnology* **23**, 425702 (2012).
242 Butterworth, M., Bell, S., Armes, S. & Simpson, A. Synthesis and characterization of polypyrrole–magnetite–silica particles. *Journal of colloid and interface science* **183**, 91-99 (1996).
243 Liu, X., Xing, J., Guan, Y., Shan, G. & Liu, H. Synthesis of amino-silane modified superparamagnetic silica supports and their use for protein immobilization. *Colloids and Surfaces A: Physicochemical and Engineering Aspects* **238**, 127-131 (2004).
244 Liu, X., Ma, Z., Xing, J. & Liu, H. Preparation and characterization of amino–silane modified superparamagnetic silica nanospheres. *Journal of Magnetism and magnetic Materials* **270**, 1-6 (2004).
245 Ding, H. *et al.* Fe3O4@ SiO2 core/shell nanoparticles: the silica coating regulations with a single core for different core sizes and shell thicknesses. *Chemistry of Materials* **24**, 4572-4580 (2012).
246 Guerrero-Martínez, A., Pérez-Juste, J. & Liz-Marzán, L. M. Recent progress on silica coating of nanoparticles and related nanomaterials. *Advanced materials* **22**, 1182-1195 (2010).
247 Stjerndahl, M. *et al.* Superparamagnetic Fe3O4/SiO2 nanocomposites: enabling the tuning of both the iron oxide load and the size of the nanoparticles. *Langmuir* **24**, 3532-3536 (2008).

248 Zeltner, M. & Grass, R. N. 3 Carbon-Coated Magnetic Metal Nanoparticles for Clinical Applications. *Clinical Applications of Magnetic Nanoparticles*, 19 (2018).
249 He, C. *et al.* Carbon-encapsulated Fe3O4 nanoparticles as a high-rate lithium ion battery anode material. *ACS nano* **7**, 4459-4469 (2013).
250 Zhu, T., Chen, J. S. & Lou, X. W. Glucose-assisted one-pot synthesis of FeOOH nanorods and their transformation to Fe3O4@ carbon nanorods for application in lithium ion batteries. *The Journal of Physical Chemistry C* **115**, 9814-9820 (2011).
251 Zhao, N. *et al.* One-pot synthesis of uniform Fe3O4 nanocrystals encapsulated in interconnected carbon nanospheres for superior lithium storage capability. *Carbon* **57**, 130-138 (2013).
252 Chen, Y.-J. *et al.* Porous Fe3O4/carbon core/shell nanorods: synthesis and electromagnetic properties. *The Journal of Physical Chemistry C* **115**, 13603-13608 (2011).
253 Zhou, Z. *et al.* Facile synthesis of porous Fe 3 O 4@ C nanospheres as high-performance anode for lithium-ion battery. *Journal of Solid State Electrochemistry* **19**, 1211-1215 (2015).
254 Li, L. *et al.* Selected-Control Synthesis of Monodisperse Fe3O4@ C Core–Shell Spheres, Chains, and Rings as High-Performance Anode Materials for Lithium-Ion Batteries. *Chemistry-A European Journal* **18**, 11417-11422 (2012).
255 Kinoshita, T., Seino, S., Mizukoshi, Y., Nakagawa, T. & Yamamoto, T. A. Functionalization of magnetic gold/iron-oxide composite nanoparticles with oligonucleotides and magnetic separation of specific target. *Journal of Magnetism and Magnetic Materials* **311**, 255-258 (2007).
256 Hoskins, C. *et al.* Hybrid gold-iron oxide nanoparticles as a multifunctional platform for biomedical application. *Journal of nanobiotechnology* **10**, 27 (2012).
257 Tamer, U. *et al.* Gold-coated iron composite nanospheres targeted the detection of Escherichia coli. *International journal of molecular sciences* **14**, 6223-6240 (2013).
258 Chiou, J.-R., Lai, B.-H., Hsu, K.-C. & Chen, D.-H. One-pot green synthesis of silver/iron oxide composite nanoparticles for 4-nitrophenol reduction. *Journal of hazardous materials* **248**, 394-400 (2013).
259 Mirzaei, A. *et al.* Synthesis, characterization and gas sensing properties of Ag@ α-Fe2O3 core–shell nanocomposites. *Nanomaterials* **5**, 737-749 (2015).
260 Lee, C. S., Chang, H. H., Bae, P. K., Jung, J. & Chung, B. H. Bifunctional Nanoparticles Constructed Using One-Pot Encapsulation of a Fluorescent Polymer and Magnetic (Fe3O4) Nanoparticles in a Silica Shell. *Macromolecular bioscience* **13**, 321-331 (2013).
261 Shevchenko, E. V. *et al.* Gold/iron oxide core/hollow-shell nanoparticles. *Advanced Materials* **20**, 4323-4329 (2008).
262 Yang, C. *et al.* Effect of ultrasonic treatment on dispersibility of Fe 3 O 4 nanoparticles and synthesis of multi-core Fe 3 O 4/SiO 2 core/shell nanoparticles. *Journal of Materials Chemistry* **15**, 4252-4257 (2005).

263 Zhang, X., Liu, Y. & Qin, G. Break Snoek limit via superparamagnetic coupling in Fe3O4/silica multiple-core/shell nanoparticles. *Applied Physics Letters* **106**, 033105 (2015).
264 Liu, J. *et al.* Hierarchical Fe3O4@ TiO2 Yolk–Shell Microspheres with Enhanced Microwave-Absorption Properties. *Chemistry-A European Journal* **19**, 6746-6752 (2013).
265 Zhang, H. *et al.* Tailoring the void size of iron oxide@ carbon yolk–shell structure for optimized lithium storage. *Advanced Functional Materials* **24**, 4337-4342 (2014).
266 Do, Q. C., Kim, D.-G. & Ko, S.-O. Catalytic activity enhancement of a Fe3O4@ SiO2 yolk-shell structure for oxidative degradation of acetaminophen by decoration with copper. *Journal of Cleaner Production* **172**, 1243-1253 (2018).
267 Yohan, D. & Chithrani, B. D. Applications of nanoparticles in nanomedicine. *Journal of biomedical nanotechnology* **10**, 2371-2392 (2014).
268 Sajid, M. *et al.* Impact of nanoparticles on human and environment: review of toxicity factors, exposures, control strategies, and future prospects. *Environmental Science and Pollution Research* **22**, 4122-4143 (2015).
269 Colvin, V. L. The potential environmental impact of engineered nanomaterials. *Nature biotechnology* **21**, 1166 (2003).
270 Ray, P. C., Yu, H. & Fu, P. P. Toxicity and environmental risks of nanomaterials: challenges and future needs. *Journal of Environmental Science and Health Part C* **27**, 1-35 (2009).
271 Klaine, S. J. *et al.* Nanomaterials in the environment: behavior, fate, bioavailability, and effects. *Environmental toxicology and chemistry* **27**, 1825-1851 (2008).
272 Nowack, B. & Bucheli, T. D. Occurrence, behavior and effects of nanoparticles in the environment. *Environmental pollution* **150**, 5-22 (2007).
273 Brohi, R. D. *et al.* Toxicity of Nanoparticles on the Reproductive System in Animal Models: A Review. *Frontiers in pharmacology* **8**, 606 (2017).
274 Nel, A., Xia, T., Mädler, L. & Li, N. Toxic potential of materials at the nanolevel. *science* **311**, 622-627 (2006).
275 Xia, T., Li, N. & Nel, A. E. Potential health impact of nanoparticles. *Annual review of public health* **30**, 137-150 (2009).
276 Simon, T. *Environmental risk assessment: a toxicological approach*. (CRC Press, 2014).
277 Fjeld, R. A., Eisenberg, N. A. & Compton, K. L. *Quantitative environmental risk analysis for human health*. (John Wiley & Sons, 2007).
278 Shatkin, J. A. *Nanotechnology: health and environmental risks*. (Crc Press, 2017).
279 Warheit, D. B., Sayes, C. M., Reed, K. L. & Swain, K. A. Health effects related to nanoparticle exposures: environmental, health and safety considerations for assessing hazards and risks. *Pharmacology & therapeutics* **120**, 35-42 (2008).

280 Guo, H. & Barnard, A. S. Naturally occurring iron oxide nanoparticles: morphology, surface chemistry and environmental stability. *Journal of Materials Chemistry A* **1**, 27-42 (2013).
281 Farré, M., Sanchís, J. & Barceló, D. Analysis and assessment of the occurrence, the fate and the behavior of nanomaterials in the environment. *TrAC Trends in Analytical Chemistry* **30**, 517-527 (2011).
282 Borm, P. J. *et al.* The potential risks of nanomaterials: a review carried out for ECETOC. *Particle and fibre toxicology* **3**, 11 (2006).
283 Estelrich, J., Escribano, E., Queralt, J. & Busquets, M. A. Iron oxide nanoparticles for magnetically-guided and magnetically-responsive drug delivery. *International journal of molecular sciences* **16**, 8070-8101 (2015).
284 Lemire, J. A., Harrison, J. J. & Turner, R. J. Antimicrobial activity of metals: mechanisms, molecular targets and applications. *Nature Reviews Microbiology* **11**, 371 (2013).
285 Wanna, Y. *et al.* Efficiency of SPIONs functionalized with polyethylene glycol bis (amine) for heavy metal removal. *Journal of Magnetism and Magnetic Materials* **414**, 32-37 (2016).
286 Li, P., Miser, D. E., Rabiei, S., Yadav, R. T. & Hajaligol, M. R. The removal of carbon monoxide by iron oxide nanoparticles. *Applied Catalysis B: Environmental* **43**, 151-162 (2003).
287 Sánchez, A. *et al.* Ecotoxicity of, and remediation with, engineered inorganic nanoparticles in the environment. *TrAC Trends in Analytical Chemistry* **30**, 507-516 (2011).
288 Fatta-Kassinos, D., Kalavrouziotis, I., Koukoulakis, P. & Vasquez, M. The risks associated with wastewater reuse and xenobiotics in the agroecological environment. *Science of the Total Environment* **409**, 3555-3563 (2011).
289 Xu, P. *et al.* Use of iron oxide nanomaterials in wastewater treatment: a review. *Science of the Total Environment* **424**, 1-10 (2012).
290 Parham, H., Zargar, B. & Shiralipour, R. Fast and efficient removal of mercury from water samples using magnetic iron oxide nanoparticles modified with 2-mercaptobenzothiazole. *Journal of hazardous materials* **205**, 94-100 (2012).
291 Gupta, V., Agarwal, S. & Saleh, T. A. Chromium removal by combining the magnetic properties of iron oxide with adsorption properties of carbon nanotubes. *Water research* **45**, 2207-2212 (2011).
292 Liu, J.-F., Zhao, Z.-s. & Jiang, G.-b. Coating Fe3O4 magnetic nanoparticles with humic acid for high efficient removal of heavy metals in water. *Environmental science & technology* **42**, 6949-6954 (2008).
293 Yantasee, W. *et al.* Removal of heavy metals from aqueous systems with thiol functionalized superparamagnetic nanoparticles. *Environmental science & technology* **41**, 5114-5119 (2007).
294 Ge, F., Li, M.-M., Ye, H. & Zhao, B.-X. Effective removal of heavy metal ions Cd2+, Zn2+, Pb2+, Cu2+ from aqueous solution by polymer-modified magnetic nanoparticles. *Journal of hazardous materials* **211**, 366-372 (2012).
295 Zhang, Z. & Kong, J. Novel magnetic Fe3O4@ C nanoparticles as adsorbents for removal of organic dyes from aqueous solution. *Journal of hazardous materials* **193**, 325-329 (2011).

296 Yang, X. *et al.* Graphene oxide-iron oxide and reduced graphene oxide-iron oxide hybrid materials for the removal of organic and inorganic pollutants. *Rsc Advances* **2**, 8821-8826 (2012).
297 Wang, X. *et al.* Cancer stem cell labeling using poly (L-lysine)-modified iron oxide nanoparticles. *Biomaterials* **33**, 3719-3732 (2012).
298 Gupta, A. K. & Gupta, M. Synthesis and surface engineering of iron oxide nanoparticles for biomedical applications. *Biomaterials* **26**, 3995-4021 (2005).
299 Novotna, B., Herynek, V., Rossner Jr, P., Turnovcova, K. & Jendelova, P. The effects of grafted mesenchymal stem cells labeled with iron oxide or cobalt-zinc-iron nanoparticles on the biological macromolecules of rat brain tissue extracts. *International journal of nanomedicine* **12**, 4519 (2017).
300 Soenen, S. J., Brisson, A. R. & De Cuyper, M. Addressing the problem of cationic lipid-mediated toxicity: the magnetoliposome model. *Biomaterials* **30**, 3691-3701 (2009).
301 Soenen, S. J., Himmelreich, U., Nuytten, N. & De Cuyper, M. Cytotoxic effects of iron oxide nanoparticles and implications for safety in cell labelling. *Biomaterials* **32**, 195-205 (2011).
302 Estelrich, J., Sánchez-Martín, M. J. & Busquets, M. A. Nanoparticles in magnetic resonance imaging: from simple to dual contrast agents. *International journal of nanomedicine* **10**, 1727 (2015).
303 Xie, J., Huang, J., Li, X., Sun, S. & Chen, X. Iron oxide nanoparticle platform for biomedical applications. *Current medicinal chemistry* **16**, 1278-1294 (2009).
304 Luo, X., Morrin, A., Killard, A. J. & Smyth, M. R. Application of nanoparticles in electrochemical sensors and biosensors. *Electroanalysis* **18**, 319-326 (2006).
305 Chauhan, N. & Pundir, C. S. An amperometric biosensor based on acetylcholinesterase immobilized onto iron oxide nanoparticles/multi-walled carbon nanotubes modified gold electrode for measurement of organophosphorus insecticides. *Analytica chimica acta* **701**, 66-74 (2011).
306 Kaushik, A. *et al.* Iron oxide nanoparticles–chitosan composite based glucose biosensor. *Biosensors and bioelectronics* **24**, 676-683 (2008).
307 Yang, L. *et al.* A novel peptide/Fe3O4@ SiO2-Au nanocomposite-based fluorescence biosensor for the highly selective and sensitive detection of prostate-specific antigen. *Talanta* **179**, 531-537 (2018).
308 Lee, J., Morita, M., Takemura, K. & Park, E. Y. A multi-functional gold/iron-oxide nanoparticle-CNT hybrid nanomaterial as virus DNA sensing platform. *Biosensors and Bioelectronics* **102**, 425-431 (2018).
309 Pusic, K. *et al.* Iron oxide nanoparticles as a clinically acceptable delivery platform for a recombinant blood-stage human malaria vaccine. *The FASEB Journal* **27**, 1153-1166 (2013).
310 Manuelli, M. *et al.* Iron oxide superparamagnetic nanoparticles conjugated with a conformationally blocked α-Tn antigen mimetic for macrophage activation. *Nanoscale* **6**, 7643-7655 (2014).
311 Parveen, S. *et al.* Preparation, characterization and antifungal activity of iron oxide nanoparticles. *Microbial pathogenesis* (2018).

312 Jagathesan, G. & Rajiv, P. Biosynthesis and characterization of iron oxide nanoparticles using Eichhornia crassipes leaf extract and assessing their antibacterial activity. *Biocatalysis and Agricultural Biotechnology* **13**, 90-94 (2018).
313 Arakha, M. & Jha, S. in *Interfacial Phenomena on Biological Membranes* 79-89 (Springer, 2018).
314 Siddiqui, M. H. *et al.* Calcium-induced amelioration of boron toxicity in radish. *Journal of plant growth regulation* **32**, 61-71 (2013).
315 Srivastava, N. Iron nanoparticles induced toxicity in Sesbania cannabina: a morphological aspect. *Advanced Science Focus* **2**, 135-139 (2014).
316 Aslani, F. *et al.* Effects of engineered nanomaterials on plants growth: an overview. *The Scientific World Journal* **2014** (2014).
317 Servin, A. *et al.* A review of the use of engineered nanomaterials to suppress plant disease and enhance crop yield. *Journal of Nanoparticle Research* **17**, 92 (2015).
318 Martins, M. *et al.* Monodisperse Pd nanoparticles assembled on reduced graphene oxide-Fe 3 O 4 nanocomposites as electrocatalysts for borohydride fuel cells. *International Journal of Hydrogen Energy* (2018).
319 Jung, J.-W., Jang, J.-S., Yun, T. G., Yoon, K. R. & Kim, I.-D. 3D Nanofibrous Air Electrode Assembled With Carbon Nanotubes Bridged Hollow Fe2O3 Nanoparticles for High Performance Lithium-Oxygen Batteries. *ACS applied materials & interfaces* (2018).
320 Matsui, I. Nanoparticles for electronic device applications: a brief review. *Journal of chemical engineering of Japan* **38**, 535-546 (2005).
321 Zhu, X., Zhu, Y., Murali, S., Stoller, M. D. & Ruoff, R. S. Nanostructured reduced graphene oxide/Fe2O3 composite as a high-performance anode material for lithium ion batteries. *ACS nano* **5**, 3333-3338 (2011).
322 Bao, S. P., Lu, X. K., Luo, W. J. & Sham, M. L. (Google Patents, 2017).
323 Yadav, T. (Google Patents, 2004).
324 Cheshire, M. C., Herpfer, M. A. & Goss, G. R. (Google Patents, 2008).
325 Choi, H. C. *et al.* Efficient formation of iron nanoparticle catalysts on silicon oxide by hydroxylamine for carbon nanotube synthesis and electronics. *Nano Letters* **3**, 157-161 (2003).
326 Kornberg, T. G. *et al.* Potential Toxicity and Underlying Mechanisms Associated with Pulmonary Exposure to Iron Oxide Nanoparticles: Conflicting Literature and Unclear Risk. *Nanomaterials* **7**, 307 (2017).
327 Pelclova, D. *et al.* Oxidative stress markers are elevated in exhaled breath condensate of workers exposed to nanoparticles during iron oxide pigment production. *Journal of breath research* **10**, 016004 (2016).
328 Rahman, M., Laurent, S., Tawil, N., Yahia, L. & Mahmoudi, L. (Springer: Berlin/Heidelberg, Germany, 2013).
329 Kokkinopoulou, M., Simon, J., Landfester, K., Mailänder, V. & Lieberwirth, I. Visualization of the protein corona: towards a biomolecular understanding of nanoparticle-cell-interactions. *Nanoscale* **9**, 8858-8870 (2017).
330 Mahmoudi, M. *et al.* Protein− nanoparticle interactions: opportunities and challenges. *Chemical reviews* **111**, 5610-5637 (2011).

331 Mahmoudi, M. *et al.* Variation of protein corona composition of gold nanoparticles following plasmonic heating. *Nano letters* **14**, 6-12 (2013).
332 Tenzer, S. *et al.* Rapid formation of plasma protein corona critically affects nanoparticle pathophysiology. *Nature nanotechnology* **8**, 772 (2013).
333 Pieper, R. *et al.* The human serum proteome: Display of nearly 3700 chromatographically separated protein spots on two-dimensional electrophoresis gels and identification of 325 distinct proteins. *Proteomics* **3**, 1345-1364 (2003).
334 Mahmoudi, M. *et al.* Crucial role of the protein corona for the specific targeting of nanoparticles. *Nanomedicine* **10**, 215-226 (2015).
335 Lundqvist, M. *et al.* Nanoparticle size and surface properties determine the protein corona with possible implications for biological impacts. *Proceedings of the National Academy of Sciences* **105**, 14265-14270 (2008).
336 Lynch, I. & Dawson, K. A. Protein-nanoparticle interactions. *Nano today* **3**, 40-47 (2008).
337 Lundqvist, M. *et al.* The evolution of the protein corona around nanoparticles: a test study. *ACS nano* **5**, 7503-7509 (2011).
338 Maiorano, G. *et al.* Effects of cell culture media on the dynamic formation of protein− nanoparticle complexes and influence on the cellular response. *ACS nano* **4**, 7481-7491 (2010).
339 Rahman, M., Laurent, S., Tawil, N., Yahia, L. H. & Mahmoudi, M. in *Protein-nanoparticle interactions* 21-44 (Springer, 2013).
340 Lynch, I., Salvati, A. & Dawson, K. A. Protein-nanoparticle interactions: what does the cell see? *Nature nanotechnology* **4**, 546 (2009).
341 Gräfe, C. *et al.* Intentional formation of a protein corona on nanoparticles: serum concentration affects protein corona mass, surface charge, and nanoparticle–cell interaction. *The international journal of biochemistry & cell biology* **75**, 196-202 (2016).
342 Monopoli, M. P. *et al.* Physical− chemical aspects of protein corona: relevance to in vitro and in vivo biological impacts of nanoparticles. *Journal of the American Chemical Society* **133**, 2525-2534 (2011).
343 Yallapu, M. M. *et al.* Implications of protein corona on physico-chemical and biological properties of magnetic nanoparticles. *Biomaterials* **46**, 1-12 (2015).
344 Thiele, L., Diederichs, J. E., Reszka, R., Merkle, H. P. & Walter, E. Competitive adsorption of serum proteins at microparticles affects phagocytosis by dendritic cells. *Biomaterials* **24**, 1409-1418 (2003).
345 Kang, T., Park, C., Choi, J.-S., Cui, J.-H. & Lee, B.-J. Effects of shear stress on the cellular distribution of polystyrene nanoparticles in a biomimetic microfluidic system. *Journal of Drug Delivery Science and Technology* **31**, 130-136 (2016).
346 Vines, R. L., Rogers, K. & Westrup, G. *The Human Cardiovascular System: The Blood Vessels*. (California State University and Benjamin/Cummings, 1995).
347 Palchetti, S. *et al.* The protein corona of circulating PEGylated liposomes. *Biochimica et Biophysica Acta (BBA)-Biomembranes* **1858**, 189-196 (2016).

348 Wilson, J. D. *et al.* Principles of internal medicine. *Pub, McGraw-Hill* **2**, 2038 (1991).
349 Hasday, J. D. & Singh, I. S. Fever and the heat shock response: distinct, partially overlapping processes. *Cell stress & chaperones* **5**, 471-480 (2000).
350 Mahmoudi, M. *et al.* Temperature: the "ignored" factor at the nanobio interface. *ACS nano* **7**, 6555-6562 (2013).
351 Bhogale, A. *et al.* Comprehensive studies on the interaction of copper nanoparticles with bovine serum albumin using various spectroscopies. *Colloids and Surfaces B: Biointerfaces* **113**, 276-284 (2014).
352 O'Brien, J. & Shea, K. J. Tuning the protein corona of hydrogel nanoparticles: the synthesis of abiotic protein and peptide affinity reagents. *Accounts of chemical research* **49**, 1200-1210 (2016).
353 Fallingborg, J. Intraluminal pH of the human gastrointestinal tract. *Danish medical bulletin* **46**, 183-196 (1999).
354 Cooper, G. M. & Hausman, R. E. *The cell: Molecular approach*. (Medicinska naklada, 2004).
355 Gatenby, R. A. & Gillies, R. J. Why do cancers have high aerobic glycolysis? *Nature Reviews Cancer* **4**, 891 (2004).
356 Estrella, V. *et al.* Acidity generated by the tumor microenvironment drives local invasion. *Cancer research* **73**, 1524-1535 (2013).
357 Ouyang, G., Wang, C. & Yang, G. Surface energy of nanostructural materials with negative curvature and related size effects. *Chemical reviews* **109**, 4221-4247 (2009).
358 Walczyk, D., Bombelli, F. B., Monopoli, M. P., Lynch, I. & Dawson, K. A. What the cell "sees" in bionanoscience. *Journal of the American Chemical Society* **132**, 5761-5768 (2010).
359 Lacerda, S. H. D. P. *et al.* Interaction of gold nanoparticles with common human blood proteins. *ACS nano* **4**, 365-379 (2009).
360 Goy-López, S. *et al.* Physicochemical characteristics of protein–NP bioconjugates: the role of particle curvature and solution conditions on human serum albumin conformation and fibrillogenesis inhibition. *Langmuir* **28**, 9113-9126 (2012).
361 Lindman, S. *et al.* Systematic investigation of the thermodynamics of HSA adsorption to N-iso-propylacrylamide/N-tert-butylacrylamide copolymer nanoparticles. Effects of particle size and hydrophobicity. *Nano letters* **7**, 914-920 (2007).
362 Mu, Q. *et al.* Protein binding by functionalized multiwalled carbon nanotubes is governed by the surface chemistry of both parties and the nanotube diameter. *The Journal of Physical Chemistry C* **112**, 3300-3307 (2008).
363 Lundqvist, M., Sethson, I. & Jonsson, B.-H. Protein adsorption onto silica nanoparticles: conformational changes depend on the particles' curvature and the protein stability. *Langmuir* **20**, 10639-10647 (2004).
364 Xu, F. *et al.* Lipid-mediated targeting with membrane-wrapped nanoparticles in the presence of corona formation. *ACS nano* **10**, 1189-1200 (2016).
365 Walkey, C. D., Olsen, J. B., Guo, H., Emili, A. & Chan, W. C. Nanoparticle size and surface chemistry determine serum protein

adsorption and macrophage uptake. *Journal of the American Chemical Society* **134**, 2139-2147 (2012).

366 Gagner, J. E., Lopez, M. D., Dordick, J. S. & Siegel, R. W. Effect of gold nanoparticle morphology on adsorbed protein structure and function. *Biomaterials* **32**, 7241-7252 (2011).

367 Mahmoudi, M., Milani, A. S. & Stroeve, P. Synthesis, surface architecture and biological response of superparamagnetic iron oxide nanoparticles for application in drug delivery: a review. *International Journal of Biomedical Nanoscience and Nanotechnology* **1**, 164-201 (2010).

368 Bradley, A. J., Devine, D. V., Ansell, S. M., Janzen, J. & Brooks, D. E. Inhibition of liposome-induced complement activation by incorporated poly (ethylene glycol)-lipids. *Archives of biochemistry and biophysics* **357**, 185-194 (1998).

369 Oku, N. *et al.* Effect of serum protein binding on real-time trafficking of liposomes with different charges analyzed by positron emission tomography. *Biochimica et Biophysica Acta (BBA)-Biomembranes* **1280**, 149-154 (1996).

370 Temming, K. *et al.* Delivery of the p38 MAPkinase Inhibitor SB202190 to Angiogenic Endothelial Cells: Development of Novel RGD-Equipped and PEGylated Drug− Albumin Conjugates Using Platinum (II)-Based Drug Linker Technology. *Bioconjugate chemistry* **17**, 1246-1255 (2006).

371 Nel, A. E. *et al.* Understanding biophysicochemical interactions at the nano–bio interface. *Nature materials* **8**, 543 (2009).

372 Hoek, E. M. & Agarwal, G. K. Extended DLVO interactions between spherical particles and rough surfaces. *Journal of Colloid and Interface science* **298**, 50-58 (2006).

373 Staufenbiel, S. *et al.* Surface characterization and protein interaction of a series of model poly [acrylonitrile-co-(N-vinyl pyrrolidone)] nanocarriers for drug targeting. *International journal of pharmaceutics* **485**, 87-96 (2015).

374 Gessner, A. *et al.* Nanoparticles with decreasing surface hydrophobicities: influence on plasma protein adsorption. *International journal of pharmaceutics* **196**, 245-249 (2000).

375 Buijs, J. *et al.* Conformational stability of adsorbed insulin studied with mass spectrometry and hydrogen exchange. *Analytical chemistry* **71**, 3219-3225 (1999).

376 Kondo, A., Oku, S., Murakami, F. & Higashitani, K. Conformational changes in protein molecules upon adsorption on ultrafine particles. *Colloids and Surfaces B: Biointerfaces* **1**, 197-201 (1993).

377 Aggarwal, P., Hall, J. B., McLeland, C. B., Dobrovolskaia, M. A. & McNeil, S. E. Nanoparticle interaction with plasma proteins as it relates to particle biodistribution, biocompatibility and therapeutic efficacy. *Advanced drug delivery reviews* **61**, 428-437 (2009).

378 Cedervall, T. *et al.* Understanding the nanoparticle–protein corona using methods to quantify exchange rates and affinities of proteins for nanoparticles. *Proceedings of the National Academy of Sciences* **104**, 2050-2055 (2007).

379 Larsericsdotter, H., Oscarsson, S. & Buijs, J. Thermodynamic analysis of proteins adsorbed on silica particles: electrostatic effects. *Journal of colloid and interface science* **237**, 98-103 (2001).
380 Yu, C. H. *et al.* Immobilization of BSA on silica-coated magnetic iron oxide nanoparticle. *The Journal of Physical Chemistry C* **113**, 537-543 (2008).
381 Dutta, D. *et al.* Adsorbed proteins influence the biological activity and molecular targeting of nanomaterials. *Toxicological Sciences* **100**, 303-315 (2007).
382 Moghimi, S. M., Muir, I., Illum, L., Davis, S. S. & Kolb-Bachofen, V. Coating particles with a block co-polymer (poloxamine-908) suppresses opsonization but permits the activity of dysopsonins in the serum. *Biochimica et Biophysica Acta (BBA)-Molecular Cell Research* **1179**, 157-165 (1993).
383 Mahmoudi, M., Simchi, A., Milani, A. & Stroeve, P. Cell toxicity of superparamagnetic iron oxide nanoparticles. *Journal of colloid and interface science* **336**, 510-518 (2009).
384 Li, N., Xia, T. & Nel, A. E. The role of oxidative stress in ambient particulate matter-induced lung diseases and its implications in the toxicity of engineered nanoparticles. *Free Radical Biology and Medicine* **44**, 1689-1699 (2008).
385 Ju-Nam, Y. & Lead, J. R. Manufactured nanoparticles: an overview of their chemistry, interactions and potential environmental implications. *Science of the total environment* **400**, 396-414 (2008).
386 Stone, V., Johnston, H. & Clift, M. J. Air pollution, ultrafine and nanoparticle toxicology: cellular and molecular interactions. *IEEE transactions on nanobioscience* **6**, 331-340 (2007).
387 Johnston, H. J. *et al.* A review of the in vivo and in vitro toxicity of silver and gold particulates: particle attributes and biological mechanisms responsible for the observed toxicity. *Critical reviews in toxicology* **40**, 328-346 (2010).
388 Wang, Y. *et al.* Excess titanium dioxide nanoparticles on the cell surface induce cytotoxicity by hindering ion exchange and disrupting exocytosis processes. *Nanoscale* **7**, 13105-13115 (2015).
389 Lankoff, A. *et al.* The effect of agglomeration state of silver and titanium dioxide nanoparticles on cellular response of HepG2, A549 and THP-1 cells. *Toxicology letters* **208**, 197-213 (2012).
390 Prasad, R. Y. *et al.* Cellular interactions and biological responses to titanium dioxide nanoparticles in HepG2 and BEAS-2B cells: Role of cell culture media. *Environmental and molecular mutagenesis* **55**, 336-342 (2014).
391 Lei, L., Ling-Ling, J., Yun, Z. & Gang, L. Toxicity of superparamagnetic iron oxide nanoparticles: research strategies and implications for nanomedicine. *Chinese Physics B* **22**, 127503 (2013).
392 Rousk, J., Ackermann, K., Curling, S. F. & Jones, D. L. Comparative toxicity of nanoparticulate CuO and ZnO to soil bacterial communities. *PloS one* **7**, e34197 (2012).
393 Zhang, Z.-Y. & Xiong, H.-M. Photoluminescent ZnO nanoparticles and their biological applications. *Materials* **8**, 3101-3127 (2015).

394 Franklin, N. M. *et al.* Comparative toxicity of nanoparticulate ZnO, bulk ZnO, and ZnCl2 to a freshwater microalga (Pseudokirchneriella subcapitata): the importance of particle solubility. *Environmental science & technology* **41**, 8484-8490 (2007).
395 Adrain, C., Creagh, E. M. & Martin, S. J. Defying death: showing Bcl-2 the way home. *Nature cell biology* **5**, 9 (2003).
396 Zhao, J. *et al.* Titanium dioxide (TiO2) nanoparticles induce JB6 cell apoptosis through activation of the caspase-8/Bid and mitochondrial pathways. *Journal of Toxicology and Environmental Health, Part A* **72**, 1141-1149 (2009).
397 Donaldson, K. *et al.* Combustion-derived nanoparticles: a review of their toxicology following inhalation exposure. *Particle and fibre toxicology* **2**, 10 (2005).
398 Huang, Y.-W., Wu, C.-h. & Aronstam, R. S. Toxicity of transition metal oxide nanoparticles: recent insights from in vitro studies. *Materials* **3**, 4842-4859 (2010).
399 Mocan, T. *et al.* Implications of oxidative stress mechanisms in toxicity of nanoparticles. *Acta Physiologica Hungarica* **97**, 247-255 (2010).
400 Risom, L., Møller, P. & Loft, S. Oxidative stress-induced DNA damage by particulate air pollution. *Mutation Research/Fundamental and Molecular Mechanisms of Mutagenesis* **592**, 119-137 (2005).
401 Knaapen, A. M., Borm, P. J., Albrecht, C. & Schins, R. P. Inhaled particles and lung cancer. Part A: Mechanisms. *International Journal of Cancer* **109**, 799-809 (2004).
402 Kehrer, J. P. The Haber–Weiss reaction and mechanisms of toxicity. *Toxicology* **149**, 43-50 (2000).
403 Harber, F. & Weiss, J. in *Proc. R. Soc. Lond. A.* 332-351 (The Royal Society).
404 Xue, X., Hanna, K. & Deng, N. Fenton-like oxidation of Rhodamine B in the presence of two types of iron (II, III) oxide. *Journal of hazardous materials* **166**, 407-414 (2009).
405 Gorski, C. A., Nurmi, J. T., Tratnyek, P. G., Hofstetter, T. B. & Scherer, M. M. Redox behavior of magnetite: Implications for contaminant reduction. *Environmental science & technology* **44**, 55-60 (2009).
406 Voinov, M. A., Pagán, J. O. S., Morrison, E., Smirnova, T. I. & Smirnov, A. I. Surface-mediated production of hydroxyl radicals as a mechanism of iron oxide nanoparticle biotoxicity. *Journal of the American Chemical Society* **133**, 35-41 (2010).
407 Cornell, R. M. & Schwertmann, U. *The iron oxides: structure, properties, reactions, occurrences and uses*. (John Wiley & Sons, 2003).
408 Kwan, W. P. & Voelker, B. M. Rates of hydroxyl radical generation and organic compound oxidation in mineral-catalyzed Fenton-like systems. *Environmental science & technology* **37**, 1150-1158 (2003).
409 Sponza, D. & Işik, M. Decolorization and azo dye degradation by anaerobic/aerobic sequential process. *Enzyme and Microbial Technology* **31**, 102-110 (2002).
410 Yang, H. *Zero-Valent Iron Decolorization of the Anthraquinone Dye Reactive Blue 4 and Biodegradation Assessment of its Decolorization Products*, Georgia Institute of Technology, (2005).

411 Lin, S.-S. & Gurol, M. D. Catalytic decomposition of hydrogen peroxide on iron oxide: kinetics, mechanism, and implications. *Environmental Science & Technology* **32**, 1417-1423 (1998).
412 Wang, C.-B. & Zhang, W.-X. Synthesizing nanoscale iron particles for rapid and complete dechlorination of TCE and PCBs. *Environmental science & technology* **31**, 2154-2156 (1997).
413 Anschutz, A. J. & Penn, R. L. Reduction of crystalline iron (III) oxyhydroxides using hydroquinone: influence of phase and particle size. *Geochemical Transactions* **6**, 60 (2005).
414 Cwiertny, D. M., Hunter, G. J., Pettibone, J. M., Scherer, M. M. & Grassian, V. H. Surface chemistry and dissolution of α-FeOOH nanorods and microrods: Environmental implications of size-dependent interactions with oxalate. *The Journal of Physical Chemistry C* **113**, 2175-2186 (2008).
415 Echigo, T., Aruguete, D. M., Murayama, M. & Hochella Jr, M. F. Influence of size, morphology, surface structure, and aggregation state on reductive dissolution of hematite nanoparticles with ascorbic acid. *Geochimica et Cosmochimica Acta* **90**, 149-162 (2012).
416 Gregor, C. *et al.* The effect of surface area and crystal structure on the catalytic efficiency of iron (III) oxide nanoparticles in hydrogen peroxide decomposition. *European Journal of Inorganic Chemistry* **2010**, 2343-2351 (2010).
417 Navrotsky, A., Mazeina, L. & Majzlan, J. Size-driven structural and thermodynamic complexity in iron oxides. *Science* **319**, 1635-1638 (2008).
418 Schwertmann, U. Solubility and dissolution of iron oxides. *Plant and soil* **130**, 1-25 (1991).
419 Larsen, O. & Postma, D. Kinetics of reductive bulk dissolution of lepidocrocite, ferrihydrite, and goethite. *Geochimica et Cosmochimica Acta* **65**, 1367-1379 (2001).
420 Roden, E. E. Fe (III) oxide reactivity toward biological versus chemical reduction. *Environmental Science & Technology* **37**, 1319-1324 (2003).
421 Bosch, J., Heister, K., Hofmann, T. & Meckenstock, R. U. Nanosized iron oxide colloids strongly enhance microbial iron reduction. *Applied and environmental microbiology* **76**, 184-189 (2010).
422 Shi, Z. *et al.* Redox reactions of reduced flavin mononucleotide (FMN), riboflavin (RBF), and anthraquinone-2, 6-disulfonate (AQDS) with ferrihydrite and lepidocrocite. *Environmental science & technology* **46**, 11644-11652 (2012).
423 Wang, B. *et al.* Physicochemical origin for free radical generation of iron oxide nanoparticles in biomicroenvironment: catalytic activities mediated by surface chemical states. *The Journal of Physical Chemistry C* **117**, 383-392 (2012).
424 Lee, S.-h., Oh, J.-y. & Park, Y.-c. Degradation of phenol with Fenton-like treatment by using heterogeneous catalyst (modified iron oxide) and hydrogen peroxide. *Bulletin of the Korean Chemical Society* **27**, 489-494 (2006).
425 Hermanek, M., Zboril, R., Medrik, I., Pechousek, J. & Gregor, C. Catalytic efficiency of iron (III) oxides in decomposition of hydrogen peroxide: competition between the surface area and crystallinity of

nanoparticles. *Journal of the American Chemical Society* **129**, 10929-10936 (2007).

426 Bataineh, H., Pestovsky, O. & Bakac, A. pH-induced mechanistic changeover from hydroxyl radicals to iron (IV) in the Fenton reaction. *Chemical Science* **3**, 1594-1599 (2012).

427 King, D. & Farlow, R. Role of carbonate speciation on the oxidation of Fe (II) by H2O2. *Marine Chemistry* **70**, 201-209 (2000).

428 Koppenol, W. & Liebman, J. F. The oxidizing nature of the hydroxyl radical. A comparison with the ferryl ion (FeO2+). *The journal of physical chemistry* **88**, 99-101 (1984).

429 Watts, R. J., Foget, M. K., Kong, S.-H. & Teel, A. L. Hydrogen peroxide decomposition in model subsurface systems. *Journal of Hazardous Materials* **69**, 229-243 (1999).

430 Go, Y.-M. & Jones, D. P. Redox compartmentalization in eukaryotic cells. *Biochimica et Biophysica Acta (BBA)-General Subjects* **1780**, 1273-1290 (2008).

431 Arbab, A. S. *et al.* A model of lysosomal metabolism of dextran coated superparamagnetic iron oxide (SPIO) nanoparticles: implications for cellular magnetic resonance imaging. *NMR in Biomedicine* **18**, 383-389 (2005).

432 Laskar, A., Ghosh, M., Khattak, S. I., Li, W. & Yuan, X.-M. Degradation of superparamagnetic iron oxide nanoparticle-induced ferritin by lysosomal cathepsins and related immune response. *Nanomedicine* **7**, 705-717 (2012).

433 Apopa, P. L. *et al.* Iron oxide nanoparticles induce human microvascular endothelial cell permeability through reactive oxygen species production and microtubule remodeling. *Particle and fibre toxicology* **6**, 1 (2009).

434 Lipczynska-Kochany, E., Sprah, G. & Harms, S. Influence of some groundwater and surface waters constituents on the degradation of 4-chlorophenol by the Fenton reaction. *Chemosphere* **30**, 9-20 (1995).

435 Valentine, R. L. & Wang, H. A. Iron oxide surface catalyzed oxidation of quinoline by hydrogen peroxide. *Journal of environmental engineering* **124**, 31-38 (1998).

436 Fukushima, M. & Tatsumi, K. Effects of humic substances on the oxidation of pentachlorophenol by peroxosulfate catalyzed by iron (III)-phthalocyanine-tetrasulfonic acid. *Bioresource technology* **97**, 1605-1611 (2006).

437 Vione, D., Merlo, F., Maurino, V. & Minero, C. Effect of humic acids on the Fenton degradation of phenol. *Environmental Chemistry Letters* **2**, 129-133 (2004).

438 Iwahashi, H., Kawamori, H. & Fukushima, K. Quinolinic acid, α-picolinic acid, fusaric acid, and 2, 6-pyridinedicarboxylic acid enhance the Fenton reaction in phosphate buffer. *Chemico-biological interactions* **118**, 201-215 (1999).

439 Sies, H. Oxidative stress: oxidants and antioxidants. *Experimental physiology* **82**, 291-295 (1997).

440 Zhang, M. *et al.* Emerging roles of Nrf2 and phase II antioxidant enzymes in neuroprotection. *Progress in neurobiology* **100**, 30-47 (2013).

441 Huang, C.-C., Aronstam, R. S., Chen, D.-R. & Huang, Y.-W. Oxidative stress, calcium homeostasis, and altered gene expression in human lung epithelial cells exposed to ZnO nanoparticles. *Toxicology in vitro* **24**, 45-55 (2010).
442 Jena, N. & Mishra, P. Formation of ring-opened and rearranged products of guanine: mechanisms and biological significance. *Free Radical Biology and Medicine* **53**, 81-94 (2012).
443 Valavanidis, A., Vlachogianni, T. & Fiotakis, C. 8-hydroxy-2′-deoxyguanosine (8-OHdG): a critical biomarker of oxidative stress and carcinogenesis. *Journal of environmental science and health Part C* **27**, 120-139 (2009).
444 Suzuki, T. & Kamiya, H. Mutations induced by 8-hydroxyguanine (8-oxo-7, 8-dihydroguanine), a representative oxidized base, in mammalian cells. *Genes and Environment* **39**, 2 (2017).
445 Cadet, J. & Davies, K. J. Oxidative DNA damage & repair: an introduction. *Free Radical Biology and Medicine* **107**, 2-12 (2017).
446 Coppedè, F. & Migliore, L. DNA damage in neurodegenerative diseases. *Mutation Research/Fundamental and Molecular Mechanisms of Mutagenesis* **776**, 84-97 (2015).
447 Girotti, A. W. Mechanisms of lipid peroxidation. *Journal of free radicals in biology & medicine* **1**, 87-95 (1985).
448 Esterbauer, H., Eckl, P. & Ortner, A. Possible mutagens derived from lipids and lipid precursors. *Mutation Research/Reviews in Genetic Toxicology* **238**, 223-233 (1990).
449 Siu, G. & Draper, H. Metabolism of malonaldehyde in vivo and in vitro. *Lipids* **17**, 349 (1982).
450 Esterbauer, H., Koller, E., Slee, R. G. & Koster, J. F. Possible involvement of the lipid-peroxidation product 4-hydroxynonenal in the formation of fluorescent chromolipids. *Biochemical Journal* **239**, 405-409 (1986).
451 Hagihara, M., Nishigaki, I., Maseki, M. & Yagi, K. Age-dependent changes in lipid peroxide levels in the lipoprotein fractions of human serum. *Journal of gerontology* **39**, 269-272 (1984).
452 Keller, J. *et al.* 4-Hydroxynonenal, an aldehydic product of membrane lipid peroxidation, impairs glutamate transport and mitochondrial function in synaptosomes. *Neuroscience* **80**, 685-696 (1997).
453 Uchida, K. *et al.* Activation of stress signaling pathways by the end product of lipid peroxidation 4-hydroxy-2-nonenal is a potential inducer of intracellular peroxide production. *Journal of Biological Chemistry* **274**, 2234-2242 (1999).
454 Dean, R., Roberts, C. & Jessup, W. Fragmentation of extracellular and intracellular polypeptides by free radicals. *Progress in clinical and biological research* **180**, 341-350 (1985).
455 Kelly, F. & Mudway, I. Protein oxidation at the air-lung interface. *Amino acids* **25**, 375-396 (2003).
456 Keck, R. G. The use of t-butyl hydroperoxide as a probe for methionine oxidation in proteins. *Analytical biochemistry* **236**, 56-62 (1996).
457 Davies, K. J. Protein damage and degradation by oxygen radicals. I. general aspects. *Journal of Biological Chemistry* **262**, 9895-9901 (1987).

458 Lyras, L., Cairns, N. J., Jenner, A., Jenner, P. & Halliwell, B. An assessment of oxidative damage to proteins, lipids, and DNA in brain from patients with Alzheimer's disease. *Journal of neurochemistry* **68**, 2061-2069 (1997).
459 Engelberg-Kulka, H., Amitai, S., Kolodkin-Gal, I. & Hazan, R. Bacterial programmed cell death and multicellular behavior in bacteria. *PLoS genetics* **2**, e135 (2006).
460 Elmore, S. Apoptosis: a review of programmed cell death. *Toxicologic pathology* **35**, 495-516 (2007).
461 Igney, F. H. & Krammer, P. H. Death and anti-death: tumour resistance to apoptosis. *Nature Reviews Cancer* **2**, 277 (2002).
462 Martinvalet, D., Zhu, P. & Lieberman, J. Granzyme A induces caspase-independent mitochondrial damage, a required first step for apoptosis. *Immunity* **22**, 355-370 (2005).
463 Kaminskyy, V. O. & Zhivotovsky, B. Free radicals in cross talk between autophagy and apoptosis. *Antioxidants & redox signaling* **21**, 86-102 (2014).
464 Yoshida, K. & Miki, Y. The cell death machinery governed by the p53 tumor suppressor in response to DNA damage. *Cancer science* **101**, 831-835 (2010).
465 Luna-Vargas, M. & Chipuk, J. E. The deadly landscape of pro-apoptotic BCL-2 proteins in the outer mitochondrial membrane. *The FEBS journal* **283**, 2676-2689 (2016).
466 Pallepati, P. & Averill-Bates, D. A. Mild thermotolerance induced at 40 C protects HeLa cells against activation of death receptor-mediated apoptosis by hydrogen peroxide. *Free Radical Biology and Medicine* **50**, 667-679 (2011).
467 Pallepati, P. & Averill-Bates, D. Mild thermotolerance induced at 40° C increases antioxidants and protects HeLa cells against mitochondrial apoptosis induced by hydrogen peroxide: Role of p53. *Archives of biochemistry and biophysics* **495**, 97-111 (2010).
468 Circu, M. L. & Aw, T. Y. Reactive oxygen species, cellular redox systems, and apoptosis. *Free Radical Biology and Medicine* **48**, 749-762 (2010).
469 Circu, M. L. & Aw, T. Y. Glutathione and modulation of cell apoptosis. *Biochimica et Biophysica Acta (BBA)-Molecular Cell Research* **1823**, 1767-1777 (2012).
470 Iv, M. *et al.* Clinical applications of iron oxide nanoparticles for magnetic resonance imaging of brain tumors. *Nanomedicine* **10**, 993-1018 (2015).
471 Kievit, F. M. & Zhang, M. Surface engineering of iron oxide nanoparticles for targeted cancer therapy. *Accounts of chemical research* **44**, 853-862 (2011).
472 Saeed, M., Ren, W. & Wu, A. Therapeutic applications of iron oxide based nanoparticles in cancer: basic concepts and recent advances. *Biomaterials science* (2018).
473 Laurent, S., Dutz, S., Häfeli, U. O. & Mahmoudi, M. Magnetic fluid hyperthermia: focus on superparamagnetic iron oxide nanoparticles. *Advances in colloid and interface science* **166**, 8-23 (2011).

474 Hilger, I. *et al.* Thermal ablation of tumors using magnetic nanoparticles: an in vivo feasibility study. *Investigative radiology* **37**, 580-586 (2002).
475 Dias, A., Hussain, A., Marcos, A. & Roque, A. A biotechnological perspective on the application of iron oxide magnetic colloids modified with polysaccharides. *Biotechnology advances* **29**, 142-155 (2011).
476 Hajipour, M. J., Laurent, S., Aghaie, A., Rezaee, F. & Mahmoudi, M. Personalized protein coronas: a "key" factor at the nanobiointerface. *Biomaterials Science* **2**, 1210-1221 (2014).
477 El-Boubbou, K. Magnetic iron oxide nanoparticles as drug carriers: clinical relevance. *Nanomedicine* (2018).
478 Li, K., Nejadnik, H. & Daldrup-Link, H. E. Next-generation superparamagnetic iron oxide nanoparticles for cancer theranostics. *Drug discovery today* **22**, 1421-1429 (2017).
479 Assa, F. *et al.* A biotechnological perspective on the application of iron oxide nanoparticles. *Nano Research* **9**, 2203-2225 (2016).

Chapter 2: Ultrafine superparamagnetic iron oxide nanoparticles (USPIONs): preparation and size characterisation

2.1 Introduction

Due to their size- and shape-dependent behaviours [1], adjusting NPs microscopic characteristics (e.g. size and shape) has attracted an increasing attention particularly in last ten years after more interdisciplinary applications for NPs (especially USPIONs) have been introduced [2]. Therefore, novel fabrication methods with strict size-controlling conditions have been thoroughly investigated. Basically, to establish a new method for ultrafine NPs fabrication, nucleation and growth theory-related parameters should be taken into consideration. In particular, for a given reaction vicinity, the residence time and mixing efficiency along with abundance rate of reactant precursors are the key elements prerequisite for controlling the characteristics of particles outcome [3-6].

With conventional batch NPs fabrication processes (such as nanoprecipitation [7,8], sol–gel [9,10], ultrasonic [11,12], microemulsion [13-16], and reduction methods [17-19]), the overlapping between both stages of new solid phase creation (nucleation and growth) is inevitably occurring due to poor controlling of the key factors mentioned before. As a result, limited uniform size reproducibility is noticed. Additionally, up-scaling a batch fabrication will result in aggravated situation and hence highly polydispersed colloidal dispersion would be expected with various physicochemical properties [20-23].

Since 1990s, a growing number of studies have devoted their efforts to microfluidic synthetic system as a strategy of non-bulk NPs production. In particular, continuous-flow microfluidic systems, is most promising design of this strategy. Contrary to conventional batch systems, the continuous-flow type is widely investigated owing to its ease of accurate control, rapid heat and mass transfer, high mixing efficacy, large reaction interfaces [24-27]. Interestingly, microfluidic system can provide a nucleation zone in a microreactor which enables excellent separation of the nucleation stage from the following NPs growth stage. This is occur as a function of distance away from the point at which reactant solutions were mixed to attain excellent control of the particle size, size distribution, and morphology [28,29], likewise, an increase in throughput synthesis with homogenous NPs could be achieved [30].

In general, systems relying on the concept of sending reactant solutions as streams into a given device can be divided into two catalogues, single-phase continuous flow and segmented flow systems. In the single-phase continuous flow a homogeneous stream of two or more reactants continuously flow in tubing system that, in turn, offers simplicity and a versatile control of the flow, reaction time, and temperature [25,31,32].

Contrary to a single-phase flow, a multiphase microfluidic flow, also known as a segmented flow, comprises of interrupted reactant streams by an immiscible phase [33]. Therefore, at the point of mixing, a recirculation motion [34] is triggered to create stretching and folding of reactant solutions that, in turn, enhances the mixing efficiency [35]. This system design offer several advantages over the continuous flow counterpart, such as superior mixing efficiency with narrow residence time within each droplet formed [36-38]. Furthermore, minimum contact

with micro-channelling system thereby reduce the risk of channel clogging caused by deposition of reactants/products on the channel. It is important to mention that the interrupting phase could be either gas or immiscible liquid so that the system will called gas–liquid flows, and liquid–liquid flows respectively.

Although, the notion of existing a restricted zone to control the size of fabricated NPs has been applied using conventional bulk system such as microemulsion, sol-gel and polyol methods, freeing NPs surfaces from surface bound surfactants, polymers, and other complexing agents is extremely challenging [39]. Therefore, creating a physical confinement for reaction zone, as explained above, could function as an alternative modification for tuning particles size where NPs impurities were excluded.

The principle of 'flow-injection analysis' suggested by Ruzicka *et al* [40] was further developed to successfully fabricate mineral NPs with controlled morphology [41]. In this concern, flow injection synthesis, with modification to the microfluidic platform, has been developed to produce USPIONs. Mechanically, the system comprises of propulsion unit, injection manifold, capillary or disc reactor and product collector. The reactants are streamed through separate carrier tubing system then, fabrication of NPs initiates at a manifold and continues over either capillary reactor system (as in microfluidic) or disc reactor as the current case. Basically, segmented type of flow systems have been tested where an injection valve could be positioned at the junction unit [42-44].

The study implemented in this chapter aimed at, first, fabricating USPIONs using the above described systems. Different USPIONs batches have been prepared upon changing operation conditions (as detailed below in methodology). Second, the resulted USPIONs were characterised for their size and morphology using two standard methods, transmission electron microscopy (TEM) and dynamic light scattering (DLS). NPs description were properly conducted for determination of particles diameter and providing details on size distribution and polydispersity. This study is applicable in the field of nanomaterial preparation and characterisation.

2.2 Materials and Methods

2.2.1 Materials

The following materials have been used to prepare USPIONs. Sigma-Aldrich was the company of origin. Ferrous chloride tetrahydrate ($FeCl_2$. $4H_2O$) 98% reagent plus®, ferric chloride hexahydrate ($FeCl_3$. $6H_2O$) ≥ 98% reagent grade. Ammonia solution 35% w/w (concentrated), hydrochloric acid (~ 37% w/w) concentrated, ethyl acetate and methylated ethanol are laboratory reagent grade were from Fischer chemical company.

2.2.2 Methods

2.2.2.1 Reactant solution preparation

The acidic reactants including both ferrous chloride tetrahydrate and ferric chloride hexahydrate were mixed in an individual vessel using two different molar ratios, 0.5 and 0.66 Fe^{+2}/Fe^{+3} to form what is called 'binary/dual iron salt solution' (BISS) while the alkaline, concentrated ammonium hydroxide, was placed in a different vessel. Both solutions (acidic and alkaline) are ready now

to be streamed into the instrument. Regardless flowrate at which both reactants were adjusted, the rate of alkaline material flow was fixed to be half of that the binary iron salt solution flows. Therefore, two peristaltic adjustable pumps were operated to inject the reactant solutions.

2.2.2.2 Production of USPIONs using Spinning Disc Reactor (SDR)

A specific custom-built system, as shown in Figure 2-1, consists of three main parts. First, a control panel by which the operational conditions (such as motor rotational speed, reactants flowrate, and chemical transferring channels on/off) could be easily adjusted via a digital display. Second, carrier tubing through which the reactive reagents are streamed at desired flowrate. Herein, digitally-tuned peristaltic pumps are positioned in the middle of stream path between reagent bottles and tubes end at which a mixing joint is located. The third part includes 3D-printed spinning disc reactor (SDR) which is connected to stainless steel electrically-rotated shift. The SDR is placed in the centre of a glass vessel chamber.

USPIONs were, in this instrumental set up, prepared according to the following standard procedure. The reactant materials (1.0 L of BISS and 500 ml of ammonium hydroxide solution) were simultaneously, separately injected within the same timeline through tubing system and combined inside a junction situated above the horizontally oriented SDR. The mixture is fed directly into the SDR. The resultant black precipitate was collected into a glass reaction bottle from the outlet at the bottom of the housing vessel.

The yield-containing reaction bottle was immediately positioned over a super-strong neodymium magnet (grade N35) to separate the produced NPs from the reaction medium. The collected black powder was washed three times with distilled water, twice with ethyl acetate, filtered under *vacuum* and finally left overnight in a *vacuum* oven at approximately 40°C. It is noteworthy to mention that neodymium magnet was used every time during washing steps. For long storage purposes, the dried powder was stored in glass vials tightly sealed with parafilm and placed inside a desiccator.

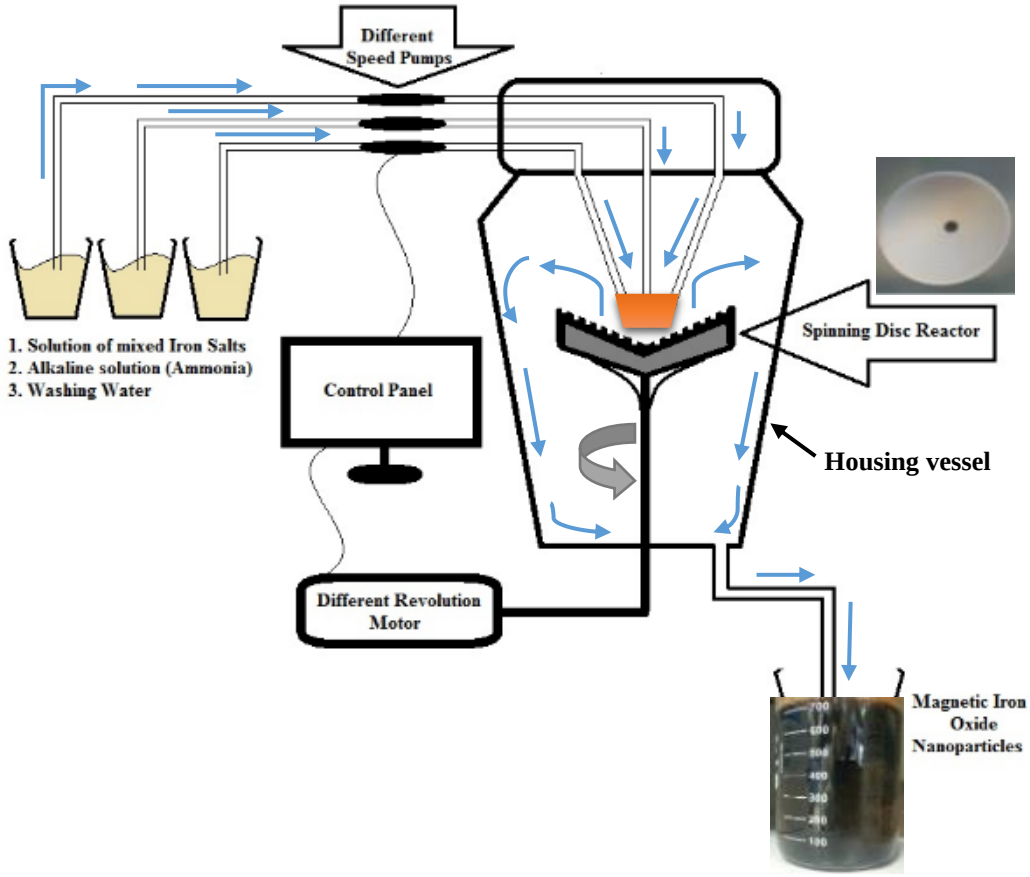


Figure 2-1: Schematic representation of the developed instrument for preparation of USPIONs.

The reagents separately flow through three carrier tubing system propelled by a peristaltic pump. They are combined just prior to addition to the rotated spinning disc reactor (SDR). The fabricated particles are, owing to centrifugal force, discharged from the spinning disc to be collected at the bottom of the housing vessel. The formed USPIONs are collected in a reagent bottle as black colloidal dispersion. (The fabrication path follows blue arrows).

2.2.2.3 USPIONs preparations under different experimental conditions

Initially, different experimental conditions were used to fabricate USPIONs. Six procedures were designed to assess the impact of fabrication parameters on the size and morphology of the resulting particles. They are summarized in sections below and illustrated in Figure 2-2.

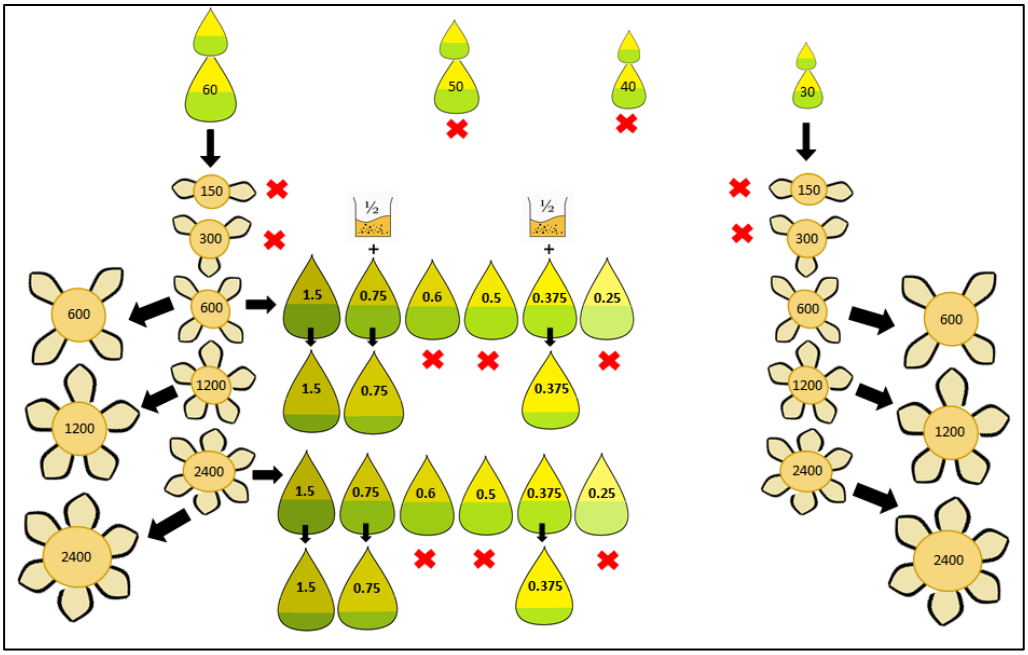


Figure 2-2 Schematic illustration of the six procedures used in preparation of USPIONs

*Different flowrates (**procedure 1**) is denoted by size increasing of the dual drop-like structure, the alteration in rotational speeds (**procedure 2**) is proportionated to the leaves number of rose-like structure, changing the size of SDR (**procedure 3**) is signified by enlarged rose-like structure. While using different color shade of the drop structure is referring to increasing the total molar concentration of the binary-iron salts solution (BISS) (**procedure 4**), altering the field area occupied by green and yellow color is used as an indication of Fe^{2+}/Fe^{3+} molar ratio change (**procedure 5**). Finally, formulas prepared by using half alkaline concentration which were compared to the corresponding ones of maximum alkaline concentration are assigned by half-filled beaker-like structure (**procedure 6**). The values of flowrate, rotational speed and concentration of BISS are written as 30, 40, 50 and 60 ml/min, 150, 300, 600, 1200, and 2400 rpm, and 0.25, 0.375, 0.5, 0.6, 0.75 and 1.5 M respectively.*

Procedure 1. BISS flowrate. Four flowrates of 30, 40, 50, and 60 ml/min were adjusted to pump the BISS solution (0.375 M with the molar ratio of Fe^{2+}/Fe^{3+} of 0.66). The rotational speed of spinning disc was fixed at 150 rpm. Concentration of ammonium hydroxide used was 35% w/w (18.08 M) and it was always injected at half rate of the BISS selected flowrate.

Procedure 2. Spinning disc speed. BISS was pumped at 30 and 60 ml/min flowrates onto the spinning disc operated at five different rotational speeds of 150, 300, 600, 1200, and 2400 rpm. In this procedure the total amount of iron salt, Fe^{2+}/Fe^{3+} ratio, and concentration of alkaline solution were kept constant at 0.375 M, ratio 0.66, and 35% w/w (18.08 M), respectively.

Procedure 3. Effect of disc size. In this case a USPIONs produced using smaller (≈ 9 cm diameter) and larger (≈ 13 cm diameter) size spinning discs (SSDR and LSDR respectively) were compared. In this procedure the total amount of iron salts, Fe^{2+}/Fe^{3+} ratio, and concentration of alkaline solution were kept constant at 0.375 M, ratio 0.66, and 35% w/w (18.08 M), respectively. The reactants were injected at the two different flowrates (30 and 60 mL/min) and at three different rotational speeds (600, 1200 and 24000 rpm) of the spinning disc.

Procedure 4. Amount of reactive precursors. BISS at six different molar concentrations were used: 0.25, 0.375, 0.5, 0.6, 0.75, and 1.5 M. These were injected at 60 ml/min flowrate, spinning disc rotation was either at 600 or 2400 rpm; the concentration of ammonium hydroxide solution was kept at 35% w/w (18.08 M) and added at half of that flowrate (i.e. 30 ml/min) of BISS as usual.

Procedure 5. Ratio of Fe^{2+}/Fe^{3+}. The ratio of Fe^{2+}/Fe^{3+} was in this case kept constant at 0.5. BISS at three different molar concentrations were used 0.375,

0.75, and 1.5 M. Other conditions were: flowrate 60 ml/min, rotational speeds 600 and 2400 rpm, and alkaline solution concentration 35% w/w, 18.08 M). Smaller size for the disc was used.

Procedure 6. Alkaline concentration. In this case the alkaline reagent was diluted to half of standard concentrated ammonium hydroxide solution to 18% w/w (9.04 M). Other reaction parameters were: flowrate and rotational speed at 60 ml/min and 600 rpm, respectively, BISS were 0.375 and 0.75 M, Fe^{+2}/Fe^{+3} ratio was 0.66 and smaller disc size was used.

2.2.2.4 Infrared analysis of USPIONs

IR of the resulted black precipitate were recorded using the attenuated total reflectance (ATR) sampling technology. An Agilent Cary 630 (Agilent Technologies, USA) equipped with a diamond crystal was used for recording the spectra of the desiccated USPIONs powder against air background at a resolution of 8 cm^{-1}, the spectral range of 4000-650 cm^{-1} wavenumber and presented in term of transmittance intensity. The background time limit and sample scans are 5 min and 256 times respectively.

2.2.2.5 Transmission electron microscopy (TEM)

The fabricated USPIONs were imaged using Jeol- JEM 2010 and FEI Tecnai G2 12 Biotwin (USA) instrument. In order to acquire TEM image, one drop of diluted USPION dispersion was applied onto 200 mesh carbon-coated 3.05 mm copper grid. After 5-10 min, the excess amount of the dispersion was removed with the aid of filter paper. The samples were further fried overnight. DigitalMicrograph from Gatan Microscopy Suite Software was used to process the micrographs. Particle size was determined by measuring the diagonal

distance between two opposite points across each individual particle and 150 particles from every image were measures. ImageJ (image processing program designed at the National Institutes of Health (NIH), USA) was also used to analyse the degree of particles circularity.

2.2.2.6 Dynamic light scattering (DLS)

Measurement the particle hydrodynamic radius was performed applying DLS technique using a Viscotek DLS instrument and OmniSIZE software package (Malvern, UK). Measurements are taken at temperature of 25°C, at a measuring angle of 90 ºC to the incident beam.

Colloidal dispersions of USPIONs (in water) were diluted using 18.2 MΩ de-ionized water in order to obtain mean count around 350-450 (kCount). The reported results represent the mean of 10 sub-measurements of three independent experiments. The standard deviation (Std Dev) is calculated as absolute value of the coefficient of variation.

2.2.2.7 Statistical analysis

Statistical comparisons were functioned by Prism application using unpaired t-test and one way ANOVA analysis. Values of $p < 0.05$ were considered statistically significant. The asterisk-sign *, **, *** and **** indicate $p < 0.05$, $p < 0.01$, $p < 0.001$ and $p < 0.0001$ respectively. Any other probabilities less than 0.0001 were denoted by ****.

2.3 Results

2.3.1 Preparation of USPIONs

The concept of ‘alkaline co-precipitation’ was principally adopted in generation of USPIONs in this work [45]. The reaction pathway selected is based on mixing ferrous and ferric salts solution with an alkaline medium, leading to the formation of black solid precipitate [46-48]. The basic equation describing the chemical reaction can be formulated as:

$$2Fe^{3+}_{(aq)} + Fe^{2+}_{(aq)} + 8OH^{-}_{(aq)} \rightarrow Fe_3O_4\downarrow + 4H_2O$$

FTIR spectrum of the resultant black precipitate (USPIONs dry powder) was recorded to confirm the formation of metal-oxide bond. As illustrated in Figure 2-3, the appearance of intense transmittance bands in range lower than 600 cm^{-1} is a strong indication of stretching vibration of Fe–O bonds which can be assigned to the structural environment of tetrahedral and octahedral sub-lattice of the NPs [49-53]. Additional peaks present at 3300 and 1628 cm^{-1} can be ascribed to stretching and bending vibration of hydroxyl group belonging to the remainder water molecules adsorbed on particles surface respectively [54-56], while the low-intense band at 1401 cm^{-1} arose from C-O bond of adsorbed air carbon dioxide [57].

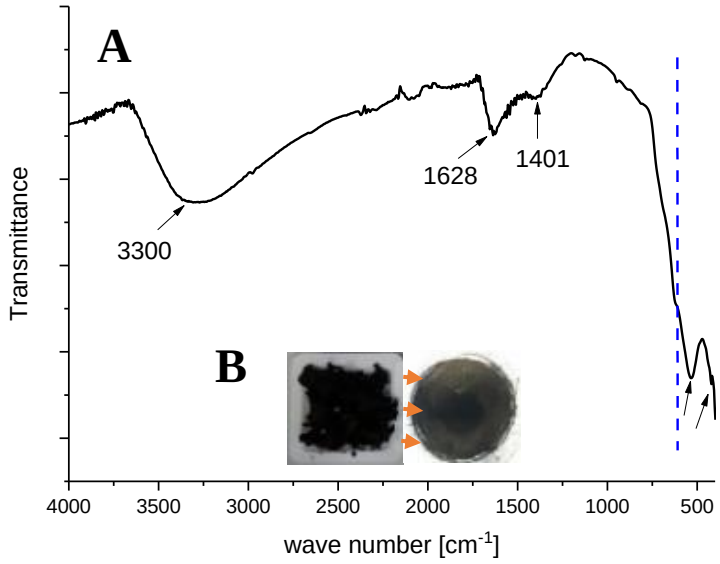


Figure 2-3: FTIR spectrum of USPIONs as dry powder

(A) The collected USPIONs were separated from the residual unreacted material of their colloidal dispersion by neodymium magnet, followed by several washings with water and ethyl acetate and vacuum filtered. Filtered material was dried in vacuum oven to obtain dry powder. For FTIR spectra detecting, the dry powder was further triturated (as in B) in a mortar.

2.3.2 Particle morphology and size analyses by TEM

Due to the high electronic density the metal oxide NPs possess, transmission electronic microscopy (TEM) is widely considered the gold standard for size and morphology characterisation of NPs [58-60]. TEM images, particle size analysis and particles circularity distribution of USPIONs batches prepared according to the different procedures described above, are shown in Figures 2-4, 7, 10, 13, 16, and 19. The particle analysis using TEM was further compared with hydrodynamic particle sizes obtained from DLS measurements.

2.3.3 Factors affecting USPIONs size and morphology

2.3.3.1 Effect of BISS flowrate

2.3.3.1.1 Size and degree of circularity distribution

As shown in Figure 2-4, the profiles of particles size histograms are gradually changing from right-skewed to nearly symmetrical with increasing the flowrate of reactant materials from 30 to 60 ml/min. This is reflected in a consistent trend towards increasing particle size, expressed as ‘median’ values (statistically defined as a quantity at the midpoint of a certain frequency distribution, such that there is an equal probability of falling above or below it); USPIONs produced at 30, 40, 50, and 60 ml/min flowrate have median particle size of 6.38, 6.77, 8.73, and 9.08 nm correspondingly.

It should be also noted that the gap between the ‘mode’ (the most frequently occurring value in certain population) and ‘median’ values is reducing as the speed at which the reagents flow is increasing, indicating that there is an increasing uniformity in the size distribution of the batches prepared at higher flowrates.

The circularity distribution in Figure 2-4 also shows changes with the flow rate with gradually increasing circularity as the flow rate is increased (disappearance of left-skewed profile) with 30, 40, 50, and 60 ml/min flowrates resulting in fabrication of USPIONs with median circularity values of 0.624, 0.713, 0.763 and 0.810 respectively.

Interestingly, USPIONs prepared at low flow rates of 30 and 40 ml/min show circularity histogram with bimodal distribution characteristics, which reveal a reduced level of population uniformity.

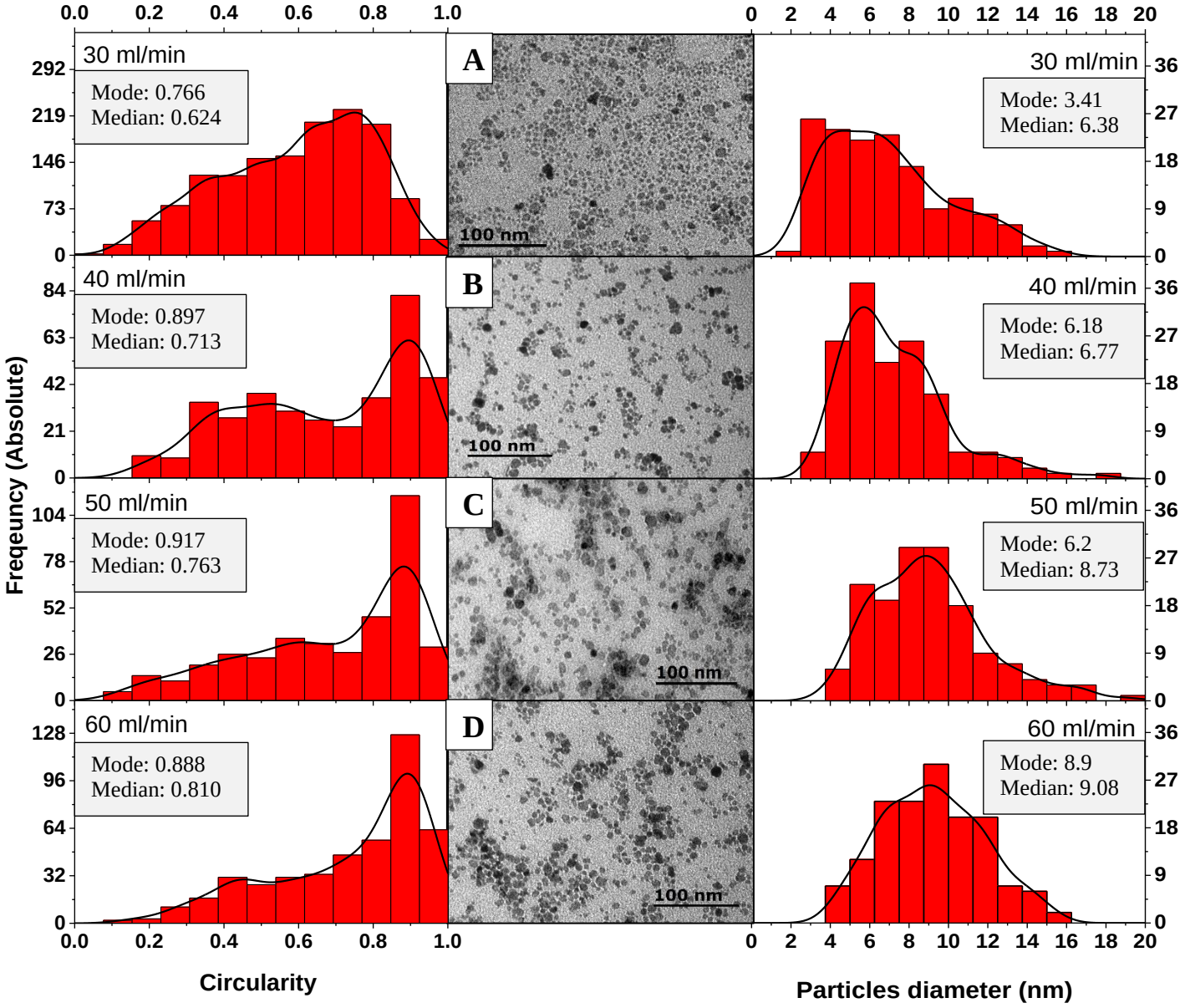


Figure 2-4: TEM micrographs with distribution histograms of USPIONs prepared using different flowrates

Four USPIONs batches prepared at each 30, 40, 50, and 60 ml/min flowrates are denoted as A, B, C, and D, respectively. The corresponding frequency histogram represent the distribution of particle diameter and circularity. Other processing conditions are: rotational speed of spinning disc150 rpm, BISS at 0.375 M, concentration of ammonium hydroxide solution.35% w/w, smaller sized spinning disc.

2.3.3.1.2 Comparison of TEM and DLS average particle sizes

The comparison of reactant flowrate effect on the average TEM and hydrodynamic diameter is shown in the Figure 2-5A and B. Although the overall trend of the line graphs show that there is a considerable increase in particle size as the flow rate is increased, the only significant rise ($p < 0.001$) in average diameter of the resultant particles was noticed upon changing the rate of reagent flow from 40 to 50 ml/min. In TEM measurements (Figure 2-5A) this increase is from 7.27 nm to 9.06 nm, and in DLS measurements (Figure 2-5B) this increase in hydrodynamic diameter is from 24.53 nm and 32.26 nm, respectively.

In general, data in Table 2-1 illustrate an increase in the size uniformity of the tested batches, whereby the polydispersity values declined dramatically from 0.195 to 0.077 as flowrate increased from 30 and 60 ml/min.

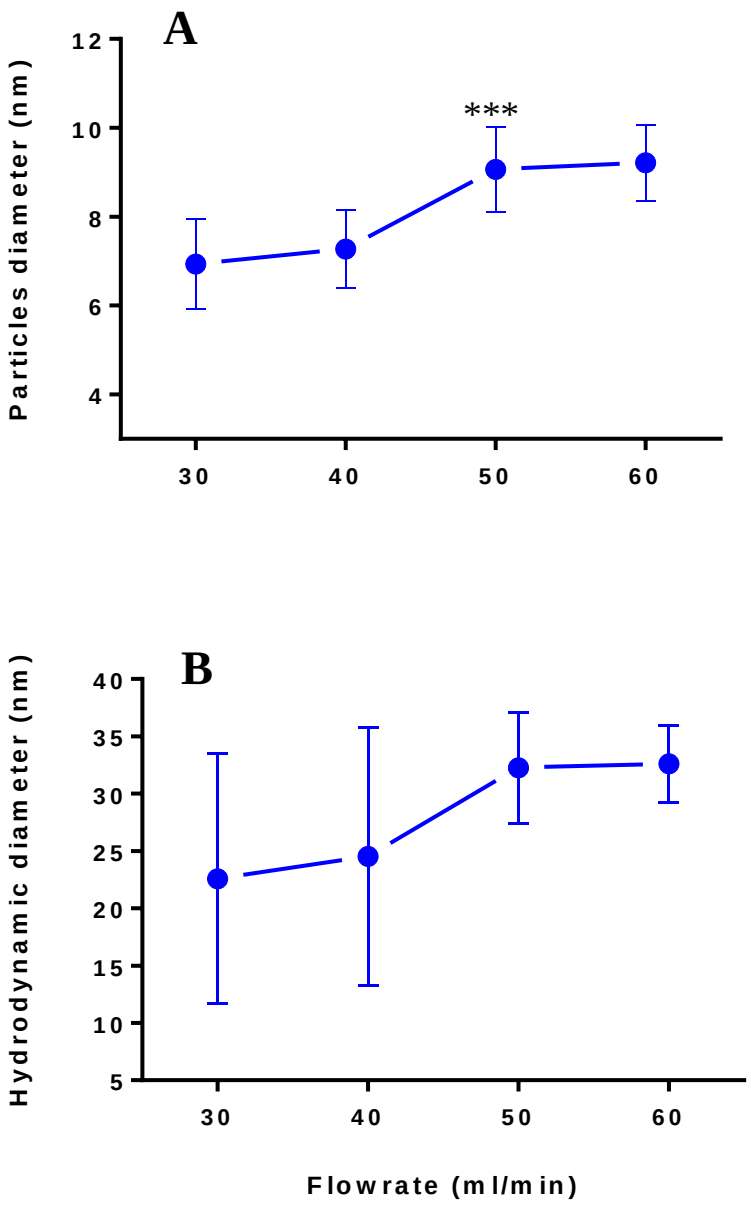


Figure 2-5: Particles diameter obtained from A) TEM images and B) DLS measurments

For particle batches prepared at different flowrates of reactant solutions. ***A)*** *The diameter of individual 150 particles measured using DigitalMicrograph programme.* ***B)*** *Hydrodynamic diameter from dynamic light scattering measurements of USPIONs dispersed in deionised water at 25°C, data expressed in term of scattering intensity. Values represent the mean of three sets of independent measurements with 10 sub-measurements each. The process conditions are the same as described in Figure2- 4. Error bars represent +/- 1SD of the average value. t-test statistical analysis has been followed to define the significant changes. *** denotes a significant increase ($p < 0.001$) in diameter value compared to size measurement of slowest flowrate used.*

Table 2-1: PDI of particles size for USPIONs batches produced at different flowrates as detected by TEM image analysis.

USPIONs (different flowrate) ml/min	**Polydispersity index (PDI) TEM ǂ**
30	0.1953
40	0.1329
50	0.0990
60	0.0775

ǂ Particles number (n) is 150 for each individual data.

2.3.3.1.3 Average of the fabricated USPIONs circularity

Figure 2-6 summaries the average of particle circularity belonging to the fabricated USPIONs according to condition of different flowrates. It is simply observed that there is a relative improvement in the uniformity of particle morphology while injecting the BISS with maximum rate. Using TEM images and ImageJ programme, the circularity values of 0.596, 0.674, 0.688, and 0.734 were recorded for flowrates of 30, 40, 50, and 60 ml/min respectively.

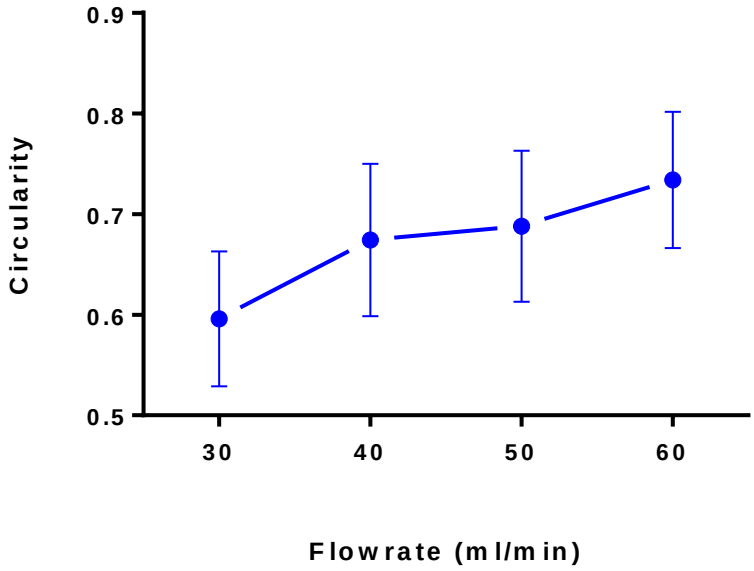


Figure 2-6: Average of circularity values of four USPIONs batches prepared at each 30, 40, 50 and 60 ml/min flowrates

ImageJ programme was used to analyse the morphology of the resulted NPs. The number of items processed is variable and depends upon the amount of particles presented in each individual TEM micrograph. The degree of circularity is expressed in absolute values lying between 0.00 and 1.00. Error bars represent +/- 1SD of the average value.

2.3.3.2 Effect of spin disc rotational speed

2.3.3.2.1 Size and degree of circularity distribution

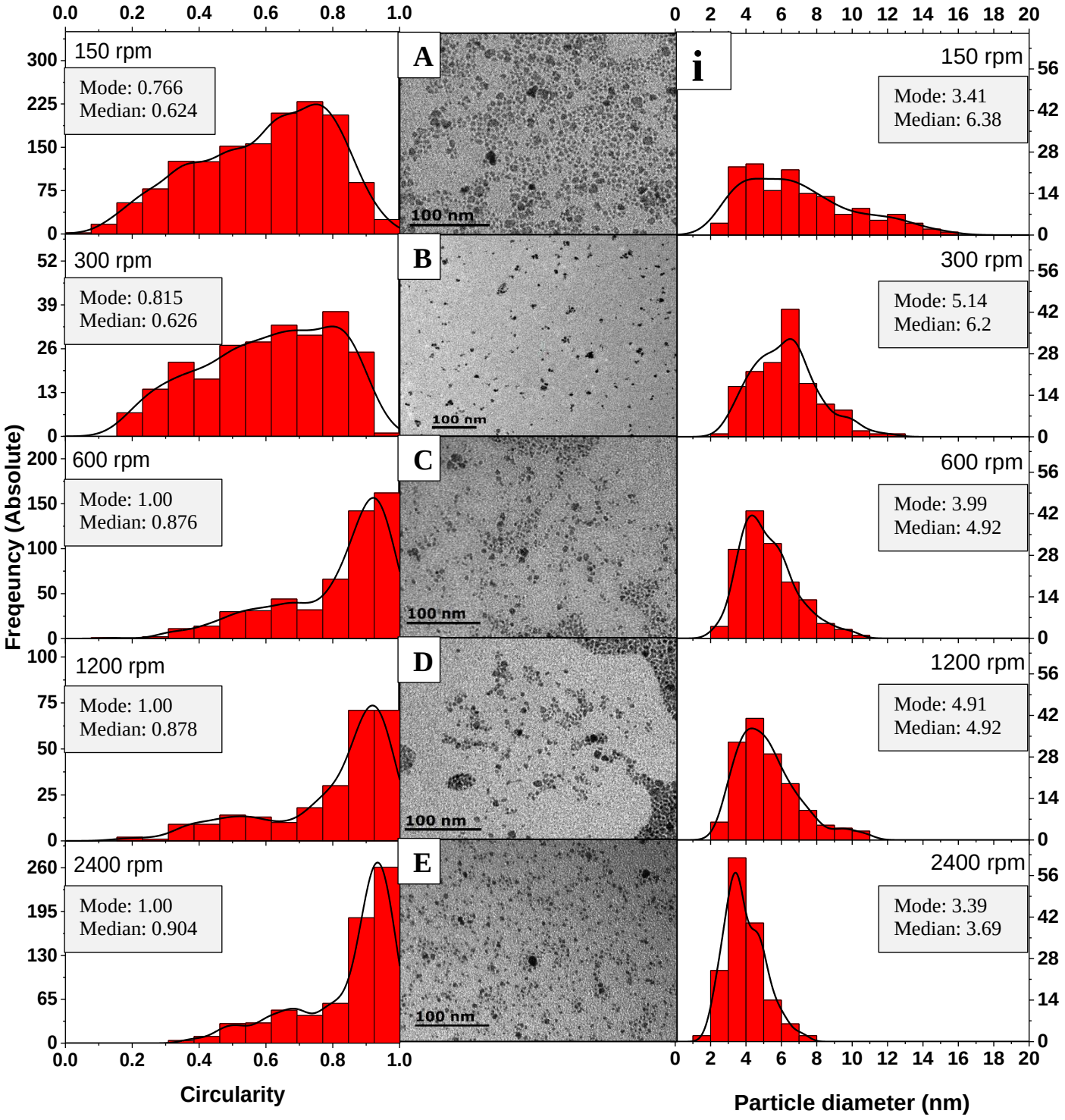
USPIONs prepared according to 'Procedure 2' were used to investigate the effect of various rotational speeds of the SDR on the particle size. In this experiment, two different flowrates, 30 ml/min and 60 ml/min were used to produce NPs at the rotations speeds of 150, 300, 600, 1200, and 2400 rpm. Data are shown in Figure 2-7.

In case of USPIONs fabricated at 30 ml/min flowrate (Figure 2-7i), the all size distribution histograms show a right-skewed profiles, except that of

USPIONs synthesised at higher rotational speed, 2400 rpm, where a nearly bell-shape of frequency distribution is seen. The data further show shift in median values towards smaller values, with a reduction in differences between maximum and minimum diameter recorded of particles populations as the SDR velocity increased where values of 6.38, 6.2, 4.92, 4.92, and 3.69 nm are ascribed to NPs resulted over operating the SDR at speeds of 150, 300, 600, 1200 and 2400 rpm respectively. This can provide with a strong evidence of producing batches having narrow size distribution curve. It is also noteworthy to mention that there is an inverse relationship between the median diameter and the velocity at which the SDR were run. In this situation, the median value diminished from 6.38 nm up to 3.69 nm over adjusting the spinning rate from 150 up to 2400 rpm.

By following the particle circularity data in Figure 2-7i, an increase in the uniformity of particles circularity is seen. While all circularity distribution curve have left-skewed shape, the vast majority of the inspected particles of batches prepared at 600, 1200, and 2400 rpm rotational speeds were clustered around values of 0.85-1.00. This signifies a proportional relationship between the disc rational speed and circularity development.

Data for batches prepared at 60 ml/min in Figure 2-7ii show a similar shift in size and circularity distributions towards smaller and more circular USPIONs as the disc rotational speed is increased.


A
i
B
C
D
E
150 rpm
Mode: 0.766
Median: 0.624
150 rpm
Mode: 3.41
Median: 6.38
300 rpm
Mode: 0.815
Median: 0.626
300 rpm
Mode: 5.14
Median: 6.2
600 rpm
Mode: 1.00
Median: 0.876
600 rpm
Mode: 3.99
Median: 4.92
1200 rpm
Mode: 1.00
Median: 0.878
1200 rpm
Mode: 4.91
Median: 4.92
2400 rpm
Mode: 1.00
Median: 0.904
2400 rpm
Mode: 3.39
Median: 3.69
100 nm
Freqeuncy (Absolute)
Circularity
Particle diameter (nm)

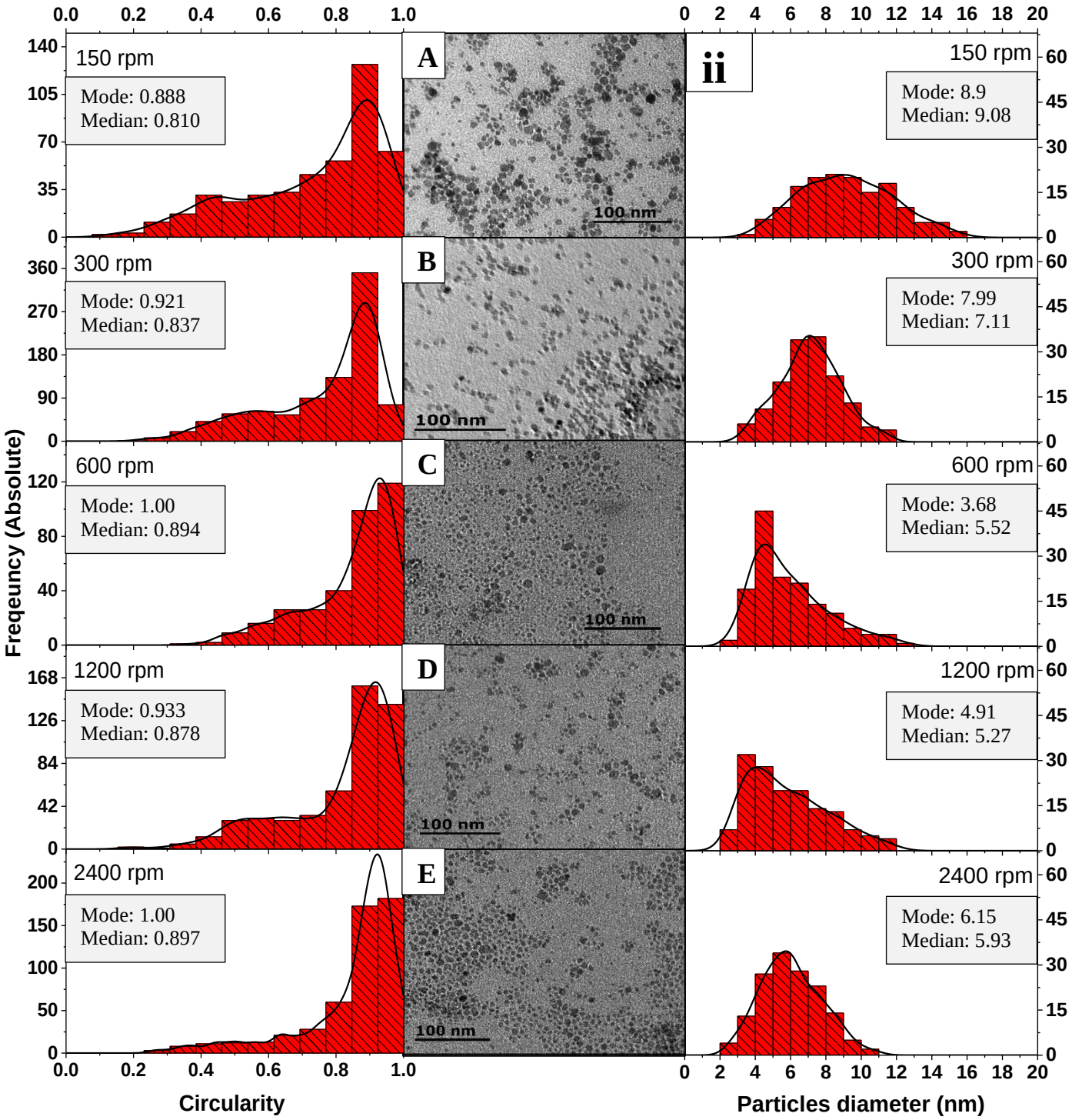


Figure 2-7: TEM micrographs with distribution histograms of USPIONs prepared using different rotational speeds.

Four USPIONs batches prepared at each 150, 300, 600, 1200, and 2400 rpm rotational speeds are denoted as A, B, C, D and E, respectively. Two sets of batches have been prepared for 30 ml/min (i) and 60 ml/min (ii). The corresponding frequency histograms represent the distribution of particle diameter and circularity. Other processing conditions are: Fe^{2+}/Fe^{3+} ratio equal to 0.66 at 0.375 M BISS, concentration of ammonium hydroxide solution is 35% w/w, smaller sized spinning disc.

2.3.3.2.2 Comparison of TEM and DLS average particle sizes

Figure 2-8A and B summarize the impact of increasing spinning disc rate on the particle size determined by from TEM and DLS measurements. The data appeared in both line graphs, representing productions at 30 ml/min and 60 ml/min flowrates, display a general tendency toward reducing particle size as the spinning speed is increased.

In detail, USPIONs batches prepared using the lower injection rate, 30 ml/min, show two stages of significant particle size reduction, the first decline started at 150 rpm rotational speed up to 600 rpm ($p < 0.05$), with particle size values of 6.93 nm and 5.24 nm, respectively, followed by a plateau at 1200 rpm wherein the diameter value is 5.22 nm. Similarly, the corresponding hydrodynamic diameter is reduced from 22.56 nm to 16.3 nm, reaching a plateau at 15.4 nm. The second significant size reduction was achieved at the rotational speed of 2400 rpm ($p < 0.01$) in which the average TEM derived and hydrodynamic particle diameters from DLS are 3.93 nm and 10.52 nm, respectively.

Similar trends were observed for USPIONs produced at 60 ml/min flowrate. Comparing the particle size at the same spinning speed but at different flow rates, it appears that at USPIONs produced at 60 ml/min flowrate are normally somewhat bigger.

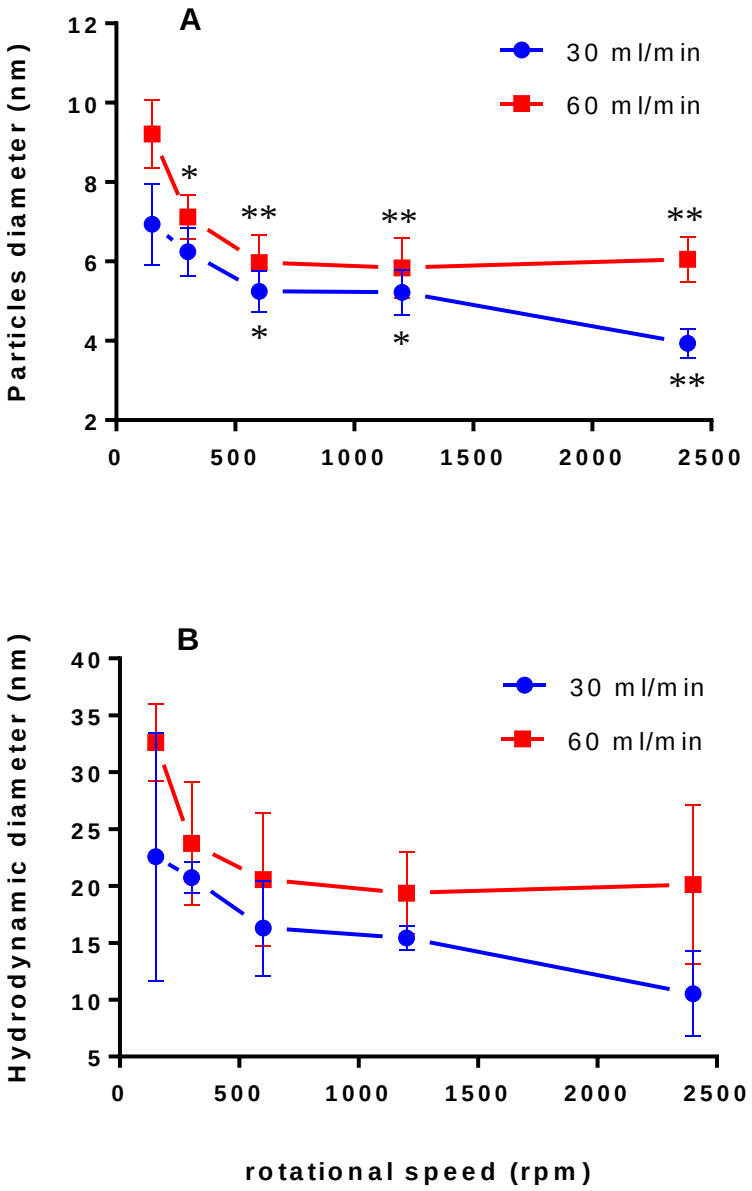


Figure 2-8: Line graphs represent the plot of particles average diameter extracted from A) TEM images and B) DLS measurements versus different SDR rotational speed

A) *The diameter of individual 150 particles measured using Digital Micrograph programme.* ***B)*** *Hydrodynamic diameter from dynamic light scattering measurements of USPIONs dispersed in deionised water at 25°C, data expressed in term of scattering intensity. Values represent the mean of three sets of independent measurements with 10 sub-measurements each. The process conditions are the same as described in Figure 2-7. Error bars represent +/- 1SD of the average value. t-test statistical analysis has been followed to define the significant changes. * and ** denote a significant decrease ($p < 0.05$ and < 0.01 respectively) in diameter value compared to size measurement of slowest spinning speed.*

Table 2-2: PDI of particles size USPIONs produced at different rotational speed and detected by TEM

USPIONs preparations (different rotational speed) Rpm	**Polydispersity index (PDI) TEM¶**	
	30 ml/min	**60 ml/min**
150	0.1952	0.0775
300	0.0856	0.0582
600	0.0888	0.1260
1200	0.1107	0.1483
2400	0.0795	0.0792

¶ Particles number (n) is 150 for each individual data.

2.3.3.2.3 Extent of the fabricated USPIONs circularity

Values manifested in figure 2-9 reveals that there is highly significant development ($p < 0.0001$) in particles circularity in case of 30 ml/min flowrate only at disc speeds below 600 rpm whereas operating the instrument at higher velocities didn't yield NPs with better morphology. As an example, particles batches resulted using 150 rpm, 600 rpm and 2400 rpm rotational speeds were found to have circularity degrees of 0.596, 0.806, and 0.843 respectively. This is also applied for those group of USPIONs (but with less extent, $p < 0.001$) that were prepared at 60 ml/min flowrate.

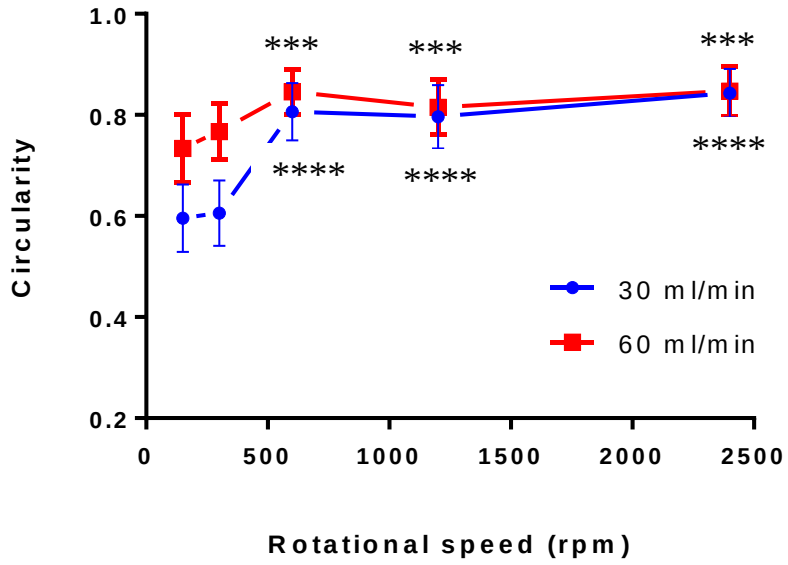


Figure 2-9: Average of circularity values of two different USPIONs sets prepared at various rotational speed

*ImageJ programme was used to analyse the morphology of the resulted NPs. The number of items processed is variable and depends upon the amount of particles presented in each individual TEM micrograph. The degree of circularity is expressed in absolute values lying between 0.00 and 1.00. Error bars represent +/- 1SD of the average value. t-test statistical analysis has been followed to define the significant changes. ***, and **** denote a significant increase ($p < 0.001$and 0.0001 respectively) in circularity value compared to size measurement of slowest rotational speed used.*

2.3.3.3 Effect of spinning disc size

2.3.3.3.1 Size and degree of circularity distribution

In order to examine the effect of introducing spinning disc with larger diameter on particles size and morphology, USPIONs fabricated under procedure 3 were characterised and data summarized in Figure 2-10. They show TEM images and associated frequency distribution data of two sets of USPIONs prepared at 30 ml/min and 60 ml/min. respectively.

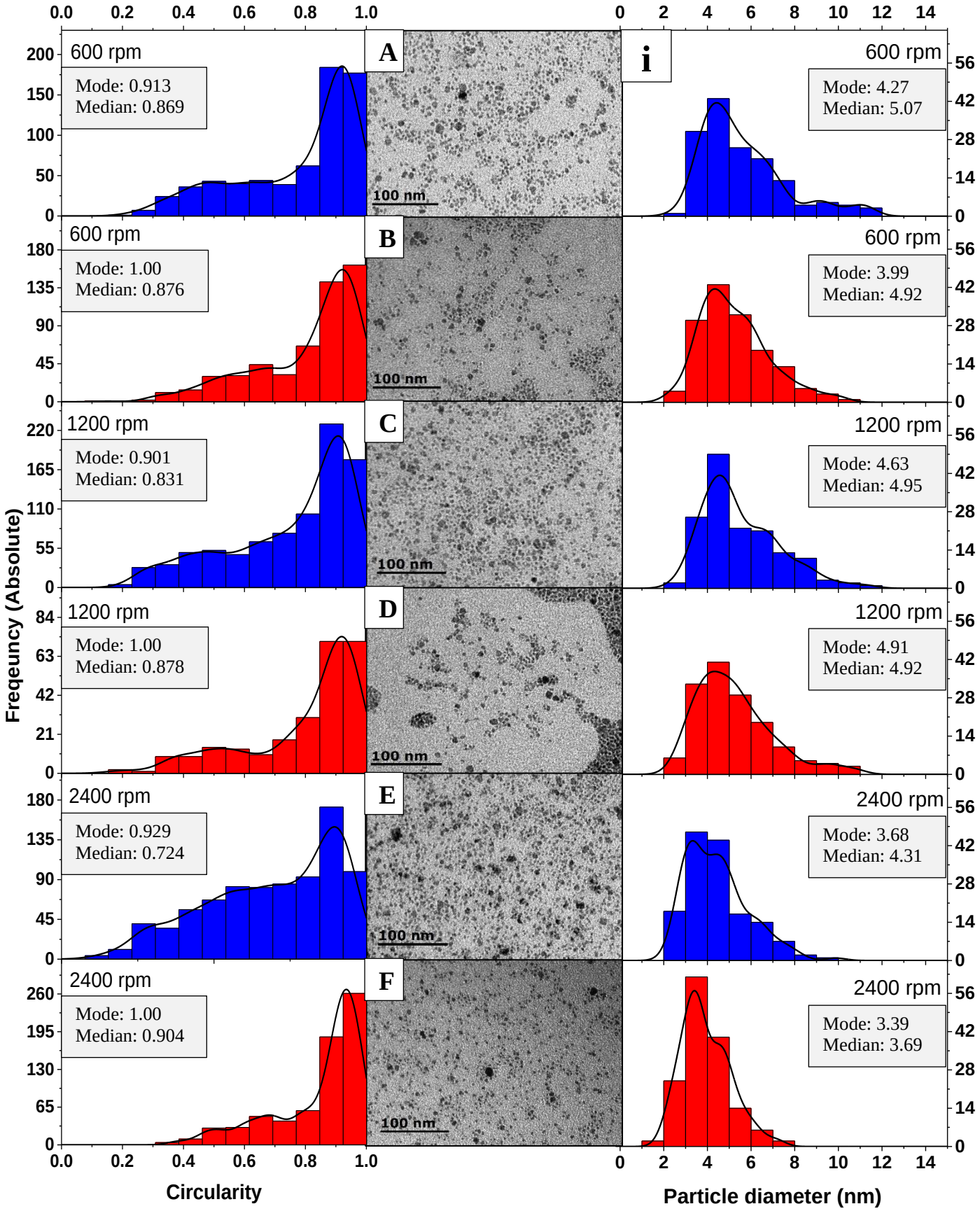
In case of the lower flowrate, 30 ml/min, using the larger spinning disc produced particle with right-skewed size distribution curves, as shown in figure 2-10iA,

C and E. Furthermore, it has been noticed that the right skewness of these histograms are somewhat higher than the corresponding size distribution curves of particles prepared using SSDR, as shown in Figure 2-10iB, D and F.

It should be noted that there was no significant change in the size histograms of USPIONs produced by SSDR or LSDR; similar mode and median sizes were obtained for smaller and larger discs (eg Figure 2-10iA and B etc sets of data).

Analysing the circularity of USPIONs (Figure 2-10i), prepared with larger spinning discs revealed frequency distribution histograms having slightly more negative (left) skewness than those prepared using smaller disc. This means that no further improvement in the morphology upon making this modification has been achieved.

Data for USPIONs batches prepared using conditions of 60 ml/min flowrate, displayed in Figure 2-10ii, show no significant changes in neither shape nor mode/median values of particle size on changing the spinning disc size. The comparable lack of effect on the circularity was observed where values of 0.886, 0.895, 0.867 values were recorded for the larger and 0.894, 0.878 and 0.897 for the smaller disc.


A
600 rpm
Mode: 0.913
Median: 0.869
100 nm
i
600 rpm
Mode: 4.27
Median: 5.07
B
600 rpm
Mode: 1.00
Median: 0.876
100 nm
600 rpm
Mode: 3.99
Median: 4.92
C
1200 rpm
Mode: 0.901
Median: 0.831
100 nm
1200 rpm
Mode: 4.63
Median: 4.95
D
1200 rpm
Mode: 1.00
Median: 0.878
100 nm
1200 rpm
Mode: 4.91
Median: 4.92
E
2400 rpm
Mode: 0.929
Median: 0.724
100 nm
2400 rpm
Mode: 3.68
Median: 4.31
F
2400 rpm
Mode: 1.00
Median: 0.904
100 nm
2400 rpm
Mode: 3.39
Median: 3.69
Freqeuncy (Absolute)
Circularity
Particle diameter (nm)

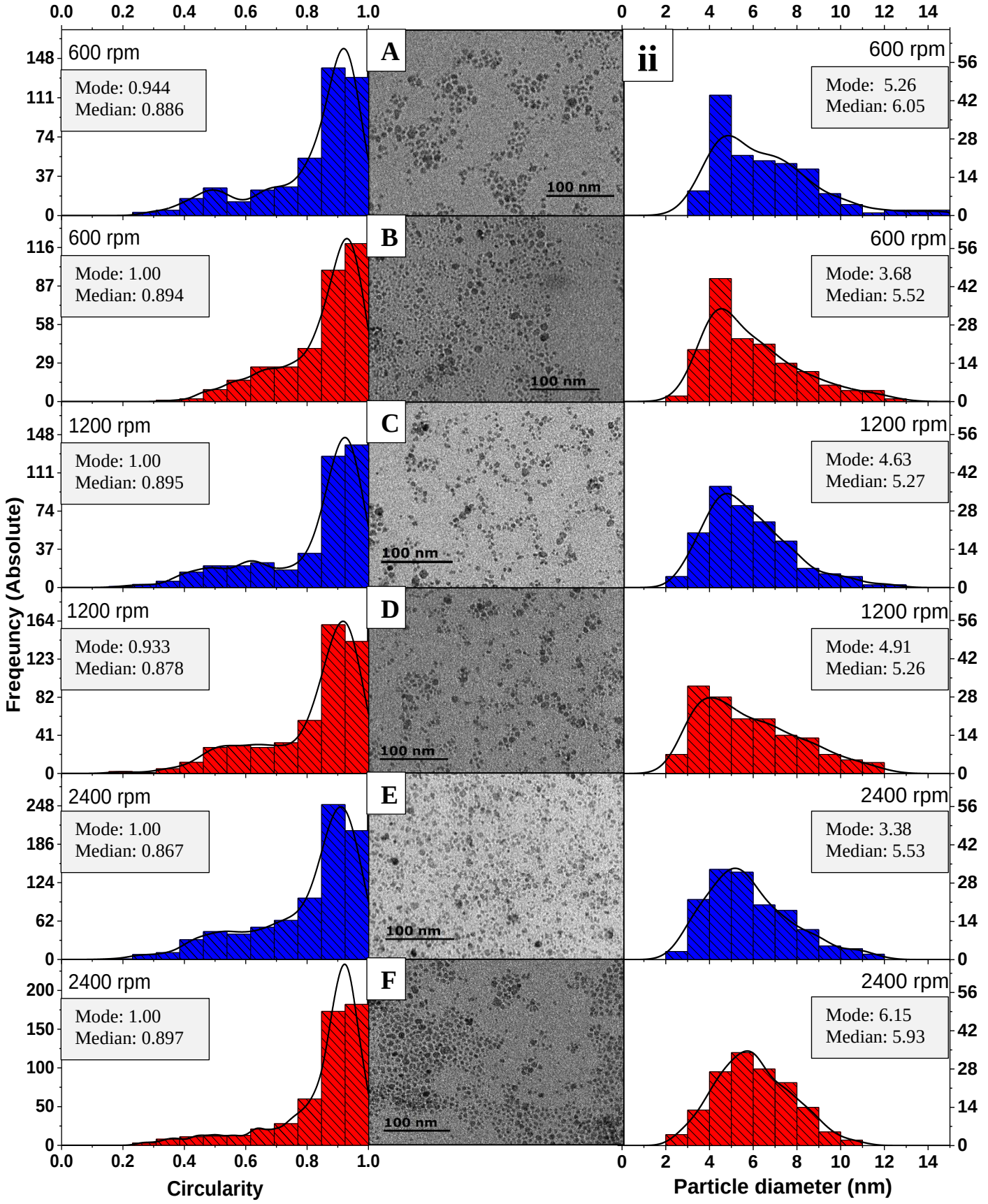


Figure 2-10: TEM micrographs with distribution histograms of USPIONs prepared using two different disc sizes *Four USPIONs batches prepared at each 600, 1200, and 2400 rpm rotational speed are denoted as **A**, **B**, **C**, **D**, **E**, and **F** respectively and in alternate regarding the large (blue histogram) and small (red histogram) spinning disc. Also, two sets of batches have been prepared for 30 ml/min **(i)** and 60 ml/min **(ii)**. The corresponding frequency histogram represent the distribution of particle diameter and circularity. Other processing conditions are: FE2+/Fe3+ ratio equal to 0.66 at 0.375 M, concentration of ammonium hydroxide solution.35% w/w.*

2.3.3.3.2 TEM and DLS average particle sizes

The influence of enlarging the spinning disc size on average TEM derived and hydrodynamic diameters of USPIONs are displayed in Figure 2-11A and B, respectively. The bar graphs in Figure 2-11A show that there is no significant increase or decrease in the average TEM particle size as the spinning disc size is changed. This is evident for different working conditions: pumping rates of 30 and 60 ml/min and spinning speeds of 600, 1200, 2400 rpm. For instance, at 60 ml/min flowrate USPIONs possess average size values of 6.50, 5.80, and 5.85, nm for larger and 5.96, 5.84 and 6.06 nm for smaller disc.

Verification of the above conclusion arises from the hydrodynamic size data of Figure 2-11B, where statistical analysis for both spinning discs used revealed absence of a significant change in particle sizes. For example, value of 21.58, 19.18, 18.6 nm are obtained for the larger and 20.56, 19.37 and 20.12 nm for smaller discs.

In general, there is no clear evidence on improvement in PDI values of the resulting USPIONs on operating the instrument with larger size spinning disc (LSDR), as displayed in Table 2-3.

For more demonstration, when the LSDR was placed in the fabricating machine, slight deterioration in particle size uniformity were observed in batches produced using rotational speeds of 600, and 2400 rpm with both high and low injection rates. For example, at 30 ml/min flowrate and aforementioned disc speeds, PDI values increased from 0.0888 up to 0.1156 and 0.0795 up to 0.1024 above running the LSDR respectively. On the other hand, opposite values were extracted in case of using 1200 rpm rotational speed.

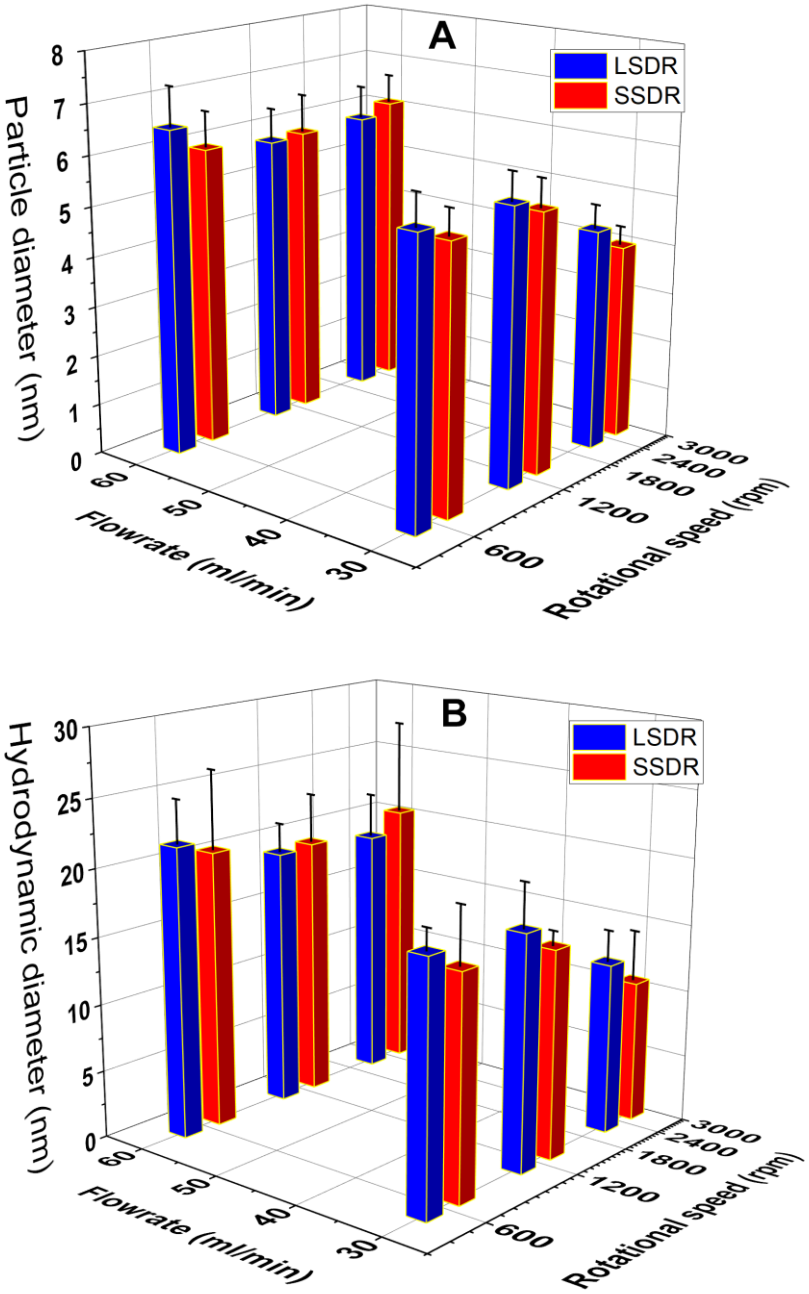


Figure 2-11: 3D bar graphs represent values of particles average diameter extracted from A) TEM images and B) DLS measurements upon using different spinning disc sizes

A) The diameter of individual 150 particles measured using DigitalMicrograph programme. B) Hydrodynamic diameter from dynamic light scattering measurements of USPIONs dispersed in deionised water at 25°C, data expressed in term of scattering intensity. Values represent the mean of three sets of independent measurements with 10 sub-measurements each. The process conditions are the same as described in Figure 2-10. Error bars represent +/- 1SD of the average value. t-test statistical analysis has been followed to define the significant changes.

Table 2-3: PDI of particles size USPIONs at different spinning discs sizes and detected by TEM.

USPIONs preparations (different rotational speed) rpm	**Polydispersity index (PDI) TEM†**			
	Larger disc		**Smaller disc**	
	30 ml/min	**60ml/min**	**30 ml/min**	**60ml/min**
600	0.1156	0.1318	0.0888	0.1260
1200	0.0985	0.1081	0.1106	0.1483
2400	0.1024	0.1107	0.0795	0.0792

† Particles number (n) is 150 for each individual data.

2.3.3.3.3 Extent of the fabricated USPIONs circularity

Figure 2-12 illustrates that modifying the instrument by changing the size of spinning disc did not yield USPIONs batches with better circularity. In contrast, data point to some deterioration in particles morphology, i.e. circularity for LSDR at flowrate of 30 ml/min and spinning speeds of 1200 and 2400 rpm.

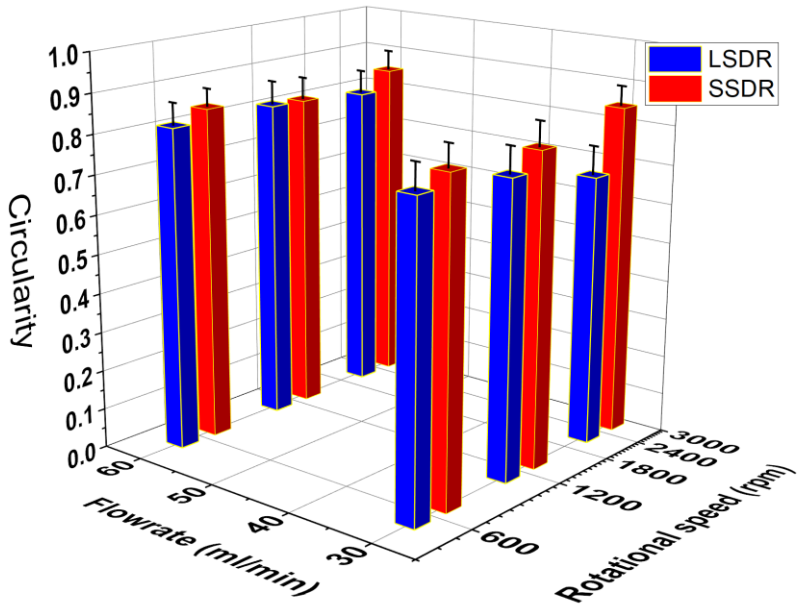


Figure 2-12: Average of circularity values of different USPIONs sets prepared using various rotational speed and flowrates. Red bar graphs represent results of SSDR, while blue bars represent readings of LSDR

ImageJ programme was used to analyse the morphology of the resulted NPs. The number of items processed is variable and depends upon the amount of particles presented in each individual TEM micrograph. The degree of circularity is expressed in absolute values lying between 0.00 and 1.00. Error bars represent +/- 1SD of the average value. t-test statistical analysis has been followed to define the significant changes.

2.3.3.4 Effect of BISS concentration

2.3.3.4.1 Size and degree of circularity distribution

The derived from TEM images of USPIONs prepared adopting procedure 4 are summarized in Figure 2-13. BISS concentrations used were 0.25 M, 0.375 M, 0.5 M, 0.6 M, 0.75 M and 1.5 M which are denoted by A, B, C, D, E, and F respectively. The fabrication was performed at 600 and 2400 rpm spinning disc rotations, assigned by i and ii respectively. SSDR and flowrate of 60 ml/min were employed.

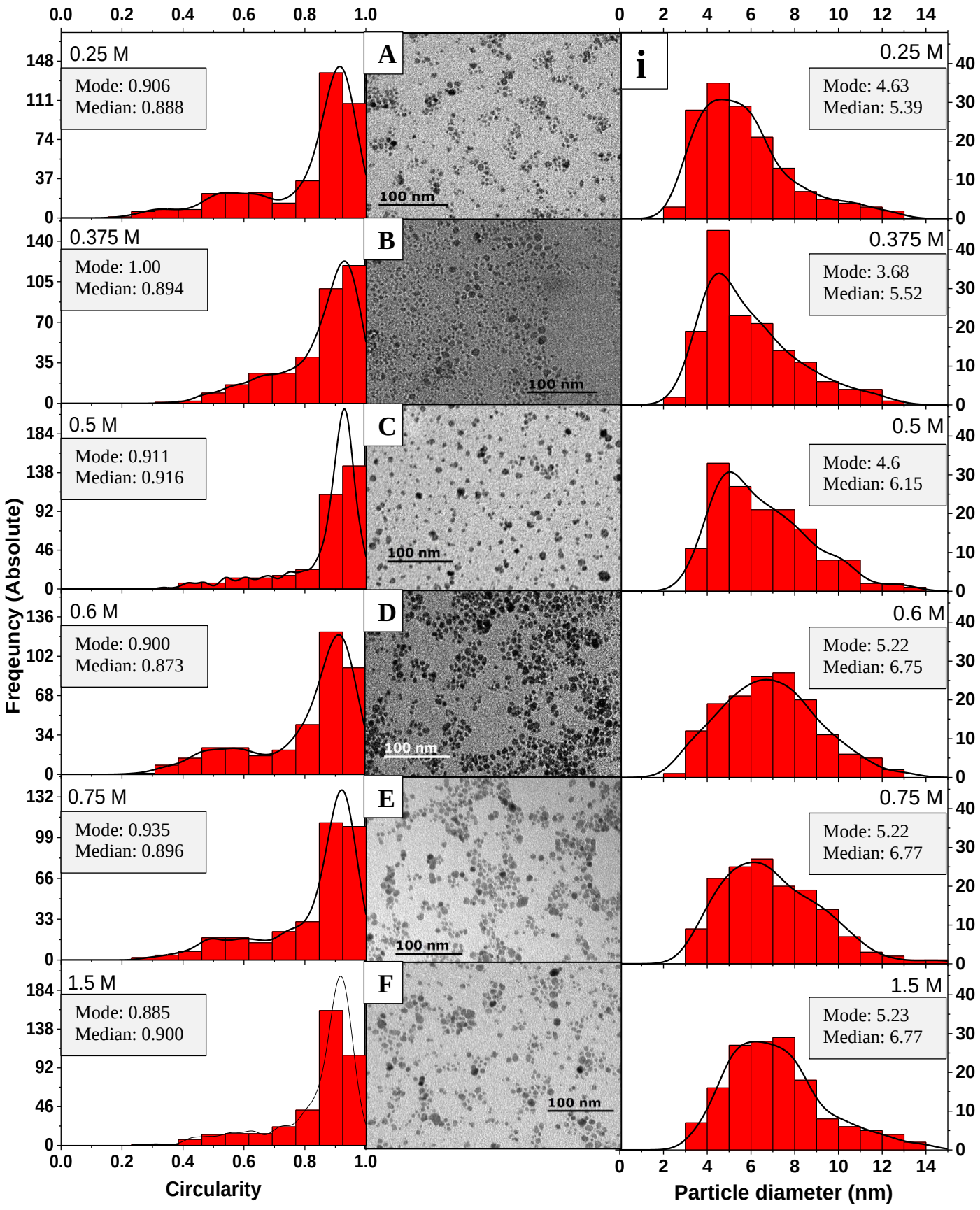
The profiles of size distribution curves does not appear to, in general, show significant difference. Somewhat increased median size values, starting from 5.39 nm up to 6.75 nm, can be seen as the concentration of the reactant solution increases from 0.25 M up to 0.6 M respectively.

Similarly, circularity distribution histograms show no significant alteration on addition of more iron salts into the production at higher BISS concentrations. For instance, median values of around 0.888, 0.916 and 0.900 were calculated for USPIONs prepared at 0.25 M, 0.5 M, and 1.5 M concentrations, respectively as illustrated Figure 2-13i.

At 2400 rpm spinning rate, the all formed USPIONs were found to possess approximately symmetrical size distribution curves with either bell or slight skewed shape. Excluding USPIONs resulted using the least iron salts concentration, 0.25 M, the all other frequency histograms did not demonstrate any change in their position and width. However, the most noticeable effect is a considerable increase in the median particle size of the tested batches from 4.05

nm up to 7.52 nm upon increasing a concentration of BISS from 0.25 M up to 1.5 M as illustrated in the right side of Figure 2-13iiA and F, respectively.

Interestingly, it was found that adding higher amounts of ferrous and ferric chloride salts into the reaction (i.e. using higher concentrations of BISS) did not introduce any significant effect on the morphology, i.e. circularity of the fabricated USPIONs; values remain within the 0.868-0.906 range. The only exception was in case 1.5 M BISS where a slight reduction in the circularity to an extent of 0.789 was recorded. As per above conclusion, majority of circularity distribution histograms have a negative-skewed shape, with values clustering around 0.885-1.00, as shown in Figures 2-13i and ii.


A
B
C
D
E
F
i
0.25 M
Mode: 0.906
Median: 0.888
0.375 M
Mode: 1.00
Median: 0.894
0.5 M
Mode: 0.911
Median: 0.916
0.6 M
Mode: 0.900
Median: 0.873
0.75 M
Mode: 0.935
Median: 0.896
1.5 M
Mode: 0.885
Median: 0.900
0.25 M
Mode: 4.63
Median: 5.39
0.375 M
Mode: 3.68
Median: 5.52
0.5 M
Mode: 4.6
Median: 6.15
0.6 M
Mode: 5.22
Median: 6.75
0.75 M
Mode: 5.22
Median: 6.77
1.5 M
Mode: 5.23
Median: 6.77
100 nm
Freqeuncy (Absolute)
Circularity
Particle diameter (nm)

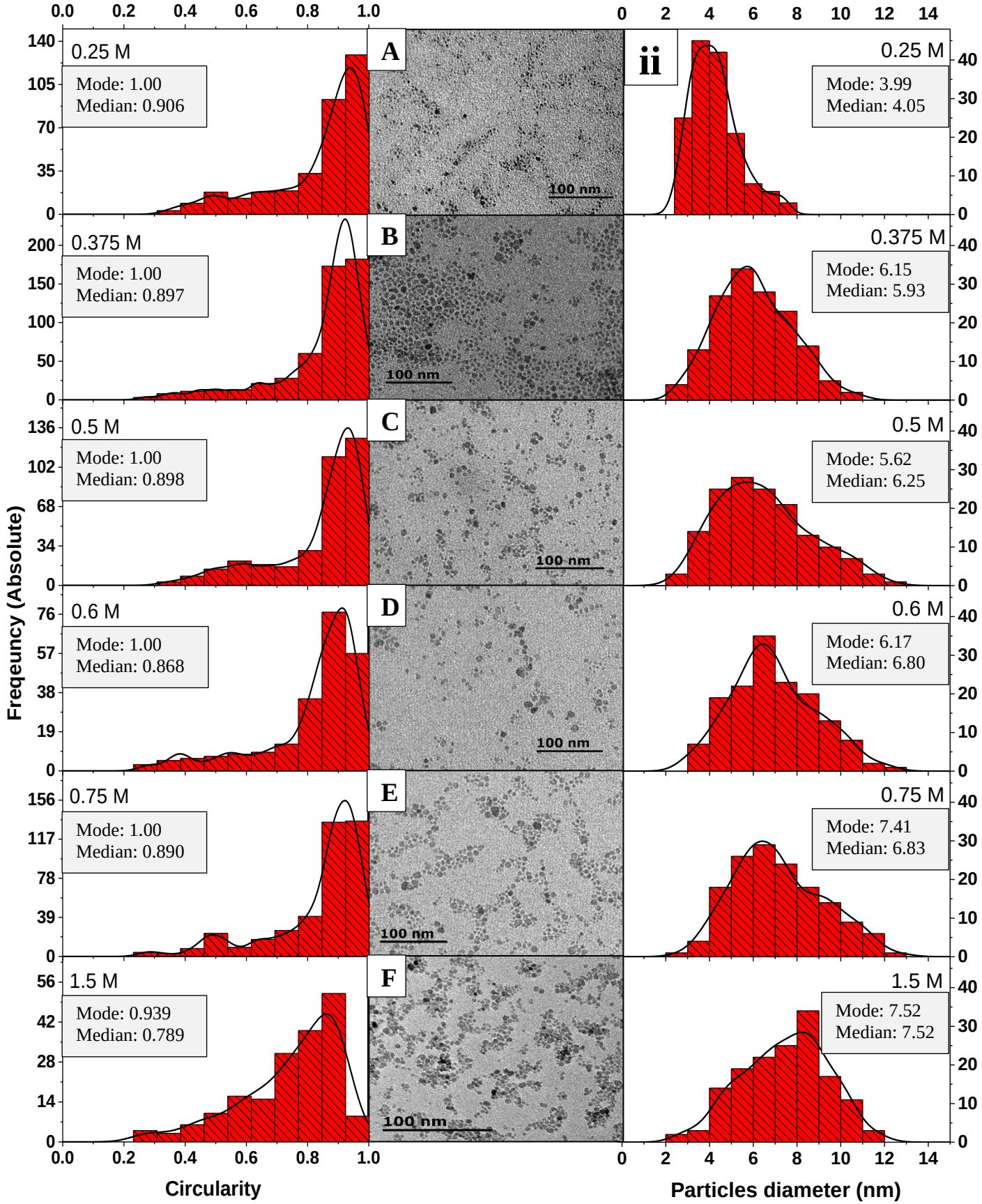


Figure 2-13: TEM micrographs with distribution histograms of USPIONs prepared using different iron amounts. *Four USPIONs batches prepared at each 0.25, 0.375, 0.5, 0.6, 0.75 and 1.5 M BISS concentration are denoted as **A**, **B**, **C**, **D, F** and **E**, respectively. Two sets of batches have been prepared for 600 rpm **(i)** and 2400 rpm rotational speed **(ii)**. The corresponding frequency histograms represent the distribution of particle diameter and circularity. Other processing conditions are: Fe^{2+}/Fe^{3+} ratio equal to 0.66 at 60 ml/min flowrate, concentration of ammonium hydroxide solution.35% w/w, and SSDR.*

2.3.3.4.2 Comparison of TEM and DLS average particle size

Figure 2-14A and B illustrate TEM-derived and hydrodynamic particle diameters *versus* after increasing concentrations of BISS. It is noticed that both profiles show inverse exponential-like increase (with highly significant difference, $p < 0.001$) in the average size of the USPIONs. For instance, hydrodynamic diameter increased from 17.54 nm up to 23.55 nm as the BISS concentration is increased.

The polydispersity of USIPONs also exhibits an inverse relationship with the increased BISS, where PDI values reduced from 0.1386 to 0.0913 upon increasing the concentration from 0.25 M to 1.5 M, respectively as tabulated in Table 2-4.

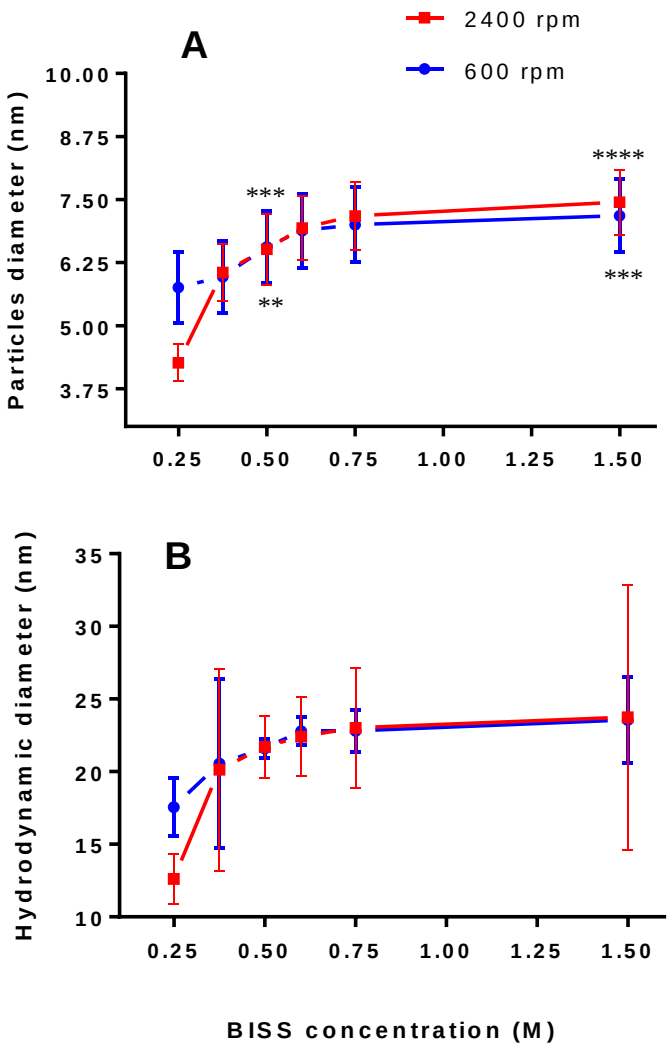


Figure 2-14: line graphs represent the plot of particles average diameter extracted from A) TEM images and B) DLS measurements versus different total iron amount used.

A) *The diameter of each single nanoparticle were individually measured using DigitalMicrograph programme. The total population of each particular point is 150 particles,* ***B)*** *dynamic light scattering of the hydrodynamic diameter (nm) of NPs dispersed in deionised water at 25°C, data expressed in term of intensity and values represent the mean of three sets of independent measurements with 10 sub-measurement each. The process conditions is the same as mentioned in figure 2-13. Error bars represent +/- 1SD of the average value. t-test statistical analysis has been followed to define the significant changes. **, *** and **** denote a significant increase ($p < 0.01$, 0.001 and 0.0001 respectively) in diameter value compared to size measurement of lowest BISS concentration.*

Table 2-4: PDI of particles size produced using different total iron amounts and detected by TEM.

USPIONs preparations (different iron concentrations) M	**Polydispersity index (PDI) TEM †(at two rotational speeds)**	
	600 rpm	**2400 rpm**
0.25	0.1386	0.0664
0.375	0.1260	0.0792
0.5	0.1053	0.1064
0.6	0.1020	0.0775
0.75	0.1012	0.0804
1.5	0.0913	0.0674

†Particles number (n) was 150 for each individual data.

2.3.3.4.3 Effect on USPIONs circularity

Figure 2-15 reveals there is no considerable change in particles circularity on increasing the BISS concentration, i.e. increasing amount of the salts in the production mixture.

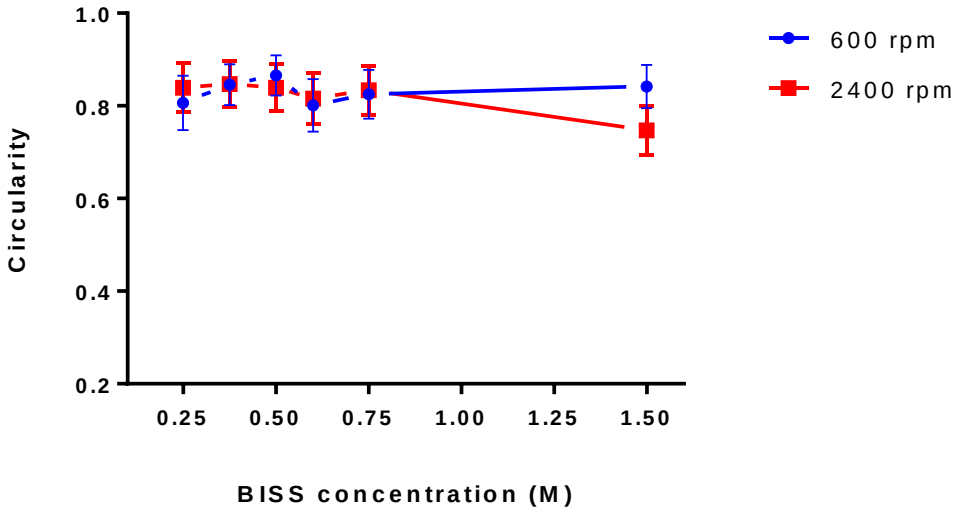


Figure 2-15: Average of circularity values of two different USPIONs sets prepared using various BISS concentration.

ImageJ programme was used to analyse the morphology of the resulted NPs. The number of items processed is variable and depends upon the amount of particles presented in each individual TEM micrograph. The degree of circularity is expressed in absolute values lying between 0.00 and 1.00. Error bars represent +/- 1SD of the average value. t-test statistical analysis has been followed to define the significant changes.

2.3.3.5 Effect of changing Fe^{2+}/Fe^{3+} ratio

2.3.3.5.1 Size and degree of circularity distribution

Procedure 5 was adopted so as to explore the influence of ferrous to ferric ions ratio on particle size and morphology. In this experiment, the ratios of 0.5 and 0.66 of Fe^{+2}/Fe^{+3} (which falls in the optimal 0.4-0.6 range) was compared.

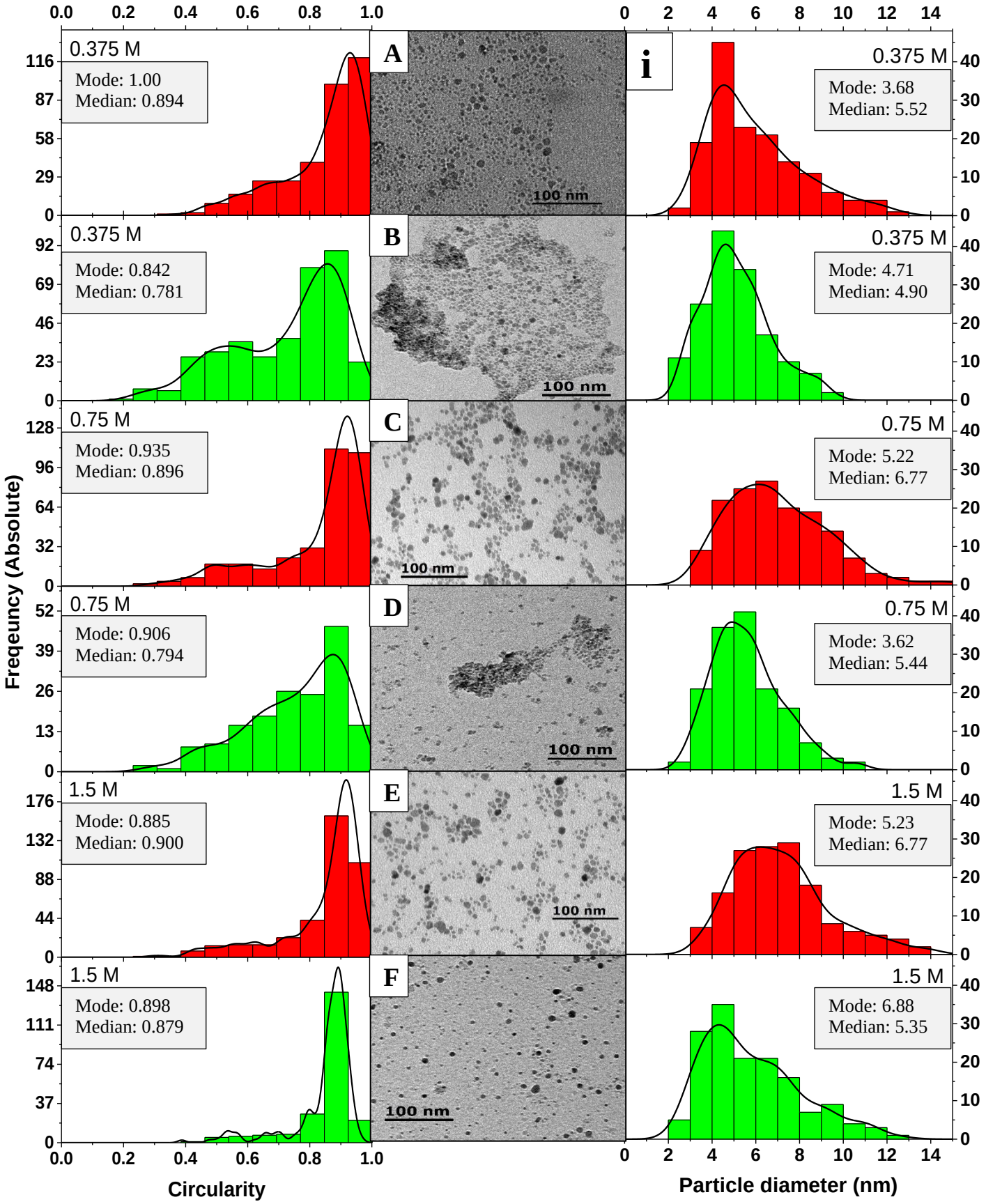
BISS concentrations of 0.375 M, 0.75 M, and, 1.5 M were used. TEM images and related frequency histograms are shown in Figures 2-16i and ii.

In case of the spinning speed of 600 rpm, using the 0.5 ratio of Fe^{+2}/Fe^{+3} produced particle size distribution curves with similar profiles to 0.66 ratio, as seen in Figure 16i A, B, C, D, F and E. The median particle size of USPIONs prepared at 0.66 Fe^{+2}/Fe^{+3} ratio was higher than the counterparts at 0.5 ratio. For instance, using 0.375 M solutions, 6.77 nm for 0.6 and 5.4 nm for 0.5 ratio.

Regarding particle circularity, the frequency distribution histograms in the Figure 2-16i all show profiles with a considerable negative skewness, i.e. shift towards more spherical particles as towards concentration of BISS is increased, but there is no apparent effect of the Fe^{+2}/Fe^{+3} ratio. The data in Figure 2-18 however indicate that ratio decreases the circularity at Fe^{2}/Fe^{+3} 0.375 M but this effects is reduced as the BISS increases to 1.5 M.

At 2400 rpm spinning speed, Figure 16ii, it was found that median sizes were notably reduced upon decreasing the Fe^{+2}/Fe^{+3} ratio to 0.5. For example, median values were 5.93 nm, 6.83 nm, and 7.52 nm for 0.66 Fe^{+2}/Fe^{+3} ratio, and 4.54 nm, 4.71 nm, and 5.43 nm for 0.5 Fe^{+2}/Fe^{+3} ratio, as shown in Figure 2-16ii A, C, and E and B, D and F, respectively.

Regarding particle circularity, excluding the data using the highest BISS concentration, 1.5 M, median circularity values are noticeably diminished from 0.897 to 0.773 and from 0.890 to 0.783 when the Fe^{+2}/Fe^{+3} ratio was lowered from 0.66 to 0.5 for both 0.375 M and 0.75 M concentrations.


0.375 M
Mode: 1.00
Median: 0.894
A
100 nm
i
0.375 M
Mode: 3.68
Median: 5.52
0.375 M
Mode: 0.842
Median: 0.781
B
100 nm
0.375 M
Mode: 4.71
Median: 4.90
0.75 M
Mode: 0.935
Median: 0.896
C
100 nm
0.75 M
Mode: 5.22
Median: 6.77
0.75 M
Mode: 0.906
Median: 0.794
D
100 nm
0.75 M
Mode: 3.62
Median: 5.44
1.5 M
Mode: 0.885
Median: 0.900
E
100 nm
1.5 M
Mode: 5.23
Median: 6.77
1.5 M
Mode: 0.898
Median: 0.879
F
100 nm
1.5 M
Mode: 6.88
Median: 5.35
Freqeuncy (Absolute)
Circularity
Particle diameter (nm)

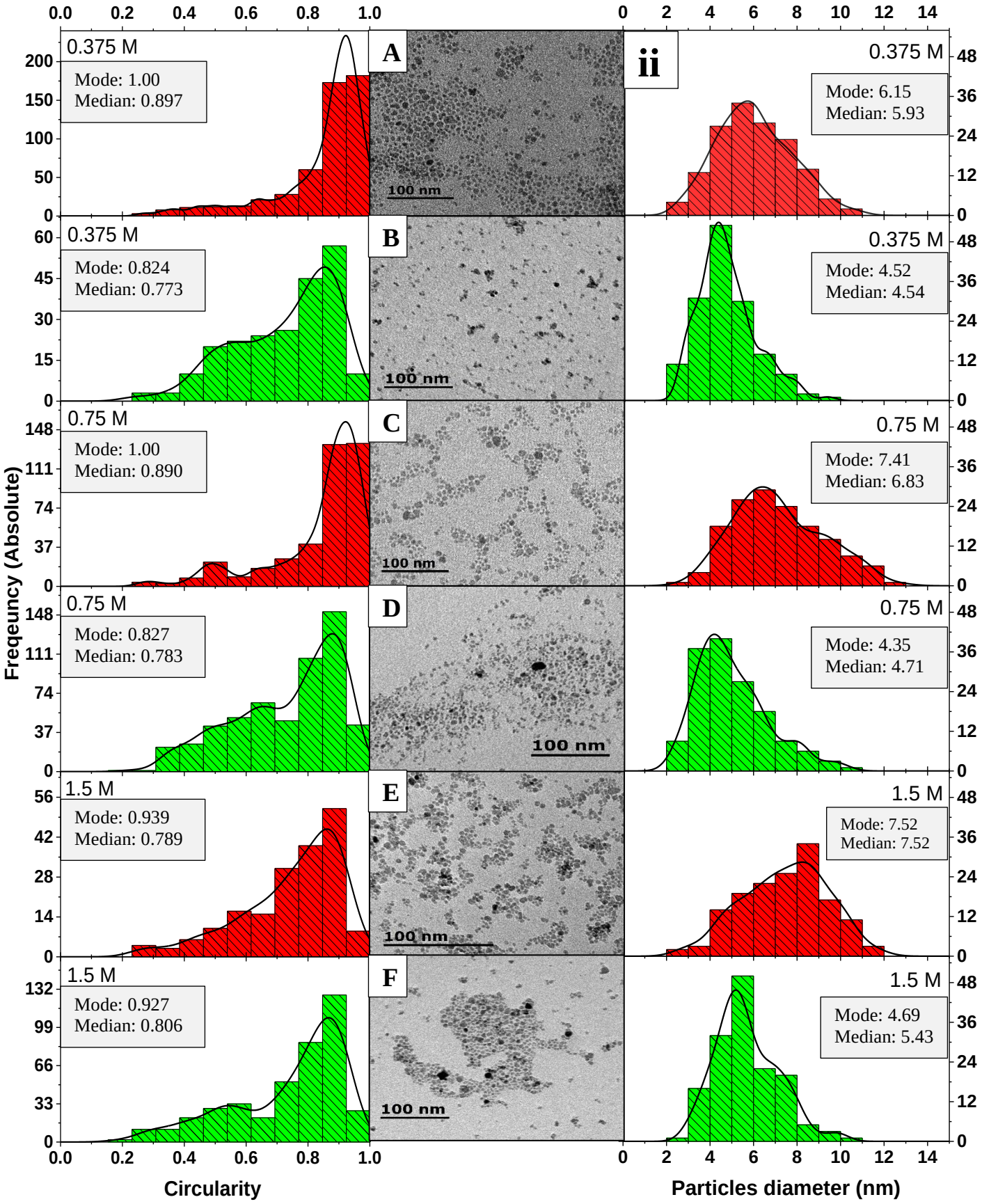


Figure 2-16: TEM micrographs with frequency distribution histograms of USPIONs prepared using two different Fe^{+2}/Fe^{+3} ratios. *Four USPIONs batches prepared at each 0.375, 0.75, and 1.5 M BISS concentration are denoted as **A**, **B**, **C**, **D**, **E**, and **F** respectively and in alternate regarding 0.66 (red histogram) and 0.5 (green histogram) Fe^{+2}/Fe^{+3} ratio. Also, two sets of batches have been prepared for 600 rpm **(i)** and 2400 rpm **(ii)** rotational speed. The corresponding frequency histograms represent the distribution of particle diameter and circularity. Other processing conditions are: flowrate at 60 ml/min, concentration of ammonium hydroxide solution.35% w/w and SSDR.*

2.3.3.5.2 Comparing TEM and DLS average particle size

The graphs displayed in Figure 2-17A and B show that USPIONs prepared using Fe^{+2}/Fe^{+3} ratio 0.5 show highly significant ($p < 0.001$) reduction in particle size in comparison to 0.66 ratio, measured by either TEM or DLS. This occurs for both 600 and 2400 rpm spinning speeds. As an example, the average particles sizes for USPIONs prepared at concentration of 0.75 M, Fe^{+2}/Fe^{+3} ratio of 0.66 and at 600 and 2400 rpm were 7.0013 nm and 7.172 nm respectively, while for those prepared using Fe^{+2}/Fe^{+3} ratio of 0.5 and other equivalent conditions, the average size were 5.63 nm and 5.04 nm respectively.

The PDI values shown in Table 2-5 manifest the presence of fluctuation in size uniformity with no clear trend in the data.

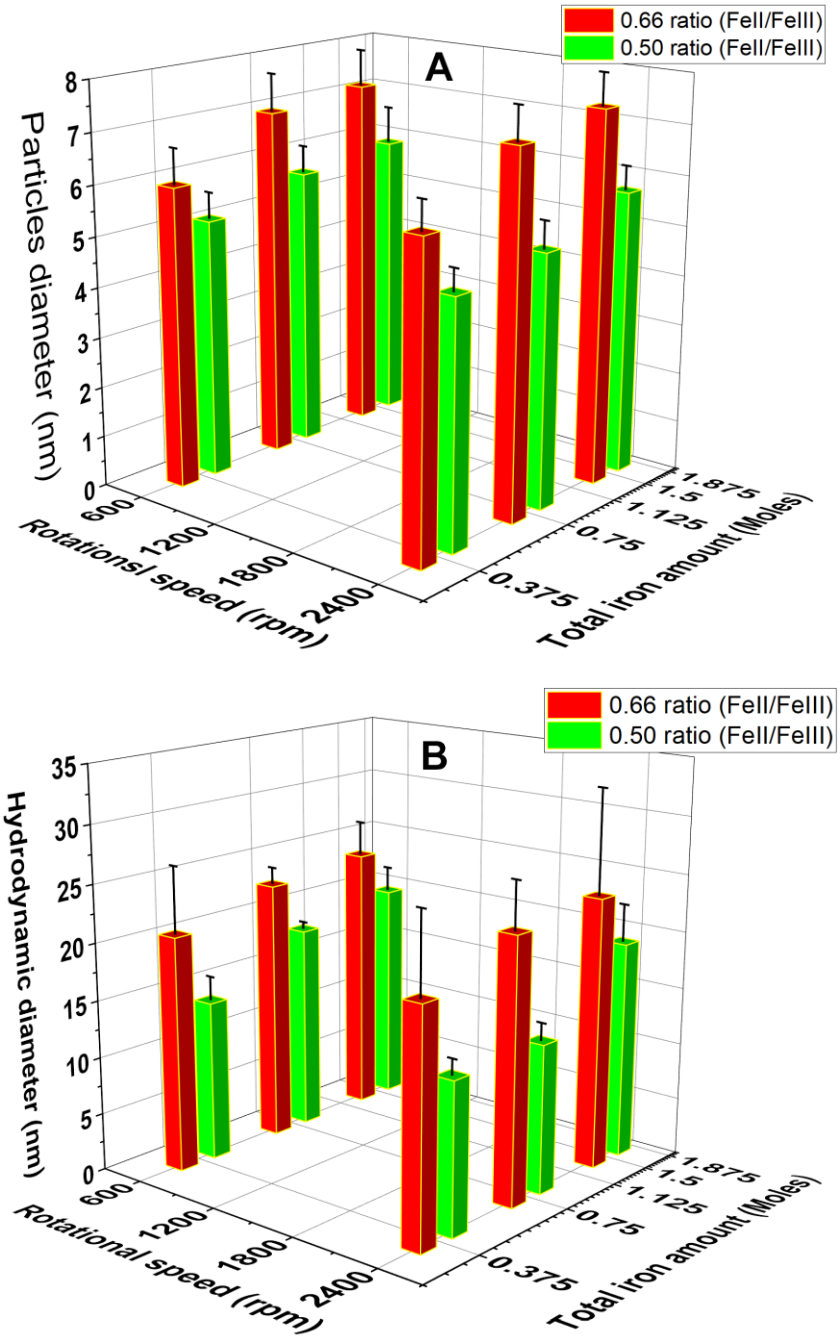


Figure 2-17: 3D bar graphs represent values of particles average diameter extracted from A) TEM images and B) DLS measurements upon using different Fe^{+2}/Fe^{+3} ratio

A) *The diameter of each single NP were individually measured using DigitalMicrograph programme. The total population of each particular point is 150 particles,* ***B)*** *DLS of the hydrodynamic diameter (nm) of NPs dispersed in deionised water at 25°C, data expressed in term of intensity and values represent the mean of three sets of independent measurements with 10 sub-measurement each. The green bars stand for collection of batches produced using 0.5 Fe^{+2}/Fe^{+3} ratio while the red bar belong to that of resulted from 0.66 Fe^{+2}/Fe^{+3} ratio. The tested flowrates is 60 ml/min. Other process conditions include 35% w/w ammonium hydroxide solution and SSDR. Error bars represent +/- 1SD of the average value.*

Table 2-5: PDI of particles size fabricated at different Fe^{+2}/Fe^{+3} ratios and detected from TEM images

USPIONs preparations (total iron concentration) M	Polydispersity index (PDI) TEM¶ (different iron salts ratios)			
	0.66 Fe^{+2}/Fe^{+3} ratio		0.5 Fe^{+2}/Fe^{+3} ratio	
	600 rpm	2400 rpm	600 rpm	2400 rpm
0.375	0.1260	0.0792	0.0909	0.0736
0.75	0.1012	0.0804	0.0795	0.1054
1.5	0.0913	0.0674	0.1415	0.0634

¶ Particles number (n) was 150 for each individual data.

2.3.3.5.3 Effect on USPIONs circularity

Data in bar graphs of Figure 2-18 display a highly significant reduction ($p < 0.01$) in circularity of USPIONs prepared from 0.5 Fe^{+2}/Fe^{+3} ratio, in comparison with those USPIONs prepared at ratio of 0.66. This is evident in case of 0.375 M and 0.75 M $Fe^{2+/}Fe^{3+}$ concentrations. For example, at 600 rpm disc speed, circularity values of 0.846 and 0.825 were recorded when using 0.375 M and 0.75 M solution with 0.66 Fe^{+2}/Fe^{+3} ratio respectively, while the corresponding batches show 0.724 and 0.752 circularity values for 0.5 Fe^{+2}/Fe^{+3} ratio. This is also seen when at disc speed of 2400 rpm.

However, at the highest BISS 1.5 M concentration, USPIONs possess comparable circularity values with no significant change for 0.5 and 0.66 Fe^{+2}/Fe^{+3} ratios.

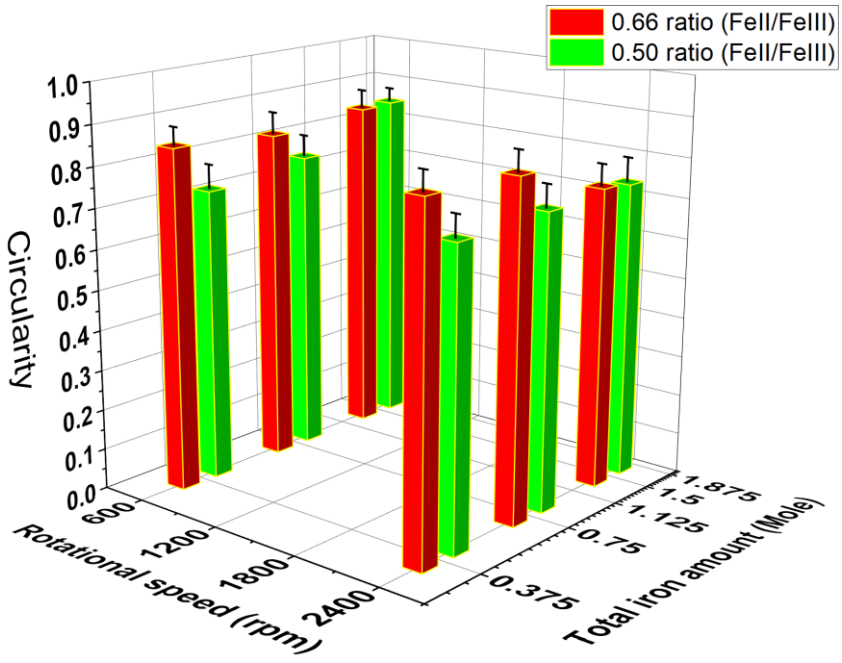


Figure 2-18: Average of circularity values of different USPIONs sets prepared using various rotational speed and BISS with two Fe^{+2}/Fe^{+3} ratios (0.66 and 0.5).

ImageJ programme was used to analyse the morphology of the resulted NPs. The number of items processed is variable and depends upon the amount of particles presented in each individual TEM micrograph. The degree of circularity is expressed in absolute values lying between 0.00 and 1.00. Error bars represent +/- 1SD of the average value.

2.3.3.6 Effect of reducing the basicity of the alkaline

2.3.3.6.1 Size and degree of circularity distribution

Following the procedure 6, the effect the alkaline material strength on the particles size and morphology was assessed. USPIONs were prepared at two different, 0.375 M and 0.75 M, BISS concentrations with concentration of the alkaline solution (ammonium hydroxide) reduced to 17.5 % w/w and compared to the counterparts prepared using the maximum ammonium hydroxide concentration, 35% w/w.

Generally, there is an absence of significant change in the shape of size distribution histograms or median diameters, with somewhat left shifted profiles for particle circularity, as seen in Figure 2-19.

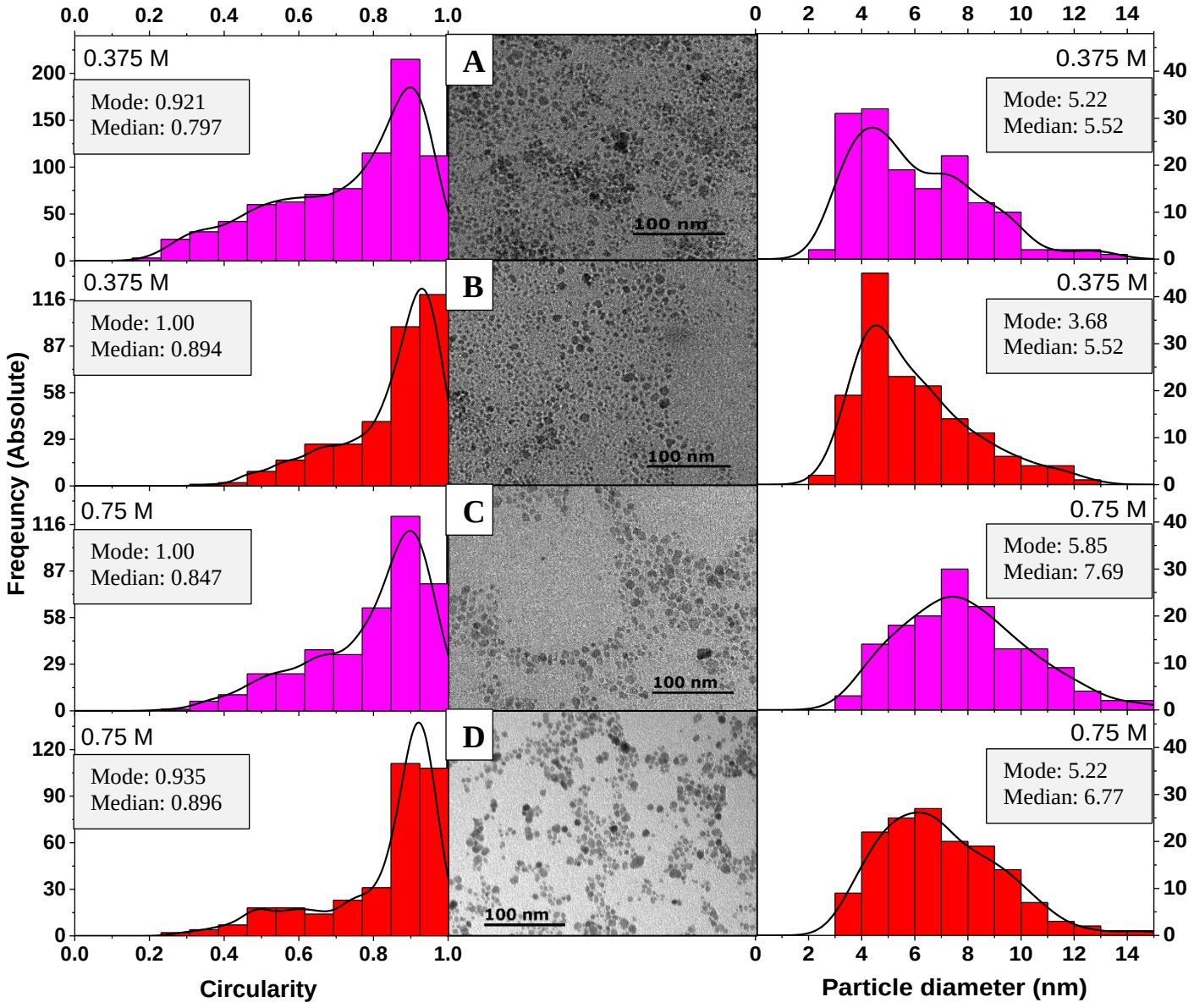


Figure 2-19: TEM micrographs with frequency distribution histograms of USPIONs prepared using two different concentrations of alkaline solution. *Preparations of NPs batches were prepared using two different concentration and denoted as **A**, **B**, **C**, and **D** alternatively. Histograms with pink color are assigned for 18% NH_4OH while those having red color are stood for 35% NH_4OH. Other process conditions include flowrate of 60 ml/min and rotational speed of 600 rpm. In addition, SSDR has been used*

2.3.3.6.2 TEM and DLS average particle sizes

Reducing the strength of alkaline media (ammonium hydroxide) by half produced a limited effect on the average size of the fabricated USPIONs using 0.75 M BISS, as illustrated in Figure 2-20A, while there is no statistically significant difference when 0.374 M solution was used. Size values of 7.0013 nm and 7.9026 nm were obtained from TEM analysis for 35% and 18% NH_4OH respectively as illustrated in figure 2-20A.

Similar trends were obtained from DLS measurements (Figure 2-20B), hence verifying the above conclusions. The size uniformity data in table 2-6 indicate absence of significant effects on PDI. For example, PDI values of 0.0910 and 0.1012 were obtained for USPIONs prepared using 18% and 35% NH_4OH, respectively.

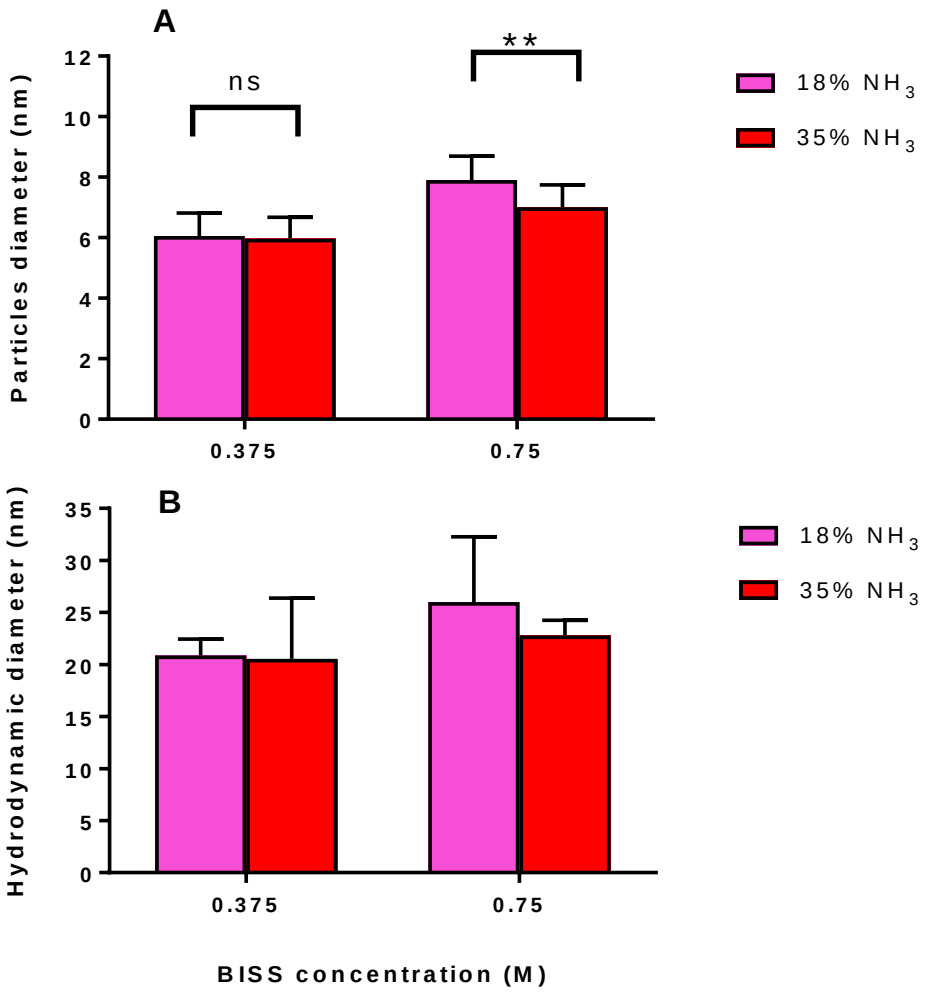


Figure 2-20: Bar graphs represent values of particles average diameter extracted from A) TEM images and B) DLS measurements upon using different NH_4OH concentrations

A) *The diameter of each single nanoparticle were individually measured using DigitalMicrograph programme. The total population of each particular point is 150 particles,* ***B)*** *dynamic light scattering of the hydrodynamic diameter (nm) of NPs dispersed in deionised water at 25°C, data expressed in term of intensity and values represent the mean of three sets of independent measurements with 10 sub-measurement each. Pink bars stand for a collection batches produced using 18% NH_4OH while red bar belong to that of resulted from 35% NH_4OH. The tested flowrates and rotational speed were 60 ml/min and 600 rpm respectively. In addition, SSDR have been used. Error bars represent +/- 1SD of the average value. t-test statistical analysis has been followed to define the significant changes. ns and ** denote no significant and highly significant change ($p < 0.01$ respectively) in diameter value..*

Table 2-6: PDI of particles size produced using different amonium hydroxide solution and detected by TEM.

USPIONs preparations (total iron concentration)M	**Polydispersity index (PDI) TEM¶ (different NH4OH conc.)**	
	18% NH4OH	**35% NH4OH**
0.375	0.1436	0.1260
0.75	0.0910	0.1012

¶ Particles number (n) was 150 for each individual data.

2.3.3.6.3 Extent of the fabricated USPIONs circularity

Circularity data contained in the bar graph below show that there is significant deterioration ($p < 0.05$) in particles morphology upon using reduced concentration of the alkaline media in fabricating USPIONs. As displayed in Figure 2-21 the circularity values of both 0.375 M and 0.75 M BISS decreased from 0.846 and 0.825 up to 0.733 and 0.792 respectively when the concentration of NH_4OH solution were halved from 35% up to 18%.

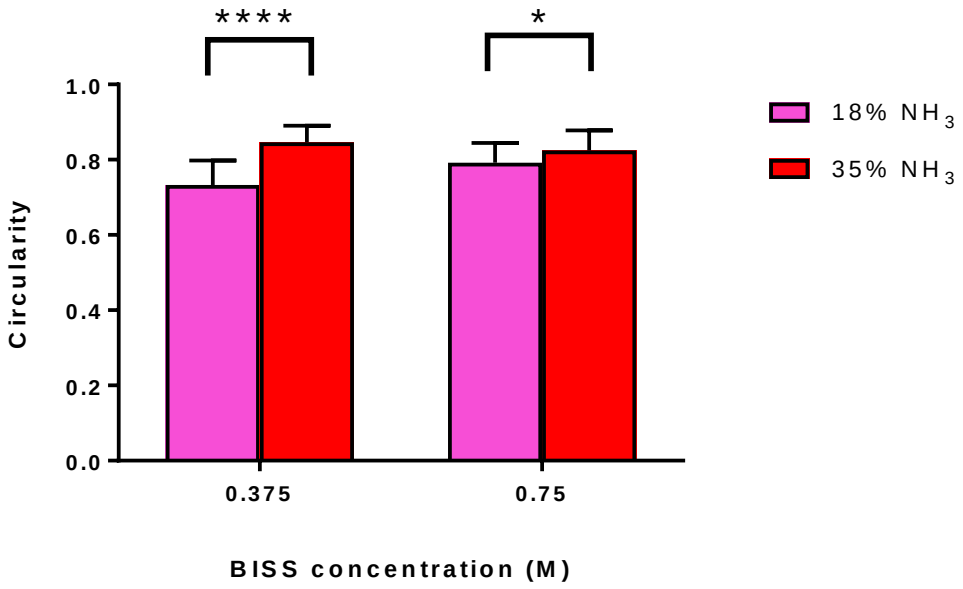


Figure 2-21: Average of circularity values of different USPIONs prepared using two total iron amounts. Red bar graphs represent results of 35% NH_4OH, while pink bars represent readings of 18% NH_4OH

*ImageJ programme was used to analyse the morphology of the resulted NPs. The number of items processed is variable and depends upon the amount of particles presented in each individual TEM micrograph. The degree of circularity is expressed in absolute values lying between 0.00 and 1.00. Error bars represents +/- 1SD of the average value. t-test statistical analysis has been followed to define the significant changes. * and **** denote a significant decrease ($p < 0.05$ and < 0.0001 respectively) in diameter value.*

2.4 Discussion

2.4.1 Mechanism of iron oxide network formation

In order to discuss the basis for USPIONs production in the work, from chemical point of view, a relevant reaction mechanism will be discussed below.

Upon dissolving in aqueous media (water), the ferric and ferrous chloride will frequently form a hexahydrated complexes called hexacoordinated aquo iron III – $[Fe(H_2O)_6]^{+3}$ ions and hexacoordinated aquo iron II - $[Fe(H_2O)_6]^{+2}$ ions respectively [61]. These ions are capable of hydroxylation reaction, depending on the pH of medium in which they exist. At room temperature, the trivalent cation undergo hydroxylation at pH 1 to ~5, while the divalent cation require pH of ~7-9 to be hydroxylated [62]. The resulting complexes of hydroxylated metal are highly unstable and tend to condense following two basic routes, depending upon the coordination environment of iron ions.

For both of the routes, an extended metal oxide network will be produced. In the first case, hydroxo bridges among hydroxylated species will form due to nucleophilic character of hydroxyl ligand. The net is one-step condensation which occurs at very high rate, due to the lability of the coordinated water molecules, as shown in Figure 2-22A. When oxohydroxo complexes exist, condensation happens *via* two-steps associative mechanism where the formed oxo-bridges result in polymerisation of the metal oxide and further water molecules elimination, as illustrated in Figure 2-22B. It should be noted that sometimes the latter process, oxolation mechanism, is indistinguishable from the first one, olation mechanism [63].

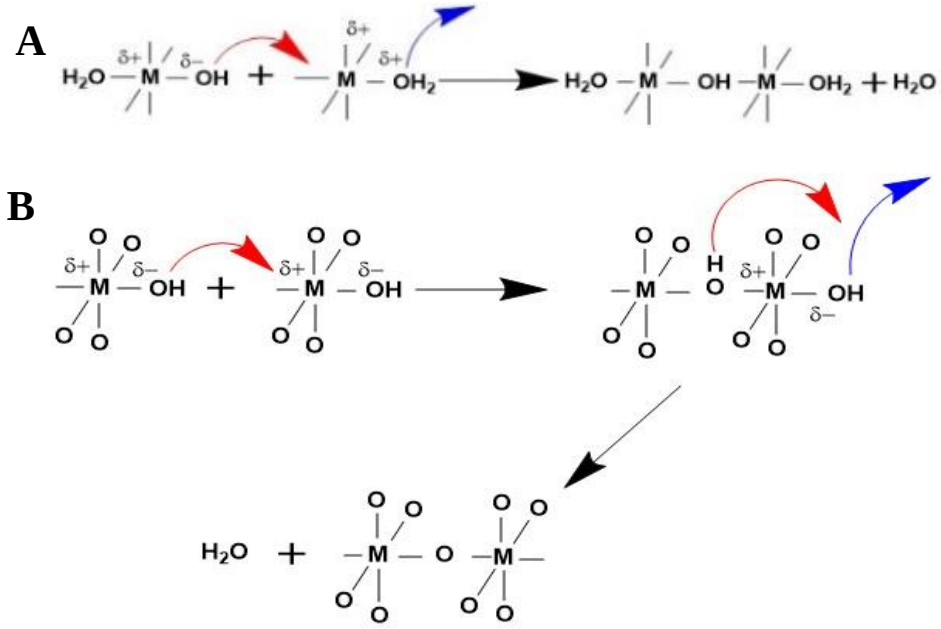


Figure 2-22: The mechanism of iron oxide network formation

A) Olation mechanism of hydroxo bridges formation, B) oxolation mechanism of oxo bridging via two-steps associative mechanism, water molecules are eliminated in both of processes

Accordingly, the presence of the characteristic iron-oxide bonds was confirmed in this work in the FTIR spectrum, where the extremely strong peaks associated with the stretching mode of the bond at range less than 600 cm^{-1} wavenumber are displayed, Figure 2-3. This is in agreement with FTIR spectrum of iron oxide nanoparticles reported in literature [56,64-68].

2.4.2 Control over particles nucleation and growth

The principle challenge in preparing nanoparticles within ultrafine size range and spherical shape, is to prevent newly constructed nanoparticles from aggregating. In order to achieve this aim. This work develops a novel strategy to control nanoparticles nucleation and growth.

In order to create a new solid phase (USPIONs) dispersed in an aqueous medium, an insoluble monomer (hydroxylated iron species) is first generated from highly soluble iron salts precursors [69]. The existence of such species is defined by both lower and higher solubility limits of a certain material. When the amount of reactive monomers is within this range, an equilibrium is present. A disruption of the thermodynamic equilibrium will result once the concentration of reactive monomer in the system exceeds the upper solubility limit, where critical supersaturation state is achieved – the only situation at which nucleation occurs. In literature, the upper solubility limit is often called 'critical supersaturation concentration' or 'equilibrium concentration' [70], but here it will refereed to using term 'nucleation cut-off', as displayed in Figure 2-23. (The lower solubility limit is denoted by C_s.)

In this context, the best description of NPs generation as two distinct phase system is provided by LaMer mechanism [71,72]. In this mechanism, there are three conceptual stages, as illustrated in a plot of a hypothetical monomer concentration *versus* time as shown in Figure 2-23A. (Here the term monomer denotes to the reacted hydroxylated iron species that are unstable and capable of forming and/or adding to NPs spontaneously). The three stages include: (i) production of the monomer and its concentration increase to nucleation cut-off level, however no solid phase is present so far, (ii) the concentration of monomer continues to increase to a level of critical supersaturation at which the creation of nuclei will be energetically favourable, and hence particles nucleation is instantaneously induced in a process often called 'burst-nucleation, and (iii) a considerable decrease in the available reactive monomer in solution continues within equilibrium state to a level that approaches the lower solubility limit (C_s)

so that not only particles nucleation was supressed, but diffusion-controlled particles growth is also quenched.

An upgrade on the above classical LaMer model was introduced by Vreeland *et al* in 2015 [73] and illustrated in Figure 2-23B. This modification is called 'extended LaMer mechanism' in which an open system is considered and hence continuous feeding of iron precursors is achieved. This is in contrast of what is proposed by LaMer, where a proposed closed system consequently limits available monomer. In the extended LaMer mechanism both of stage (i) and (ii) match the corresponding stages of the classical proposal, while stage (iii) diverges because continuous production of monomers is allowed. Although the concentration of monomers declined below the initial peak level that is required for nucleation to proceed (nucleation cut-off), exhausting the monomer availability during nucleation event to approach the lower solubility (Cs) is prevented. This compensation will maintain the quantities of the reactive species within the equilibrium solubility range. Accordingly, an additional stage (iv) is introduced in which the formed particle undergo size enlargement via diffusion-controlled growth mechanism over specified timeframe.

The main advantage of the extended LaMer mechanism is that the well-known mechanism of size distribution formation, Ostwald ripening [74-76], is avoided and hence particle with low size dispersity will be produced. In more detail, in the classical LaMer mechanism, the amount of monomer in stage (iii) continues to deplete to the extent close to Cs. At this point no further particles growth will occur by monomer diffusion and/or attachment to the surface of existed particles; instead, the Ostwald ripening mechanism will dominate in order to keep the system thermodynamically stable with least surface free

energy, thereby larger particles will grow at the expense of smaller ones. Finally a particles population with wide size distribution will result [77].

Appreciating both classical and extended LaMer mechanism, the fabrication equipment used in this work was developed to produce inorganic NPs, USPIONs. The design of the equipment was such to allow for manipulation of parameters controlling the particles nucleation and growth.

As illustrated in Figure 2-1, the Y-junction at which the reactant materials are combined, represents the zone of reaction where the 'burst nucleation' occurs while the rotating disc over which the newly formed particle nuclei are spread stands for the zone where the particles growth proceeds. In order to convert this design to the schematic in Figure 2-23C, stages I and II corresponds to the event occurring in Y-junction zone, while the line of particles growth in stage (iii) is what is occurring over the surface of spinning disc.

The main difference in the Figure 2-23C diagram includes an immediate and sharp decline in the available monomer from a micro-environment region due to constant release of the combined mixture out from the Y-junction to be spread over the rotating disc. Therefore, the normal stage (iii) (present in both 23A and B diagrams), in which a gradual reduction of monomer concentration occurs has disappeared in this equipment design. The advantage of this situation is a generation of highly uniform and constant number of nuclei resulting from instant decline in reactants concentration, which in turn leads to 'freezing' of the nucleation event [78]. Therefore, this creates a good preface for consistent particles growth in the following stage, as clearly illustrated in stage (ii) in figure 2-23C. Additionally, the stage IV in the equipment design does not actually correspond

that of extended LaMer mechanism (Figure 2-23B); instead, it is standing for abrupt and precise point of growth phase termination which occurs once the rotating spinning disc ‘throws’ the ‘descending’ particles outwards into the space of the of housing vessel due to acting centrifugal motion. It should be mention that this design can be considered as an open system, as there is still continuous addition of free monomer injected along with the formed nuclei.

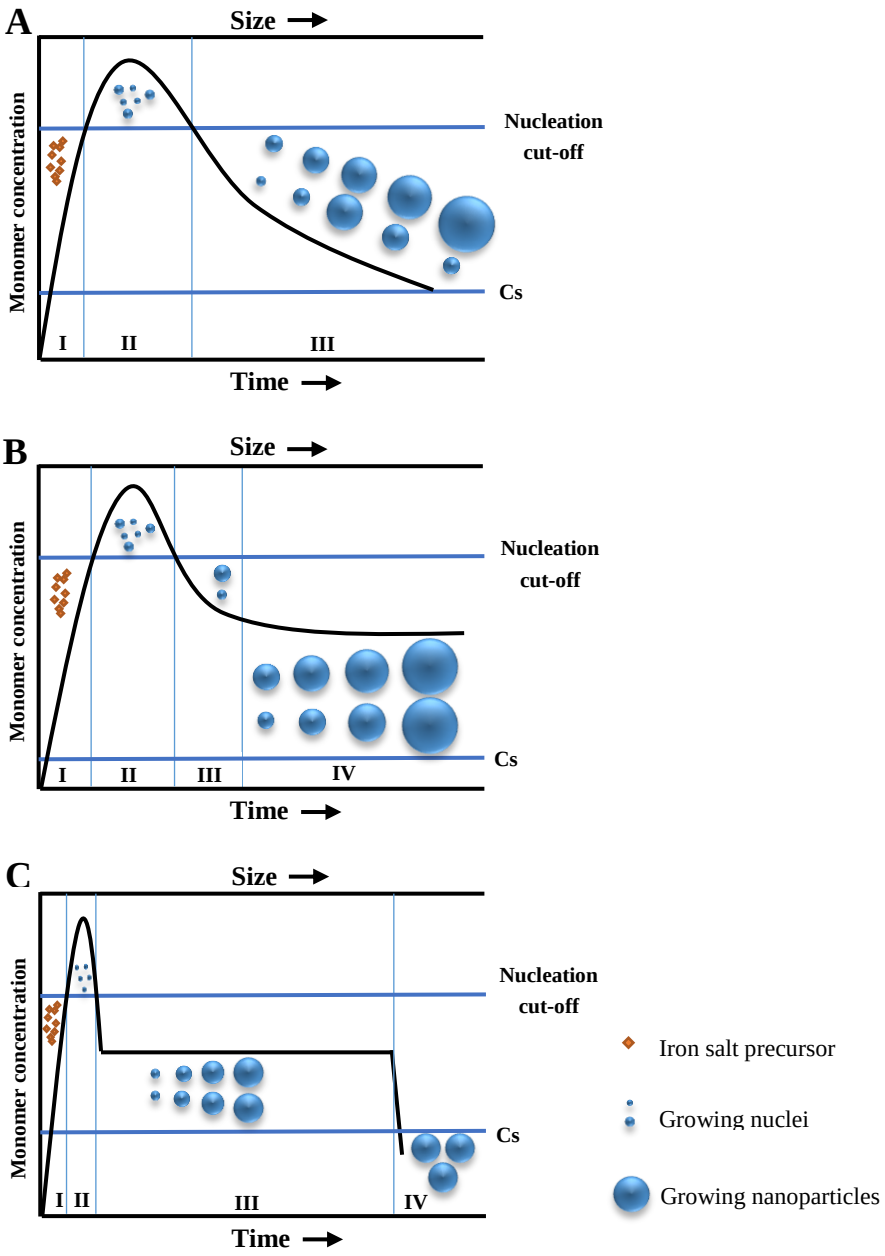


Figure 2-23: ***Schematic illustration of NPs nucleation and growth.*** ***(A)*** *An explanation of classic LaMer mechanism for NPs growth in which stage I represents the monomer concentration increase up to the critical supersaturation concentration (nucleation cut-off), stage II is nucleation event in which reactants concentration start to relieve, stage III is the phase where growth event take place. Under condition of limited availability of free monomer, their concentration continue to reduce until approach the lower solubility limit (Cs) and further NPs growth proceed by Ostwald ripening.* ***(B)*** *Extended LaMer mechanism for NPs growth proposed by Vreeland E. C. et al. Stages I and II mimic the classic LaMer mechanism. In this case, monomers concentration in Stage III does not approach the solubility limit but are gradually stabilised at certain steady-state level below the nucleation cut-off. Stage IV is the extension of stage III where the continuous feeding of free monomers ensure uniform NPs growth along with size distribution.* ***(C)*** *The proposal of creating a physical separation of nucleation zone form NPs growth field. Stage I is similar to the aforementioned both mechanisms. Stage II is shorter and more uniform burst nucleation due to constrained environments. There is no corresponding stage III as a result of the proposed physical barrier. Therefore the stage III in this situation is equivalent to stage IV of the previous assumption in which short period of continuous monomers feeding and intermediate particles colliding is proposed. This stage ends with releasing of USPIONs to the collecting vessel that is represented in stage IV wherein no additional growth occurred because the concentration of reactant materials are below the lower solubility limit (Cs).*

2.4.3 Reactant injection into confined zone of nucleation

To further expand on the above proposed principle that an interval exists between the nucleation and growth stage, which is vital in controlling the particle size and size uniformity, the importance of the way reactant materials are introduced into a confined zone will be briefly discussed.

One of the pioneering applications of flow injection strategy was performed by Wang and Muhammed in 1999 [41]. They fabricated zinc oxide NPs via designing a system that consisted of T-shaped manifold in which the streamed reactants were combined and passed through carrier channel reactor. They also installed valves on the path of reactant stream to create constant time intervals of flow interruption upon closing them. Their way of controlling NPs size and morphology was to throughout the process restrict Ostwald ripening mechanism. This system was further modified by Salazar-Alvarez et al in 2006 [79] for preparation of iron oxide NPs where peristaltic pumps were added to adjust the rate at which the reactive materials flow. In that upgraded system, different flow patterns were proposed: continuous and segmented, with and without insertion of interrupting medium, in addition to the capability of switching from one reactive reagent to another. These flow modes were driven by two kinds of computer-operated valves including on-off and switching valves.

It is important that efficiency of materials mixing in the case of continuous mode of flow is lower than that of segmented mode. This is because the movement of materials close to tube wall is slower than in the centre of stream which in turn leads to the reduced uniformity of free monomers dispersion and increase in the local residence time of nuclei at boundary of the main stream, as shown in Figure 2-24A. This will generate so-called ‘parabolic’ fluid velocity

style in which diffusion and axial and/or laminar flow dominate as a way of mixing. Accordingly NPs with wide size distribution are expected as a result. In contrary, interrupting reactant streams will result in absence of such pattern of fluid flow and hence segmentation in flow will create so-called 'slugs' containing reactive monomers separated by either gas or inert medium. The travelling of 'slugs' in the channel reactor generates recirculation movement and convective flow rather than axial and/or laminar flow which in turn drive monomer and nuclei mixing resulting in highly uniform growth and hence size distribution [36,38,44,80-82] as illustrated in figure 2-24B. It is worth noting that under the same applied condition, the yield of NPs in continuous injection is higher than of segmented injection because of flow interruption, however, a trial to develop a multi-tubular reactor having continuous segmentation in flow has been reported to scale-up the product [42].

It is important to mention that both of continuous and segmented flow methods are established for NPs fabrication, depending on stages of particles nucleation and growth. Normally the channel reactors installed are sufficiently long to support the growth of NPs as the freshly formed nuclei are passing along. However, the variation in fluid dynamics, illustrated in figure 2-24A and B, does not occur in the case in our design - as the length of the projected tube beyond the Y-shaped junction does not allow the formed nuclei to grow, instead the growth stage occurs later in separate part of the equipment - represented by the SDR.

Therefore, in the present design, the uniform nucleation results from two sub-stages. The first stage represents the initial turbulent mixing and vortex formation at the point where the reactant streams are combining to allow creation

of uniform ‘embryos’, and this is equivalent to what is happening in both continuous and interrupted flow. The second stage, the development of ‘embryos’ into larger nuclei occurs *via* another steady-state turbulent flow process in which convective mixing with free monomers leads to mass transfer and circulation. This occurs when the mixture of suspended species is released from the junction exit to form a drop of liquid (figure 2-24C). The second, weak turbulence at this point originates as a result of nozzle-like effect by which the forced volumes of two streams merging into one stream creates a short-lived internal pressure, which is then spontaneously removed upon the liquid drop ‘release’ through the orifice. The slight fluctuations in pressure have significant effect on the inner mass movement within the formed droplet, whereby the orifice at the exit point applies an effect that mimics that of a nozzle [83]. The pattern of mass circulation within the released liquid drop is in a clockwise and counter-clockwise directions, as illustrated in figure 2-24C. Finally, at the point of drop release, an even mixing will occur due to both continuous and segmented flow.

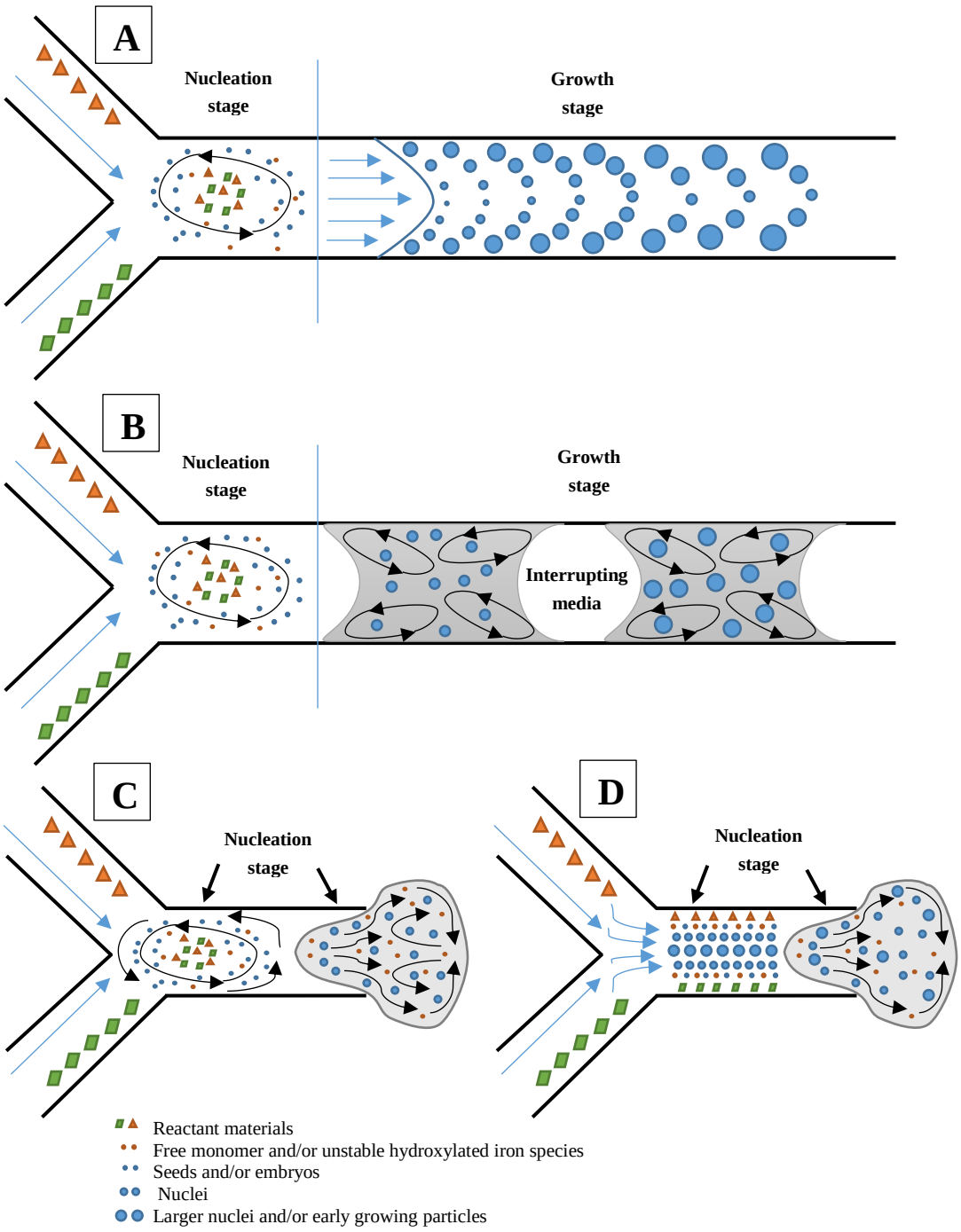


Figure 2-24: ***Schematic of injection flow synthesis****.* ***(A)*** *The continuous flow system synchronously combine reactant ▲ and ■ in one main stream. The point of combination is considered to be the nucleation region while the following extended channel reactor is the field of NPs growth as properly denoted. NPs in this system undergo non-uniform growing due to parabolic liquid flow.* ***(B)*** *The segmented flow system for NPs synthesis is similar to the continuous system in regard to nucleation event. However, the growth of NPs take place within segment of liquid mixture separated by inert medium of liquid or gas. In this case the material mixing is completely different from the former design leading to increase particles size uniformity.* ***(C)*** *Both of the reactants are continuously injected toward Y-shaped junction resulting in the same nucleation event as in (A) and (B). The proposed design in this case prevents NPs from growing. Therefore, intensive burst nucleation may occur as a result of high flowrate, 60 ml/min, and liquid drop release. This is in contrary to the assumption* ***(D)*** *in which diffusive mixing dominates the turbulence due to the low flowrate, 30ml/min resulting in reduced uniformity of nuclei size and unwanted primary growth may take place.*

2.4.4 The role spinning disc reactor (SDR) as a space for NPs growth

Giving that the nucleation event was performed in a three-dimensional confinement zone within a junction in which the flowing reactants were simultaneously brought to contact, the SDR was installed to be the space (vessel) in which the growth of formed nuclei progressed.

The principle aim of inserting such disc is to create a space for uniform and efficient product mixing at micro-level, so called 'micro-mixing' [84-86]. By rotating the disc, a centrifugal and shear forces are generated to allow radial spread of thin film of liquid media throughout the spinning disc [87]. The ultimate objective of this situation is to approach a state of 'plug flow' regime of material dispersion within the thin film formed [88]. The 'plug flow' ensures, firstly, an even density of interactive species i.e. building blocks (free monomer and meso-stable intermediate primary particles) in the micro-environment surrounding larger, stable nuclei and, secondly, a similar exposure time of these nuclei to their micro-environment during growth period and hence. This might lead to more uniform particle size distribution.

In relation to SDR properties, the surface texture was designed to be either smooth or grooved, as illustrated in Figure 2-25 (A-D). Testing smooth surfaces showed that they have favoured flow pattern similar to that of rivulets, which in turn results in non-uniform mass transfer and discontinuous waves [89,90]. On the other side, the grooved texture supports thinner film flow with more steady and continuous waves and ripples and hence effective mass transport may be expected [85,91,92]. In literature, these differences in hydrodynamic characteristics

of the liquid flow are well reported, and 'work' in favour of grooved surfaces for reducing particles size and narrowing size distribution [93-96].

In present study, we have used a 3D-printing technology, to fabricate a funnel-like disc. In this geometry, the freshly formed nuclei and free monomers and/or meso-stable intermediate primary particles were released from Y-shaped junction directly onto the central point of the disk (Figure 2-25D). We believed that deposited material rotates in a circular orbit of the printed grooves due to the influence of centrifugal force. The orbiting species were noticed to continuously roll in the grooves promoting the particles growth.

Regarding NPs growth, there are two proposed scenarios that could mainly be applied. First assumption refers to the classical theory of NPs ripening as a major mechanism. In essence, this scenario states that the nucleated crystals grow by surface diffusion and integration of unstable precursor (free monomers (Fe_3O_4 units) or hydroxylated metal aquo-complexes) [97,98]. The second scenario relies upon an increasingly supported proposal of that NPs may grow *via* accretion (deposition) of sub-nanometre intermediate primary particles (in their meso-crystal and quasi-hydrated state) [99-104] on the outer surfaces of the original nuclei.

In the present experimental design, the size uniformity of growing nuclei was promoted due to 'controlled' aggregation of metastable species and nuclei under intense micro-mixing [86,105,106], achieved by both actions of shear and turbulence in the thin liquid film flow. We thought that a shearing effect [107] arises during NPs orbiting in the circular grooves, while the turbulence [95,108,109] develops upon 'jumping' of the accelerated particles to the next, further orbit

(grove) that has higher level of centrifugal force and so on, until the SDR edge is approached, as illustrated in Figure 2-25 D.

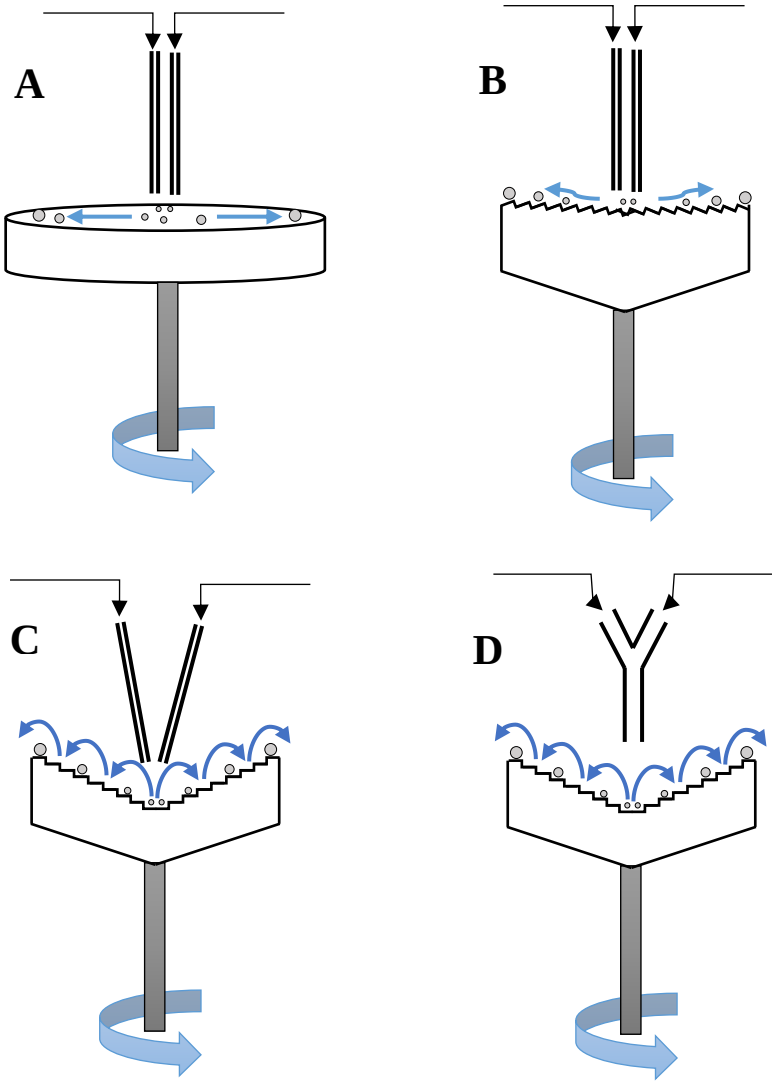


Figure 2-25: ***Cross sectional view of spinning disc reactor (SDR) with different designs.*** *The liquid movement regime varies from irregular ripples and discontinuous film to more ordered waves due to the grooves that have been introduced into the surface texture of disc reactor as in* ***(A)*** *and* ***(B)*** *designs respectively. Enhanced mass transfer was attained by further changes in the design of disc reactor where more turbulence has taken place as a result of NPs jumping over circular orbits of the added trenches as in* ***(C)*** *design. The zone at which nucleation event was physically separated from NPs growth field via combining reactant precursors inside a Y-shaped Junction before spreading the mixture over SDR as in design* ***(D)*** *where strict control of the process could be achieved. Here, in all previous designs both nucleation and growth events were occurring over SDR.*

2.4.5 Effect of BISS flowrate on particles size, size distribution, polydispersity and circularity

In order to investigate the effect of different flowrates on size uniformity, the lowest SDR speed, 150 rpm, was operated where the effect of rotation is at minimum level. In our results, the significant improvement in NPs polydispersity is achieved upon increasing the reactant flowrate, and was first attributed to the narrower timeframe available [110] and a better initial mixing at the point of bringing the reactants into contact. In case of using higher flowrate, 60 ml/min, an increased turbulence in flow at two different positions is believed to be the reason of 'burst nucleation' which is necessary for production of monodispersed particles population [111]. Also the nozzle-like effect created when the droplet is released from the junction exit (as discussed above) plays an important role in intensifying the nucleation stage.

At a slower flowrate, 30 ml/min, the situation is different due to critical differences in micro-mixing regime and 'local residence time distribution' (LRTD). In this context, the effect of turbulent mixing is dominated by laminar mixing in which the slow diffusive movement of free monomers and 'embryos' is the major driving force of mixing. It is well-known that the effectiveness of turbulence is much higher than that of diffusion in mixing material mass. Therefore, as illustrated in figure 2-24D, it can be assumed that the early formed 'embryos' first start to appear in the centre of main stream, where the interphase between the two reactants exist, before this occurs at the boundaries. Herein, the laminar and diffusive mixing, along with relatively prolonged period of nucleation (due to slower flowrate) is considered to allow the polydispersity of particles to propagate [111]. In the view of the latter aspect, broadening in LRTD

is expected to augment the polydispersity, owing to marked discrepancy between the residence time which is spent by the materials located in axial region of the main path (centre) and that in boundary flow areas close the junction tube wall. However, it is worth mentioning that for processes with longer reaction period, the impact of LRTD becomes negligible [112]

It important to discuss that this inconsistent nucleation may either increased or decreased, according to the conditions of the growth stage, as we will illustrate. For instance, PDI values of 0.1953 and 0.0775 are recorded for NPs prepared using flowrates of 30 ml/min and 60 ml/min, respectively, as summarized in table 2-1, which is in agreement with the trend of polydispersity data for TiO_2 NPs in a previous study [96]. Moreover, our data in Figure 2-4, obtained from frequency size distribution curves, provide an additional evidence for uniformity in particles diameter distribution, as the difference between median and mode values are notably decreased from 2.97 nm (6.38 – 3.41 nm) to 0.18 nm (9.08 – 8.9 nm) for lower and higher flowrates, respectively.

There is another possible reason of broadening of particle size distribution, 'Ostwald ripening'. Although this mechanism may not play an important role during the particles growth on the SDR, as will discussed later, its influence is still important on the ultimate particles size. This means that the triggering factor for Ostwald ripening to occur is the deficit in 'building blocks' required for particles growth. Therefore, at a slow material flowrate, 30 ml/min, the shortage of free monomer available on SDR for NPs building may be a decisive factor in the particles formation and size. Increasing the flowrate will lead to an increase the amount of both free monomer and intermediate particles required for NPs enlargement. Accordingly, either diffusion- or coagulation-controlled growth of

already formed NPs on the rotating disc will result. Consequently average particle sizes of 6.93 nm and 9.21 nm are obtained for USPIONs prepared using slower 30 ml/min and faster 60 ml/min flowrates respectively, as displayed in Figure 2-5. These results are in agreement with particles size data obtained in synthesis of functionalised silver NPs, copper oxide NPs, and magnesium hydroxide and oxide NPs [82,113,114], but in contrast to the reported data of titanium oxide NPs sizes [96].

The low particles circularity of USPIONs obtained for the all tested batches in this experiment may be mainly ascribed to the low rotational speed of SDR used in their fabrication, 150 rpm. However, the somewhat improved particles circularity noticed in Figure 2-6 may be attributed to the steadiness in the availability of total quantity of NPs at every moment in every local region of the SDR where the highest flowrate maintain greater balance between the rate of releasing of metastable species (free monomers and primary particles) from the Y-shaped junction and the rate of radial spreading of growing NPs across the SDR. Therefore, as the reactants were streamed faster, more uniform distribution of materials over the SDR surface could have been achieved, and hence improved particles circularity distribution. Values of 0.596, and 0.734 were calculated for both 30 and 60 ml/min, respectively.

2.4.6 The effect of SDR rotational speed on the particles size, size distribution, polydispersity and circularity

Regarding the results obtained, it is noticeable that the particle size was significantly reduced upon increasing spinning speed, for both the highest and the lowest flowrates used. The major reason for that may be due to the fact that

the time available for the particles growth is reduced as the SDR is increased [81]. In addition, a more detailed analysis of the process would indicate the following. According to the non-classical hypothesis of particles growth, increasing rotational speed will reduce the opportunity for intermediate primary particles to attach and integrate with the surface of bigger nuclei, therefore, the rate of coagulation-controlled particles growth will be significantly reduced. On the other hand, if we consider the classical theory of diffusion-controlled growth, the process of surface diffusion of free monomers in the system is increasing by the impact of centrifugal force [115-118]. Although the latter applies, the resulted particles still experience reduction in size. This may be because the influence of molecular diffusion on particles growth is relatively lower than that of the surface growth due to coagulation-controlled growth. This may be illustrated in the fact that at the slowest rotational speed, 150 rpm, TEM determined average particle size was 6.93 nm and 9.21 nm, for 30 and 60 ml/min flowrate, respectively, while for the fastest disc speed, 2400 rpm, the average TEM diameters were 3.93 nm and 6.05 nm, for both highest and lowest flowrates, respectively, as displayed in Figure 2-8. The comparable trends of NPs size reduction were reported in the literature [84,96,113,114,119-121].

It is important to mention that NPs prepared at 60 ml/min flowrate and rotational speeds of 600 rpm, 1200 rpm and 2400 rpm did not show significant particle size changes, where the values of 5.96 nm, 5.84 nm and 6.05 nm were recorded, respectively. It may be proposed that under these fabrication conditions a state similar to that of 'plug flow' was maintained due to a constant and continuous displacement of NPs quantity *per* unit time above the defined area of SDR, as suggested previously [87,95], which offers a greater uniformity in

a degree of solid and liquid phases movement (transverse and radial) extended from central point of rotating disc towards its periphery, i.e. periphery of the growth zone [86,90]. In order to illustrate this situation, one can presume two hypothetical variables: of 'mass input' (mass of materials added *per* unit time to the SDR) and of 'mass output' (mass of materials leaving the SDR *per* unit time), at certain flowrate and rotational speed, respectively. If the mass input is higher than mass output, an accumulation of building material/blocks on the SDR over the time will occur (figure 2-26 A and B) and consequently an increase in NPs size can be expected [78]. On the other hand, when the mass of material leaving SDR from its periphery exceeds that of material addition to SDR, then discontinuation of the process will occur (figure 2-26 C) and consequently a reduction in particle size will be seen. Accordingly, a combination of higher flowrate and spinning speed could mainly offer smooth and continuous mass input and output, as illustrated in figure 2-26 D.

Data for size polydispersity in table 2-2 illustrate a considerable improvement in PDI values upon accelerating the rotational speed of SDR, particularly in NPs batches prepared by using 30 ml/min. To explain this observation, it was well-established that the origin of broadening size distribution is 'Ostwald ripening'. The environment that potentiate this process is the deficiency in amount of free monomers available for diffusion-controlled growth to proceed. Therefore, as a compensatory mechanism, smaller particles start to 'shrink' (dissolve) to act as a source of free monomers for growth of larger particles. In the present study this becomes increasingly obvious once the free monomer feeding rate was reduced, especially at slower disc speed (Figure 2-26 A). When the SDR speed was increased (Figure 2-26 B), the micro-mixing

process (shearing and turbulence) became more efficient, where the liquid film over SDR becomes thinner an in that way reduces the time for complete molecular dispersion [84]. Therefore the micro-environment surrounding each nuclei ensures a uniform availability of monomers at every moment and every region of the disc, which in turn produces an even NPs growth. In addition, a shorter period of growth significantly reduces the opportunity of 'Ostwald ripening' to occur. On the contrary, the process of 'digestive ripening' is expected to occur. The latter process depends on the principle of that the growing of smaller particles is faster than of larger ones, which will produce more uniform NPs population. In conclusion, inhibition of 'Ostwald ripening' and promotion of 'digestive ripening' will result. Accordingly, PDI values are reduced from 0.1952 to 0.0795 when the rotational speed is increased from 150 rpm to 2400 rpm, respectively. Similar reduction in size polydispersity was reported for preparation of Titanium oxide, zinc oxide and barium sulfate NPs in the previous studies [84,96,108].

At both running flowrates, 30 ml/min and 60 ml/min, an improvement was noticed in circular morphology which is attributed to the acceleration in rolling of NPs within their orbits by means of increasing SDR speed. Therefore, the degree of circularity was increased from 0.596 up to 0.806 and from 0.734 up to 0.846 upon using lowest and highest flowrates and increasing disc speed from 150 rpm up to 600 rpm respectively as illustrated in Figure 2-9. Nonetheless, further speeding of SDR beyond 600 rpm showed no upgrade in particles circularity. The reason may be, at that level of faster spinning, the aggravated agitation and turbulence during thin film mixing will minimise the effect of rolling on developing NPs with higher degree of circularity.

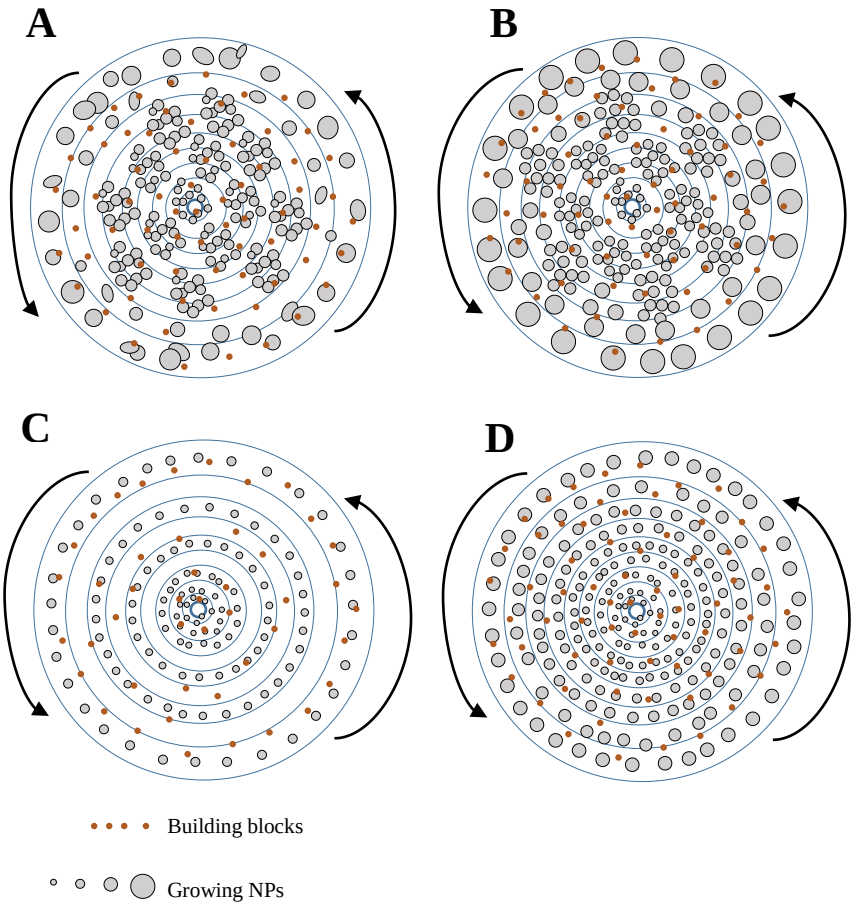


Figure 2-26: ***Schematic illustration of dual effect of reactant flowrate and rotational speed of SDR on NPs size.*** *Within the spectrum of present study and distribution uniformity,* ***(A)*** *Relatively large NPs with wide size dispersity were gained by using slow flowrate (30 ml/min) and disc rotational speed (150 rpm).* ***(B)*** *Larger size and tight dispersity resulted from increasing flowrate up to 60 ml/min with keeping disc speed at 150 rpm.* ***(C)*** *Smaller NPs with uniform size distribution were obtained upon accelerating spinning speed up to 2400 rpm while the flowrate is 30 ml/min.* ***(D)*** *similar value regarding size uniformity as in (C) has been obtained but with larger as a result of increasing reactant flowrate up to 60 ml/min. The efficiency of liquid and mass mixing were achieved after disc speed was accelerated as in (C) and (D).*

2.4.7 The effect of SDR size on the particles size, size distribution, polydispersity and circularity.

The third physical variable in preparation of USPIONs that we have tested includes the use SDR with larger diameter. Interestingly, particles size and size distribution data showed no significant change when using LSDR, where the effects are clearly evident for operating flowrates. In this case, the LSDR will provide an increased magnitude of centrifugal force at the disc periphery [122,123], in comparison with SSDR revolving at the same speed. If we consider a growing metal NPs as heavy mass circling around an axis of rotation, then the amount of centrifugal force could be calculated according to the following expression [124]:

$$Centrifugal\ Force\ (F) = \frac{Mass\ (W) * (Tangential\ Velocity\ (V))^2}{Radius\ (R)}$$

Where $Tangential\ Velocity\ (V) = (\frac{Disc\ Circumference\ (C)}{Time\ (t)})^2$

$$Time\ (t) = \frac{1}{rpm} \quad \text{and} \quad Disc\ Circumference\ (C) = 2 * \pi * R$$

The higher magnitude of tangential velocity (V) at the edges of the LSDR [125] will lead to an increase in the force applied on NPs which in turn functions to enhance mass disintegration and hence reduction in particles size will be expected [123]. One can hence envisage that the meso-stable, intermediate primary particles adhered to the NPs surface and yet to be fully 'fused' because of their quasi-hydrated state, they will be highly vulnerable to detach from NPs surfaces on increased applied force. If this is not the case, then they should undergo further contraction and merging as a result of water loss during olation/oxolation bond formation while the process of growth continues [126]. Accordingly, we believe that the 'atomising effect' [123,127-130] of the higher centrifugal force works

in parallel with coagulation-controlled growth previously described, leading to cancelling out any significant changes in particles size. As an example, the average size of USPIONs prepared at 1200 rpm rotational speed and 60 ml/min flowrate are 5.80 nm and 5.84 nm for LSDR and SSDR, respectively. The similar was observed for the lowest flowrate, 30ml/min, and spinning speeds, 600 rpm and 2400 rpm, as displayed in Figure 2-10 and 2-11.

Consistently with the above results and their rationalisation, the fluctuation in polydispersity values when using LSDR further augment the ineffectiveness of employing increased SDR size in improving the quality of NPs. Data related to rotational speed of 600 rpm showed deterioration in NPs size uniformity index from 0.0888 to 0.1156 for 30 ml/min flowrate when SSDR replaced with LSDR. Similar worsening in PDI is seen when using 2400 rpm, while the situation is opposite in the case of 1200 rpm spinning speed. The similar variations are seen using 60 ml/min flowrate, for all rotational speed tested. In this regard, an additional explanation might be presented. A 3D computational modelling performed by Bhatelia TJ *et al* [131] to calculate the liquid film thickness over SDR has revealed that film thickness reduces along the radius of the spinning disc as the rotational speed increased. Once the film thickness reduces to a certain limit, a collapse in liquid layer starts to appear, especially in a region close to disc perimeter - as a result of centrifugal force increment. Enlarging disc size will exacerbate the liquid film and ripples instability and discontinuity, because of an additional centrifugal force and film thickness reduction [122,132]. The break in liquid layer over the rotating disc will produce irregular micro-mixing and microenvironment around NPs and therefore, uneven growth rate may be anticipated.

The circularity of USIPONs fabricate using LSDR showed deterioration in their values. One could suggest that this may be due to an increased liquid film deformation, due to enlarging the SDR, including discontinuation and thickness variation which play a crucial rule in particles circularity - where inconsistent local pressure may arise especially at the disc periphery. In addition, the aforementioned competition between NPs coagulation-controlled growth and disintegration, along with variations in local pressure, may give rise to instant oriented coalescence of primary particles at one face of NPs, on the expense of other faces. It was also noticed that the circularity decline was intensified at highest spinning speed, 2400 rpm, at which the 'aggressive' conditions are expected due to a high speed and forces applied. Here, the recorded values are 0.688 and 0.799 for the LSDR at 30 and 60 ml/min, respectively while for the small SDR, circularity values of 0.847 and 0.843 were observed. As mentioned before, the circularity range was reduced at slower rotational speed due, to lower level of 'aggressive' conditions. For example, at 1200 rpm and 30 ml/min, values are 0.751 and 0.796 for the LSDR and SSDR, respectively, as illustrated in Figure 2-12.

2.4.8 The effect of total iron amount (TIA) in the BISS on the particle size, size distribution, polydispersity and circularity

The first chemical factor to discuss is the increase in both ferrous and ferric ions amount (mass) present in the fixed volume of aqueous solution used in the USPIONs fabrication. The data obtained here reveal its significant proportional impact on particle size ($p < 0.001$). It is well established that the kinetics of a reaction is strictly related to the amount of reacting materials [133,134], especially

during a primary nucleation event in which higher level of supersaturation is expected to be maintained [109].

Given that the nucleation event in our design occurs within highly limited period of time and in a confined zone, the higher reaction rate (due to higher mass of the reactants) will result in creation of a higher number of metastable primary intermediate particles along with nuclei [135], at the expense of a lower amount of free monomer. Therefore an order of interacting species population of primary intermediate particles > nuclei > free monomers may be present, and hence, an increasing density of particles (in a certain volume) are available once the mixture was released onto the spinning disc. In more details, at total iron salt amount lower than 0.75 moles, the both proposed mechanisms of aggregation (coagulation)-controlled and diffusion-based growth are allowed to function simultaneously towards producing larger NPs, with possibly some dominance of the first mechanism (aggregation-controlled growth) [126,136]. This is because there is still a balance among the aforementioned factors. As the TIA of BISS was increased above 0.75 moles, conditions for enhancing growth retardation [137] will be highly favourable in which extreme depletion in free monomer and, to less extent, primary intermediate particles are presumed in favour of increasing number and size of embryos and/or nuclei due faster reaction kinetic. Therefore, another order of building species population is assumed: nuclei > primary intermediate particles >> free monomers. The change in the postulated order is thought to be due to intensification in the very initial stage of nuclei growth (short-lived growth) that arises from rapid diffusion and surface-integration and/or reaction processes [70,98]. As a consequence, once the slug spreads over SDR, the high number of formed, bigger nuclei experience the regular growth

stage – however at a slower rate due to other building blocks (primary particles and monomers) exhaustion [137].

Regarding our results, increasing the total iron amount from 0.25 to 0.75 mole have increased the average USPIONs particle size by approximately 3 nm, from 4.26 nm to 7.17 nm, while the size gain is only 0.28 nm, to 7.44 nm, upon further doubling the iron amount in binary-solution to 1.5 moles (at rotational speed and flowrates 2400 rpm and 60 ml/min, respectively), as illustrated in Figure 2-14. The data hence support the proposal that an equilibrium exists between processes occurring in the nucleation and that in the growth, and these could explain the reason of the negligible size increase noticed at the latter fabrication conditions. Similar trend is obtained using operating spinning speed of 600 rpm. The trends of these results are in agreement with the literature [79,113,114,138].

An increase in TIA present in USPIONs fabrication resulted in narrower size distribution. This is particularly evident at rotational speed of 600 rpm, in comparison to 2400 rpm at which particle size does not significantly change over the tested range, illustrated in table 2-4. The low PDI values noticed when using the highest TIA of BISS, 1.5 moles, are attributed to very fast initial reaction rate, along with a subsequent early construction processes of sub-nanometre intermediate primary particles, embryos, and nuclei. Moreover, if we take into consideration that there is extremely limited time for nucleation to occur, as a result, highly uniform nuclei should be created which in turn grew to uniform NPs population. To illustrate, readings of 0.0913 and 0.0674 PDI are recorded for 600 and 2400 rpm spinning speeds respectively when 1.5 moles of TIA was

used, whereas PDI values are 0.1386 and 0.0664 for the same speeds, respectively when reacting 0.25 mole of TIA.

The circularity degree of all USPIONs batches fabricated generally showed no significant changes when the total TIA of BISS was increased. This trend could be understood according to the above discussion whereby the related conditions, including rotational speeds of 600 and 2400 rpm and flowrate of 60 ml/min, are capable of fabricating particles possessing high levels of circularity. This gives an indication on how much the applied variables are capable of effectively maintaining the circular morphology of NPs produced within the range of 0.801 – 0.866. The only exception in our case is the considerable deterioration in the circularity of NPs prepared using highest amount of iron, 1.5 moles, at 2400 rpm rotations speed where value of 0.747 was obtained, as displayed in Figure 2-15. This might be explained as a consequence of a congestion that may arise from overloading the SDR with high amount of interacting species.

2.4.9 The effect of Fe^{+2}/Fe^{+3} ratio on the particles size, size distribution, polydispersity and circularity

The role of ferrous ion is expected to be mainly related to nucleation stage of USPIONs fabrication, particularly in the current fabrication set up. For constructing Fe_3O_4 units, at pH medium high than 8.0, the very initial solid phase of ferric hydroxide undergoes a process of dissolution-recrystallization in which the divalent iron ions are coordinated [139] and involved to form a metal oxide polymer [62,63,121]. This event occurs through three complementary processes: 1) combination of ferrous aquo-complexes with ferric complexes, 2) bridges and bond formation via olation/oxolation mechanism leading to water elimination

and dehydration, 3) crystallisation and structural rearrangement [140-143]. In order to describe the process, these steps are considered to be repeated in a cycle so the early (first) cycle results in appearance of Fe_3O_4 units which undergo a grouping with similar units to trigger another cycle. As the process of iron (II) sequestration continue, more condensed product (iron oxide) will result [144], which will result in a construction of intermediate seeds and nuclei. Therefore, increasing the amount of Fe^{+2} will lead to a formation of larger nuclei at the expense of their number. With this in mid, it is believed that any further growth of nuclei should occur *via* surface adsorption and attachment of smaller species and hence additional cycle of dissolution-recrystallization is required. In addition, the presence of both Fe^{+2} and Fe^{+3} provides a redox pair in which the electron transfer and hopping occur through overlapping d-orbitals. For that reason, this electron-delocalisation will enhance structural rearrangements towards more energetically favourable and ordered crystalline structure and hence intensify initial growth process of nuclei. Ultimately, increasing the Fe^{+2}/Fe^{+3} ratio results in a production of USPIONs of larger size, due to presence of lower number of nuclei with increased size. It is important to mention that changing the Fe^{+2}/Fe^{+3} ratio might play an indirect role in the mechanism of NPs growth occurring over rotating SDR, which may be markedly different from its role in the very initial growth stage of nuclei.

Considering our results, the average particle size of USPIONs, prepared at 2400 rpm spinning speed, 60 ml/min flowrate and 0.75 mole TIA, showed a highly significant reduction ($p < 0.001$) from 7.172 nm to 5.04 nm when the Fe^{+2}/Fe^{+3} ratio was decreased from 0.66 to 0.5. TEM and DLS data of all the other tested NPs, prepared under different conditions of rotational speed and

TIA, affirm the above observation on the particle size reduction upon changing ferrous to ferric ratio, as illustrated in Figures 2-16 and 2-17. These data are in agreement with those reported in the literature [145-149].

The values tabulated in Table 2-5 show absence of apparent trend towards either narrowing or broadening of particle size distribution when the Fe^{+2}/Fe^{+3} ratio was changed. At 600 rpm spinning speed, there is noticeable reduction in PDI values from 0.1260 to 0.0909 for 0.375 mole and from 0.1012 to 0.795 at 0.75 mole TIA when reducing the Fe^{+2}/Fe^{+3} ratio from 0.66 to 0.5, respectively. Contrary results were obtained when 1.5 mole total iron was used. In general, at 2400 rpm spinning speed, PDI values have not changed for all TIAs and Fe^{+2}/Fe^{+3} ratios, which is another example on inconsistency in PDI data trends. It is beyond the scope of present work, to further study and provide a clear explanation for the above results. The present set of data more than one variable controlling the outcome are changing. However, in general, a reduction in ferrous to ferric ratio, along with increasing the TIA, may play a major role in shaping the relationship between rate changes of both iron precursors reaction and Fe_3O_4 network formation. As a result, a different pattern of nucleation may take place, especially if we take into account the environment that confined zones and SDR may provide.

Alterations in circularity degrees show similar pattern to that of PDI, where the change is controlled by a simultaneous effects of both, TIA and Fe^{+2}/Fe^{+3} ratio. This may prove an additional evidence to the above suggestion. Using rotational speeds of 600 and 2400 rpm, it was found that circularity of NPs prepared using 0.375 and 0.75 mole of total iron was reduced with a decrease in Fe^{+2}/Fe^{+3} ratio, while no reduction was observed when the TIA of BISS is

increased to 1.5 moles, as illustrated in Figure 2-18. Therefore, further studies on a degree of crystallinity might be beneficial in constructing a more detailed rationalisation.

2.4.10 The effect of reducing alkaline medium strength on the particle size, size distribution, polydispersity and circularity

It is extensively reported in the literature that high pH of the reaction medium (especially pH > 8) could function as a precipitating agent for iron oxide [62,63]. Therefore, medium alkalinity could have a significant impact on controlling the nucleation event [97]. As hydroxylation reaction of both ferrous and ferric ions continue, the pH of nucleation zone starts to decrease and hence the process in which structural rearrangement of ferrous and ferric aquo-complexes to oxide species occur is hindered at a given timeframe [143]. This prevents the following processes to proceed, causing a reduction in number of free monomers (Fe_3O_4 units) and meta-stable primary particles. This will consequently enhance the Ostwald ripening mechanism to drive NPs growth when they are, in our case, released to SDR. This situation supports the 'conditions of closed system' in which NPs ripening occurs under environment of depleted and/or limited amounts of building blocks. Ultimately, one would expect larger particles size of USPIONs to be produced.

However, there may be another rationalisation which would suggest production of smaller USPIONs at the higher pH medium. Herein, the formed USPIONs will be thermodynamically stable and experience no dimensional changes due to the equilibrium that can be achieved between a number of hydroxyl moiety associated with outer surfaces of NPs and that in the liquid

medium [150]. In case of low pH (low amount of hydroxyl functionality), the new solid phase tries to reduce its total surface area in order to maintain the equilibrium state with liquid phase *via* reducing the total amount of adsorbable hydroxyl ion, and hence larger particles will form. The opposite would occur by increasing the amount of hydroxyl ions of alkaline medium [151]. However, this postulation seem to be more appropriate for stabilising USPIONs over long-term storage conditions in which the NPs will be prevented from undergoing slow growth process as a result of coalescence upon ageing.

In our experiments, at 0.375 mole of total iron, there is no significant change in average NPs size when reducing ammonium hydroxide concentration from 35% to 18%, while at higher total iron amount of 0.75 mole a significant increase ($p < 0.01$) in NPs size, from 7.0013 nm to 7.9026 nm, respectively, was seen, as shown in Figure 2-20. The discrepancy of the particles size results with above discussed mechanisms, may be rationalized by the role of SDR in mitigating the effect of reducing precipitating agent (NH_4OH) strength. However, using a higher TIA along with a reduced ammonium hydroxide concentration could have produced a dual effect on depletion of free monomers (higher reaction and pH lowering rate) giving rise to Ostwald ripening which then lessens the impact of SDR on controlling particles size. Similar has been reported in the literature [79,142,150]

Despite of Ostwald ripening potentially occurring at TIA above 0.75 mole, the particle size distribution of NPs did not exhibit any broadening. This gives an indication that SDR is still playing a positive role in the process of fabricating USPIONs. PDI values of 0.1012 and 0.0910 for NPs prepared using 35% and 18% ammonium hydroxide, respectively, as illustrated in Table 2-6 (other

operation variable include: 600 rpm spinning speed, 60 ml/min flowrate) further confirm this.

In addition, the reduction in medium pH (especially pH < 8) will favour production of mixed iron oxide/hydroxide, by changing the preferential reaction mechanism from oxolation to olation, and therefore non-spherical particulate may appear due to poor structural and morphological evolution [142]. For example, circularity degree deteriorated from 0.846 to 0.733 upon halving the precipitating agent concentration (NH_4OH) from 35% to 18%, respectively when using 0.375 mole TIA.

2.5 Conclusions

The present study set to test the applicability of a new SDR instrumentation for fabrication of inorganic NPs. The instrument was designed to provide a physical separation between nucleation and growth stages in the USPIONs formation and to allow a continuous feeding of building blocks (free monomers and intermediate meso-stable primary particles). This was aimed at establishing optimised conditions for controlling particle size distribution and uniformity of USPIONs – a desirable, key requirement for an ideal USPIONs synthesis process. The instrument design allows for nucleation and growth stages to be controlled in their defined spatial zones *via* adjusting two operational (physical) variables; reactant flowrate and SDR rotational speed. The work presented in this chapter shows that as a result of this design, the particle size and morphology of formed USPIONs could be finely-tuned within the 4 - 9 nm size range. Moreover, the data show that manipulating one of the chemical reaction

variables (TIA of BISS) could also be employed to control the NPs growth, taking the advantage of distinctive operational characteristics of the instrument, so that fine-tuning in the 4.26 to 7.44 nm range can be achieved.

The uniformity of particle size was improved upon increasing reactant flowrate, where a uniform burst nucleation (at the Y-shaped junction) is supposed to be achieved by a shortening in 'residence' time and enhanced mixing [21,78,110]. The data further show that by increasing a spinning speed of SRD one can produce NPs with low PDI value, as a result of controlling an effect of Ostwald ripening, along with intense micro-mixing and a superior mass transport mechanisms [95,96]. Accordingly, very low PDI values of around 0.05 to 0.08 were recorded on more than one occasion, which gives an indication of the process and instrument versatility, where similar results could be obtained using different settings of physical and chemical variables. This is applicable for both NPs size and polydispersity, where similar nanoparticles attributes can be obtained by different adjustments in experimental conditions, e.g. reactant flowrate and SDR rotational speeds. For example, average sizes of around 6-7 nm were obtained for both the flowrates and spinning speeds of 30 and 60 ml/min and 150 and 2400 rpm respectively, whereby the expected increase in the NPs size because of increasing feeding rate was counteracted by increasing of disc spinning speed.

In general, superior size and morphological characteristics of USPIONs were obtained as the reactants flowrate was increased from 30 to 60 ml/min, and as the SDR operated at speeds higher than 600 rpm, but no improvements in the NPs attributes were seen when LSDR was used. In addition, increasing TIA showed maintained morphological features of the NPs.

Accordingly, several USPIONs preparations were found suitable for further experiments, as described in the next chapter, as, for instance, USPIONs prepared at 60 ml/min flowrate, 600 rpm rotational speed, TIA of 0.5-0.75 mole, smaller size SDR, and 0.66 Fe^{+2}/Fe^{+3} ratio.

2.6 References

1 Grassian, V. H. When size really matters: size-dependent properties and surface chemistry of metal and metal oxide nanoparticles in gas and liquid phase environments. *The Journal of Physical Chemistry C* **112**, 18303-18313 (2008).

2 Bao, Y., Wen, T., Samia, A. C. S., Khandhar, A. & Krishnan, K. M. Magnetic nanoparticles: material engineering and emerging applications in lithography and biomedicine. *Journal of materials science* **51**, 513-553 (2016).

3 Polte, J. *et al.* Nucleation and growth of gold nanoparticles studied via in situ small angle X-ray scattering at millisecond time resolution. *ACS nano* **4**, 1076-1082 (2010).

4 Wagner, J., Tshikhudo, T. & Köhler, J. Microfluidic generation of metal nanoparticles by borohydride reduction. *Chemical Engineering Journal* **135**, S104-S109 (2008).

5 Zhang, R., Khalizov, A., Wang, L., Hu, M. & Xu, W. Nucleation and growth of nanoparticles in the atmosphere. *Chemical Reviews* **112**, 1957-2011 (2011).

6 Gavi, E., Marchisio, D. & Barresi, A. On the importance of mixing for the production of nanoparticles. *Journal of Dispersion Science and Technology* **29**, 548-554 (2008).

7 Bilati, U., Allémann, E. & Doelker, E. Development of a nanoprecipitation method intended for the entrapment of hydrophilic drugs into nanoparticles. *European Journal of Pharmaceutical Sciences* **24**, 67-75 (2005).

8 Burda, C., Chen, X., Narayanan, R. & El-Sayed, M. A. Chemistry and properties of nanocrystals of different shapes. *Chemical reviews* **105**, 1025-1102 (2005).

9 Liu, C., Zou, B., Rondinone, A. J. & Zhang, Z. J. Sol− gel synthesis of free-standing ferroelectric lead zirconate titanate nanoparticles. *Journal of the American Chemical Society* **123**, 4344-4345 (2001).

10 Gharibshahian, M., Nourbakhsh, M. & Mirzaee, O. Evaluation of the superparamagnetic and biological properties of microwave assisted synthesized Zn & Cd doped CoFe2O4 nanoparticles via Pechini sol–gel method. *Journal of Sol-Gel Science and Technology*, 1-9 (2018).

11 Bang, J. H. & Suslick, K. S. Applications of ultrasound to the synthesis of nanostructured materials. *Advanced materials* **22**, 1039-1059 (2010).

12 Nugraha, A. D. *et al.* in *IOP Conference Series: Materials Science and Engineering.* 012066 (IOP Publishing).

13 Santra, S. *et al.* Synthesis and characterization of silica-coated iron oxide nanoparticles in microemulsion: the effect of nonionic surfactants. *Langmuir* **17**, 2900-2906 (2001).

14 Zhao, X., Bagwe, R. P. & Tan, W. Development of Organic-Dye-Doped Silica Nanoparticles in a Reverse Microemulsion. *Advanced Materials* **16**, 173-176 (2004).

15 Zarur, A. J. & Ying, J. Y. Reverse microemulsion synthesis of nanostructured complex oxides for catalytic combustion. *nature* **403**, 65 (2000).

16 Lopez-Quintela, M. A. Synthesis of nanomaterials in microemulsions: formation mechanisms and growth control. *Current Opinion in Colloid & Interface Science* **8**, 137-144 (2003).
17 Jana, N. R., Gearheart, L. & Murphy, C. J. Evidence for seed-mediated nucleation in the chemical reduction of gold salts to gold nanoparticles. *Chemistry of Materials* **13**, 2313-2322 (2001).
18 Pillai, Z. S. & Kamat, P. V. What factors control the size and shape of silver nanoparticles in the citrate ion reduction method? *The Journal of Physical Chemistry B* **108**, 945-951 (2004).
19 Lee, Y., Choi, J.-r., Lee, K. J., Stott, N. E. & Kim, D. Large-scale synthesis of copper nanoparticles by chemically controlled reduction for applications of inkjet-printed electronics. *Nanotechnology* **19**, 415604 (2008).
20 Krishna, K. S., Li, Y., Li, S. & Kumar, C. S. Lab-on-a-chip synthesis of inorganic nanomaterials and quantum dots for biomedical applications. *Advanced drug delivery reviews* **65**, 1470-1495 (2013).
21 Song, Y., Hormes, J. & Kumar, C. S. Microfluidic synthesis of nanomaterials. *small* **4**, 698-711 (2008).
22 Abou-Hassan, A., Sandre, O. & Cabuil, V. Microfluidics in inorganic chemistry. *Angewandte Chemie International Edition* **49**, 6268-6286 (2010).
23 Marre, S. & Jensen, K. F. Synthesis of micro and nanostructures in microfluidic systems. *Chemical Society Reviews* **39**, 1183-1202 (2010).
24 Niu, G., Ruditskiy, A., Vara, M. & Xia, Y. Toward continuous and scalable production of colloidal nanocrystals by switching from batch to droplet reactors. *Chemical Society Reviews* **44**, 5806-5820 (2015).
25 Ma, J., Lee, S. M.-Y., Yi, C. & Li, C.-W. Controllable synthesis of functional nanoparticles by microfluidic platforms for biomedical applications–a review. *Lab on a Chip* **17**, 209-226 (2017).
26 Khan, I. U., Serra, C. A., Anton, N. & Vandamme, T. Microfluidics: a focus on improved cancer targeted drug delivery systems. *Journal of controlled release* **172**, 1065-1074 (2013).
27 Zhao, C.-X., He, L., Qiao, S. Z. & Middelberg, A. P. Nanoparticle synthesis in microreactors. *Chemical Engineering Science* **66**, 1463-1479 (2011).
28 Xu, S. *et al.* Generation of monodisperse particles by using microfluidics: control over size, shape, and composition. *Angewandte Chemie* **117**, 734-738 (2005).
29 Edel, J. B. & Fortt, R. Microfluidic routes to the controlled production of nanoparticles. *Chemical Communications*, 1136-1137 (2002).
30 Liu, D. *et al.* A versatile and robust microfluidic platform toward high throughput synthesis of homogeneous nanoparticles with tunable properties. *Advanced Materials* **27**, 2298-2304 (2015).
31 Abou-Hassan, A., Bazzi, R. & Cabuil, V. Multistep Continuous-Flow Microsynthesis of Magnetic and Fluorescent γ-Fe2O3@ SiO2 Core/Shell Nanoparticles. *Angewandte Chemie International Edition* **48**, 7180-7183 (2009).
32 Lim, J.-M. *et al.* Parallel microfluidic synthesis of size-tunable polymeric nanoparticles using 3D flow focusing towards in vivo study.

Nanomedicine: Nanotechnology, Biology and Medicine **10**, 401-409 (2014).

33 Günther, A. & Jensen, K. F. Multiphase microfluidics: from flow characteristics to chemical and materials synthesis. *Lab on a Chip* **6**, 1487-1503 (2006).

34 Shui, L., Eijkel, J. C. & van den Berg, A. Multiphase flow in microfluidic systems–Control and applications of droplets and interfaces. *Advances in Colloid and Interface Science* **133**, 35-49 (2007).

35 Song, H., Chen, D. L. & Ismagilov, R. F. Reactions in droplets in microfluidic channels. *Angewandte chemie international edition* **45**, 7336-7356 (2006).

36 Knauer, A. *et al.* Au/Ag/Au double shell nanoparticles with narrow size distribution obtained by continuous micro segmented flow synthesis. *Chemical engineering journal* **166**, 1164-1169 (2011).

37 Knauer, A. *et al.* Microsegmented flow-through synthesis of silver nanoprisms with exact tunable optical properties. *The Journal of Physical Chemistry C* **116**, 9251-9258 (2012).

38 Sebastian Cabeza, V., Kuhn, S., Kulkarni, A. A. & Jensen, K. F. Size-controlled flow synthesis of gold nanoparticles using a segmented flow microfluidic platform. *Langmuir* **28**, 7007-7013 (2012).

39 Stein, A. & Schroden, R. C. Colloidal crystal templating of three-dimensionally ordered macroporous solids: materials for photonics and beyond. *Current Opinion in Solid State and Materials Science* **5**, 553-564 (2001).

40 Růžička, J. & Hansen, E. Flow-injection analysis and its early history. *Talanta* **29**, 157 (1982).

41 Wang, L. & Muhammed, M. Synthesis of zinc oxide nanoparticles with controlled morphology. *Journal of Materials Chemistry* **9**, 2871-2878, doi:10.1039/A907098B (1999).

42 Jongen, N. *et al.* Development of a Continuous Segmented Flow Tubular Reactor and the "Scale-out" Concept–In Search of Perfect Powders. *Chemical engineering & technology* **26**, 303-305 (2003).

43 Donnet, M., Jongen, N., Lemaitre, J. & Bowen, P. New morphology of calcium oxalate trihydrate precipitated in a segmented flow tubular reactor. *Journal of materials science letters* **19**, 749-750 (2000).

44 Harries, N., Burns, J., Barrow, D. & Ramshaw, C. A numerical model for segmented flow in a microreactor. *International journal of heat and mass transfer* **46**, 3313-3322 (2003).

45 Massart, R. Preparation of aqueous magnetic liquids in alkaline and acidic media. *IEEE Transactions on Magnetics* **17**, 1247-1248, doi:10.1109/TMAG.1981.1061188 (1981).

46 Kang, Y. S., Risbud, S., Rabolt, J. F. & Stroeve, P. Synthesis and characterization of nanometer-size Fe3O4 and γ-Fe2O3 particles. *Chemistry of Materials* **8**, 2209-2211 (1996).

47 Bee, A., Massart, R. & Neveu, S. Synthesis of very fine maghemite particles. *Journal of Magnetism and Magnetic Materials* **149**, 6-9 (1995).

48 Van Ewijk, G., Vroege, G. & Philipse, A. Convenient preparation methods for magnetic colloids. *Journal of Magnetism and Magnetic Materials* **201**, 31-33 (1999).

49 Răcuciu, M., Creangă, D. & Airinei, A. Citric-acid-coated magnetite nanoparticles for biological applications. *The European Physical Journal E: Soft Matter and Biological Physics* **21**, 117-121 (2006).
50 Soler, M. *et al.* Study of molecular surface coating on the stability of maghemite nanoparticles. *Surface Science* **601**, 3921-3925 (2007).
51 Abbas, M., Rao, B. P., Naga, S., Takahashi, M. & Kim, C. Synthesis of high magnetization hydrophilic magnetite (Fe 3 O 4) nanoparticles in single reaction—surfactantless polyol process. *Ceramics International* **39**, 7605-7611 (2013).
52 Hajdú, A. *et al.* Enhanced stability of polyacrylate-coated magnetite nanoparticles in biorelevant media. *Colloids and Surfaces B: Biointerfaces* **94**, 242-249 (2012).
53 Basti, H. *et al.* Catechol derivatives-coated Fe 3 O 4 and γ-Fe 2 O 3 nanoparticles as potential MRI contrast agents. *Journal of Colloid and Interface Science* **341**, 248-254 (2010).
54 Petcharoen, K. & Sirivat, A. Synthesis and characterization of magnetite nanoparticles via the chemical co-precipitation method. *Materials Science and Engineering: B* **177**, 421-427 (2012).
55 Cai, W. & Wan, J. Facile synthesis of superparamagnetic magnetite nanoparticles in liquid polyols. *Journal of colloid and interface science* **305**, 366-370 (2007).
56 Santos, A. F. *et al.* Hybrid Self-Assembled Materials Constituted by Ferromagnetic Nanoparticles and Tannic Acid: a Theoretical and Experimental Investigation. *Journal of the Brazilian Chemical Society* **27**, 727-734 (2016).
57 Maity, D. & Agrawal, D. Synthesis of iron oxide nanoparticles under oxidizing environment and their stabilization in aqueous and non-aqueous media. *Journal of Magnetism and Magnetic Materials* **308**, 46-55 (2007).
58 Carlton, C. & Ferreira, P. In situ TEM nanoindentation of nanoparticles. *Micron* **43**, 1134-1139 (2012).
59 Chen, X. & Wen, J. In situ wet-cell TEM observation of gold nanoparticle motion in an aqueous solution. *Nanoscale research letters* **7**, 598 (2012).
60 Hondow, N. *et al.* in *Journal of Physics: Conference Series.* 012020 (IOP Publishing).
61 Baumgartner, J. & Faivre, D. Iron solubility, colloids and their impact on iron (oxyhydr) oxide formation from solution. *Earth-Science Reviews* **150**, 520-530 (2015).
62 Jolivet, J.-P., Chanéac, C. & Tronc, E. Iron oxide chemistry. From molecular clusters to extended solid networks. *Chemical Communications*, 481-483 (2004).
63 Jolivet, J.-P., Tronc, E. & Chanéac, C. Iron oxides: From molecular clusters to solid. A nice example of chemical versatility. *Comptes Rendus Geoscience* **338**, 488-497 (2006).
64 Woo, K., Lee, H. J., Ahn, J. P. & Park, Y. S. Sol–gel mediated synthesis of Fe2O3 nanorods. *Advanced Materials* **15**, 1761-1764 (2003).
65 Yufanyi, D. M., Ondoh, A. M., Foba-Tendo, J. & Mbadcam, K. J. Effect of Decomposition Temperature on the Crystallinity of α-Fe 2 O 3

(Hematite) Obtained from an Iron (III)-Hexamethylenetetramine Precursor. *American Journal of Chemistry* **5**, 1-9 (2015).

66 Gao, M. *et al.* A simple pathway to the synthesis of magnetic nanoparticles with immobilized metal ions for the fast removal of microcystins in water. *Small* **3**, 1714-1717 (2007).

67 Roto, R., Yusran, Y. & Kuncaka, A. Magnetic adsorbent of Fe 3 O 4@ SiO 2 core-shell nanoparticles modified with thiol group for chloroauric ion adsorption. *Applied Surface Science* **377**, 30-36 (2016).

68 Liu, X. *et al.* Preparation of carriers based on magnetic nanoparticles grafted polymer and immobilization for lipase. *Biochemical engineering journal* **56**, 142-149 (2011).

69 Jolivet, J.-P., Henry, M. & Livage, J. *Metal oxide chemistry and synthesis: from solution to solid state*. (Wiley-Blackwell, 2000).

70 Cao, G. *Nanostructures and nanomaterials: synthesis, properties and applications*. (World Scientific, 2004).

71 LaMer, V. K. & Dinegar, R. H. Theory, production and mechanism of formation of monodispersed hydrosols. *Journal of the American Chemical Society* **72**, 4847-4854 (1950).

72 Mer, V. K. L. Nucleation in Phase Transitions. *Industrial & Engineering Chemistry* **44**, 1270-1277 (1952).

73 Vreeland, E. C. *et al.* Enhanced nanoparticle size control by extending LaMer's mechanism. *Chemistry of Materials* **27**, 6059-6066 (2015).

74 Ostwald, W. Über die vermeintliche Isomerie des roten und gelben Quecksilberoxyds und die Oberflächenspannung fester Körper. *Zeitschrift für physikalische Chemie* **34**, 495-503 (1900).

75 Lifshitz, I. M. & Slyozov, V. V. The kinetics of precipitation from supersaturated solid solutions. *Journal of physics and chemistry of solids* **19**, 35-50 (1961).

76 Wagner, C. Theory of precipitate change by redissolution. *Z. Elektrochem.* **65**, 581-591 (1961).

77 Sugimoto, T. Preparation of monodispersed colloidal particles. *Advances in Colloid and Interface Science* **28**, 65-108 (1987).

78 Xu, L. *et al.* Synthesis of copper nanoparticles by a T-shaped microfluidic device. *RSC Advances* **4**, 25155-25159 (2014).

79 Salazar-Alvarez, G., Muhammed, M. & Zagorodni, A. A. Novel flow injection synthesis of iron oxide nanoparticles with narrow size distribution. *Chemical engineering science* **61**, 4625-4633 (2006).

80 Yen, B. K., Günther, A., Schmidt, M. A., Jensen, K. F. & Bawendi, M. G. A Microfabricated Gas–Liquid Segmented Flow Reactor for High-Temperature Synthesis: The Case of CdSe Quantum Dots. *Angewandte Chemie* **117**, 5583-5587 (2005).

81 Khan, S. A., Günther, A., Schmidt, M. A. & Jensen, K. F. Microfluidic synthesis of colloidal silica. *Langmuir* **20**, 8604-8611 (2004).

82 Kumar, D. R. *et al.* Continuous flow synthesis of functionalized silver nanoparticles using bifunctional biosurfactants. *Green Chemistry* **12**, 609-615 (2010).

83 Bai, H. & Thomas, B. G. Turbulent flow of liquid steel and argon bubbles in slide-gate tundish nozzles: Part I. model development and validation. *Metallurgical and Materials Transactions B* **32**, 253-267 (2001).

84 Jacobsen, N. C. & Hinrichsen, O. Micromixing efficiency of a spinning disk reactor. *Industrial & Engineering Chemistry Research* **51**, 11643-11652 (2012).
85 Aoune, A. & Ramshaw, C. Process intensification: heat and mass transfer characteristics of liquid films on rotating discs. *International Journal of Heat and Mass Transfer* **42**, 2543-2556 (1999).
86 Boodhoo, K. V. & Al-Hengari, S. R. Micromixing Characteristics in a Small-Scale Spinning Disk Reactor. *Chemical Engineering & Technology* **35**, 1229-1237 (2012).
87 Feng, X., Patterson, D. A., Balaban, M. & Emanuelsson, E. A. C. Characterization of liquid flow in the spinning cloth disc reactor: Residence time distribution, visual study and modeling. *Chemical Engineering Journal* **235**, 356-367 (2014).
88 Schmidt, L. D. *The engineering of chemical reactions*. (Oxford University Press, USA, 1998).
89 Jachuck, R. & Ramshaw, C. Process intensification: heat transfer characteristics of tailored rotating surfaces. *Heat Recovery Systems and CHP* **14**, 475-491 (1994).
90 Mohammadi, S. & Boodhoo, K. V. Online conductivity measurement of residence time distribution of thin film flow in the spinning disc reactor. *Chemical engineering journal* **207**, 885-894 (2012).
91 Iso, Y. & Chen, X. Flow transition behavior of the wetting flow between the film flow and rivulet flow on an inclined wall. *Journal of Fluids Engineering* **133**, 091101 (2011).
92 Matar, O. K., Sisoev, G. M. & Lawrence, C. J. Evolution scales for wave regimes in liquid film flow over a spinning disk. *Physics of Fluids* **16**, 1532-1545 (2004).
93 Boodhoo, K. & Jachuck, R. Process intensification: spinning disk reactor for styrene polymerisation. *Applied Thermal Engineering* **20**, 1127-1146 (2000).
94 Iyer, K. S., Raston, C. L. & Saunders, M. Continuous flow nano-technology: manipulating the size, shape, agglomeration, defects and phases of silver nano-particles. *Lab on a Chip* **7**, 1800-1805 (2007).
95 Chin, S. F., Iyer, K. S., Raston, C. L. & Saunders, M. Size selective synthesis of superparamagnetic nanoparticles in thin fluids under continuous flow conditions. *Advanced Functional Materials* **18**, 922-927 (2008).
96 Mohammadi, S., Harvey, A. & Boodhoo, K. V. Synthesis of TiO 2 nanoparticles in a spinning disc reactor. *Chemical Engineering Journal* **258**, 171-184 (2014).
97 Kashchiev, D. (Butterworth-Heinemann, Oxford, 2000).
98 Bachhar, N. & Bandyopadhyaya, R. Role of coating agent in iron oxide nanoparticle formation in an aqueous dispersion: Experiments and simulation. *Journal of colloid and interface science* **464**, 254-263 (2016).
99 Banfield, J. F., Welch, S. A., Zhang, H., Ebert, T. T. & Penn, R. L. Aggregation-based crystal growth and microstructure development in natural iron oxyhydroxide biomineralization products. *Science* **289**, 751-754 (2000).

100 Navrotsky, A. Energetic clues to pathways to biomineralization: Precursors, clusters, and nanoparticles. *Proceedings of the National Academy of Sciences of the United States of America* **101**, 12096-12101 (2004).
101 Gebauer, D., Völkel, A. & Cölfen, H. Stable prenucleation calcium carbonate clusters. *Science* **322**, 1819-1822 (2008).
102 Pouget, E. M., Bomans, P. H., Goos, J. A., Frederik, P. M. & Sommerdijk, N. A. The initial stages of template-controlled CaCO 3 formation revealed by cryo-TEM. *Science* **323**, 1455-1458 (2009).
103 Yuwono, V. M., Burrows, N. D., Soltis, J. A. & Penn, R. L. Oriented aggregation: formation and transformation of mesocrystal intermediates revealed. *Journal of the American Chemical Society* **132**, 2163-2165 (2010).
104 Dey, A. *et al.* The role of prenucleation clusters in surface-induced calcium phosphate crystallization. *Nature materials* **9** (2010).
105 Chen, Y.-S., Lin, F.-Y., Lin, C.-C., Tai, C. Y.-D. & Liu, H.-S. Packing characteristics for mass transfer in a rotating packed bed. *Industrial & engineering chemistry research* **45**, 6846-6853 (2006).
106 Chen, Y.-S., Liu, H.-S., Lin, C.-C. & Liu, W.-T. Micromixing in a rotating packed bed. *Journal of chemical engineering of Japan* **37**, 1122-1128 (2004).
107 Vicevic, M., Boodhoo, K. V. & Scott, K. Catalytic isomerisation of α-pinene oxide to campholenic aldehyde using silica-supported zinc triflate catalysts: II. Performance of immobilised catalysts in a continuous spinning disc reactor. *Chemical Engineering Journal* **133**, 43-57 (2007).
108 Hartlieb, K. J., Raston, C. L. & Saunders, M. Controlled scalable synthesis of ZnO nanoparticles. *Chemistry of Materials* **19**, 5453-5459 (2007).
109 Cafiero, L., Baffi, G., Chianese, A. & Jachuck, R. Process intensification: precipitation of barium sulfate using a spinning disk reactor. *Industrial & engineering chemistry research* **41**, 5240-5246 (2002).
110 Xu, L., Peng, J., Srinivasakannan, C., Chen, G. & Shen, A. Q. Synthesis of copper nanocolloids using a continuous flow based microreactor. *Applied Surface Science* **355**, 1-6 (2015).
111 Tian, Z.-H., Wang, Y.-J., Xu, J.-H. & Luo, G.-S. Intensification of nucleation stage for synthesizing high quality CdSe quantum dots by using preheated precursors in microfluidic devices. *Chemical Engineering Journal* **302**, 498-502 (2016).
112 Yen, B. K., Stott, N. E., Jensen, K. F. & Bawendi, M. G. A Continuous-Flow Microcapillary Reactor for the Preparation of a Size Series of CdSe Nanocrystals. *Advanced Materials* **15**, 1858-1862 (2003).
113 Chang, M.-H., Liu, H.-S. & Tai, C. Y. Preparation of copper oxide nanoparticles and its application in nanofluid. *Powder technology* **207**, 378-386 (2011).
114 Tai, C. Y., Tai, C.-T., Chang, M.-H. & Liu, H.-S. Synthesis of magnesium hydroxide and oxide nanoparticles using a spinning disk reactor. *Industrial & engineering chemistry research* **46**, 5536-5541 (2007).

115 Lin, C.-C. & Liu, H.-S. Adsorption in a centrifugal field: basic dye adsorption by activated carbon. *Industrial & engineering chemistry research* **39**, 161-167 (2000).
116 Chen, Y.-S. & Liu, H.-S. Absorption of VOCs in a rotating packed bed. *Industrial & engineering chemistry research* **41**, 1583-1588 (2002).
117 Lin, C.-C., Liu, W.-T. & Tan, C.-S. Removal of carbon dioxide by absorption in a rotating packed bed. *Industrial & engineering chemistry research* **42**, 2381-2386 (2003).
118 Liu, H.-S., Lin, C.-C., Wu, S.-C. & Hsu, H.-W. Characteristics of a rotating packed bed. *Industrial & engineering chemistry research* **35**, 3590-3596 (1996).
119 Anantachoke, N. *et al.* Fine tuning the production of nanosized β-carotene particles using spinning disk processing. *Journal of the American Chemical Society* **128**, 13847-13853 (2006).
120 De Caprariis, B., Di Rita, M., Stoller, M., Verdone, N. & Chianese, A. Reaction-precipitation by a spinning disc reactor: Influence of hydrodynamics on nanoparticles production. *Chemical Engineering Science* **76**, 73-80 (2012).
121 Hua, C. C. *et al.* Size-controlled Synthesis and Characterization of Fe3O4 Nanoparticles by Chemical Coprecipitation Method. *Sains Malaysiana* **37**, 389-394 (2008).
122 de Caprariis, B., Stoller, M., Chianese, A. & Verdone, N. CFD model to predict hydroxyapatite nanoparticle production in a spinning disk reactor. *CHEMICAL ENGINEERING* **43** (2015).
123 Sungkhaphaitoon, P., Wisutmethangoon, S. & Plookphol, T. Influence of Process Parameters on Zinc Powder Produced by Centrifugal Atomisation. *Materials Research*, 0-0 (2017).
124 Khurmi, R. & Gupta, J. *Theory of machines*. (Eurasia, 1976).
125 De Caprariis, B., Stoller, M., Chianese, A. & Verdone, N. in *Chemical Engineering Transactions* (Italian Association of Chemical Engineering-AIDIC, 2015).
126 Baumgartner, J. *et al.* Nucleation and growth of magnetite from solution. *Nature materials* **12** (2013).
127 Xie, J., Zhao, Y. & Dunkley, J. Effects of processing conditions on powder particle size and morphology in centrifugal atomisation of tin. *Powder metallurgy* **47**, 168-172 (2004).
128 Angers, R., Tremblay, R. & Dube, D. Formation of irregular particles during centrifugal atomization of AZ91 alloy. *Materials Letters* **33**, 13-18 (1997).
129 Sheikhaliev, S. M., Sheikhalieva, Z. I. & Dunkley, J. J. Spin atomisation makes tighter, safer aluminium. *Metal Powder Report* **63**, 28-30 (2008).
130 Plookphol, T., Wisutmethangoon, S. & Gonsrang, S. Influence of process parameters on SAC305 lead-free solder powder produced by centrifugal atomization. *Powder technology* **214**, 506-512 (2011).
131 Bhatelia, T. J., Utikar, R. P., Pareek, V. K. & Tade, M. O. in *Proceedings of the Seventh International Conference on CFD in the Minerals and Process Industries, CSIRO, Melbourne, Australia*. 9-11.
132 Pan, Y., Witt, P., Kuan, B. & Xie, D. CFD modelling of the effects of operating parameters on the spreading of liquids on a spinning disc. *The Journal of Computational Multiphase Flows* **6**, 49-64 (2014).

133 Connors, K. A. *Chemical kinetics: the study of reaction rates in solution*. (John Wiley & Sons, 1990).
134 Clark, G. & Smart, L. E. *Chemical kinetics and mechanism*. (Royal Society of Chemistry, 2007).
135 Tai, C., Wang, Y., Kuo, Y., Chang, M. & Liu, H. Synthesis of silver particles below 10nm using spinning disk reactor. *Chemical Engineering Science* **64**, 3112-3119 (2009).
136 Dehsari, H. S. *et al.* Effect of precursor concentration on size evolution of iron oxide nanoparticles. *CrystEngComm* (2017).
137 Kashchiev, D. *Nucleation*. (Butterworth-Heinemann, 2000).
138 Tai, C. Y., Wang, Y.-H., Tai, C.-T. & Liu, H.-S. Preparation of silver nanoparticles using a spinning disk reactor in a continuous mode. *Industrial & Engineering Chemistry Research* **48**, 10104-10109 (2009).
139 Cornell, R. The influence of some divalent cations on the transformation of ferrihydrite to more crystalline products. *Clay Minerals* **23**, 329-332 (1988).
140 Tronc, E., Belleville, P., Jolivet, J. P. & Livage, J. Transformation of ferric hydroxide into spinel by iron (II) adsorption. *Langmuir* **8**, 313-319 (1992).
141 Jolivet, J., Belleville, P., Tronc, E. & Livage, J. Influence of Fe (II) on the formation of the spinel iron oxide in alkaline medium. *Clays and Clay Minerals* **40**, 531-531 (1992).
142 Blanco-Andujar, C., Ortega, D., Pankhurst, Q. A. & Thanh, N. T. K. Elucidating the morphological and structural evolution of iron oxide nanoparticles formed by sodium carbonate in aqueous medium. *Journal of Materials Chemistry* **22**, 12498-12506 (2012).
143 Tamaura, Y., Ito, K. & Katsura, T. Transformation of γ-FeO (OH) to Fe 3 O 4 by adsorption of iron (II) ion on γ-FeO (OH). *Journal of the Chemical Society, Dalton Transactions*, 189-194 (1983).
144 Hansel, C. M. *et al.* Secondary mineralization pathways induced by dissimilatory iron reduction of ferrihydrite under advective flow. *Geochimica et Cosmochimica Acta* **67**, 2977-2992 (2003).
145 Babes, L., Denizot, B., Tanguy, G., Le Jeune, J. J. & Jallet, P. Synthesis of iron oxide nanoparticles used as MRI contrast agents: a parametric study. *Journal of colloid and interface science* **212**, 474-482 (1999).
146 Lodhia, J., Mandarano, G., Ferris, N., Eu, P. & Cowell, S. Development and use of iron oxide nanoparticles (Part 1): Synthesis of iron oxide nanoparticles for MRI. *Biomedical imaging and intervention journal* **6** (2010).
147 Forge, D. *et al.* Optimization of the synthesis of superparamagnetic contrast agents by the design of experiments method. *The Journal of Physical Chemistry C* **112**, 19178-19185 (2008).
148 Yu, W.-G., Zhang, T.-L., Qiao, X.-J., Zhang, J.-G. & Yang, L. Effects of synthetical conditions on octahedral magnetite nanoparticles. *Materials Science and Engineering: B* **136**, 101-105 (2007).
149 Roth, H.-C., Schwaminger, S. P., Schindler, M., Wagner, F. E. & Berensmeier, S. Influencing factors in the CO-precipitation process of superparamagnetic iron oxide nano particles: a model based study. *Journal of Magnetism and Magnetic Materials* **377**, 81-89 (2015).

150 Vayssières, L., Chanéac, C., Tronc, E. & Jolivet, J. P. Size tailoring of magnetite particles formed by aqueous precipitation: an example of thermodynamic stability of nanometric oxide particles. *Journal of colloid and interface science* **205**, 205-212 (1998).
151 Jolivet, J., Tronc, E. & Chanéac, C. Synthesis of iron oxide-and metal-based nanomaterials. *The European Physical Journal-Applied Physics* **10**, 167-172 (2000).

Chapter 3: Surface Modification of USPIONs with Different Amino acids: Preparation and Characterisation.

3.1 Introduction

Because of the inherent properties of iron oxide NPs, USPIONs are prone to aggregating into large clusters upon dispersion in an aqueous medium. The high surface area to volume ratio of these colloids enhances the magnetic dipole-dipole interactions and, in conjugation with an increased surface free energy, and hence the attractive VDW forces, dominates and drive NPs aggregation [1-4]. It is well-known that the NPs aggregation reduces a long term stability of their colloidal dispersions and limits their applications. Therefore, ways of counteracting the attractive forces are necessary for a production of stable magnetic ferrofluid that can have a diverse utilisation in different fields [5].

In essence, there are two different strategies have been adopted in order to achieve a thermodynamically stable colloidal dispersion. The principle motif that all these mechanism is the control of attractive inter-particulate forces, classically described in Derjaguin-Landau-Verwey-Overbeek (DLVO) theory [6,7]. In fairly stable system, the maximum energy of the ever-present attractive forces must be sufficiently small to permit gentle thermal activity or agitation to re-disperse the flocculated particles. Creating an electrical double layer that is e.g. constructed from counter ions at the solid-liquid interface, is the first strategy used to provide a repulsive force which interrupt the inter-particulate attraction force (VDW). This is termed electrostatic stabilisation mechanism [8], in which the interrupting force arises from either net positive or negative

charges. These forces are equal or exceed other counter-forces [9]. However, the presence of high concentration of free ions in the medium may conceal the effect of repulsive double layer. In addition, adjusting pH media to be close to the isoelectric point (IEP) of the associated ionic moieties will diminish the repulsion [10]. Therefore this approach has restricted use in stabilising NP, and is mainly effective in media of low polarity and ionic strength [11,12].

The second strategy normally employs a long chain polymers, strongly adsorbed on a solid NPs surface with a good coverage. This generates so-called 'steric layer' (or stealth layer). The flexible, solvated polymer segments extended from the surface into surrounding medium and prevent attraction between different particles, ensuring a reduction in NPs randomness and hence a system with positive Gibbs free energy that resists a flocculation [13]. Hence, the entropic stabilisation effectively screens the inter-particulate attractive forces to stabilize such colloidal suspensions [7,14-16].

There are some distinctive advantages of steric (entropic) stabilisation which include: (1) independence on ionic strength, particles concentration, and nature of dispersion media, (2) such dispersions do not form a hard cake when sedimentation occurs, and (3) high stability upon freeze-thaw and dry-rehydrate cycles is normally achieved [17].

In addition to the major concepts of stabilisation mentioned above, there is a third approach by which a thermodynamically stable dispersion could be achieved. This is electrosteric stabilisation, the concept that simultaneously benefits from both, electrostatic and polymer-induced steric repulsions [18]. In this case a polyelectrolyte might be used to modify the surface of NPs and prevent

their aggregation. Polyacrylic acid (PAA), which has been widely used in this field is a good example of metal oxide NPs stabilising agent [19-22].

In order to obtain water dispersible and biologically compatible iron oxide NPs, several approaches can be adapted. For example, an aqueous solution of a surface adsorbing material can be added to a pre-prepared NPs to produce a modified surface NPs [23]. Also, ligand exchange is a another popular technique that could be used for NPs surfaces functionalisation [24,25]. It is principally accomplished through different interactions such as H-bonding, acid –base, and electrostatic interaction [26,27]. In addition electrosteric stabilisation is often considered, as mentioned above [28,29].

The experimental work of the present chapter aims at following: (1) to prepare a highly biologically-compatible hydrophilic USPIONs employing surfaces modification with different amino acids (as 'monomers') by applying a new technique of 'dry mixing/milling under mechanical pressure' developed in the G Cave's research groups, (2) to investigate how effective is the NPs modification procedure regarding the population of USPIONs that are successfully modified and in relation the amount of surface-modifying material associated with the NPs, and (3) to reveal aminoacid monomer-NP association mechanism.

In order to test both, the applicability of dry mixing technique to surface modification of USPIONs, and the use of amino acids monomers and stabilizing agents, a panel of nine amino acids is employed in the present work. The selection covers the diverse classes of the essential and non-essential amino

acids regarding the hydropathy, volume, chemical, physicochemical, charge, polarity and hydrogen donor or acceptor properties [30].

3.2 Materials and Methods

3.2.1 Materials

Nine different amino acids obtained from non-animal source ~≥ 98.5% (Glycine, Phenylalanine, Methionine, Aspartic acid, Threonine, Glutamic acid, Leucine, Lysine dihydrochloride and L-Histidine dihydrochloride). Concentrated hydrochloric acid (~ 37%) from Fisher scientific. Fluorescamine powder was purchased from Sigma-Aldrich.

3.2.2 Methods

3.2.2.1 USPIONs surface modification

The surface of the fabricated NPs was modified following the dry hand mixing process with applied mechanical pressure according to a previously developed and patented procedure [31]. From nine different amino acids selected to modify USPIONs, seven amino acids (threonine, glycine, phenylalanine, leucine, methionine, glutamic acid, and aspartic acid) were converted to hydrochloride salts by dissolving the powders in 4M HCl and then dried using rotary evaporator (Buchi Rotavapor, Cole-Parmer, UK), while the other two amino acids (lysine and histidine) have been ordered as dihydrochloride form (Sigma Aldrich, UK). For every amino acid tested, seven different quantities (31.25, 62.5, 125, 250, 500, 750, and 1000 µmole) were mixed and triturated using a mortar and pestle with 28.75 mg of a freshly fabricated USPIONs powder. After 5-10 min of hand mixing, 10 ml of deionised (Elga purification system) water was added to disperse the mixture. The next step include filtering of powder

suspension, whereby only successfully surface modified USPIONs will be suspended (not aggregated) to pass across the 0.2 µm syringe filter (Millipore, UK). Figure 3-1 illustrates the process of filtration to collect the modified USPIONs.

In addition, the classical NPs surface coating method was performed in which the aqueous solution of different amino acid hydrochloride salt was mixed and sonicated for half an hour with freshly fabricated USPIONs. The quantities of both amino acid monomers and 'bare' USPIONs powder suspended in aqueous mixture corresponded to amounts used in dry mixing method.

In another experiment, dry mixing method was adopted to attempt to modify the surface of USPIONs with the nine amino acids as their base form, under corresponding experimental conditions as described above.

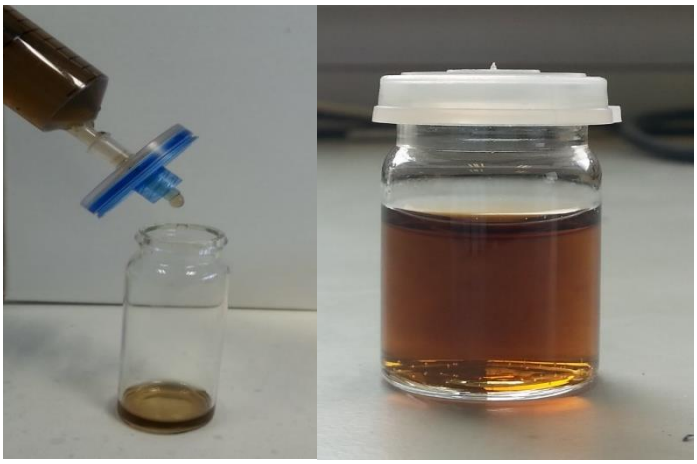


***Figure 0-1**: **Illustrative photographs of filtering aminoacid-modified USPIONs prepared using dry mixing method with applied mechanical pressure**.*

For the all nine amino acids used, seven different quantities (31.25, 62.5, 125, 250, 500, 750, and 1000 µmoles) were mixed with 28.75mg bare USPIONs powder. After 5 min of hand-mixing, the mixtures were dispersed in 10 ml of deionised water and filtered through 0.2µm syringe filter in order to remove aggregated, and obtain a suspension of modified USPIONs.

3.2.2.2 Purification of amino acid-modified USPIONs

Purified, 'clean' aminoacid-modified USPIONs, were considered to be those where insufficiently surface modified and hence aggregated USPIONs were removed during filtration and those where excess of non-adsorbed aminoacid monomers was removed. As described above, a filtration of USPIONs dispersion represents the first step of purification which removes the aggregated USPIONs, while repeated centrifugation of the filtered colloidal dispersion achieves the second step. Here, the NPs colloidal dispersion was aliquoted into several Eppendorf tubes®, 1.5 ml, and centrifuged for 3 hours at speed of 20,000 rpm using fixed angle centrifuge (Eppendorf 5430 Benchtop, Germany). After that, the supernatant was carefully aspirated from each tube to leave a small pellet of pure modified USPIONs at the bottom, as showed in Figure 3-2.

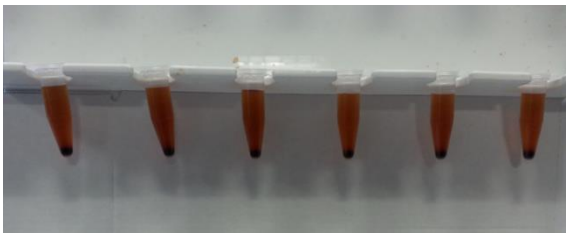


Figure 0-2: A photograph of Eppendorf tubes shows small pellets of pure modified USPIONs deposited at the bottom after centrifugation.

3.2.2.3 Detection Iron oxide amount

The amount (yield) of aminoacid-modified USPIONs was determined by using the inductively coupled plasma-atomic emission spectroscopy (ICP-AES) instrument (PerkinElmer). 1.0 ml of filtered colloidal dispersion of USPIONs was mixed with an equal volume of concentrated hydrochloric acid (1.0 ml, 37% w/w) for 4 hours, until all metal oxide NPs were dissolved. After that, 3 ml of deionised water was added in order to dilute the acidic sample so that the final

HCl concentration will be around 2.25-2.5 M. This was necessary so that the tested samples would not damage the instrument's tubing system. The samples were prepared using the nine amino acids chosen, whereby each amino acid was used in the range extended from 31.25 to 1000 µmole.

The experimental readings were expressed in term of percent mass amount of USPIONs that are successfully modified in relation to the initial total amount used *via* preparing appropriate standard curve with known elemental iron amount was detected by ICP-AES. The recorded data were from three independent trials and are presented as mean ± SD.

3.2.2.4 Detection of amino acid monomer associated with the surface of USPIONs

In this analysis fluorescamine probe was used for detection of amino acids present in its solution. The intensity of the fluorescence from the reaction of the probe with the primary amine of a specific aminoacid was measured using a Cary Eclipse Fluorescence Spectrophotometer (Australia). In order to calculate the amount of an amino acid in a particular sample, five serial dilutions (8, 16, 24, 36, 48 ppm) of the all selected amino acids were used to construct the relevant standard curves. It is important to mention that the optimum intensity has been obtained when the pH of the aqueous solution was adjusted to be around pH 8.8 by using a standard borate buffer.

The unknown samples were prepared according to the following protocol. 500 µl of an aminoacid-modified USPIONs dispersion was added to a centrifugal concentrator (Vivaspin) with a 3000 Da molecular cut-off membrane and centrifuged at 4500 x *g* centrifugal force for 15 min. 20 µl of the filtered sample was then diluted with borate buffer (pH 8.8) solution for 500 – 5000 times,

depending on the amount of aminoacid initially used. To this diluted sample, 1 ml of fluorescamine solution (0.77 mg/ml in acetone) was added, vortexed for 10 seconds and incubated in the dark for 20 min. The florescence intensity of the sample was then measured at the emission wavelength of 484 nm and excitation wavelength of 385 nm against a blank of borate buffer with fluorescamine. Amount of aminoacid was determined from a corresponding calibration curve, and after subtracting from the initial amino acid amount, the amount associated with USPIONs was expressed as a number of associated monomer molecules with every individual NP for each amino acid and molar amount used.

The same protocol was applied for detection NPs-associated amino acids in a samples prepared by 'coating' of USPIONs dispersion in aqueous solution of amino acid HCl salt. In this case the measurements were at different incubation time points: 0.5, 1.5, 4, 8, 20, 36 and 48 hours. The recorded data were from three independent trials and are presented as mean ± SD.

3.2.2.5 TEM imaging and hydrodynamic size measurement

Electron microscopy on NPs was performed on a Jeol- JEM 2010 (USA) microscope with accelerating voltage 120 Kv at the Nottingham Trent University laboratories. To acquire TEM images, one drop of diluted colloidal dispersion of USPIONs was applied onto 200 mesh carbon-coated 3.05 mm copper grid. After 5 min, the excess amount of the dispersion was removed with a filter paper to accelerate drying of the samples for imaging.

The particle size and size dispersion of USPIONs was measured by DLS. The diluted colloidal dispersions in 18.2 MΩ de-ionized (Elga) water were

measured using Zetasizer Nano ZS (Malvern Instruments Ltd., UK). The data represent the mean values of 10-15 readings from three independent trials.

3.2.2.6 Infrared analysis of USPIONs

Infrared spectra of amino acid functional groups and their coordination with USPIONs were recorded using the ATR sampling technology. An Agilent Cary 630 (Agilent Technologies, USA) equipped with a diamond crystal was used for recording the spectra of desiccated aminoacid-modified USPIONs along with amino acid hydrochloride powders against air background at a resolution of 8 cm^{-1}, the spectral range of 4000-650 cm^{-1} wavenumber and presented in term of transmittance intensity. The background time limit and sample scans are 5 min and 256 times respectively.

3.2.2.7 Thermogravimetric analysis (TGA)

The thermal stability measurements of both amino acid hydrochlorides and the corresponding aminoacid-modified USPIONs in addition to the bare NPs powder were conducted on TGA Q500 V6.7 Build 203 (TA Instrument, USA). The samples were heated over a range of temperature extended from 30°C up to 900°C at the rate of 20°C/min and under nitrogen gas atmosphere that was flowed at 100ml/min so as to prevent any 176hermos-oxidative degradation. A platinum pan was used to house the tested powders of variable weights. The results were expressed as line graphs of percent weight and weight loss per Celsius degree *versus* temperature.

3.2.2.8 Colloidal dispersion stability of the aminoacid-modified USPIONs as a function of pH

The zeta potential, IEP and hydrodynamic size measurements were determined for the nine aminoacid-modified NPs along with the bare NPs by using ZS

Malvern Zetasizer coupled with automatic titrator (MPT-2, Malvern Instruments, UK). The pH of the dispersion medium were automatically altered by the instrument from pH 2.0 to 9.0 using three 'stock' solutions connected to the titrator (0.25 M hydrochloric acid, and 0.025 and 0.25 M sodium hydroxide solutions). The initial colloidal dispersion has NaCl concentration of 10 Mm. The readings presented in line graphs stand for the average of reading taken and calculated by the instrument's software.

3.2.2.9 Statistical analysis

Statistical comparisons were functioned by Prism application using unpaired t-test and one way ANOVA analysis. Values of $p < 0.05$ were considered statistically significant. The asterisk-sign *, **, *** and **** indicate $p < 0.05$, $p < 0.01$, $p < 0.001$ and $p < 0.0001$ respectively. Any other probabilities less than 0.0001 were denoted by ****.

3.3 Results

3.3.1 Yield of aminoacid-modified USPIONs

Yield of colloidally suspended, i.e. surface modified USPIONs was presented in terms of weight percent out of the initial powder amount mixed with the selected panel of amino acids. Applying the 'dry mixing technique with applied mechanical pressure', the effect of using two different amino acid forms, base or HCl salt, was initially tested. The data in Table 3-1 show that there is a highly significant difference ($p < 0.001$) between yields of the modified USPIONs, depending on the amino acid form. The data illustrate that the base form of an amino acid normally results in less than 0.5% of the NPs being modifies, i.e. successfully colloidally dispersed in the aqueous medium. On the other hand,

mixing of amino acids in their HCl salt form with USPIONs yielded improved, but variable percent of modified NPs, from 7.97% (in case of glutamic acid HCl salt) up to 66.48% (in case of lysine 2HCl).

The USPIONs stabilisation through mixing of the dispersion with the amino acids salts solutions method was assessed at a specific time points, at day 0, 1, 2 and 30 and then compared them against the corresponding results from the dry mixing method, as illustrated in Figure 3-3. On day zero , there are highly significant differences in the methods used ($p < 0.01, 0.001, 0.0001$) whereby, for example the yields were 23.5%, and 34.5% for the dry mixing method and 0.2% and 15.7% for the 'dispersion in the aminoacid solution method' for leucine HCl and methionine HCl, respectively. The only exception was in the case of glutamic acid HCl where a no significant change was noticed between the two methods.

Although some of yields recorded on day 1, 2, and 30 showed a significance increase ($p < 0.01$), the dispersion in the amino acid solution method is however, significantly ($p < 0.001$) less successful in stabilizing USPOINs colloidal suspension, in comparison to the dry mixing technique, for all experimental data collected. For example, on day 30 the yields of stabilised NPs were 53.6%, 45.3% and 66.6 % for dry mixing method, and 40.4%, 26.7% and 35.9% for the dispersion in the amino acid solution method, for glycine HCl, threonine HCl and lysine 2HCl salts, respectively.

In the second stage, the dry mixing method was employed to assess the effect of increasing a ratio of aminoacid salts to USPIONs on the yield of colloidally stable USPIONs. The profiles summarized in Figure 3-4 could be generally

viewed in two 'sections'. The first part represent a sharp increase in the percent of the modified, colloidally stable USPIONs upon increasing the amino acids amounts from 31.25 to approximately 125 or 250 µmole, while the second part might represent a plateau at which the yield is not further increased and, in some cases, in fact decreases as the concertation of amino acid is increased from 500 to 1000 µmole. It is interesting to note that using methionine HCl to stabilise the USPIONs gave rise to a slightly different trend from the above description, where the values show continuous increase in the yield of colloidally stable USPIONs as the methionine HCl concentration is increased from 31.25 to 1000 µmole.

Table 0-1: The yield of colloidally stable USPIONs using either amino acids as base or HCl salts. *'Dry powder mixing with applied mechanical pressure' method was applied. The initial quantity for all amino acids used was 62.5 µmole, and the initial amount of USPIONs was 28.75 mg. The samples were filtered through 0.2µm syringe filter to obtain the colloidally stable modified NPs dispersion. T-test statistical analysis has been followed to define the significant changes.*

Surface modifying agent	**Yield (%) of the modified USPIONs**	
	Amino acids (Base form)	**Amino acids (HCl salt form)**
Threonine	0.12 ± 0.0300	45.29 ± 1.8628
Glycine	0.18 ± 0.0305	53.63 ± 5.4247
Histidine	0.15 ± 0.0251	23.79 ± 7.2579
Leucine	0.13 ± 0.0316	23.49 ± 2.2010
Phenylalanine	0.09 ± 0.0200	34.56 ± 11.1085
Methionine	0.11 ± 0.0349	32.25 ± 0.1234
Lysine	0.20 ± 0.0737	66.48 ± 16.9256
Aspartic acid	0.37 ± 0.0929	38.90 ± 0.0165
Glutamic acid	0.26 ± 0.1305	7.97 ± 4.0810

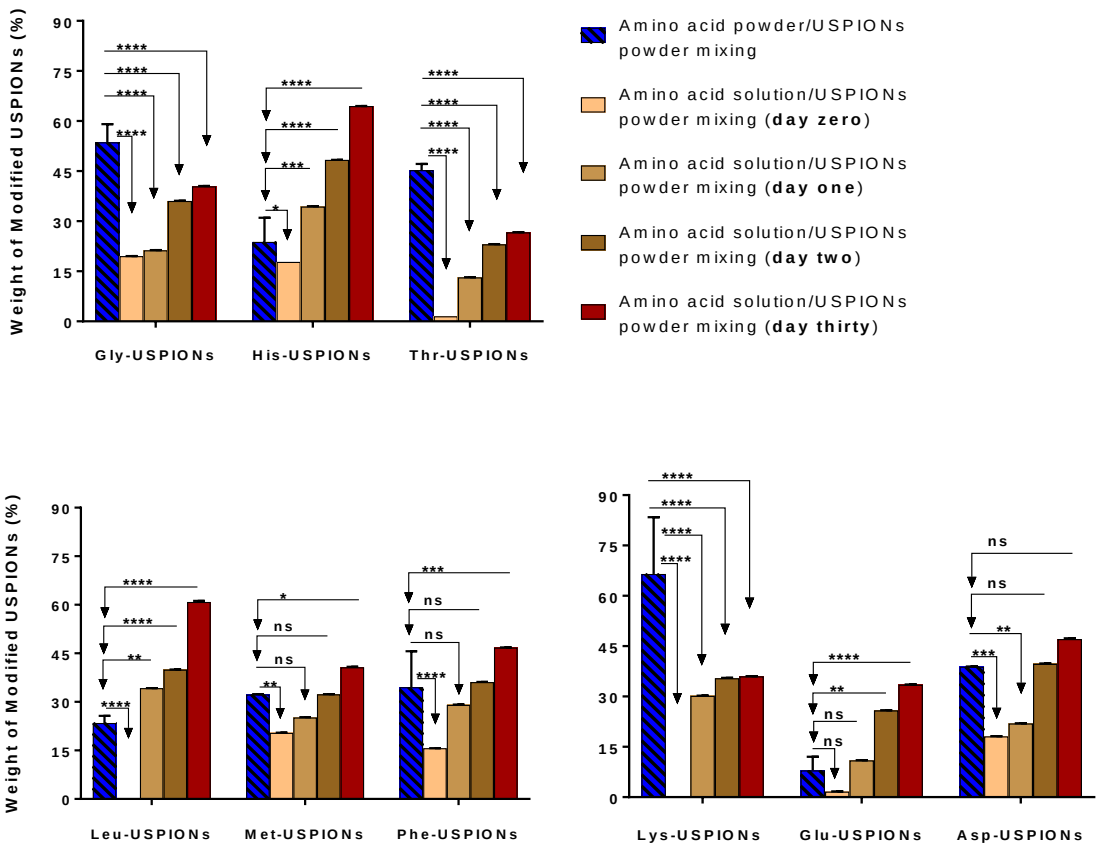


Figure 0-3: A bar graph showing the yields of aminoacid-modified USPIONs prepared using two different methods.

*Dry powder mixing with applied mechanical pressure (blue bars) and dispersion in aminoacid solution (beige to dark brawn bars) are included. USPIONs amounts were expressed in term of weight percent in relation to the initial amount used. The initial quantities of each aminoacid were fixed to be 62.5 µmole while the mass of the USPIONs was 28.75 mg as determined from ICP-MS instrument. Error bars represent +/- 1SD of the average value. T-test statistical analysis has been followed to define the significant changes. *, **, *** and **** denotes a significant increase ($p < 0.05$, 0.01, 0.001 and 0.0001 respectively) in USPIONs amount successfully modified. 'ns' refer to no significant change in the recorded values*

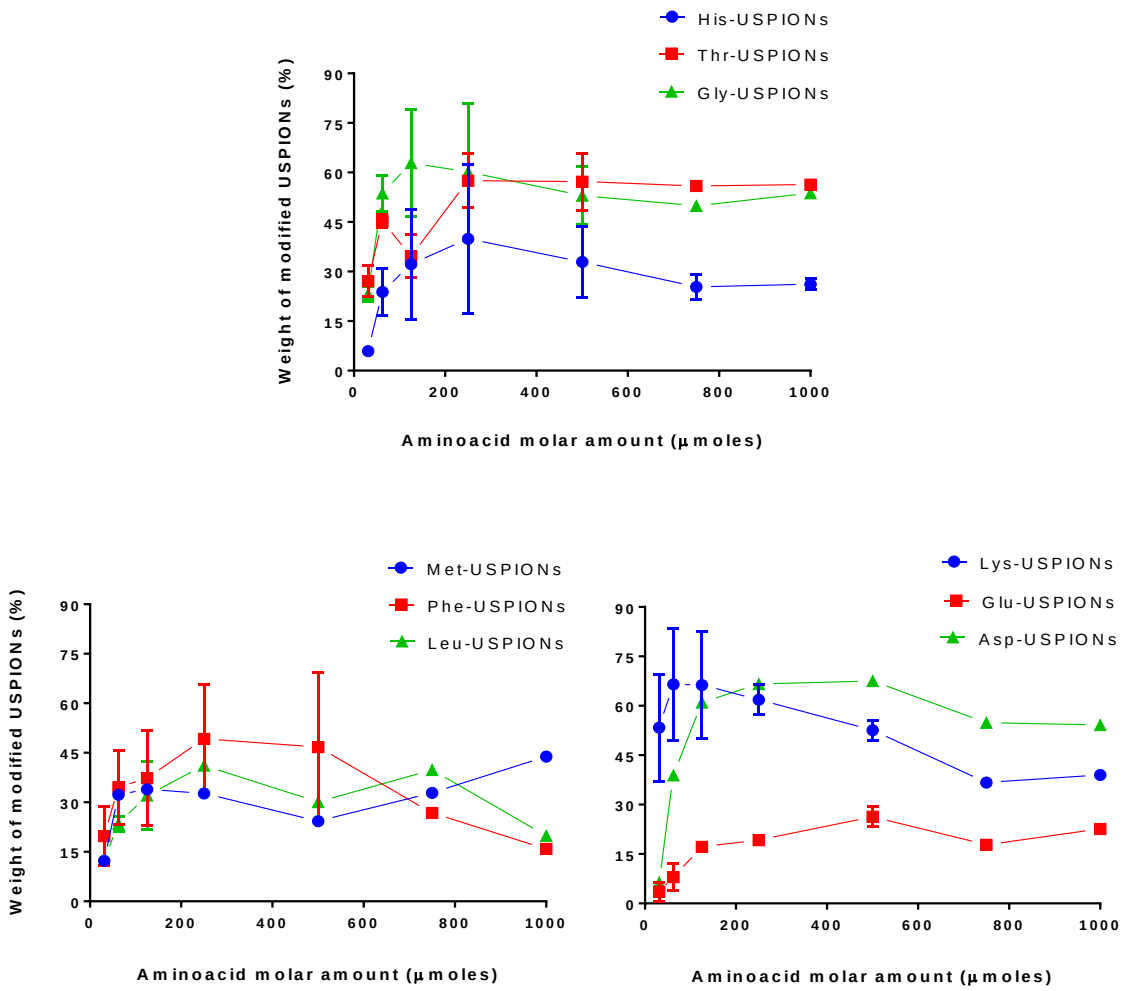
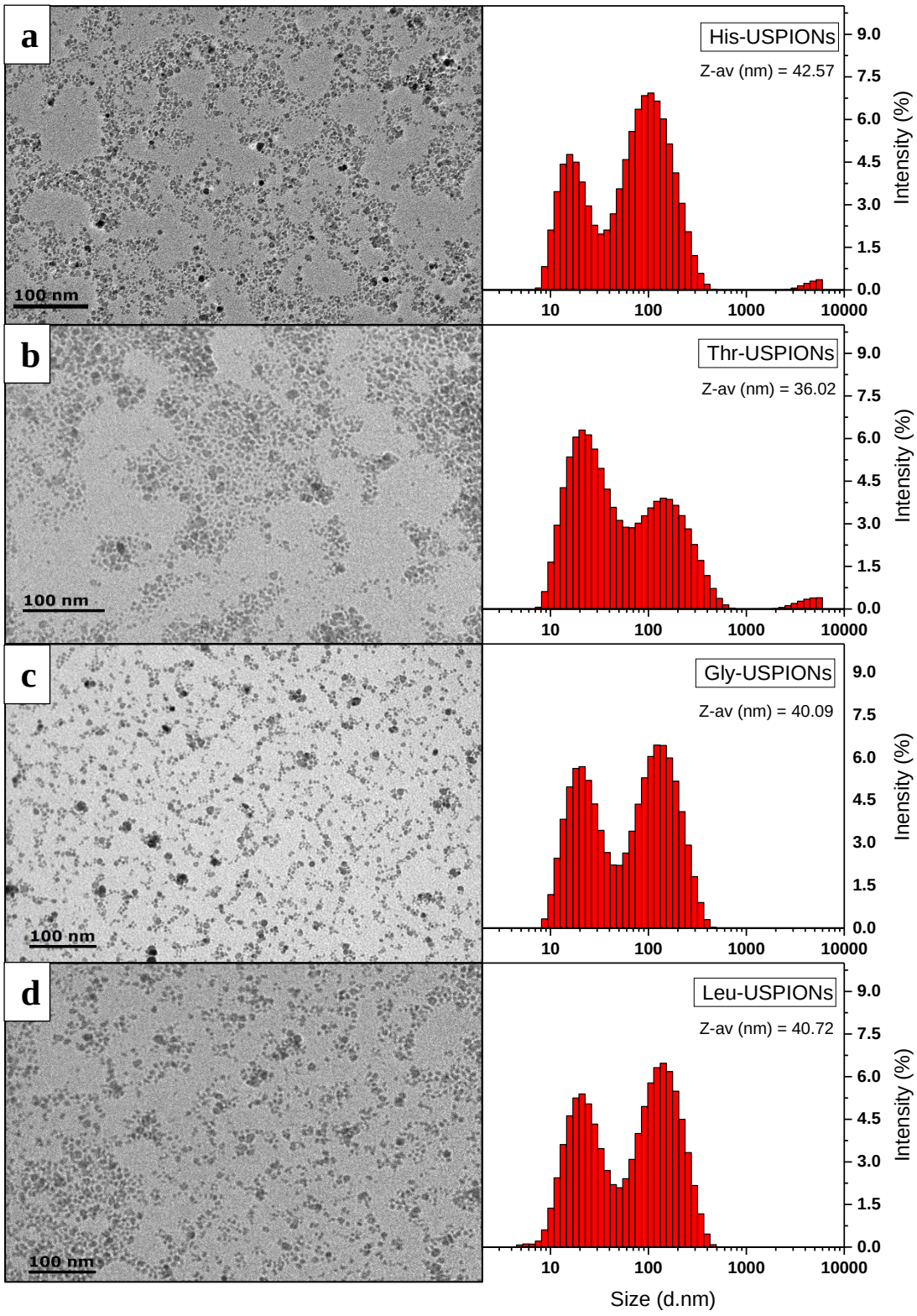


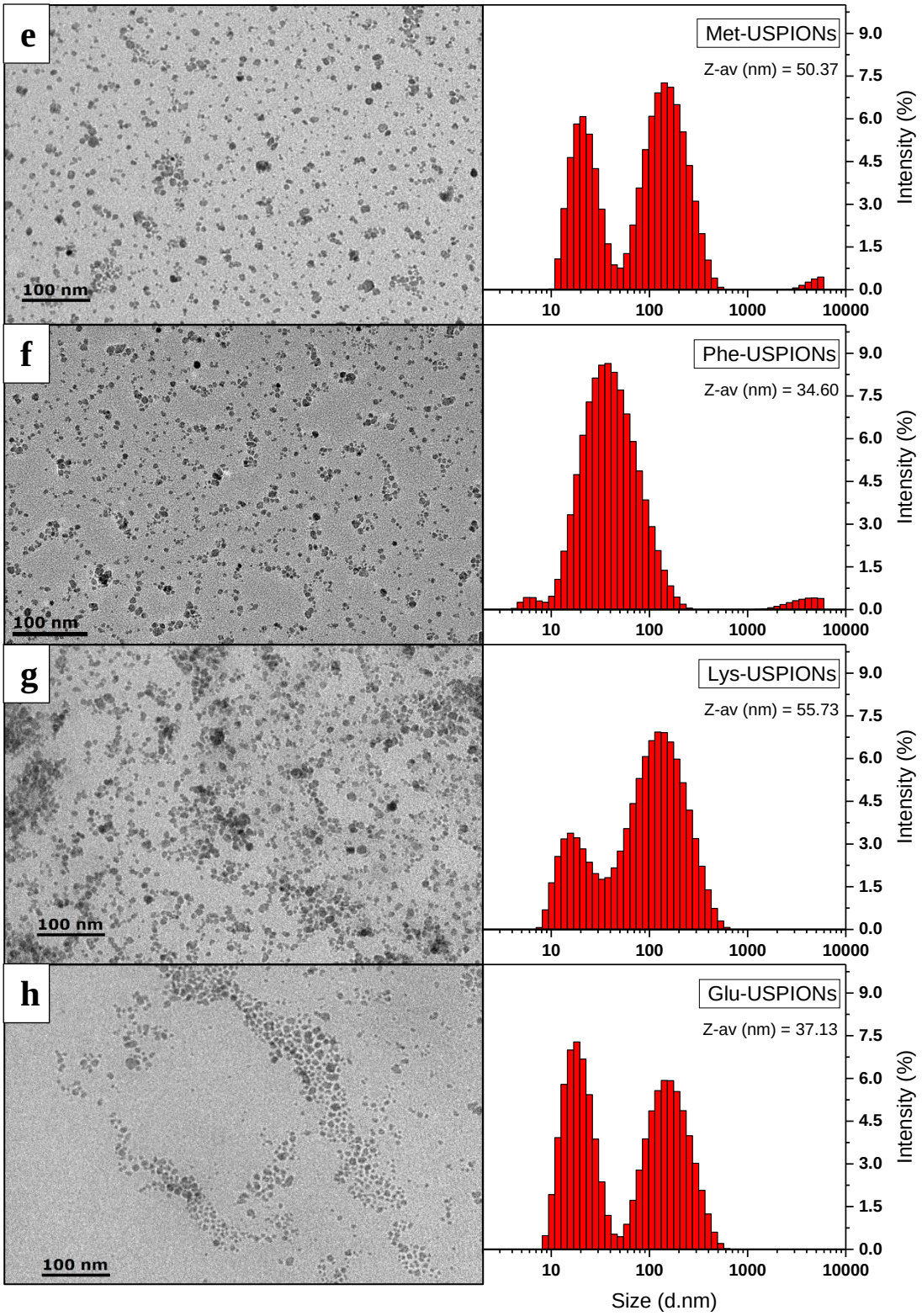
Figure 0-4: Yield of aminoacid-modified, colloidally stable USPIONs versus different quantities of amino acids monomers.

The USPIONs amounts were expressed in term of weight percent in relation to the initial amount used. As a powder, amino acid HCl salts were mixed with a fixed quantity of NPs (28.75 mg) in a mortar with an applied hand pressure for around 5min. The mixture was suspended in 10 ml of water and filtered through 0.2µm syringe filter to yield colloidally stable, modified NPs. Amount of USPIONs was determined from ICP-MS analysis. Error bars represent +/- 1SD of the average value.

3.3.2 Particle size and TEM images of aminoacid-modified USPIONs

Measurements of hydrodynamic size of aminoacid-modified USPIONs are summarized in Figure 3-5. The data illustrate that most of the particle size distributions, determined using light scattering, show presence of two intensity peaks at 15-21 nm and at 100-250 nm, with exception of NPs modified with phenylalanine (figure 3-5f) which have a distribution histogram with only one peak at around 37.8 nm. Morphology of coated USPIONs, from TEM analysis, is illustrated next to the corresponding histograms.


a
100 nm
His-USPIONs
Z-av (nm) = 42.57
b
100 nm
Thr-USPIONs
Z-av (nm) = 36.02
c
100 nm
Gly-USPIONs
Z-av (nm) = 40.09
d
100 nm
Leu-USPIONs
Z-av (nm) = 40.72
Intensity (%)
Inensity (%)
9.0
7.5
6.0
4.5
3.0
1.5
0.0
10
100
1000
10000
Size (d.nm)


e
100 nm
Met-USPIONs
Z-av (nm) = 50.37
f
100 nm
Phe-USPIONs
Z-av (nm) = 34.60
g
100 nm
Lys-USPIONs
Z-av (nm) = 55.73
h
100 nm
Glu-USPIONs
Z-av (nm) = 37.13
Intensity (%)
0.0
1.5
3.0
4.5
6.0
7.5
9.0
10
100
1000
10000
Size (d.nm)

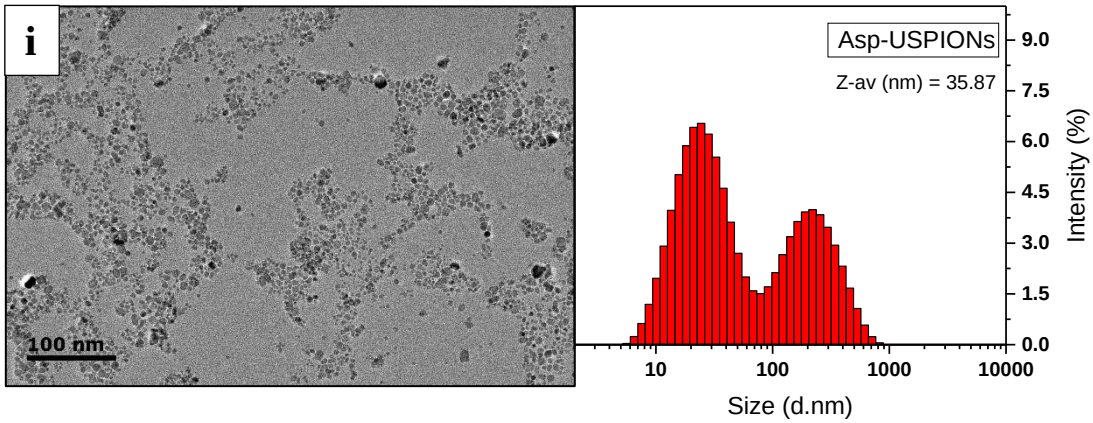


Figure 0-5: Morphology (TEM micrographs) and particle size distribution histograms for aminoacid-modified USPIONs.

The modified USPIONs were prepared according the standard procedure by 'dry mixing method' where 250 µmole of aminoacid was mixed with 28.75 mg of bare USPIONs. After 5 min mixing, the powder was dispersed in 10 ml of deionised water and filtered through 0.2µm syringe filter to obtain the colloidally stable modified NPs dispersion. For the hydrodynamic size, three independent measurement with 15 sub-runs were performed. The mean particles size values shown in the graphs.

3.3.3 TGA of amino acids associated with USPIONs

The data from TGA are shown in Figures 3-6 and 3-7. In addition, Figure 3-6 shows a comparison between the thermal stability of both bare and surface modified NPs. The line graph of the bare USPIONs shows that only 6.2% out of the starting weight (i.e. 93.8% remaining) was lost by the end of heating process at 900°C. On the contrary, more than 65% of the initial weight was lost for aminoacid-modified USPIONs samples. This indicate that for histidine, threonine, and glycine, 32.8%, 29.2% and 27.5%, respectively, of the sample mass could be ascribed to the USPIONs-associated aminoacid.

It was also noticed that the thermal behaviour of the modified NPs is characterised by multi-step gradual degradation and weight loss. Figure 3-7 allows the USPIONs thermal behaviour to be discussed in more details, as follows. For histidine HCl salt, the weight loss observed at temperature equal and below 200°C can be ascribed to the physically and chemically (lattice) associated water [32] where the maximum rate of weight loss recorded at this stage is 0.21%/°C. The next stage of weight loss likely represents histidine degradation, which occurs at two steps, 250.8°C and 312.7°C for the free histidine and 296.9°C and 425.2°C for histidine modified USPIONs. The rate of decomposition was ranging between 0.43-0.35%/°C and 0.12-0.07%/°C for both samples, respectively. An additional degradation stage was detected between > 600°C and < 750°C with a peak rate of 0.28%/°C at 735.6°C for the histidine modified USPIONs.

For threonine HCl salt, the first stage that can be attributed to the water loss occurred at a temperature below 150°C, where the maximum rate of loss was noticed at 138.3 and 122.5°C for free salt and the coated USPIONs. Rates of 1.15 and 0.29%/°C for the peaks of a second weight reduction can be related to threonine decomposition at 220.4 and 179.9°C, respectively. Moreover, decomposition of the threonine modified USPIONs underwent further decay steps extended from 275.5 to 795.3°C.

For glycine HCl, the thermogravimetric line graphs of the free amino acid (red and blue lines) show one major weight loss period with maximum pyrolysis rate of 0.75%/°C at temperature of 249.7°C in which around 58.3% (94.6% - 36.3%) of the initial mass was lost [33,34]. It is also noticed that the lattice water was responsible for the initial stage of mass reduction seen at temperature less than

167.5°C. In addition, the decomposition of residual product continued over the range of experimental temperature up to 900°C so that the final mass remained was equal to 16.2%.

The thermal behaviour of glycine modified USPIONs (red and blue dashed-lines) illustrate the presence of five stages of mass loss with degradation rate peaks at 146.2°C, 241.8°C, 295.8°C, 660.3°C, and 829.1°C. The first weight reduction stage is again associated with the physically and chemically adsorbed water, while the further stages are related to the decomposition of glycine monomer and its thermal fragments. It is important to note that the rate of mass degradation did not exceed 0.16%/°C at the maximum and the weight remained at the end of the experiment is ~ 27.5%.

For free methionine HCl, thermal behaviour analysis (denoted by red and blue lines) shows three distinctive mass reduction stages. The initial weight loss occurred at 174.3°C, and is clearly related to lattice water release, while the second and third reductions in weight likely result from aminoacid's condensation and degradation [35]. The dual-step methionine decomposition at 244.1°C and 293.6°C accounts for 81.5% (91.2% – 9.7%) of observed mass loss. In addition, decomposition of thermal fragments are responsible for the further reduction in weight up to 2.6%.

TGA analysis of methionine modified USPIONs, exhibits two mass reduction stages. The early weight loss with the rate peaks at 101.2°C and 168.7°C could be attributed to the physical and chemical water elimination, respectively while the following stages of weight loss with rate peaks at 244.1°C and 300.3°C are related to the coordinated aminoacid's pyrolysis. The later stage gives rise to

weight loss of around 35.9% (87.4% – 51.5%). There is also a gradual decomposition of thermal product from ~350°C to the end of operated temperature range, which results in the final residues with approximately 20% (50% - 30%) out of the initial mass.

In case of phenylalanine HCl, the initial peak of water loss is observed at 184.4°C for the free aminoacid, while in the case of modified USPIONs this occurs at 159.7°C. Further major weight losses, equal to between 100% and 62.2% (90.4% - 28.2%), occurred at temperature ranges of 210°C to 323°C and 190°C to 400°C [36] and are related to decomposition and volatilisation of both free and coordinated amino acid, respectively. It was further notices that the mass of phenylalanine modified USPIONs continued to decrease down to 10.2% of the initial mas, indicating thermal pyrolysis. The maximum rate of weight loss is 1.97%/°C and 1.45%/°C for the free and 0.5%/°C and 0.38% for phenylalanine modified USPIONs.

In case of leucine HCl, both free aminoacid and modified USPIONs released their water at maximum rate of 0.37%/°C at 151.8°C, and 0.07%/°C at 116.9°C, respectively. Compound decomposition occurred in one sharp step, with rate of 2.3%/°C at 251.9°C, is responsible for 86.7% of the mass loss for the free leucine, while for the corresponding USPIONs samples, 84.8% of the initial mass underwent slow pyrolysis process over four separate steps of descending rates as the temperature increased from 232.8°C to 553.4°C.

In case of lysine HCl salt, the lattice water was lost released from free amino acid samples at 187.8°C, while for the corresponding coordinated one this occurred over two steps at 158.6°C and 188.9°C. Similar to leucine TGA, the

thermal behaviour of free lysine shows decomposition stage of two major and minor steps with the rate of 0.93%/°C at 307.1°C, and 0.16%/°C at 421.8°C, respectively in which around 86.8% of the initial mass was lost. On the other hand, pyrolysis for the modified USPIONs exhibits four-step degradation process with a moderate rate and extended over a wide range of temperatures where peaks of 335.2°C, 408.3°C, 593.9°C, and 704.2°C were observed, as illustrated Figure 3-7. The weight loss for the modified USPIONs was calculated to be approximately 51.8%.

With glutamic acid HCl, thermal analysis of the free amino acid reveals no separate water release phase, instead, a massive mass reduction stage which has three distinct peaks at 212.6°C, 256.5°C, and 302.6°C is related to a glutamic acid decomposition [37]. For the corresponding modified USPIONs, the pyrolysis pattern underwent a remarkable change in which an earlier sharp and slower mass reduction stage, with a lower maximum rate (0.61%/°C at 177.7°C), extended from ~ 107.7°C to 245.8°C and was followed by a second decomposition phase with double peaks at 320.6°C and 363.3°C. An additional late phase of mass reduction was observed at a high temperature (> 600°C) with peak rate of 0.15%/°C at 771.7°C, and could be attributed to thermal fragments degradation.

In case of aspartic acid, the thermal behaviour of both free amino acid and USPIONs associated is characterised by an initial water desorption phase and a dual-step compound decomposition stage. The aspartic acid sample released most of its lattice water molecules in one step with a peak rate at 170.9°C. In contrast, water desorption for the corresponding USPIONs associated samples occurred over a wider temperature range from 88.83°C to 123.70°C. For the

main decomposition, a dual-step stage occurred at lower temperature with slower weight loss rate (maximum rate ~0.36%/°C at 192.3°C and ~0.2%/°C at 328.4°C) for modified USPIONs in comparison with that of the corresponding free aspartic acid (maximum rate ~0.85%/°C at 203.6°C and 0.7%/°C at 364.4°C). An additional, delayed mass loss was noticed at high temperature of 615.3°C which could be attributed to the pyrolysis of modified USPIONs' aspartic acid.

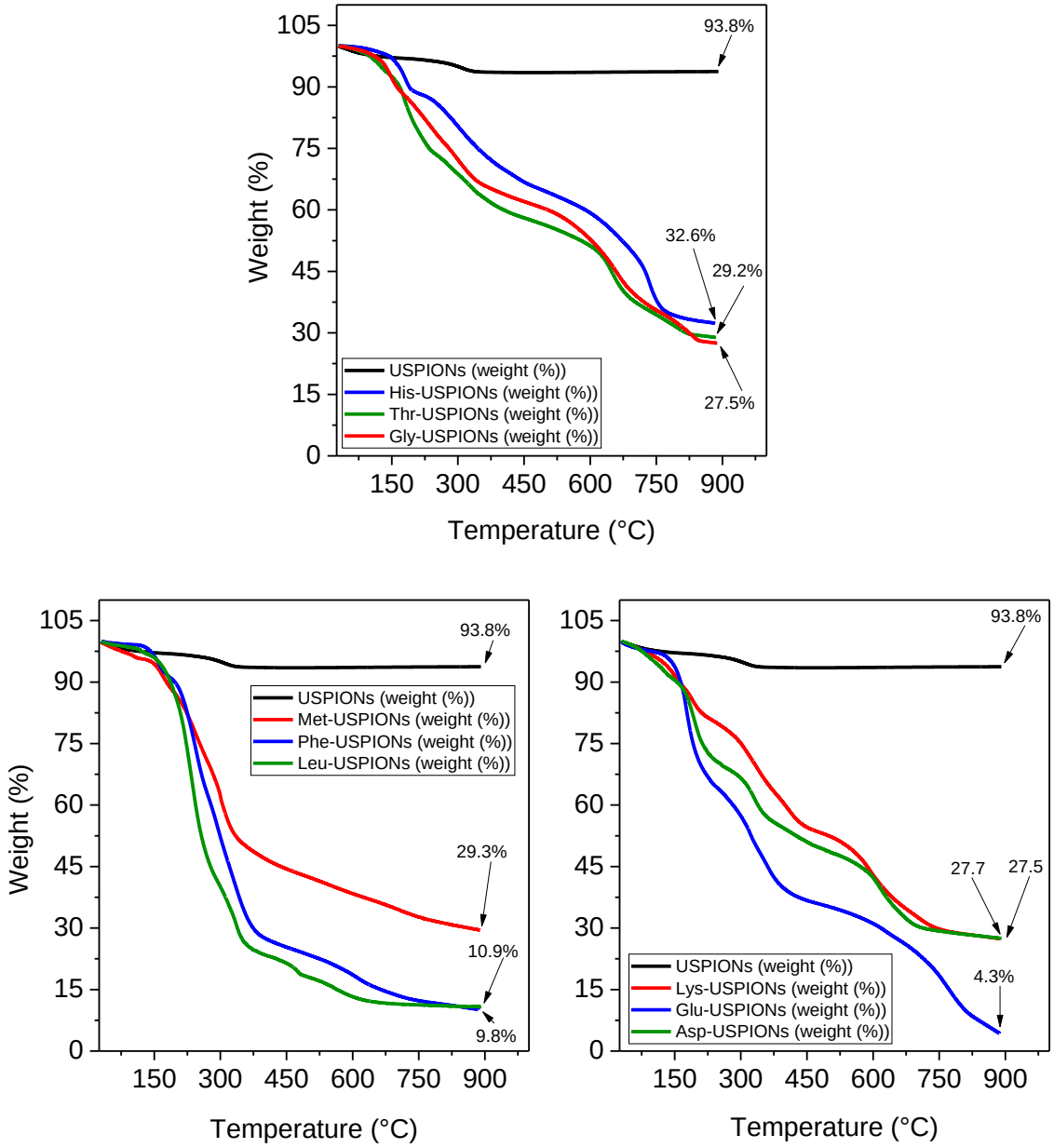
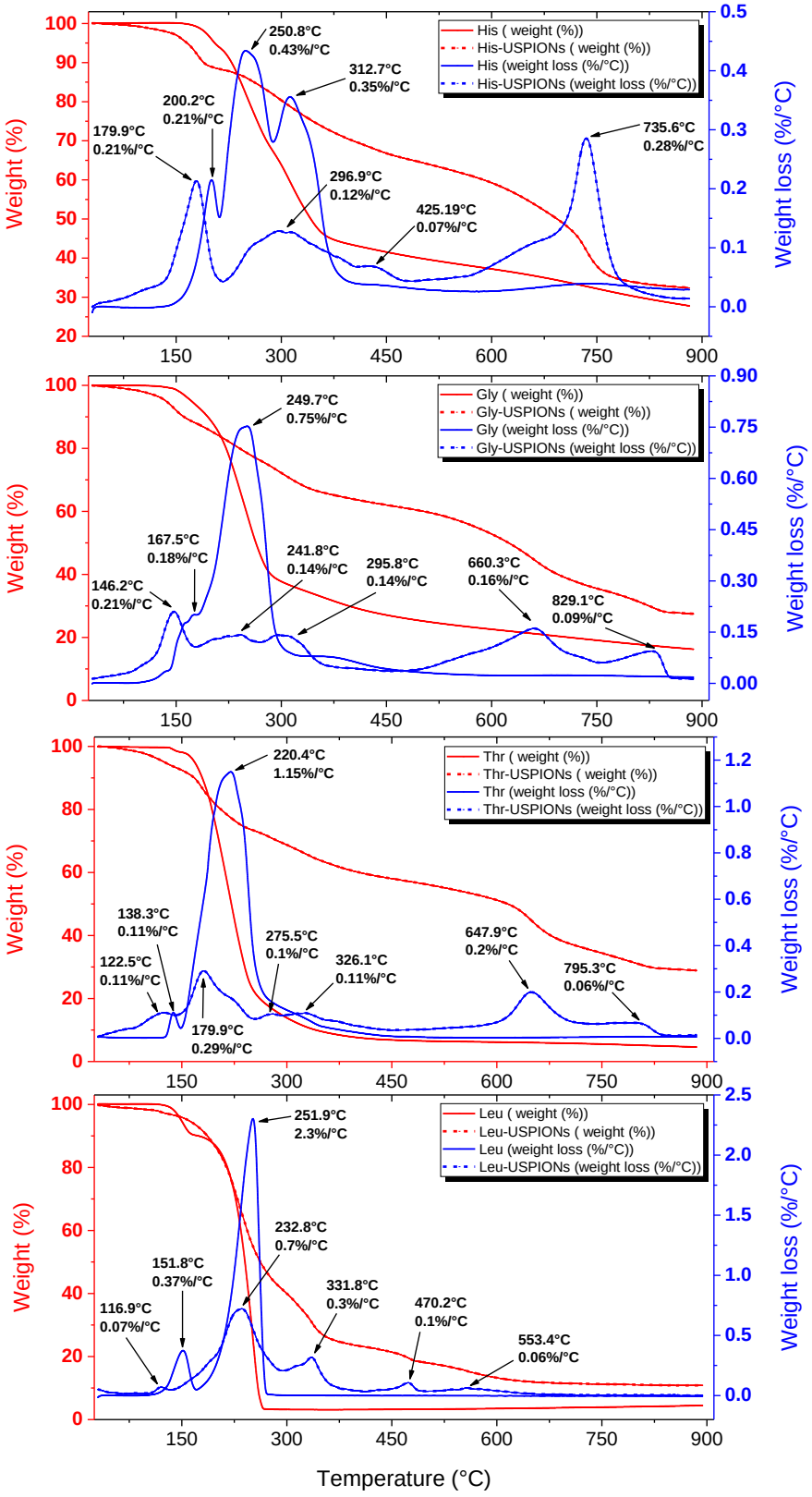
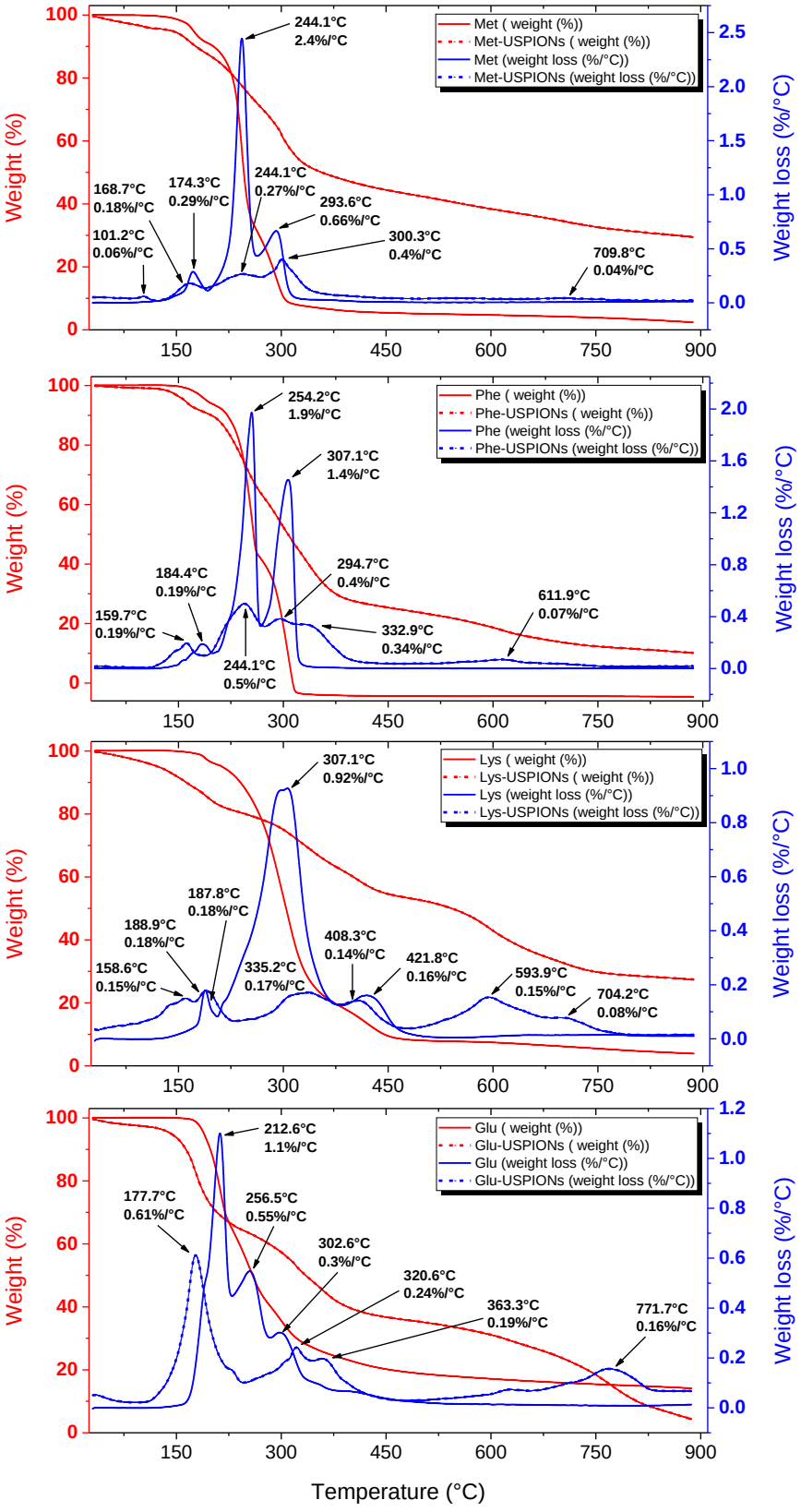


Figure 0-6: TGA of bare and USPIONs modified with selected amino acids.

The samples were heated up to 900°C at rate of 20°C/min and under nitrogen gas atmosphere of 100 ml/min so as to prevent any thermoxidative degradation. A platinum pan was used to house the tested powders of variable weights. The results were expressed as line graphs of a percent mass loss as a function of temperature.


His (weight (%))
His-USPIONs (weight (%))
His (weight loss (%/°C))
His-USPIONs (weight loss (%/°C))
250.8°C
0.43%/°C
312.7°C
0.35%/°C
200.2°C
0.21%/°C
179.9°C
0.21%/°C
735.6°C
0.28%/°C
296.9°C
0.12%/°C
425.19°C
0.07%/°C
Gly (weight (%))
Gly-USPIONs (weight (%))
Gly (weight loss (%/°C))
Gly-USPIONs (weight loss (%/°C))
249.7°C
0.75%/°C
167.5°C
0.18%/°C
241.8°C
0.14%/°C
295.8°C
0.14%/°C
660.3°C
0.16%/°C
146.2°C
0.21%/°C
829.1°C
0.09%/°C
Thr (weight (%))
Thr-USPIONs (weight (%))
Thr (weight loss (%/°C))
Thr-USPIONs (weight loss (%/°C))
220.4°C
1.15%/°C
138.3°C
0.11%/°C
275.5°C
0.1%/°C
326.1°C
0.11%/°C
647.9°C
0.2%/°C
122.5°C
0.11%/°C
795.3°C
0.06%/°C
179.9°C
0.29%/°C
Leu (weight (%))
Leu-USPIONs (weight (%))
Leu (weight loss (%/°C))
Leu-USPIONs (weight loss (%/°C))
251.9°C
2.3%/°C
232.8°C
0.7%/°C
151.8°C
0.37%/°C
331.8°C
0.3%/°C
470.2°C
0.1%/°C
116.9°C
0.07%/°C
553.4°C
0.06%/°C
Weight (%)
Weight loss (%/°C)
Temperature (°C)


Met (weight (%))
Met-USPIONs (weight (%))
Met (weight loss (%/°C))
Met-USPIONs (weight loss (%/°C))
244.1°C
2.4%/°C
168.7°C
0.18%/°C
174.3°C
0.29%/°C
244.1°C
0.27%/°C
293.6°C
0.66%/°C
101.2°C
0.06%/°C
300.3°C
0.4%/°C
709.8°C
0.04%/°C
Phe (weight (%))
Phe-USPIONs (weight (%))
Phe (weight loss (%/°C))
Phe-USPIONs (weight loss (%/°C))
254.2°C
1.9%/°C
307.1°C
1.4%/°C
184.4°C
0.19%/°C
294.7°C
0.4%/°C
159.7°C
0.19%/°C
611.9°C
0.07%/°C
332.9°C
0.34%/°C
244.1°C
0.5%/°C
Lys (weight (%))
Lys-USPIONs (weight (%))
Lys (weight loss (%/°C))
Lys-USPIONs (weight loss (%/°C))
307.1°C
0.92%/°C
187.8°C
0.18%/°C
188.9°C
0.18%/°C
408.3°C
0.14%/°C
421.8°C
0.16%/°C
158.6°C
0.15%/°C
335.2°C
0.17%/°C
593.9°C
0.15%/°C
704.2°C
0.08%/°C
Glu (weight (%))
Glu-USPIONs (weight (%))
Glu (weight loss (%/°C))
Glu-USPIONs (weight loss (%/°C))
212.6°C
1.1%/°C
177.7°C
0.61%/°C
256.5°C
0.55%/°C
302.6°C
0.3%/°C
320.6°C
0.24%/°C
363.3°C
0.19%/°C
771.7°C
0.16%/°C
Weight (%)
Weight loss (%/°C)
Temperature (°C)

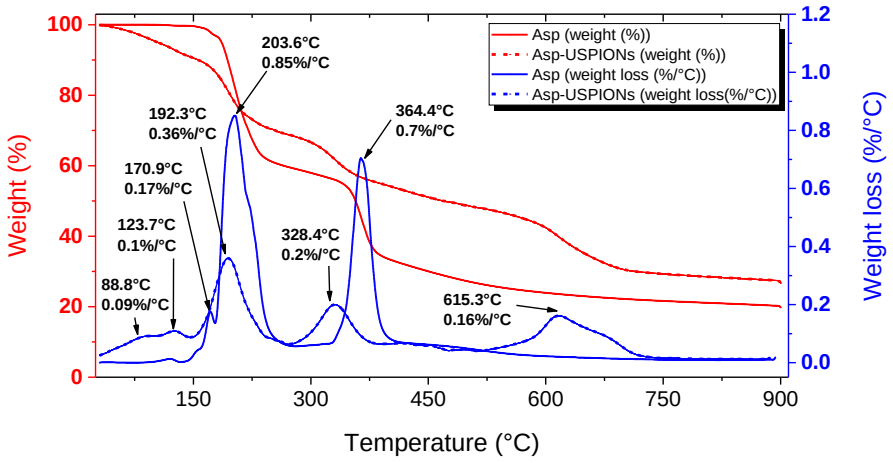


Figure 0-7: Thermal stability analysis of free amino acids and corresponding USPIONs-coordinated.

The both red lines represent a decline in mass as a function of temperature, while the blue line represents the rate of mass loss within the same temperature range. USPIONs were modified with amino acids using equal mass quantities. The samples were heated to 900°C at 20°C/min and under nitrogen gas atmosphere at 100 ml/min so as to prevent thermoxidative degradation. A platinum pan was used to house the tested powders of variable weights.

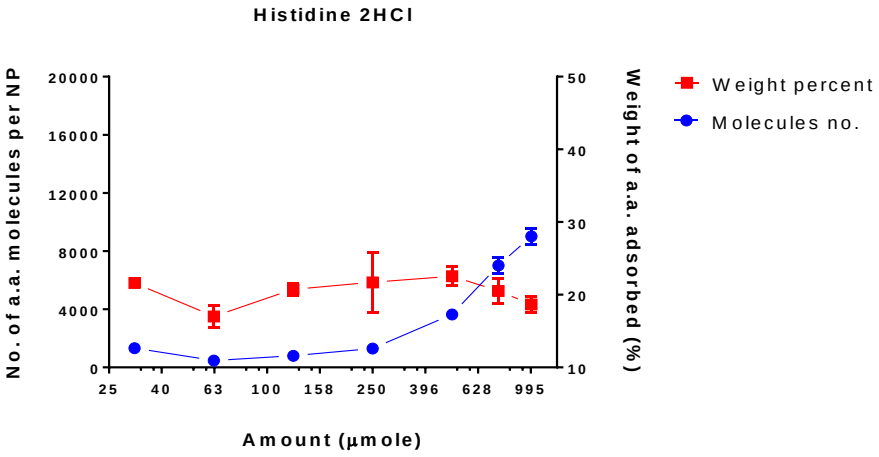
3.3.4 The mass and number of molecules of the adsorbed amino acids on USPIONs surfaces

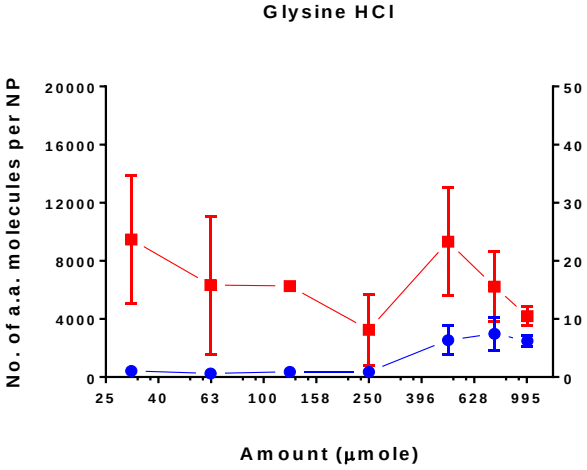
The amount of surface modifying amino acids associated with the USPIONs was assessed for two separate experiments, USPIONs modified by ‘dry powder mixing’ and the ‘dispersion in solution’ protocol and the data are shown in Figures 3-8 and 3-9.

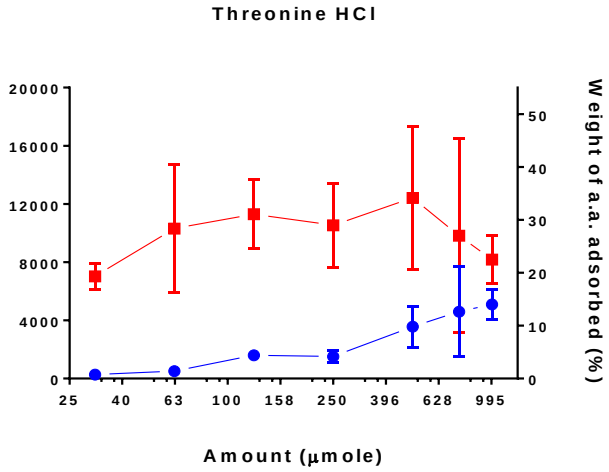
Figure 3-8 presents the amount of USPIONs associated amino acid in terms of (i) weight percent (red line), and (ii) number of molecules (blue line). It was found that, for the all amino acids HCl salts used, the number of USPIONs associated molecules increased in proportion to the aminoacids’ amount initially mixed with USPIONs. This increase occurred in two distinctive stages. The first

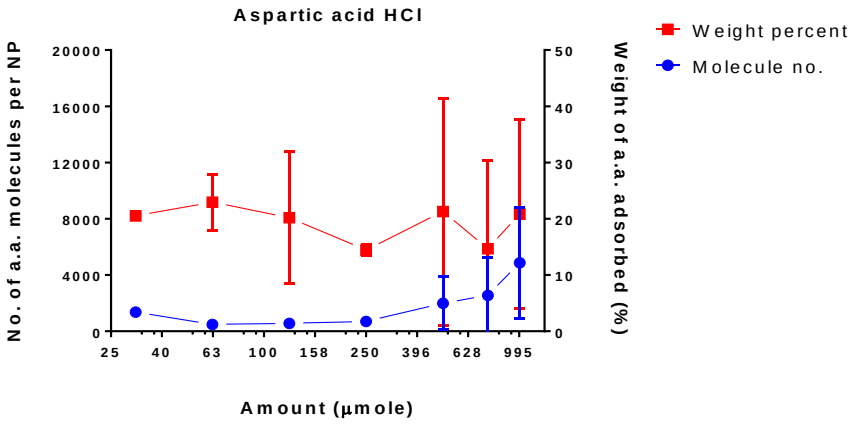
smaller increment was noticed upon using amino acids quantities less than 250 µmole, while the second, sharp raise occurred when the amino acids amounts were increased from ~250-500 µmole up to the highest amount selected of 1000 µmole. As an example, for threonine, lysine and phenylalanine, the average number of molecules adsorbed onto the surface of each individual NP increased from around 270, 76 and 339 to 1514, 1634 and 1741, when the initial amounts of the three amino acids were increased from 31.25 µmole up to 250 µmole respectively. The values of 5098, 11116, and 12672 molecules were found to be associated with individual NPs when 1000 µmole of the amino acid powder was used, respectively.

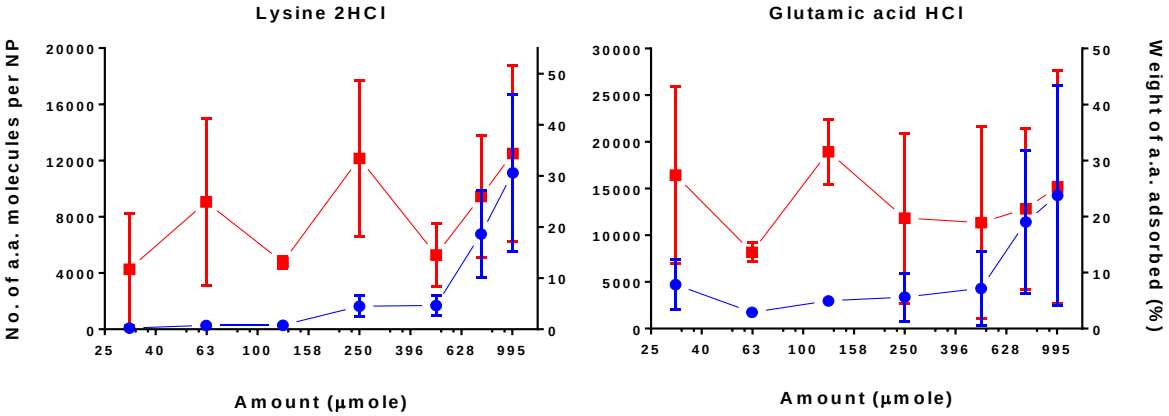
Table 3-2 clearly exhibits significant differences ($p < 0.01$) between the amounts of the amino acids that are associated with the surface of USPIONs using the 'dry powder' and the 'dispersion in solution' mixing techniques. The tabulated data indicate a dramatic increase in the weight percent of the NPs-associated monomers after using the 'dry powder' mixing method in comparison with these of the 'dispersion in solution' mixing where, as an example, for leucine HCl, glutamic acid HCl and histidine salts, the weight increase is found to be 13.8%, 13.6%, and 17.0% after the 'dry mixing' method while for the 'dispersion in solution' protocol the corresponding values are 2.8%, 1.5%, and 2.5%, respectively.


Histidine 2HCl
No. of a.a. molecules per NP
Weight of a.a. adsorbed (%)
Weight percent
Molecules no.
Amount (µmole)


Glysine HCl
No. of a.a. molecules per NP
Amount (µmole)


Threonine HCl
Weight of a.a. adsorbed (%)
Amount (µmole)


Aspartic acid HCl
Weight percent
Molecule no.
No. of a.a. molecules per NP
Weight of a.a. adsorbed (%)
20000
16000
12000
8000
4000
0
50
40
30
20
10
0
25
40
63
100
158
250
396
628
995
Amount (µmole)


Lysine 2HCl
Glutamic acid HCl
No. of a.a. molecules per NP
Weight of a.a. adsorbed (%)
20000
16000
12000
8000
4000
0
30000
25000
20000
15000
10000
5000
50
40
30
20
10
25
40
63
100
158
250
396
628
995
Amount (µmole)
Amount (µmole)

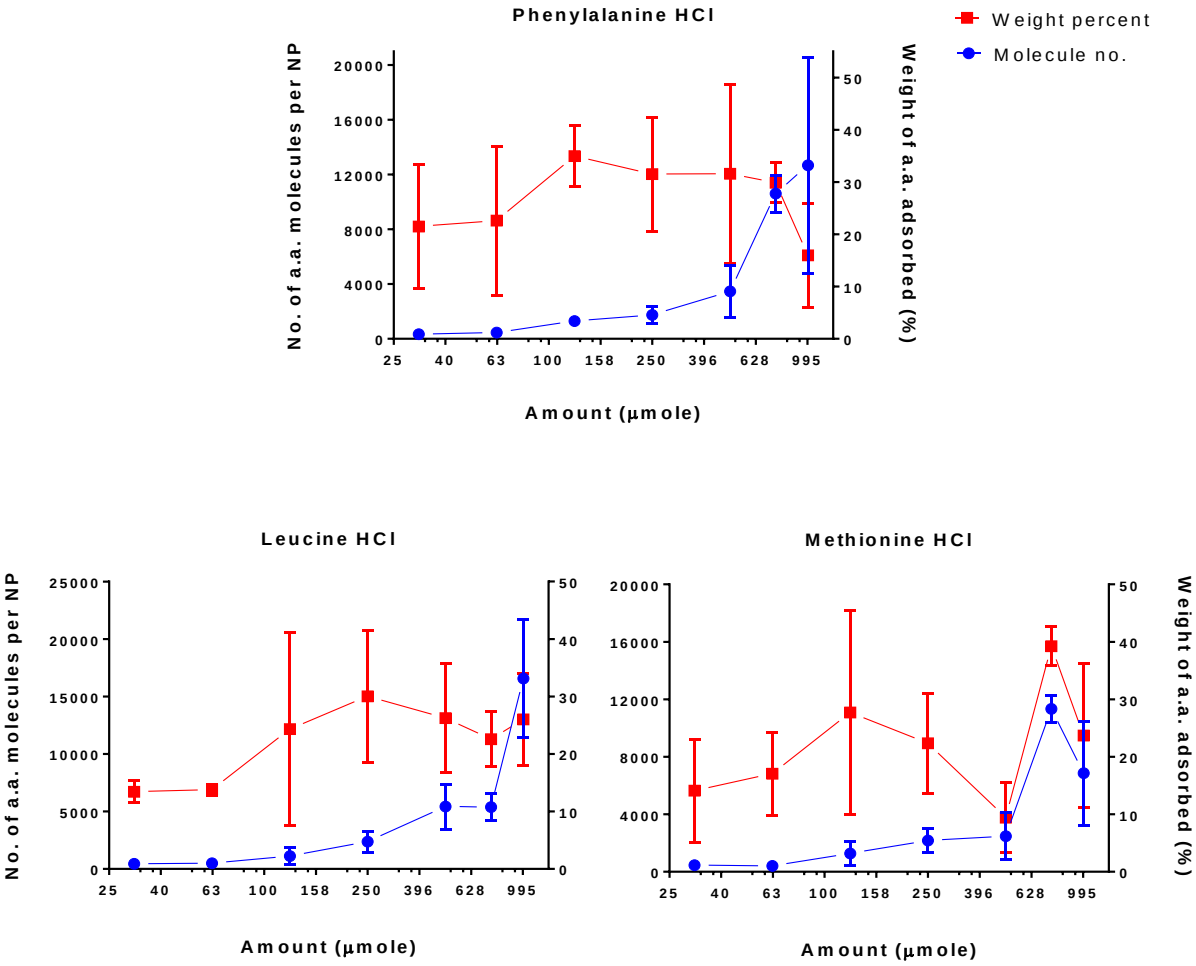


Figure 0-8: USPIONs surface modification at increasing aminoacids' amounts

For each amino acid used, the associated amount was expressed in terms of weight percent (red line) and number of molecules (blue line). 'Dry mixing with applied pressure' was adapted for USPIONs surface modification with amino acids. The USPIONs amount was fixed at 28.75 mg and triturated with increasing amounts of amino acid powder for ~ 5 min. The final mixtures were suspended in 10 ml of deionised water. The amount of the USPIONs associated amino acid was detected by fluorescamine test of the USPIONs supernatant following centrifugation. The data represents mean ± 1SD (error bar) of three independent experiments.

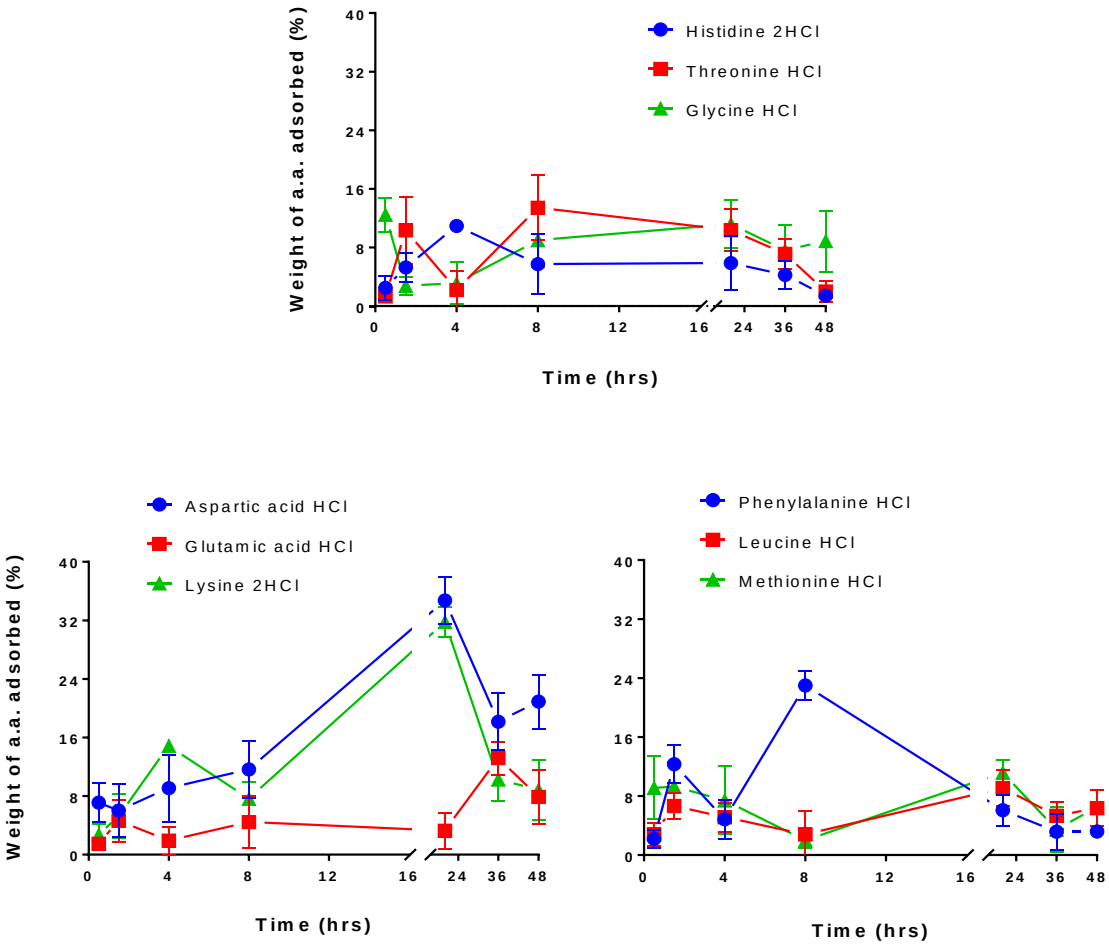


Figure 0-9: Amount of USPIONs associated amino acid as a function of time.

The NPs modification method is 'dispersion in amino acid solution'. For each amino acid used, the USPIONs associated amount was expressed in terms of weight percent. Aqueous solutions of amino acid HCl salts were first prepared by dissolving 62.5 µmole in 10.0 ml of deionised water and then mixed with 28.75 mg of USPIONs dry powder. The amount of USPIONs associated aminoacid was detected by fluorescamine test and discrete time points over 48 hrs. The data represents mean ± 1SD (error bar) of three independent experiments.

Table 0-2: Amounts of USPIONs associated amino acid following two different NPs modification methods.

For the both mixing strategies, the initial amount of amino acid used was 62.5 µmole, the weight of the USPIONs was fixed at 28.75 mg. The tabulated data represent mean ± SD of three different experiments.

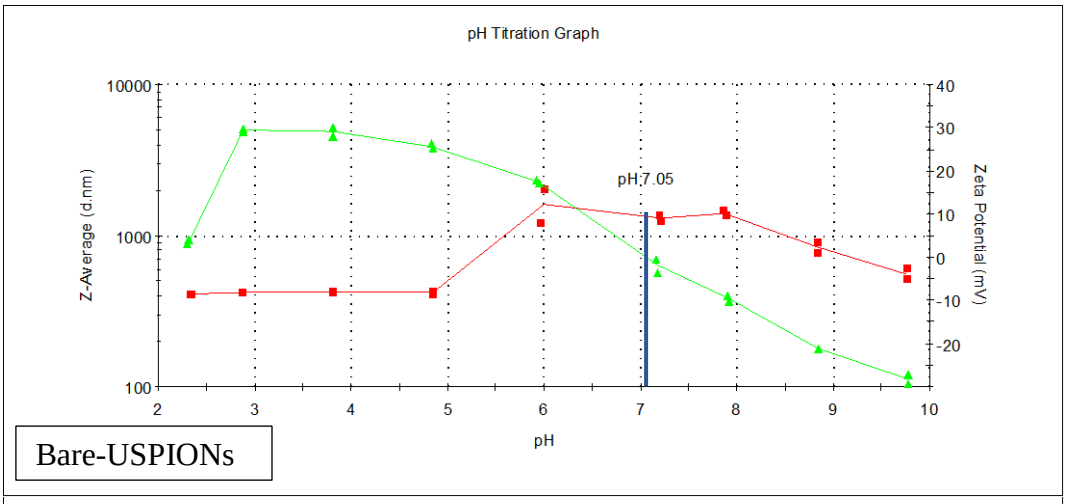
Surface modifying aminoacid (salt)	**USPIONs associated aminoacid (% w/w)**	
	'Dry powder mixing' method	**'Dispersion in solution' method**
Histidine 2HCl	17.0 ± 1.53	2.5 ± 1.65
Threonine HCl	28.3 ± 12.05	1.3 ± 0.72
Glycine HCl	15.9 ± 11.90	12.4 ± 2.31
Aspartic acid HCl	22.9 ± 5.00	7.1 ± 2.68
Glutamic acid HCl	13.6 ± 1.70	1.5 ± 0.79
Lysine 2HCl	24.9 ± 16.34	2.7 ± 1.52
Phenylalanine HCl	22.6 ± 14.28	2.2 ± 1.25
Leucine HCl	13.8 ± 0.98	2.8 ± 1.58
Methionine HCl	17.1 ± 7.24	9.1 ± 4.27

3.3.5 Colloidal properties of dispersion of aminoacid-modified USPIONs

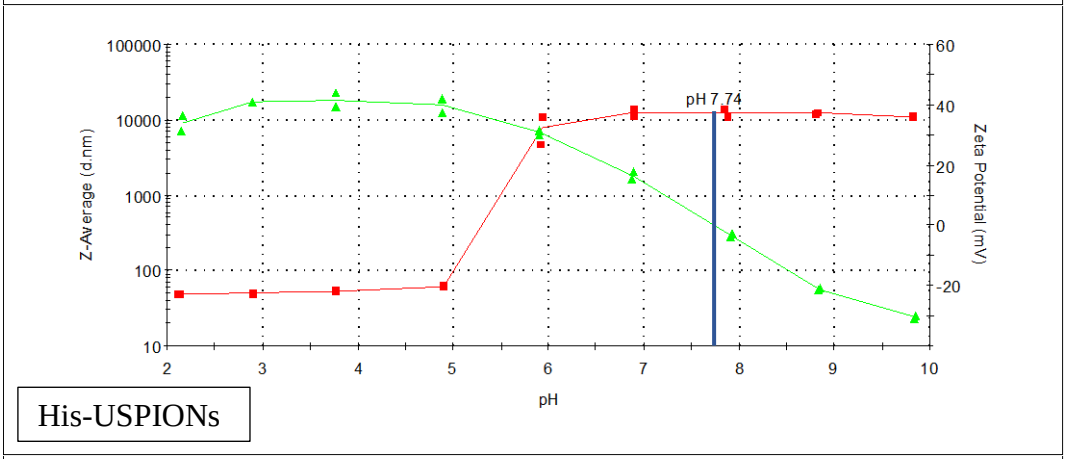
Figure 3-10 illustrates the change in the zeta potential and hydrodynamic particle size over increasing pH of the suspending medium from ~ pH 2 to 10. In general, the zeta potential trend shows an initial phase of slight reduction in values from around +40 / +35Mv to around +35 / +30Mv when the medium acidity was decreased from pH 2 to pH 5. In the neutral pH region, a sharp decline in the particles charge was observed, where this reduction continued to a reversal in the zeta potential to -20 Mv to -25Mv in alkaline solution with pH 9.0. At higher pH values only slight changes in zeta potential were observed.

For the hydrodynamic particles size, all USPIONs colloidal dispersions exhibit a reasonable stability in the suspending media with pH from 2 to 5. The hydrodynamic particle size in the range of 30-50 nm was seen. Dramatic increase in particle size was noticed when the dispersions pH was increased from pH 5 to pH 7. Values higher than 10000 nm were measured. Further increasing in pH resulted in variations in particle size, with a tendency to actually reduce the size – potentially indicating reduced extent of particles aggregation.

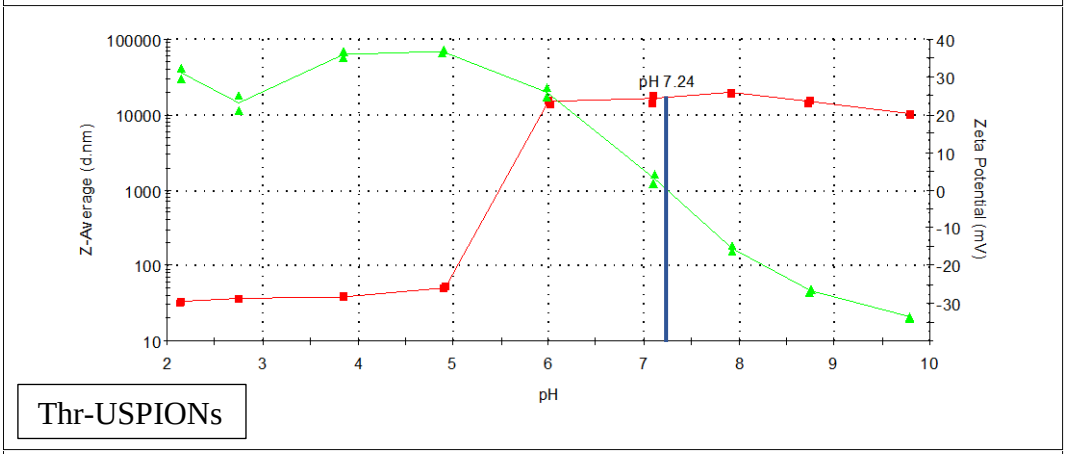
Moreover, it was found that Glu- and Asp- modified USPIONs display a slightly different pattern with an early (at pH ~ 4) sharp reduction in zeta potential values and a corresponding increase in particles size.



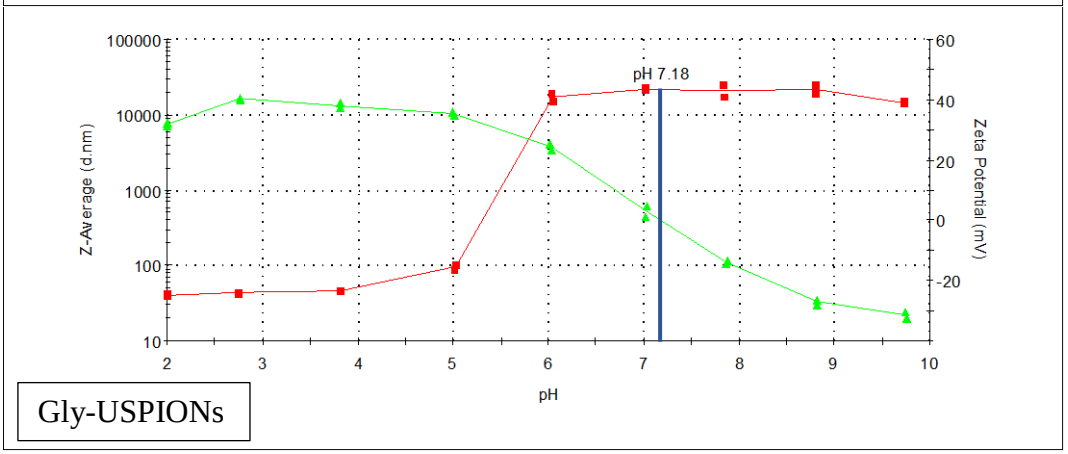
Bare-USPIONs



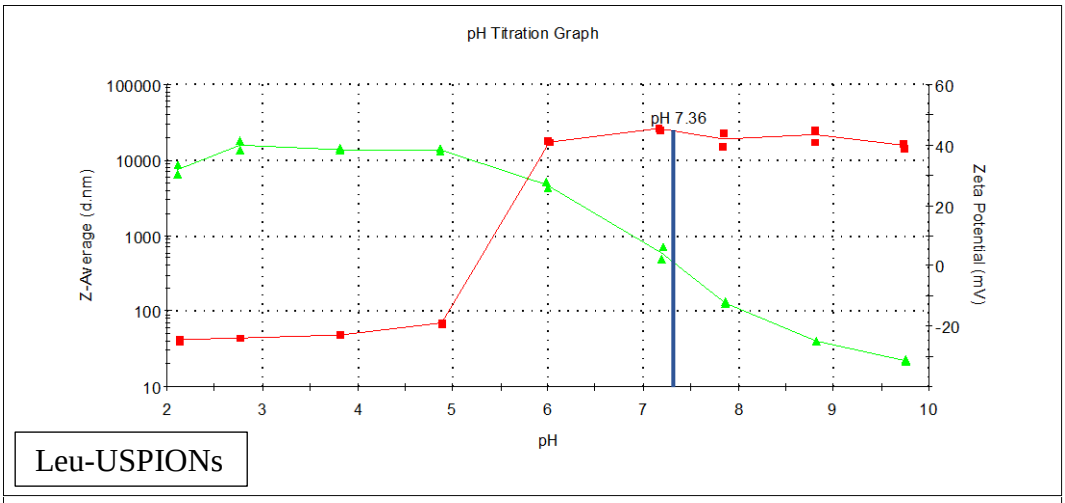
His-USPIONs



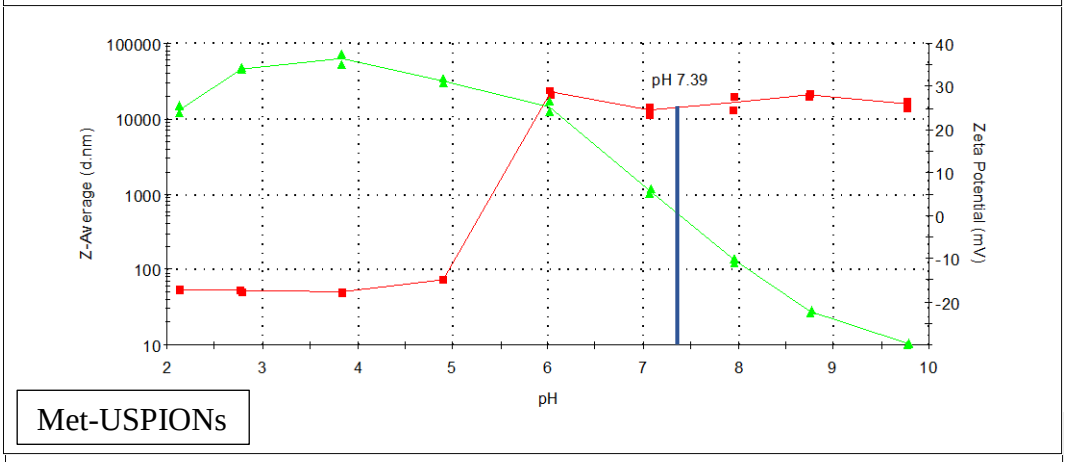
Thr-USPIONs



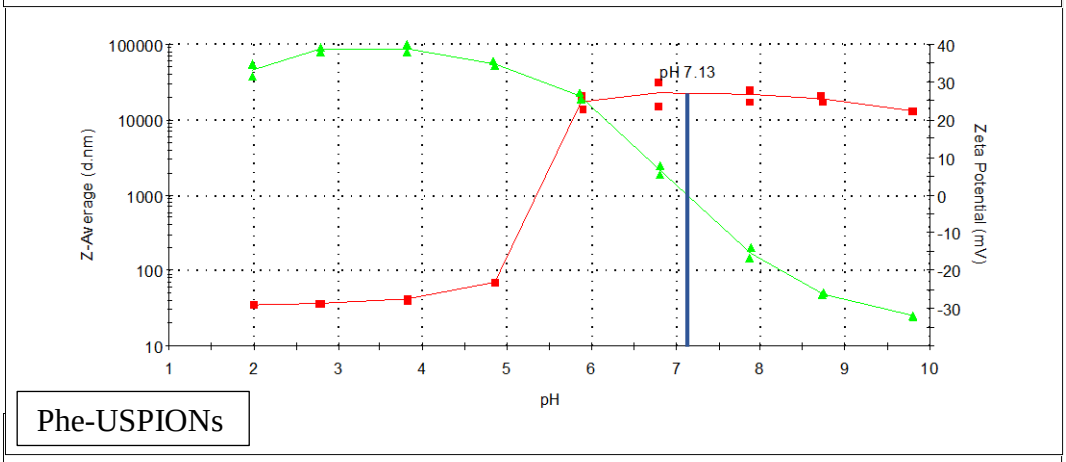
Gly-USPIONs



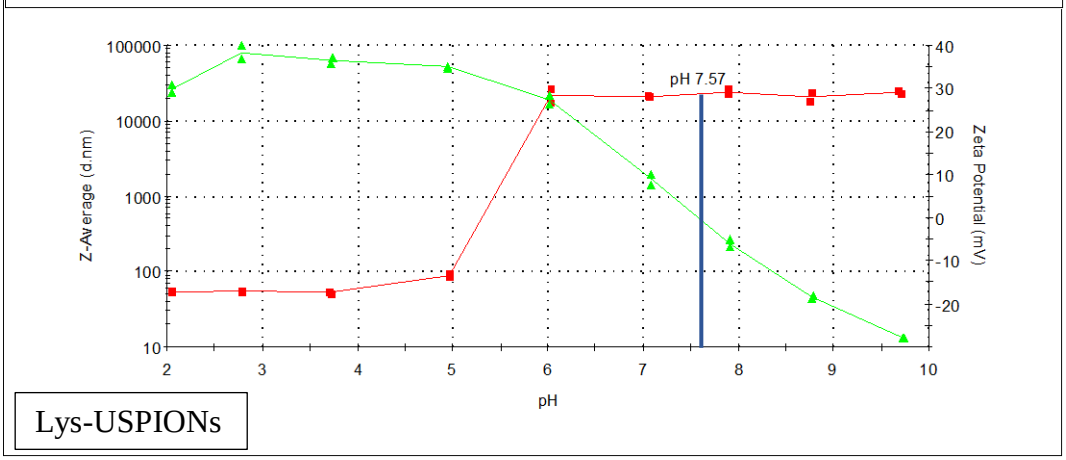
Leu-USPIONs



Met-USPIONs



Phe-USPIONs



Lys-USPIONs

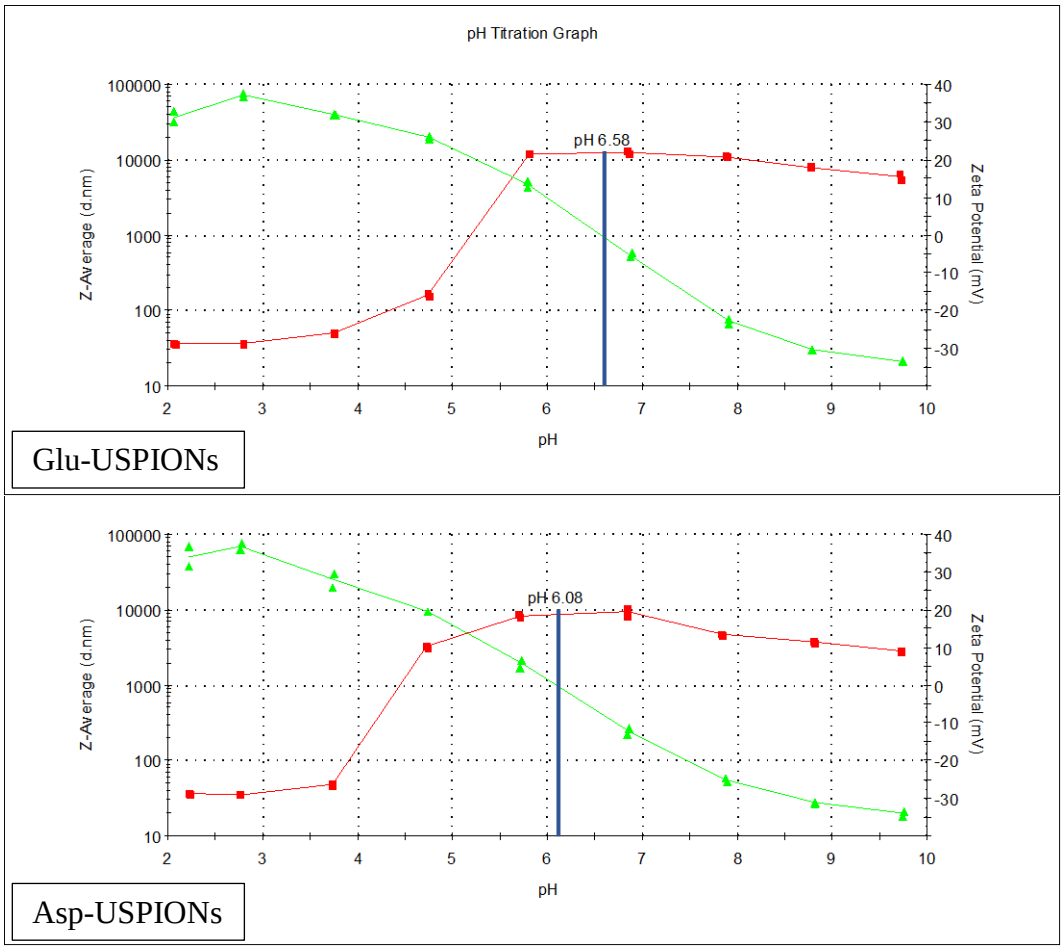


Figure 0-10: Zeta potential (green line) and hydrodynamic size (red line) of bare USPIONs and the corresponding aminoacid-modified USPIONs as a function of pH.

Colloidal dispersions of modified and bare USPIONs were prepared in 10 Mm NaCl solution at the concentration of 400 µg/ml. An automatic titrator was used to adjust the medium pH within the chosen range (2-10) by mixing three solutions (0.25 Mm HCl, 0.25 Mm NaOH and 0.025 Mm NaOH). 28.75 mg of USPIONs was modified with 1000 µmole of selected amino acids. Both hydrodynamic size and zeta potential data represent two repetitions with 10-15 sub-measurements in each.

3.3.6 FTIR analysis

For selected amino acids, infrared spectra were recorded for the free amino acid as HCl salt, and for the corresponding aminoacid modified USPIONs. Data are presented in Figures 3-11 and 3-12. In order to define possible differences between the free and USPIONs associated amino acid, the interpretation /

assignment of vibrational bands present in the medium-frequency spectral region (2000-1000 cm^{-1}) and a part of low-frequency region (1000-700 cm^{-1}) was performed.

3.3.6.1 Assignments of lysine IR spectra

In case of lysine HCl salt, a relatively strong and large band located at 1730 cm^{-1} principally originates from carbonyl stretching vibration (ν(C=O)) which is one of the most important characteristics of a protonated (uncharged) carboxyl functional group (-COOH) [38-41]. The bands with double peaks located at 1615 and 1581 cm^{-1} are assigned to antisymmetric deformation (bending) vibration (δas) mode of the protonated amino group (NH_3^+) in which the one with higher wavenumber may be attributed to the distal (side chain) NH_3^+ while the other are associated with the main NH_3^+ ion. The second doublet band that has peaks at 1522 and 1503 cm^{-1} can be ascribed to the symmetric deformation (bending) vibration (δs) mode of the both amino groups, side chain and main backbone, respectively [42]. The less intense peak occurring at 1408 cm^{-1} may belong to either bending mode of vibration (δ) of CH_2 or to the δ(C-OH). The peaks at 1176 and 1128 cm^{-1} are related to rocking mode of vibration of the both protonated amino groups, distal side chain and main backbone, respectively [40]. The transmittance peak laying in the region of 1201 cm^{-1} is associated with both ν(C-O) bond and δ(O-H). The strongest band in the spectral region below 1000 cm^{-1} occurred at 817 cm^{-1} and can be assigned to wagging and torsion of N-H bond [43,44].

For the samples of lysine modified USPIONs, a shoulder at 1723 cm^{-1} could be noticed and assigned to ν(C=O). In addition, the peak at 1678 cm^{-1} may be attributed to the same carbonyl group in its coordinated state [41,45,46]. The band with less sharp (rounded) peaks located at 1630 and 1592 $cm^{-1,}$ suggesting the

δas, is still present for the both charged ammonium groups, i.e. side chain and main backbone respectively, while the δs of the above protonated ammonium groups have merged into one broad and intense transmittance peak positioned at 1490 cm^{-1}. The vibrational coupling of C-OH underwent shifting towards lower wavenumber at 1182 cm^{-1} which is the same region of the distal ammonium group rocking mode, whereas the rocking mode of vibration of α-ammonium group has shifted for around 7 cm^{-1} towards higher wavenumber at 1135 cm^{-1}. In addition, the wagging and torsion of N-H bond has moved for ~ 28 cm^{-1} towards higher values at 845 cm^{-1}.

3.3.6.2 Assignments for aspartic acid IR spectra

The FTIR spectra of the free aspartic acid HCl salt crystal powder is illustrated Figure 3-11, where peaks interpretation is as follows. As expected, both carboxyl functional groups are protonated, and the sharp and intense band centred at 1713 cm^{-1} wavenumber is ascribed to ν(C=O) of both distal and α-COOH functionalities, however, the distal carbonyl stretching mode might contribute to the shoulder at 1742 cm^{-1}. The peaks at spectral region from 1606 to 1561 cm^{-1} are assigned to different δas of the protonated ammonium group (NH_3^+) which may arise from variable environment of the intramolecular interaction [43]. Nonetheless, there is a minor possibility of that the transmittance peak at 1606 cm^{-1} could be particularity (for aspartic acid only) assigned to δas of carboxylate anion (COO^-) as a result of a strong intramolecular interaction [43]. The strong peak at 1513 cm^{-1} clearly belongs to δsNH_3^+ group [47]. The peak with weak intensity at 1431 cm^{-1} may be assigned to νs(COO^-). The vibrational coupling of ν(C-O) and δ(O-H) for aspartic acid HCl free salt give rise to bands at 1389 cm^{-1} (mainly δ(O-H)), 1355 cm^{-1} (both ν(C-O) and δ(O-H)) and 1281-

1250 cm^{-1} (mainly ν(C-O) in different environment) [48-50]. It is also worth noting that the C-H, and CH_2 bending modes occur in this spectral region [47]. The intense peak centred at 1173 cm^{-1} is mainly related to the rocking mode of NH_3^+. The assignment of C-N stretching and C-C stretching is at 1097-1071 $cm^{-1,}$ while bands laying below 1000 cm^{-1} (955-843 and 776 cm^{-1}) correspond the δ(C-C-C) skeleton, δ(COO^-), δ(OCO), and δ(HOCC) [47].

For the aspartic acid modified USPIONs, a strong band with two peaks occurring at 1713 and 1688 cm^{-1} could be attributed to the carbonyl stretching of both distal and α-COOH, respectively. A weak peak at 1641 cm^{-1} and a broad band centred at 1599 cm^{-1} are associated with either δas(NH_3^+) of different environments or νas(COO^-), but the latter is less possible. The peak at 1497 cm^{-1} is related the δs(NH_3^+). The split band located between 1421 and 1389 cm^{-1} can either be ascribed to the νs(COO^-) or being a part of the vibrational coupling of ν(C-O) and δ(O-H) along with 1323, 1281, and 1250 cm^{-1} (as detailed above). The NH_3^+ rocking mode of the USPIONs associated aspartic acid is divided into two peaks that are located at 1177 and 1154 cm^{-1}. As in the case of free aspartic acid HCl, peaks at 1097 and 1071 cm^{-1} are related to both ν(C-N) and ν(C-C). In addition, the low-frequency spectral region is still showing peaks at 989-776 cm^{-1} where they correspond the δ(C-C-C) skeleton, δ(COO^-), δ(OCO), and δ(HOCC) (as assigned above).

3.3.6.3 Assignment of glutamic acid IR spectra

The assignments of the free glutamic acid HCl (red line) IR spectrum include the following. The peaks at 1718 and 1667 cm^{-1} refer to the carbonyl moieties of the both distal (side chain) and α-carboxyl groups respectively [51]. The both δas and δs of NH_3^+ give rise to a weak and relatively strong peaks at 1607 and

1506 cm^{-1} respectively. The sharp peak positioned at 1425 cm^{-1} is due to $\delta(CH_2)$. There is minor possibility of that the relatively wide and intense band at 1667 cm^{-1} and the strong one at 1425 cm^{-1} are related to νas and νs of COO^- respectively [41,52,53]. The characteristic coupling of δ(OH) and ν(C-O) is responsible for, first, the weak peak originated at 1371 cm^{-1} and, second, the bands that are extended from 1269 up to 1205cm^{-1} [49,50,54,55]. The minor vibrational modes of NH_3^+ rocking, CH_2 twisting, and C-C-C, and COO^- deformations are responsible for the recorded peaks arising at 1142, 1079, 996, and 818 cm^{-1} respectively.

For the IR spectrum of the glutamic acid modified USPIONs, the characteristic peak occurring at 1708 cm^{-1} can clearly be attributed to a carbonyl stretching mode of vibration under the effect of strong H-bonding environment [38], while the weak broad band centred at 1607 cm^{-1} could be mainly assigned to $\delta as(NH_3^+)$. The peaks having similar width and intensity that are at 1502 and 1408 cm^{-1} are related to the $\delta s(NH_3^+)$ and $\delta(CH_2)$ respectively. There is a considerable probability of νas and $\nu s(COO^-)$ contributing to the peaks at 1607 and 1408 cm^{-1}, respectively. The influence of the characteristic vibrational coupling of C-O-H gives rise to the minor peak occurring at 1349 cm^{-1} (which is due to δ(OH)) and also to the broad band occupying the spectral region around 1209 cm^{-1} (generated from the ν(C-O)). It was noticed that no IR frequencies with significant strength can be seen in the spectral region lower than 1150 cm^{-1}.

3.3.6.4 Assignments for histidine IR spectra

As there are two HCl molecules associated with each histidine molecule, it can be expected that the three related functional groups (an imidazole ring, an amine

and a carboxylic group) are protonated. The prominent peak located at 1736 cm^{-1} results from νs(C=O) [56,57] while the peak laying at 1619 cm^{-1} corresponds to both ring νs of C=C and C-N and δas(NH_3^+) [58,59]. Because of the two protonated tautomers, the ring-related νs(C=C) may cause the doublet peak at 1593-1577 cm^{-1}. The intense peak with shoulder originated at 1482 cm^{-1} is strongly related to δs(HN_3^+). The sharp peak at 1389 cm^{-1} is assigned to Δoh and that of 1355 cm^{-1} may be attributed CH_2 bending (wagging) [56,59-61]. There is a minor possibility that the νs(COO^-) is contributing to the peak located at 1389 cm^{-1}, while the antisymmetric stretching mode of the same group participate in the peak of 1593 cm^{-1}. The both 1275 and 1260 cm^{-1} IR frequencies belong to the νs(C-O) of different environments [56,62] where it is under the influence of the characteristic vibrational coupling of ν(C-O) and δ(OH) [47]. Two strong sharp bands extended from 1221 to 1180 cm^{-1} and from 1123 to 1066 cm^{-1} are related to the ring vibration (NH and CH bending and CN stretching) [59,63]. The deformation mode of the imidazole ring contributes in the bands at low-frequency spectral region where the peaks at 989-900 cm^{-1} are attributed to ring bending, while the peaks at 815 and 767 cm^{-1} wavenumbers are associated with ring torsion.

For the histidine modified USPIONs, the weak and downshifted peak located at 1704 cm^{-1} is due to some carbonyl stretching, while the more intense and broader band centred at 1609 cm^{-1} might originate from both δs ring of C=C and C-N and δas(NH_3^+). In addition, there is possibility of a carboxylate anion antisymmetric stretching contributing to the latter peak. The symmetric deformation of NH_3^+ appeared at two different peaks, 1504 cm^{-1} and 1479 cm^{-1} (very weak). The peak of doublets at 1434 and 1405 cm^{-1} can either be attributed

to the bending of complexed OH in different environment, or to the both δ (OH and CH_2) wagging for the first and second frequency maxima, respectively. It is worth noting that the frequency maxima at 1408 cm^{-1} may be attributed to νs(COO-). The weak peak positioned at 1301 cm^{-1} may be related to ν(C-O). The bands extended from 1126 to 1053 cm^{-1} are correlated to the ring vibration (NH and CH bending and CN stretching) while the broad band centred at 799 cm^{-1} is clearly associated with the torsion of a coordinated imidazole ring.

3.3.6.5 Assignment of threonine IR spectra

Threonine HCl has an alcoholic hydroxyl in addition to the α-amine and carboxylic acid group which are normally protonated in the present case. The intense and sharp peaks located at 1730, 1596, and 1501 cm^{-1} are associated with ν(C=O) and δ_{as} and δs (NH_3^+ modes respectively [45]. As mentioned above, there is a minor possibility of the IR frequency at 1596 cm^{-1} is being related to νas COO^-. The doublet peak visible at 1425 to 1409 cm^{-1} wavenumbers may result from contribution of three vibrational modes as follows: (a) δas(CH_3) (major) [64], (b) δ(C-OH) of the alcoholic side chain [63], and (c) δs(COO^-) (minor possibility). The bending mode of alcoholic hydroxyl is also observed at 1272 cm^{-1}, while that for acid hydroxyl, the bending vibration, could be seen at 1222 cm^{-1}. The ν(C-O) of both acidic and alcoholic group results in the doublet at 1126-1110 cm^{-1} and sharp singlet at 1034 cm^{-1} respectively. It is also important to notice that the NH_3^+ rocking mode appears at the same spectral region. The IR maxima below 1000 cm^{-1} is mainly related to the skeleton stretching and other minor modes of vibration.

Regarding threonine modified USPIONs samples, a peak at 1720 cm^{-1} is related to ν(C=O) while the doublet peak located at 1640 cm^{-1} and 1584 cm^{-1} is

associated with δas(NH_3^+) of different environment. For the IR maximum at 1640 cm^{-1}, there is very minor possibility of being related to coordinated O-C-O group. The δs(NH_3^+) mode is mainly observable at 1491 cm^{-1} maximum. The weak doublet peak visible at 1438-1408 cm^{-1} is ascribed to both δas(CH_3) (major) and δ(C-OH) of the alcoholic side chain. The bending mode of alcoholic OH also causes the minimal IR peak at 1294cm^{-1} while the slightly stronger peak is situated at 1222 cm^{-1}. The ν(C-O) of both acidic and alcoholic group give rise to the doublet peak at 1107-1084 cm^{-1} and singlet at 1037 cm^{-1}, respectively. The rocking mode of vibration of NH_3^+ is contributing to the latter spectral region. In addition, the side chain skeleton and other minor modes of vibration are associated with IR maxima recorded at wavenumber zone below 1000 cm^{-1}.

3.3.6.6 Assignment of leucine IR spectra

The presence of a protonated carboxylic acid group of the free leucine molecules is detected at 1730 cm^{-1} where it is clearly associated with νas(C=O). The doublet peak located at 1609-1584 cm^{-1} is attributed to δas(NH_3^+) of different environments. Like previous assignment, there is a minor possibility that the νas(COO^-) contributes to the latter band. Two modes of vibration associated with two different groups including δas(CH_3) and δs(NH_3^+) result in strong sharp peak at 1492 cm^{-1}, while the weaker peaks extended from 1421 to 1371 cm^{-1} are mainly due to δ(C-OH) and δs(CH_3) vibrations. The IR frequency maximum observed at 1209 cm^{-1} is related to ν(C-O). The peak at 1129 cm^{-1} may be resulting from NH_3^+ rocking mode. For the present case of hydrophobic monomer, the low-frequency region (1000-700 cm^{-1}) show less distinguishable spectrum peaks, however, the bands in this region could be attributed to different vibrational modes and groups like C-N and C-C stretching and CH_2 rocking [44,65].

In the case of leucine modified USPIONs, the strong broad band centred at 1675 cm^{-1} could be mainly attributed to the coordinated carbonyl of the carboxylic acid. While the week band occurred at 1580 cm^{-1} is assigned to $\delta asNH_3^+$, the vibrational modes of $\delta s(NH_3^+)$ and $\delta as(CH_3)$ result in an intense band at 1488 cm^{-1}. The peaks included in the spectral region of 1389-1368 cm^{-1} are associated with both δ(C-OH) and $\delta s(CH_3)$ vibrations. The very week IR frequency at 1209 cm^{-1} is due to the coordinated C-O of carboxylic acid. The NH_3^+ rocking mode of vibration is the reason for the relatively wide band observed at 1133 cm^{-1}. The side chain skeleton of the coordinated monomer is still showing considerable IR intensities at the spectral region laying below 1000 cm^{-1}.

3.3.6.7 Assignments of methionine IR spectra

The very prominent peak observed at 1730 cm^{-1} is clearly due to carbonyl stretching vibration of the protonated carboxylic acid group of fee methionine sample. The two IR peaks, weak and intense, located at 1599 and 1495 cm^{-1} are strongly associated with $\delta as(NH_3^+)$ and $\delta s(NH_3^+)$ respectively, however, there is a small chance that $\nu as(COO^-)$ may contribute to 1599 cm^{-1}. The doublet peak noticed at 1440 and 1418 cm^{-1} arises from the effects of both antisymmetric bending of methyl and hydroxyl groups respectively [44,66]. Symmetric stretching mode of carboxylate anion may participate in the 1418 cm^{-1} but with very minimum probability [67]. The symmetric bending mode of the side chain methyl group causes a peak at 1358 cm^{-1} while the wagging vibrational mode of CH_2 has produced two adjacent peaks at 1336 and 1314 cm^{-1} [66]. In addition, the bending vibration of hydroxyl group also contributes to the latter peaks [66]. The sharp and intense peaks extended over the spectral region below 1250 cm^{-1} are attributed to CH_2 twisting at 1218 cm^{-1}, NH_3^+ rocking at 1186 cm^{-1}, ν(C-O) at

1145 cm^{-1}, CH_2 rocking at 1002 and 767 cm^{-1}, ν(C-C) at 837 cm^{-1} and ν(C-S-C) at 739 cm^{-1} [44,66].

The IR spectrum of methionine modified USPIONs is mainly characterised by four intense and relatively wide peaks at 1634, 1502, 1432, and 1345 cm^{-1}. The first peak (at 1634 cm^{-1}) mainly results from combination of νs(O-C-O) and δasNH_3^+ while the weaker second peak (at 1502 cm^{-1}) is attributed to δs(NH_3^+). The third peak (at 1432 cm^{-1}) originates from merging of both antisymmetric bending of methyl and hydroxyl groups. The same case is for the forth peak in which the bending vibrational modes of CH_3, CH_2 and OH contribute to the formation of the IR frequency maximum at 1345 cm^{-1}. Furthermore, the important week peaks appeared in the spectral region below 1250 cm^{-1} are associated with CH_2 twisting at 1241 cm^{-1}, NH_3^+ rocking at 1189 cm^{-1} and ν(C-O) at 1139 cm^{-1}.

3.3.6.8 Assignment of phenylalanine IR spectra

For phenylalanine, a very sharp and strong peak found at 1730 cm^{-1} is due to ν(C=O) of the protonated carboxylic acid group. The weak band at 1571 cm^{-1} is associated with δas(NH_3^+) while the 1479 cm^{-1} IR peak having identical strength to that of carbonyl is associated with δs(NH_3^+). The phenyl ring vibrational modes (ν (C-C)) are visible at more than one spectral region where the stretching mode is responsible for peaks at 1602, and 1447 cm^{-1} and contributes to 1479 and 1205 cm^{-1} IR maxima, while the ring C-H bending mode dominates most of the spectrum lower than 1200 cm^{-1}. The second component of phenylalanine side chain (CH_2) shows strong bending vibration at 1224 cm^{-1}. The vibrational coupling of ν(C-O) and δ(OH) are accountable for the peak at 1285 cm^{-1} [44,68]. It is important to notice that because of the ring effect, some modes of vibration

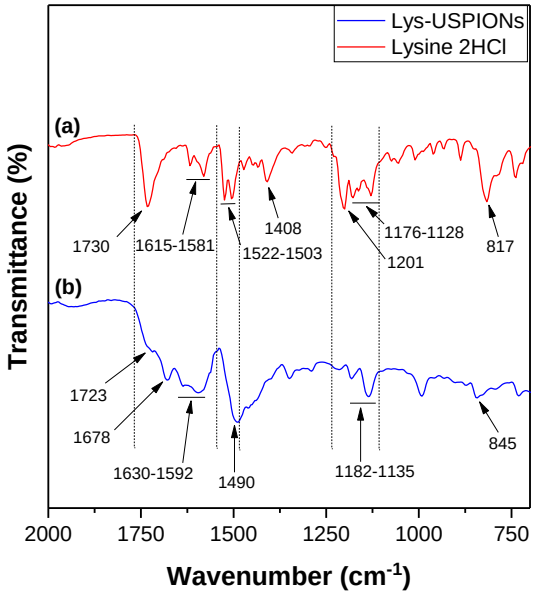
cannot be easily distinguished, like NH_3^+ rocking, however, it might participate in the band occurred at 1135 cm^{-1} [69].

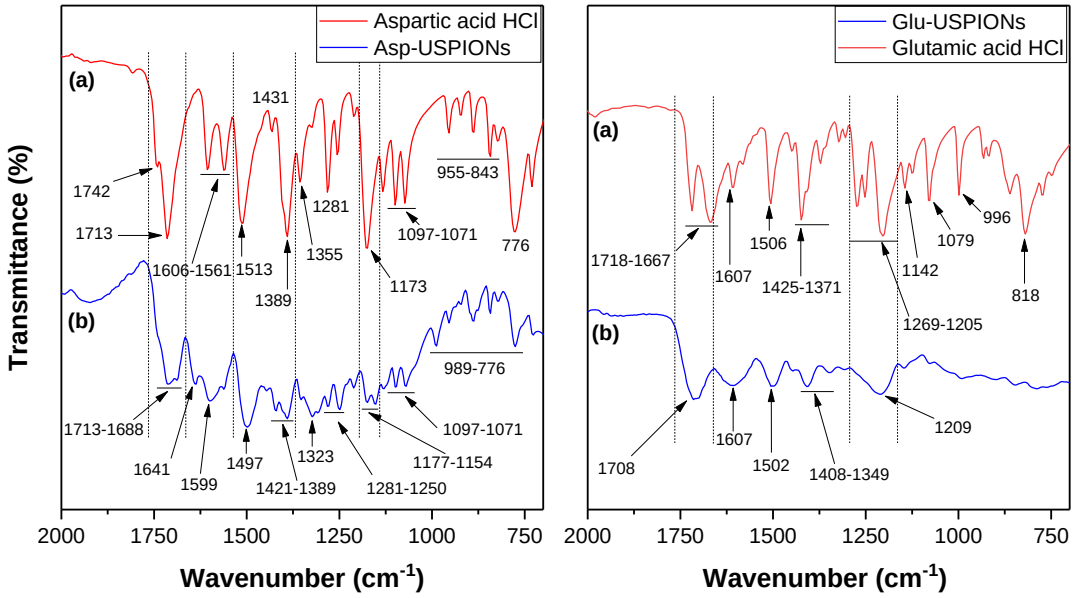
For the coordinated phenylalanine monomer, there are three characteristic peaks that could be assigned in the present case. They are include 1679, 1590, and 1479 cm^{-1} that could be attributed carboxylic acid stretching, δas(NH_3^+) and δs(NH_3^+) respectively. The ring vibration could contribute the last two peaks.

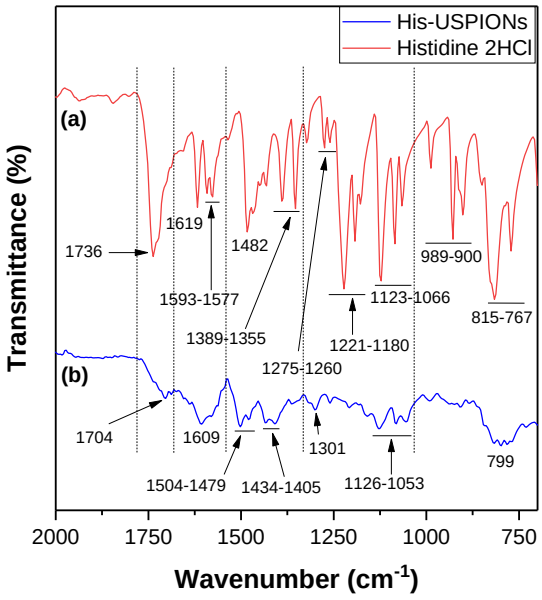
3.3.6.9 Assignment of glycine IR spectra

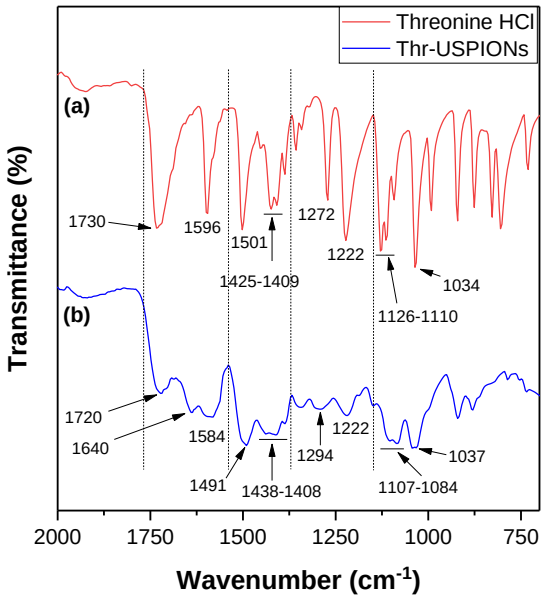
The IR spectrum of the free glycine sample shows sharp and intense peaks at 1733, 1599, and 1486 cm^{-1} which resulted from ν(C=O), δas(NH_3^+), and δs(NH_3^+) respectively. It was found the vibrational coupling of δ(OH) and ν(C-O) are responsible for four big peaks located at 1422 cm^{-1} (mainly CO), 1339 cm^{-1} (OH and CO), 1218 cm^{-1} (OH and CO), and 1123 cm^{-1} (OH mainly). δ(CH_2) contributes to the peak at 1422 cm^{-1}, while bands that are observed at 1040 and 847 cm^{-1} could be attributed to NH_3^+ rocking.

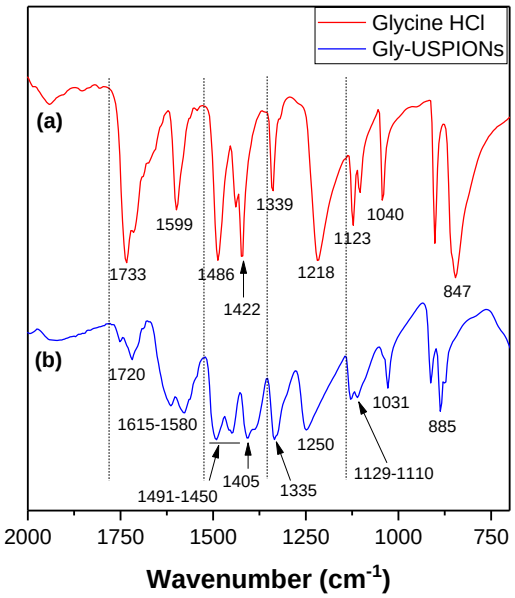
For the glycine modified USPIONs, the relatively weak band at 1720 cm^{-1} is related to C=O while the doublet bands at 1615-1580 and 1491-1450 cm^{-1} are associated with δas(NH_3^+), and δs(NH_3^+) respectively. Peaks at 1405, 1335, 1250 and 1129-1110 cm^{-1} (doublet) are due to coupling δ(OH) and ν(C-O). The coordinated amine group shows rocking mode of vibration at 1031 and 885 cm^{-1}.


Lys-USPIONs
Lysine 2HCl
(a)
(b)
Transmittance (%)
1730
1615-1581
1408
1522-1503
1176-1128
1201
817
1723
1678
1630-1592
1490
1182-1135
845
2000
1750
1500
1250
1000
750
Wavenumber (cm-1)


Aspartic acid HCl
Asp-USPIONs
(a)
(b)
Transmittance (%)
1742
1713
1606-1561
1513
1431
1389
1355
1281
1173
1097-1071
955-843
776
1713-1688
1641
1599
1497
1421-1389
1323
1281-1250
1177-1154
1097-1071
989-776
2000
1750
1500
1250
1000
750
Wavenumber (cm-1)
Glu-USPIONs
Glutamic acid HCl
(a)
(b)
1718-1667
1607
1506
1425-1371
1142
1269-1205
1079
996
818
1708
1607
1502
1408-1349
1209
2000
1750
1500
1250
1000
750
Wavenumber (cm-1)


His-USPIONs
Histidine 2HCl
(a)
(b)
Transmittance (%)
1736
1619
1593-1577
1482
1389-1355
1275-1260
1221-1180
1123-1066
989-900
815-767
1704
1609
1504-1479
1434-1405
1301
1126-1053
799
2000
1750
1500
1250
1000
750
Wavenumber (cm-1)


Threonine HCl
Thr-USPIONs
(a)
(b)
Transmittance (%)
1730
1596
1501
1425-1409
1272
1222
1126-1110
1034
1720
1640
1584
1491
1438-1408
1294
1222
1107-1084
1037
2000
1750
1500
1250
1000
750
Wavenumber (cm-1)


Glycine HCl
Gly-USPIONs
(a)
(b)
1733
1599
1486
1422
1339
1218
1123
1040
847
1720
1615-1580
1491-1450
1405
1335
1250
1129-1110
1031
885
2000
1750
1500
1250
1000
750
Wavenumber (cm-1)

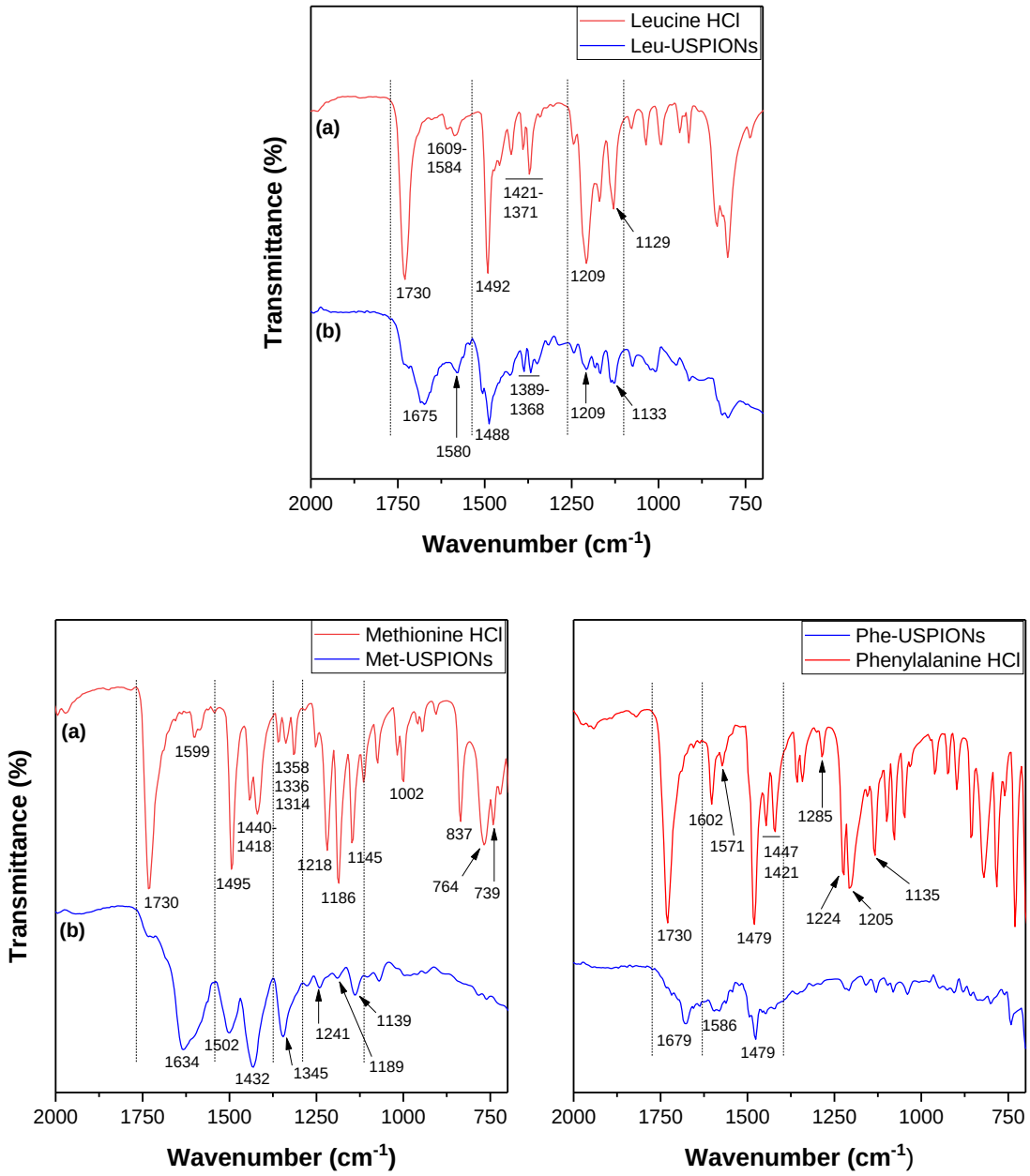


Figure 0-11: FTIR spectra for free amino acid and aminoacid modified USPIONs

The 'dry mixing' method was adopted to prepare a powder of aminoacid-modified USPIONs. In each case 250 µmole of amino acid powder was hand-mixed for 5 min with 28.75 mg of freshly fabricated USPIONs powder. The powder mixture was then suspended 10 ml deionised water the formed suspension filtered through 0.2 µm syringe filter. The collected colloidal dispersions were dried and stored in a desiccator for a week.

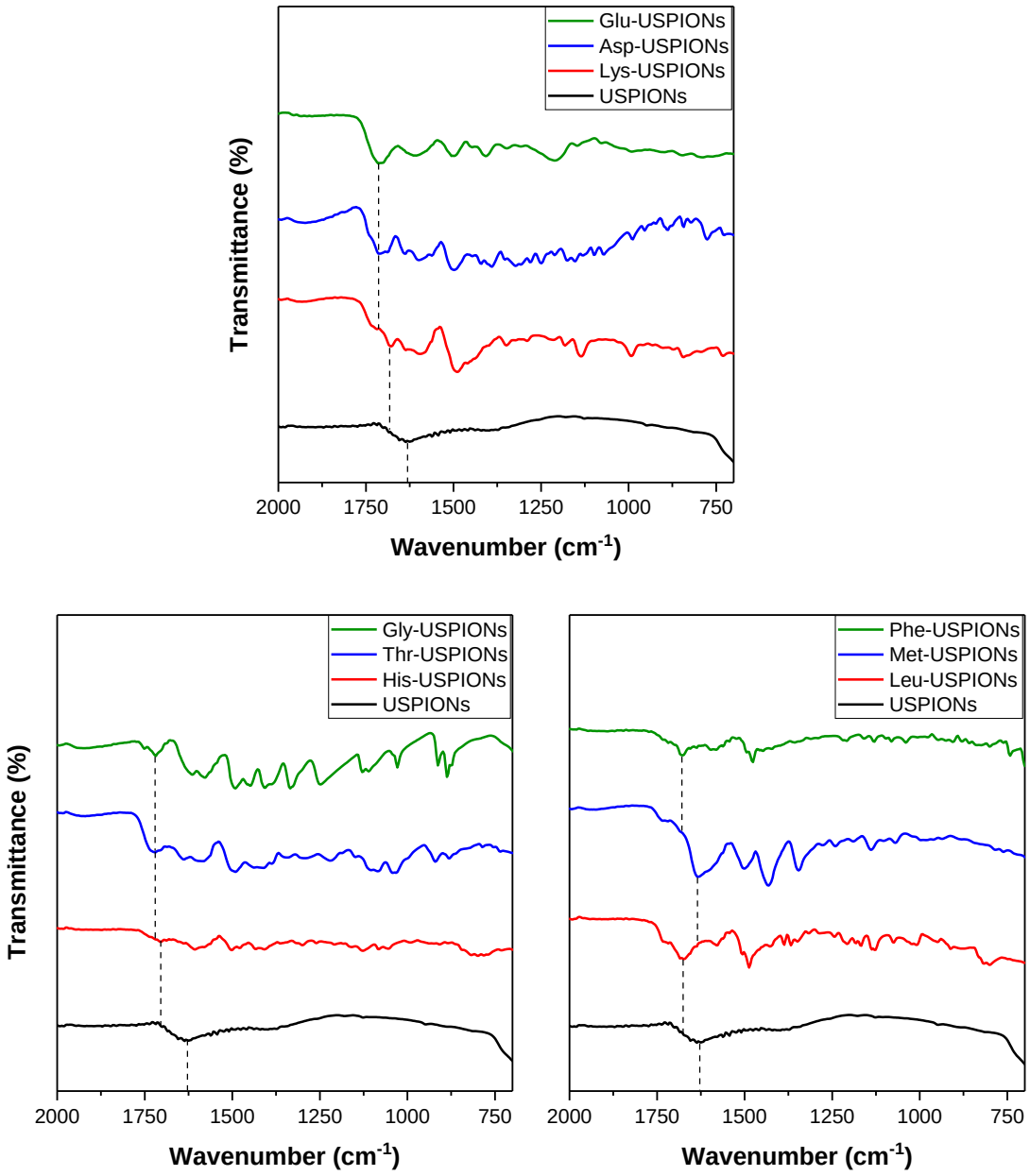


Figure 0-12: FTIR spectra for free amino acid and aminoacid modified USPIONs

The 'dry mixing' method was adopted to prepare a powder of aminoacid-modified USPIONs. In each case 250 µmole of aminoacid powder was hand-mixed for 5 min with 28.75 mg of freshly fabricated USPIONs powder. The powder mixture was then suspended 10 ml deionised water the formed suspension filtered through 0.2 µm syringe filter. The collected colloidal dispersions were dried and stored in a desiccator for a week.

3.4 Discussion

It is well established that metal oxides are insoluble in aqueous media, and iron oxide is not an exception. In an aqueous suspension, a sedimentation starts rapidly on dispersing freshly synthesised USPIONs, independently of the medium pH. Therefore, treating the surface of USPIONs with freely soluble materials (like amino acids) is normally adopted to form a stable colloidal dispersion. It was found out that a dry, mechanical mixing of dry USPIONs powder with a coating material is a surprisingly efficient protocol for creating surface modified metal oxide NPs (previous work in Dr G Cave research group). The present work applies this previously described protocol to fabricate USPIONs surface modified with a panel of amino acid (as monomers).

Initially the USPIONs modification yield was assessed, and the experiments confirmed the superiority of the dry mixing vs 'classical' solution mixing process. The data in table 3-1 clearly indicate that surface modification of USPIONs with amino acids in their HCl salt form produce a good yield of colloidally stable dispersions. This is understandable as ionisation of amine group by HCl dramatically improves the solubility of amino acid molecules and their association with USPIONs and hence produces a hydrophilic surface. This is in line with the literature, which demonstrates that amino acids are readily adsorbed onto NPs in an aqueous dispersion with acidic pH [70-72]. This is not the case when amino acids in their base form were used, and a very low yield of modified USPIONs was obtained even after using water soluble amino acids in their base form. For aspartic acid, the yield was only 0.37% for base and 38.9% for the HCl salt forms, respectively.

Figure 3-3 evidently clearly indicate that using ‘dry mixing with mechanical pressure’ protocol allows USPIONs surface modification with a series of amino acids in the quantities of material and in the short time that NPs cannot be achieved by applying a traditional USPIONs surface modification in a suspension. For instance, 45.3% and 1.6% yields were obtained for the modified USPIONs adopting dry and suspension mixing processes, respectively. It should be noted that a number of protocols were tested attempt to improve powder mixing by e.g. using a grinding machine rather than pestle and mortar however, at the laboratory scale this was not shown advantageous [31].

Combining TEM images of USPIONs morphology and particle size measurements from DLS, shown in Figure 3-5, clearly indicates a formation of such well dispersed USPIONs following ‘coating’ with amino acids. An average particle size range of 34-55 nm, without obvious variations in the particles morphology and without presence of significant aggregation, was observed for all amino acids tested. Considering USPIONs formulation attributes phenylalanine-modified USPIONs showed the most favourable dispersion properties. This is somewhat surprising as the relatively bulky hydrophobic side chain of phenylalanine would be expected to be aggregation prone functionality (as seen in nature in protein aggregation) rather than generating a steric stabilization needed to achieve particles separation and colloidal stabilization [73].

To conform that the adopted surface modification ‘dry powder’ procedure resulted in association of selected amino acid with USPIONs TGA, analyses of un-modified, bare, and the modified USPIONs were compared. This comparison shows no significant mass loss for bare USPIONs at temperatures approaching 900°C. This clearly indicates the absence of any organic material, in contrast to

the modified NPs. The significant mass reductions, as illustrated in Figure 3-6, were found for aminoacid modified USPIONs, similar to previous literature reports[74-77]. A more detailed analysis in Figure 3-7 indicates three crucial differences which can be taken as an evidence of aminoacid-USPIONs surface association. First, the release of the physically and chemically bound water happened at lower temperatures for modified USPIONs samples was, in some instances, gradual without sharp peak of mas loss as seen for 'free' amino acids aspartic acid, leucine, lysine, methionine, and threonine. The reasons behind this phenomenon may be arising from a dissociation of water molecules from the lattice structure of free amino acids, where the USPIONs associated aminoacid molecules are thought to have no such a lattice structure that is capable of binding water molecule until higher temperatures [78,79].

The second important difference is a considerable reduction in the rate of aminoacid decomposition. For example, the two-step decomposition stage of free phenylalanine has occurred at rates of 1.9 and 1.4%/°C while the USPIONs associated phenylalanine has mainly undergone thermal degradation at 0.5 and 0.4%/°C. In addition, some USPIONs associated aminoacids exhibit an earlier thermolysis stage, which may be attributed to catalytic effect of iron atoms that may accelerate the process [80]. As an example, 203.6°C and 364.4°C are the temperatures at which a free aspartic acid is degraded, while the corresponding USPIONs associated aspartic acid started to degrade at temperature that is10-40°C lower.

The other degradation behaviour difference noticed is a late mass reduction step at higher temperatures (above 500°C). This could be ascribed to the strong interaction between aminoacid side groups and the metal USPIONs. This is

particularly evident in case of amino acids without hydrophobic character, where the highly reactive functional groups are expected to be involved (as discussed in more details below). Histidine-modified USPIONs show a prominent late degradation phase (maximum at ~ 735.6°C), a behaviour which might be explained by the pyrolysis of the 'engaged' imidazole ring [81-83].

Quantitative analysis of amino acids effectively associated with the surface of USPIONs is important for demonstrating the efficiency in surface modification of the 'dry mixing process'. In line with an increase in the yield of colloidally stable USPIONs, the analysis of the mass amino acids associated with the USPIONs indicate that by 'dry mixing and applying mechanical pressure' one can indeed bring amino acid molecules and surface of USPIONs into an intimate proximity to create adsorptive forces at the solid-solid interfaces. The data further indicate that more than one layer of aminoacid molecules normally associates with the USPIONs surface.

In the same context, Figure 3-8 shows the increase in number of USPIONs-associated aminoacid molecules. The data may be mainly explained by the formation of called 'molecular associates' at the surface in which hydrogen bonding and/or electrostatic interaction could govern the accumulation of individual molecules to create such associates [84]. In our case, due to the protonated state of monomers used, H-bonding might drive the process of molecules orientation in the adsorbed multilayers around an individual USPION particle. Our experiment revealed, for most amino acids, that the surface association of aminoacid molecules increased dramatically after 250 µmole of the aminoacid powder has been used to coat 28.75 mg of USPOINs. Some fluctuations in the data (red line in Figure 3-8) may give an indication that the

additional adsorbed layers of molecules may be relatively easily dissociated, as a result (e.g) suspension medium stirring whereby they may undergo continuous exchange with 'free' aminoacid molecules in the medium when the modified USPIONs are suspended in the excess of aminoacid. This resembles a similar phenomenon of 'hard' and 'soft' adsorptive protein layers formation around NPs [85].

Evaluating the modified NPs colloidal stability is of critical step for the potential application of USPIONs in biological environment [86]. Therefore characterisation of USPIONs surface electrostatic potential and its correlation with their particle size was studied. The experiment is conducted over a pH range of 2-10 to follow the evolution of both measured characters.

In general, when metal oxide NPs are dispersed in water medium, the H_2O molecules are hydrating the solid surface by accumulation of hydroxyl groups. Here, the possible presence of crystalline defect on the surfaces of NPs may play a crucial role [87]. On changing pH of the medium the acquired surface net charge, originating from a dissociation of surface hydroxyl groups, will change according to reaction scheme below [88]:

$M\text{-}OH_2^+ \leftrightarrow M\text{-}OH \leftrightarrow M\text{-}O^-$

The positive ($M\text{-}OH_2^+$) form is mainly seen in acidic media while the negatively charged surfaces ($M\text{-}O^-$) are formed in alkaline media [88-90]. Therefore, it could be expected that USPIONs would bear no net charge (M-OH) around neutral pH zone, and this is what was found in our study using bare USPIONs dispersion, where the IEP was found equal to 7.05 (Figure 3-10). This is in agreement with values reported in the relevant literature [91,92].

For aminoacid-modified USPIONs, zeta potential measurements continue showing IEPs in the neutral region (green lines in figure 3-10). As mentioned above, this could be explained by the formation of multilayers (in a form of molecular associate) of amino acids around individual particles where the monomers of the very outer layer will be responsible for the net charge acquired [84]. In general,, the pH of zero charge of an amino acid is normally in the middle between pKa values of anionic (~2.3) and cationic (~9.6) groups [93]. However, IEP readings of 7.74 and 6.08 for histidine and aspartic acid-modified USPIONs were recorded, as a result of the additional amine and carboxyl group, respectively in their molecular structure. Literature data on IEP for lysine modified USPIONs are in agreement with our results [75].

Based on the zeta potential data, all USPIONs modified with amino acids experience colloidal instability (red line of figure 3-10) once they enter the neutral pH region, with some slight changes in their agglomeration behaviour pattern for some aminoacid modified USPIONs. This clearly indicate that the main mechanism of colloidal stabilization of the aminoacids modified USPIONs is mainly controlled by electrostatic repulsive forces, and hence, particles start to agglomerate once medium pH is close to their IEP. This also means that the aminoacid modification does not provide steric stabilisation of the USPIONs that could work to exceed the attractive forces and keep USPIONs dispersed in water medium [10,94,95].

3.4.1 Aminoacid-USPIONs binding mechanism

Spectroscopic FTIR-ATR technology was applied in order to investigate possible mechanisms of the amino acids monomers association with the metal

NPs (USPIONs) [96], and to understand which functional groups are involved in this association.

The interaction between amino acids and metal NPs is normally expected to occur *via* complexation of either one or both oxygen atoms of the carboxyl functional group [97-99]. Additionally, the contribution of the protonated ammonium group was also observed and evidenced by weakening and broadening of the associated IR peaks [95]. In this situation, it is difficult to suggest the nature of association from just one frequency band and hence, we investigate a range of bands related with COOH group (Figure 3-11).

3.4.1.1 Lysine salt and Lys-USPIONs

For lysine salt, the significant downshifting in stretching vibration mode related to C=O for around 52 cm^{-1} (from 1730 cm^{-1} to 1678 cm^{-1}) indicate formation of bidentate surface complexation with USPIONs in which the coordinated –O-C-O- group show stretching vibration at 1678 cm^{-1}. However, the shoulder noticed at 1723 cm^{-1} may be related to C=O groups of those monomers situated within multilayer formed around NPs that have less intense interaction. In this case, the oxygen of carbonyl (C=O) is H-bonded with adjacent carboxylate group [100,101]. Furthermore, there are two additional spectral changes related to (hydroxyl bending and C-O stretching) of the protonated carboxyl that could augment our suggestion. They include, first, the disappearance of 1408 cm^{-1} peak and, second, shifting of 1201 cm^{-1} peak for around 19 cm^{-1} towards lower wavenumber values (at 1182 cm^{-1}). This reveals deprotonation of α-carboxyl group as a result of C-O-iron interaction.

Regarding the two protonated ammonium groups of lysine HCl salt, it seems that they strongly interact with the surface of USPIONs. In this context, there are three spectral changes that could be argued. The first includes upshifting of IR peaks of both antisymmetric and rocking modes of vibration. For the distal (side chain) NH_3^+ group, higher wavenumbers by 15 cm^{-1} (from 1615 to 1630 cm^{-1}) and by 6 cm^{-1} (from 1176 to 1182 cm^{-1}) have been recorded for antisymmetric and rocking vibrations respectively, while for α-NH_3^+ group upshifting by 11 cm^{-1} (from 1581 to 1592 cm^{-1}) and by 7 cm^{-1} (from 1128 to 1135 cm^{-1}) were noticed for antisymmetric and rocking vibrations respectively. The second spectral change noticed is represented in the overlapping of symmetrical vibrational modes of both distal and α-NH_3^+ groups to form broad intense band centred at 1490 cm^{-1}. Finally, the third spectral alteration occurs via shifting of wagging and torsion mode of N-H bond towards higher wavenumbers value from 817 to 845 cm^{-1}. All these spectral modifications might be attributed to the crucial effect of nitrogen atom complexation and/or H-bond formation with surface-bound hydroxyl groups or surface ions of USPIONs [40,45]. Similar interaction pattern was proposed for lysine adsorption to TiO_2 from aqueous solution [49,102].

3.4.1.2 Aspartic acid HCl salt association with USPIONs

In this situation, numerous spectral changes indicate formation of Asp-USPIONs association which favours monodentate surface complexation [103] between only one carboxylate group (α- one mainly) with the surface iron ions. In more detail, for carbonyl related peaks, the splitting of intense band at 1713 cm^{-1} into two IR peaks at 1713 and 1688 cm^{-1} has occurred, while for C-O and O-H related IR peaks, the appearance of a new IR maximum at 1421 cm^{-1} and

downshifting of the peak at 1355 cm^{-1} towards broad band centred at 1323 cm^{-1} would evidently propose such a mode of association. In addition, the lack of changes in 1389, 1281 and 1250 cm^{-1} IR peaks indicates that only one C-O moiety is interacting with USPIONs [104].

For the protonated amino group, it was found that a direct involvement of the whole functionality complexation could be assumed. The peaks of $\delta as(NH_3^+)$ have undergone up-shift for around (38-35 cm^{-1}) from 1606 and 1561 cm^{-1} to 1641 and 1599 cm^{-1}, while the peak of $\delta s(NH_3^+)$ has shifted to lower wavenumber from 1513 up to 1497 cm^{-1}. In addition to this, there are other important spectral modification noticed which include the splitting of the sharp intense peak of NH_3^+ rocking located at 1173 cm^{-1} into two weak peaks laying at 1177 and 1154 cm^{-1} which in turn indicate a generation of two different rocking modes. The latter change indicates that NH_3^+ group was strongly associated with NPs surface *via* either H-bonds with two separate surface hydroxyl moieties or direct coordination of N atom with surface iron along with one H-bond with surface present hydroxyl. The broadening of 1599 cm^{-1} transmittance peak is strongly related to the variable microenvironment provided by the presence of H-bonding type of interaction [43].

It is also important to mention that peaks occurring at low frequency region (less than 1000 cm^{-1}) in the spectrum of Asp-USPIONs support the suggestion of monodentate aspartic acid carboxylate surface complexation. As a justification, the existence of such peaks (that represent the bending modes of C-C-C skeleton, COO-, OCO, and HOCC) emphasises there is no strong NPs surface association with the distal carboxyl which in turn result in quenching of skeleton- and carboxylate- related peaks of bending vibration.

3.4.1.3 Glutamic acid HCl association with USPIONs

Like in case of aspartic acid, glutamic acid has α- and distal carboxylic acid group that are expected to be protonated in case of HCl salt form. Following the IR spectrum of Glu-USPIONs complex, we believe that both carboxylate are equally involved in the association with the surficial iron ion of USPIONs, which is in contrary to the previous case of aspartic acid. For more detail, the merging of the two carbonyl-related stretching modes (at 1718 and 1667 cm^{-1}) into one relatively broad band located at 1708 cm^{-1} clearly indicate there is identical environments around them (the two carboxyl groups) that in turn denote equivalent interaction with the NPs. Another support to this finding is that the combination of bands related to vibrational coupling of δ(OH) and ν(C-O) into one broad band that has IR maximum laying at 1209 cm^{-1}. Moreover, quenching of skeleton-related IR peaks (at spectral region less than 1100 cm^{-1}) provides an additional evidence about involvement of the distal carboxyl group with the NPs surface. Therefore, similar to what was reported in the literature, we postulate that there is a strong bidentate surface complexation with USPIONs in which both α- and distal carboxylate are coordinated [105-107].

Regarding the protonated amine group, it was found that there is no significant association with the surface ions. The spectral changes noticed include broadening of δas(NH_3^+) related peak without any shifting (at 1607 cm^{-1} for both IR spectra) along with slight downshifting of δs(NH_3^+) vibration from 1506 to 1502 cm^{-1}. This indicates a formation of weak H-bonding with either a USPOINs surface-adsorbed hydroxyl group (minor) or an adjacent amine group (major). The latter proposal suppose an orientation of the amine away from NPs.

3.4.1.4 Histidine 2HCl association with USPIONs

In case of histidine, the focus will be placed upon the three functional groups (α-carboxyl, α-amine and imidazole ring) that this molecule possess. For the protonated carboxylate, the dramatic change in the strength and position of carbonyl-associated peak (downshift from 1736 cm^{-1} to a weak peak at 1704 cm^{-1}) strongly indicates an involvement of this group in complexation of histidine monomers with NPs, which in turn suggest the formation of bidentate surface complexation. This could be supported by two additional spectral modifications that are related the characteristic vibrational coupling of ν(C-O) and δ(OH). In more detail, the first change includes upshifting and probably splitting of δ(OH) from 1389 cm^{-1} to 1434 and 1404 cm^{-1} while the second one is associated with upshifting and merging of 1275 and 1260 cm^{-1} IR frequencies to a weak peak occurred at 1301 cm^{-1}.

The second important functional group is the protonated α-amine (NH_3^+). It is assumed that there is an engagement with the surficial ions *via* either H-bonding or electrostatic interaction. In this situation, the (δas) underwent a downshift from 1619 to 1609, while the (δs) of some groups has moved to a higher wavenumber at 1504 cm^{-1}. However, we believe that this group has weaker interaction in comparison with other groups (imidazole ring and α-carboxyl)

The third crucial functional group of histidine is the imidazole ring where we have found that there is a very strong interaction between the protonated ring and USPIONs. This is clearly evidenced by either disappearance, weakening or combining of its peaks. In this regard, the characteristic ring stretching peaks occupied a spectral region extended from 1619 to 1577 cm^{-1} and the ring torsion peaks at 815 and 767 cm^{-1} have undergone merging to broad bands centred at

1609 and 799 cm^{-1} respectively. In addition, the two peaks groups spread from 1221 to 1180 cm^{-1} and from 1123 to 1066 cm^{-1} has either disappeared or extensively weakened respectively upon surficial complexation. Schwaminger *et al* assumed that similar is occurring in imidazole ring contribution to the complexation of histidine with magnetite NPs [108].

3.4.1.5 Threonine HCl association with USPIONs

Threonine salt shows a surface association with USPIONs that might be characterised by the formation of monodentate surface complexation of carboxylic acid group with surficial iron ions. This could be evidenced by the downshifting of the sharp peak of ν(C=O) from 1730 cm^{-1} to 1720 cm^{-1} and widening and downshifting of the doublet band of ν(C-O), occurred at 1126 - 1110 cm^{-1} to 1107-1084 cm^{-1}. Here, the unchanged peak position of the acidic hydroxyl bending mode, at 1222 cm^{-1}, indicates a possibility of that the carboxylate group did not undergo deprotonation upon complexation with the NPs. Therefore the monodentate coordination is believed to happen *via* C-O side of the protonated carboxylic acid.

Regarding α-amine, there is a strong sign that this group is effectively involved in the association of threonine with USPIONs where two spectral alterations have occurred to its vibrational modes. First, the sharp peak at 1596 cm^{-1} that is ascribed to δas(NH_3^+) has widened and split into a double-peak band at 1640 and 1584 cm^{-1} and, second, downshifting of δs(NH_3^+) by 10 cm^{-1} wavenumber from 1501 cm^{-1} to 1491 cm^{-1}. Accordingly, this could be explained by the presence of strong H-bonding and electrostatic interaction between USPIONs surface-adsorbed hydroxyl and the amino group.

Moreover, the alcoholic hydroxyl group of the side chain was found to be profoundly affected by the association process. For δ(OH), the band of the doublet peak underwent increased splitting from 16 cm^{-1} (at 1425-1409 cm^{-1}) to 30 cm^{-1} (at 1438-1408 cm^{-1}) while the second sharp band at 1272 cm^{-1} experienced massive reduce in intensity along with upshifting for around 22 cm^{-1} (to 1294 cm^{-1}). These spectral changes could be explained by the interaction with NPs, but we think this is not the case due to two reasons. First, absence of a significant shift in the alcoholic ν(C-O) peak at 1034 cm^{-1} and, second, the steric strain of threonine monomers that restrict the orientation toward USPIONs. We believe that the above observation could be attributed to interaction with adjacent molecules [81].

3.4.1.6 Leucine HCl association with USPIONs

In contrast to other amino acids, comparing IR spectra of the free and coordinated leucine molecules reveals a presence of weak or no interaction of the protonated amine group with the NPs surfaces, while the COOH-related peaks exhibit a formation of bidentate surface complexation with the surficial iron. In more details, for carboxylic acid group, the downshifting and broadening of ν(C=O) associated peak from 1730 to 1675 cm^{-1}, downshifting of δ(OH) related peaks from spectral region of 1421-1371 cm^{-1} to 1389-1368 cm^{-1}, and, weakening of the sharp peak located at 1209 cm^{-1} would support our assumption.

Regarding the protonated ammonium group, the slight shift in the position of antisymmetric and symmetric bending and rocking modes of NH_3^+, respectively from 1584 to 1580 cm^{-1}, from 1421-1371 cm^{-1} to 1389-1368 cm^{-1} and from 1129 to 1133 cm^{-1} all indicate that there is week electrostatic interaction with the surface of USPIONs and/or with a second layer of leucine molecules.

We believe that the side chain of leucine molecule is not involved in its complexation with USPIONs surface. This is evidenced by, first, the effective contribution of δas(CH_3) to the moderately wide band with a sharp peak at 1488 cm^{-1} and, second, the appearance of several peaks of different IR intensities in the spectral region lower than 1000 cm^{-1} which are associated with vibrational modes of bonds like C-N, C-C and CH_2.

3.4.1.7 Methionine HCl association with USPIONs

In the case of methionine association with USPIONs, IR peaks related to the protonated carboxyl group have undergone three distinctive changes that firmly suggest a formation of bidentate complexation with the surface of USPIONs. These changes include the following: (a) an appearance of a new wide and intense band at 1634 cm^{-1}, instead of that at 1730 cm^{-1}, (b) a merging of hydroxyl bending mode that occurred at the both regions of 1418 and 1336-1314 cm^{-1} with δas(CH_3) and δs(CH_3) respectively, and (c) a weakening and minor downshifting of ν(C-O) from 1145 to 1139 cm^{-1}. In this case, we can hence propose a formation of a deprotonated carboxylate as a result of this complexation [101,109].

Regarding the NH_3^+ group, the disappearance of 1599 cm^{-1} peak δas(NH_3^+) and upshifting of both symmetric bending and rocking modes from 1495 and 1186 cm^{-1} to 1502 and 1189 cm^{-1} respectively favour formation of strong H-bonding with surficial adsorbed hydroxyl group.

Similar to glutamic acid, the side chain seems to be efficiently involved in complexation of methionine monomer with the NPs surface. This could be proved by either massive weakening or complete disappearance of side chain

related peaks such as CH_2 rocking at 1002 and 767 cm^{-1}, and ν(C-S-C) at 739 cm^{-1}. The reason for this situation is probably due to sulphur atom that may directly interact with the surficial iron atom, as previously suggested [110,111], and hence lead to the quenching or limiting the vibrational modes of the side chain bonds.

3.4.1.8 Phenylalanine HCl association with USPIONs

In the same manner as glutamic acid and methionine, the IR spectrum of the USPIONs associated phenylalanine implies the presence of a considerable interaction between its side chain and the surface of USPIONs, where all the peaks of the aromatic ring either disappeared or are considerably weakened, as illustrated in Figure 3-11.

For the carboxylic acid group, the disappearance of the normal C=O stretching peak and emergence of weaker IR maximum at 1679 cm^{-1} strongly suggest formation a bidentate complexation with the surficial iron atoms. An additional evidence for this suggestion is that no IR band that would correspond to the hydroxyl bending mode could be seen after association with USPIONs.

The protonated amino group is not excluded from this interaction, however, the binding here is supposed to be not very significant. We believe that H-bonds is mediating the interaction in this situation where the $\delta as(NH_3^+)$ has upshifted for around 15 cm^{-1} (from 1571 to 1586 cm^{-1}) while the $\delta s(NH_3^+)$ underwent only some weakening without shifting.

Importantly, the interesting finding related to the phenylalanine hydrophobic side chain binding to the surface of USPIONs is in agreement with the literature

on the adsorption of phenylalanine on zeolites, whereby Munsch *et al* [112] have explained his phenomenon in term of VDW interactions.

3.4.1.9 Glycine HCl association with USPIONs

The IR spectrum of USPIONs associated glycine proposes a slight, but distinct divergence in the mechanism of the amino acids association from other tested amino acids. For the protonated carboxylic acid, there are two observed spectral changes which favour formation of an interaction between one oxygen atom (from C-O side mainly) and the NPs surface *via* monodentate surface complexation. In this regard, the peak that is attributed to C=O stretching underwent a downshifting, compared to a free monomer, from 1733 cm^{-1} to 1720 cm^{-1}. Second, the vibrational coupling related to ν(C-O) and δ(OH) has experienced two different shifts to a lower and higher wavenumber values at the same time for around 17 cm^{-1} (from 1422 to 1405 cm^{-1}) and 32 cm^{-1} (from 1218 to 1250 cm^{-1}) respectively. In addition, splitting of IR frequency maximum at 1123 cm^{-1} to doublet at 1129-1110 cm^{-1} is another supportive observation to our suggested mechanism.

Interestingly, it seems that the protonated amine group has experienced strong binding to USPIONs. This is clearly evident from the widening and splitting of both antisymmetric and symmetric bending modes and upshifting of rocking mode from 847 to 885 cm^{-1}. H-bonding together with strong electrostatic interaction are thought to be the reason.

Although this finding is not good agreement with Schwaminger *et al* proposal [81], we believe that the small molecular size of glycine monomer provides a steric

strain which in turn restrict the interaction between carboxylic acid group and surficial iron in favour of the protonated amine group.

3.5 Conclusions

The data in this chapter demonstrate that the 'dry mixing' with applied shear force protocol, adopted for surface modification of iron USPIONs, is highly effective in preparing modified particles. It produces a stable colloidal dispersions of USPIONs in aqueous media, stabilized by electrostatic forces. In the present case, amino acids of different molecular attributes (hydropathy, volume, physicochemical, charge, and polarity) were successfully used for the stabilization of USPIONs dispersions.

The data from elemental iron analysis revealed an important finding in that improving water solubility of the surface modifying aminoacid (by converting them to HCl salt) results in a dramatic increase in the population of modified USPIONs that are dispersed in a water solvent, indicating their surface modification with associated aminoacid molecules.

Given that 0.26 nm^2 is the area required for a carboxyl group to associate with USPIONs surface [113], the calculation related to numbers of amino acids molecules clearly indicate formation of multilayers of the aminoacid molecules around individual particles (which has an average surface area of 153.94 nm^2). This could be attributed to both the chemical nature of aminoacid molecules [84], but also to the mixing procedure adopted.

Interestingly, the use of ATR-FTIR analysis [96], found that different amino acids exhibited different mechanisms of association with the USPIONs surface, although the interactions are in general mainly mediated *via* α-carboxyl and, to

less extent, amine groups. Regarding α-carboxylate, both uni- and bi-dentate surface complexation with USPIONs are suggested, depending on the molecular structure of the amino acids. Lys, Glu, His, Leu, Met, and Phe showed bidentate carboxylate complexation with USPIONs, while the carboxylic acid group of other amino acids tested (Asp, Thr, and Gly) were associated with USPIONs *via* monodentate complexation. On the other hand, the protonated amino group of all aminoacids exhibited different degree of association with NPs ranging from weak or no interaction (as in Leu and Glu) to strong or direct coordination (for Gly and Asp). In addition, the extent of side chains involvement varies, depending on the nature of the functional group present. The proposed mechanisms of interaction are found in agreement with those reported in the literature [105,114].

Taking into account the results presented in this chapter together, Asp-, His-, and Phe-USPIONs prepared with 250 µmol of amino acid *per* 28.75 mg of USPIONs powder were selected for further studies on their behaviour in biological system, represented by Caco-2 cell model for intestinal epithelium.

3.6 References

1 Buzea, C., Pacheco, I. I. & Robbie, K. Nanomaterials and nanoparticles: Sources and toxicity. *Biointerphases* **2**, MR17-MR71 (2007).

2 Jun, Y.-w., Seo, J.-w. & Cheon, J. Nanoscaling laws of magnetic nanoparticles and their applicabilities in biomedical sciences. *Accounts of chemical research* **41**, 179-189 (2008).

3 Woźniak, E. *et al.* Stabilization of aqueous dispersions of poly (methacrylic acid)-coated iron oxide nanoparticles by double hydrophilic block polyelectrolyte poly (ethylene oxide)-block-poly (N-methyl-2-vinylpyridinium iodide). *Colloids and Surfaces A: Physicochemical and Engineering Aspects* **514**, 32-37 (2017).

4 Xia, T. *et al.* Novel complex-coprecipitation route to form high quality triethanolamine-coated Fe 3 O 4 nanocrystals: their high saturation magnetizations and excellent water treatment properties. *CrystEngComm* **14**, 5741-5744 (2012).

5 Lim, E. W. C. in *Molecular Dynamics-Theoretical Developments and Applications in Nanotechnology and Energy* (InTech, 2012).

6 Derjaguin, B. & Landau, L. Theory of the stability of strongly charged lyophobic sols and of the adhesion of strongly charged particles in solutions of electrolytes. *Acta physicochim. URSS* **14**, 633-662 (1941).

7 Verwey, E. J. W. & Overbeek, J. T. G. Theory of the stability of lyophobic colloids. *Journal of Colloid Science* **10**, 224-225 (1955).

8 Schwertmann, U. & Cornell, R. M. *Iron oxides in the laboratory: preparation and characterization*. (John Wiley & Sons, 2008).

9 Dunn, A. Polymeric stabilization of colloidal dispersions. By DH Napper, Academic Press, London, 1984. pp. xviii+ 428, price£ 39.50, $65.00. ISBN 0-12-513980-2. *Polymer International* **18**, 278-278 (1986).

10 Jiang, J., Oberdörster, G. & Biswas, P. Characterization of size, surface charge, and agglomeration state of nanoparticle dispersions for toxicological studies. *Journal of Nanoparticle Research* **11**, 77-89 (2009).

11 Van der Hoeven, P. C. & Lyklema, J. Electrostatic stabilization in non-aqueous media. *Advances in Colloid and Interface Science* **42**, 205-277 (1992).

12 Widegren, J. & Bergström, L. The effect of acids and bases on the dispersion and stabilization of ceramic particles in ethanol. *Journal of the European Ceramic Society* **20**, 659-665 (2000).

13 Birdi, K. *Handbook of surface and colloid chemistry*. (CRC Press, 2015).

14 Vennapusa, R., Hunegnaw, S. M., Cabrera, R. B. & Fernández-Lahore, M. Assessing adsorbent–biomass interactions during expanded bed adsorption onto ion exchangers utilizing surface energetics. *Journal of Chromatography A* **1181**, 9-20 (2008).

15 Van Oss, C. J. *Interfacial forces in aqueous media*. (CRC press, 2006).

16 Mohapatra, S., Pramanik, N., Ghosh, S. K. & Pramanik, P. Synthesis and characterization of ultrafine poly (vinylalcohol phosphate) coated magnetite nanoparticles. *Journal of nanoscience and nanotechnology* **6**, 823-829 (2006).

17 Storm, G., Belliot, S. O., Daemen, T. & Lasic, D. D. Surface modification of nanoparticles to oppose uptake by the mononuclear phagocyte system. *Advanced drug delivery reviews* **17**, 31-48 (1995).
18 Romero-Cano, M., Martin-Rodriguez, A. & De Las Nieves, F. Electrosteric stabilization of polymer colloids with different functionality. *Langmuir* **17**, 3505-3511 (2001).
19 Raychoudhury, T., Naja, G. & Ghoshal, S. Assessment of transport of two polyelectrolyte-stabilized zero-valent iron nanoparticles in porous media. *Journal of contaminant hydrology* **118**, 143-151 (2010).
20 Ma, Y.-H. *et al.* Magnetically targeted thrombolysis with recombinant tissue plasminogen activator bound to polyacrylic acid-coated nanoparticles. *Biomaterials* **30**, 3343-3351 (2009).
21 Iversen, N. K. *et al.* Superparamagnetic iron oxide polyacrylic acid coated γ-Fe 2 O 3 nanoparticles do not affect kidney function but cause acute effect on the cardiovascular function in healthy mice. *Toxicology and applied pharmacology* **266**, 276-288 (2013).
22 Mahdavian, A. R. & Mirrahimi, M. A.-S. Efficient separation of heavy metal cations by anchoring polyacrylic acid on superparamagnetic magnetite nanoparticles through surface modification. *Chemical engineering journal* **159**, 264-271 (2010).
23 Zhang, Y., Kohler, N. & Zhang, M. Surface modification of superparamagnetic magnetite nanoparticles and their intracellular uptake. *Biomaterials* **23**, 1553-1561 (2002).
24 Huang, G. *et al.* A novel strategy for surface modification of superparamagnetic iron oxide nanoparticles for lung cancer imaging. *Journal of materials chemistry* **19**, 6367-6372 (2009).
25 Bergemann, C., Müller-Schulte, D., Oster, J., à, à Brassard, L. & Lübbe, A. Magnetic ion-exchange nano-and microparticles for medical, biochemical and molecular biological applications. *Journal of Magnetism and Magnetic Materials* **194**, 45-52 (1999).
26 Neouze, M.-A. & Schubert, U. Surface modification and functionalization of metal and metal oxide nanoparticles by organic ligands. *Monatshefte für Chemie/Chemical Monthly* **139**, 183-195 (2008).
27 Farrokhpay, S. A review of polymeric dispersant stabilisation of titania pigment. *Advances in Colloid and Interface Science* **151**, 24-32 (2009).
28 Faure, B. *et al.* Dispersion and surface functionalization of oxide nanoparticles for transparent photocatalytic and UV-protecting coatings and sunscreens. *Science and technology of advanced materials* **14**, 023001 (2013).
29 Pettersson, A., Marino, G., Pursiheimo, A. & Rosenholm, J. B. Electrosteric stabilization of Al2O3, ZrO2, and 3Y–ZrO2 suspensions: effect of dissociation and type of polyelectrolyte. *Journal of colloid and interface science* **228**, 73-81 (2000).
30 Pommié, C., Levadoux, S., Sabatier, R., Lefranc, G. & Lefranc, M. P. IMGT standardized criteria for statistical analysis of immunoglobulin V-REGION amino acid properties. *Journal of Molecular Recognition* **17**, 17-32 (2004).
31 Cave, G. W. V. & Mundell, V. J. (Google Patents, 2015).

32 Madhavan, J. *et al.* Growth and characterization of L-histidine hydrochloride monohydrate single crystals. *Crystal Research and Technology* **42**, 59-64 (2007).
33 Huang, M., Lv, S. & Zhou, C. Thermal decomposition kinetics of glycine in nitrogen atmosphere. *Thermochimica acta* **552**, 60-64 (2013).
34 Li, J. *et al.* Evaluate the pyrolysis pathway of glycine and glycylglycine by TG–FTIR. *Journal of analytical and applied pyrolysis* **80**, 247-253 (2007).
35 Ramachandran, E. & Natarajan, S. Gel growth and characterization of β-DL-methionine. *Crystal Research and Technology* **41**, 411-415 (2006).
36 Caroline, M. L. & Vasudevan, S. Growth and characterization of l-phenylalanine nitric acid, a new organic nonlinear optical material. *Materials Letters* **63**, 41-44 (2009).
37 Rodante, F. & Marrosu, G. Thermal analysis of some α-amino acids using simultaneous TG-DSC apparatus. The use of dynamic thermogravimetry to study the chemical kinetics of solid state decomposition. *Thermochimica acta* **171**, 15-29 (1990).
38 Dioumaev, A. Infrared methods for monitoring the protonation state of carboxylic amino acids in the photocycle of bacteriorhodopsin. *Biochemistry (Moscow)* **66**, 1269-1276 (2001).
39 Edsall, J. T., Otvos, J. W. & Rich, A. Raman Spectra of amino acids and related compounds. VII. Glycylglycine, cysteine, cystine and other amino acids1. *Journal of the American Chemical Society* **72**, 474-477 (1950).
40 Mary, M. B., Umadevi, M. & Ramakrishnan, V. Vibrational spectral analysis of L-lysine L-lysinium dichloride nitrate. *Spectrochimica Acta Part A: Molecular and Biomolecular Spectroscopy* **61**, 3124-3130 (2005).
41 Aydın, M., Kartal, Z., Osmanoğlu, Ş., Başkan, M. H. & Topkaya, R. EPR and FT-IR spectroscopic studies of L-lysine monohydrochloride and L-glutamic acid hydrochloride powders. *Journal of Molecular Structure* **994**, 150-154 (2011).
42 Petrosyan, A. & Ghazaryan, V. Vibrational spectra of L-lysine monohydrochloride dihydrate and its two anhydrous forms. *Journal of Molecular Structure* **917**, 56-62 (2009).
43 Venyaminov, S. Y. & Kalnin, N. Quantitative IR spectrophotometry of peptide compounds in water (H2O) solutions. I. Spectral parameters of amino acid residue absorption bands. *Biopolymers* **30**, 1243-1257 (1990).
44 Wolpert, M. & Hellwig, P. Infrared spectra and molar absorption coefficients of the 20 alpha amino acids in aqueous solutions in the spectral range from 1800 to 500cm− 1. *Spectrochimica Acta Part A: Molecular and Biomolecular Spectroscopy* **64**, 987-1001 (2006).
45 Lin-Vien, D., Colthup, N. B., Fateley, W. G. & Grasselli, J. G. *The handbook of infrared and Raman characteristic frequencies of organic molecules*. (Elsevier, 1991).
46 Colthup, N. *Introduction to infrared and Raman spectroscopy*. (Elsevier, 2012).

47 Navarrete, J., Hernandez, V. & Ramirez, F. Ir and Raman spectra of L-aspartic acid and isotopic derivatives. *Biopolymers* **34**, 1065-1077 (1994).
48 Shimanouchi, T., Tsuboi, M., Takenishi, T. & Iwata, N. A strong band at 1200 cm− 1, characteristic of the− CH2− COOH group. *Spectrochimica Acta* **16**, 1328-1332 (1960).
49 Roddick-Lanzilotta, A. D., Connor, P. A. & McQuillan, A. J. An in situ infrared spectroscopic study of the adsorption of lysine to TiO2 from an aqueous solution. *Langmuir* **14**, 6479-6484 (1998).
50 Pearson, J. & Slifkin, M. The infrared spectra of amino acids and dipeptides. *Spectrochimica Acta Part A: Molecular Spectroscopy* **28**, 2403-2417 (1972).
51 Kumararaman, S., Kirubavathi, K. & Selvaraju, K. Growth and Characterization of l-glutamic acid hydro chloro bromide, a new nonlinear optical material. *Journal of Minerals and Materials Characterization and Engineering* **10**, 49 (2011).
52 Zhang, Y. J., Shu, Z., Xu, W., Chen, G. & Li, Z.-G. l-Glutamic acid hydrochloride at 153 K. *Acta Crystallographica Section E: Structure Reports Online* **64**, o446-o446 (2008).
53 Natarajan, S., Chitra, G., Dhas, B., Martin, S. & Athimoolam, S. Growth, structural, thermal and optical studies on L-glutamic acid hydrobromide–A new semiorganic NLO material. *Crystal Research and Technology* **43**, 713-719 (2008).
54 Ramirez, F. & Navarrete, J. L. Force field and normal coordinate calculations for glutamic acid. *Spectrochimica Acta Part A: Molecular and Biomolecular Spectroscopy* **51**, 293-302 (1995).
55 Wagner, C. C. & Baran, E. J. Vibrational and Magnetic Properties of a Cu/Mg Glutamate Complex. *Acta Farmacéutica Bonaerense* **22**, 137-142 (2003).
56 Marti, E. M., Methivier, C., Dubot, P. & Pradier, C. Adsorption of (S)-histidine on Cu (110) and oxygen-covered Cu (110), a combined Fourier transform reflection absorption infrared spectroscopy and force field calculation study. *The Journal of Physical Chemistry B* **107**, 10785-10792 (2003).
57 Martusevičius, S., Niaura, G., Talaikyté, Z. & Razumas, V. Adsorption of L-histidine on copper surface as evidenced by surface-enhanced Raman scattering spectroscopy. *Vibrational spectroscopy* **10**, 271-280 (1996).
58 Wellner, N. & Zundel, G. Proton transfer processes in the hydrogen-bonded structure of the active centre of serine proteases—an FT—IR study. *Journal of molecular structure* **317**, 249-259 (1994).
59 Hasegawa, K., Ono, T.-a. & Noguchi, T. Vibrational spectra and ab initio DFT calculations of 4-methylimidazole and its different protonation forms: infrared and Raman markers of the protonation state of a histidine side chain. *The Journal of Physical Chemistry B* **104**, 4253-4265 (2000).
60 Ramírez, F. J., Tunón, I., Collado, J. A. & Silla, E. Structural and vibrational study of the tautomerism of histamine free-base in solution. *Journal of the American Chemical Society* **125**, 2328-2340 (2003).
61 de Andrade Leite, S. R., dos Santos, M. A. C., Carubelli, C. R. & Massabni, A. M. G. l-Histidine-europium (III) complex: a

spectroscopical study. *Spectrochimica Acta Part A: Molecular and Biomolecular Spectroscopy* **55**, 1185-1191 (1999).

62 Mesu, J. G., Visser, T., Soulimani, F. & Weckhuysen, B. M. Infrared and Raman spectroscopic study of Ph-induced structural changes of L-histidine in aqueous environment. *Vibrational spectroscopy* **39**, 114-125 (2005).

63 Barth, A. The infrared absorption of amino acid side chains. *Progress in biophysics and molecular biology* **74**, 141-173 (2000).

64 Pawlukojć, A., Leciejewicz, J., Tomkinson, J. & Parker, S. Neutron scattering, infra red, Raman spectroscopy and ab initio study of L-threonine. *Spectrochimica Acta Part A: Molecular and Biomolecular Spectroscopy* **57**, 2513-2523 (2001).

65 Kumar, S. Spectroscopic studies of valine and leucine molecules a comparative study. *Elixir Vib. Spec* **39**, 4996-4999 (2011).

66 Rajkumar, B. J. & Ramakrishnan, V. Vibrational spectroscopic study of DL-methionine dihydrogen phosphate. *Spectrochimica Acta Part A: Molecular and Biomolecular Spectroscopy* **57**, 247-254 (2001).

67 Grunenberg, A. & Bougeard, D. The Observed and Calculated Vibrational Spectra of DL-methionine in the Study of the Solid State Phase Transition. *Berichte der Bunsengesellschaft für physikalische Chemie* **90**, 485-492 (1986).

68 Olsztynska, S., Komorowska, M., Vrielynck, L. & Dupuy, N. Vibrational spectroscopic study of L-phenylalanine: Effect of Ph. *Applied Spectroscopy* **55**, 901-907 (2001).

69 Cao, X. & Fischer, G. The infrared spectra and molecular structure of zwitterionic L-β-phenylalanine. *Journal of Molecular Structure* **519**, 153-163 (2000).

70 Sousa, M., Rubim, J., Sobrinho, P. & Tourinho, F. Biocompatible magnetic fluid precursors based on aspartic and glutamic acid modified maghemite nanostructures. *Journal of magnetism and magnetic materials* **225**, 67-72 (2001).

71 Mikhaylova, M. *et al.* BSA immobilization on amine-functionalized superparamagnetic iron oxide nanoparticles. *Chemistry of Materials* **16**, 2344-2354 (2004).

72 Viota, J., Arroyo, F., Delgado, A. & Horno, J. Electrokinetic characterization of magnetite nanoparticles functionalized with amino acids. *Journal of colloid and interface science* **344**, 144-149 (2010).

73 Qu, H., Ma, H., Zhou, W. & O'Connor, C. J. In situ surface functionalization of magnetic nanoparticles with hydrophilic natural amino acids. *Inorganica Chimica Acta* **389**, 60-65 (2012).

74 Ünal, B. *et al.* L-Histidine coated iron oxide nanoparticles: synthesis, structural and conductivity characterization. *Journal of Alloys and Compounds* **505**, 172-178 (2010).

75 Durmus, Z. *et al.* L-lysine coated iron oxide nanoparticles: synthesis, structural and conductivity characterization. *Journal of Alloys and Compounds* **484**, 371-376 (2009).

76 Durmus, Z. *et al.* Synthesis and characterization of l-carnosine coated iron oxide nanoparticles. *Journal of Alloys and Compounds* **509**, 2555-2561 (2011).

77 Aghazadeh, M., Karimzadeh, I., Ganjali, M. R. & Morad, M. M. A novel preparation method for surface coated superparamagnetic Fe 3 O 4 nanoparticles with vitamin C and sucrose. *Materials Letters* **196**, 392-395 (2017).
78 Anandan, P. *et al.* Crystal growth and characterization of L-histidine hydrochloride monohydrate semiorganic nonlinear optical single crystals. *Optical Materials* **34**, 1225-1230 (2012).
79 Anandan, P. & Jayavel, R. Crystal growth and characterization of semiorganic single crystals of L-histidine family for NLO applications. *Journal of crystal growth* **322**, 69-73 (2011).
80 Culita, D. C. *et al.* Superparamagnetic nanomagnetites modified with histidine and tyrosine. *Materials Chemistry and Physics* **111**, 381-385 (2008).
81 Schwaminger, S. P. *et al.* Nature of Interactions of Amino Acids with Bare Magnetite Nanoparticles. *Journal of Physical Chemistry C* **119**, 23032-23041, doi:10.1021/acs.jpcc.5b07195 (2015).
82 Ranninger, M. N., Andrade, M. G. & Franco, M. A. Thermal decomposition of some imidazole and N-methyl substituted imidazole complexes of palladium (II). *Journal of Thermal Analysis and Calorimetry* **14**, 281-290 (1978).
83 Chandrasekaran, J., Ilayabarathi, P., Maadeswaran, P., Kutty, P. M. & Pari, S. Growth and characterization of l-histidine cadmium chloride monohydrate a semiorganic nonlinear optical crystals. *Optics Communications* **285**, 2096-2100 (2012).
84 Pušnik, K. *et al.* Adsorption of Amino Acids, Aspartic Acid, and Lysine onto Iron-Oxide Nanoparticles. *The Journal of Physical Chemistry C* **120**, 14372-14381 (2016).
85 Rahman, M., Laurent, S., Tawil, N., Yahia, L. & Mahmoudi, M. *Protein-nanoparticle interactions*. (Springer, 2013).
86 Moore, T. L. *et al.* Nanoparticle colloidal stability in cell culture media and impact on cellular interactions. *Chemical Society Reviews* **44**, 6287-6305 (2015).
87 Pugh, R. J. & Bergstrom, L. *Surface and colloid chemistry in advanced ceramics processing*. Vol. 51 (CRC Press, 1993).
88 Lucas, I., Durand-Vidal, S., Dubois, E., Chevalet, J. & Turq, P. Surface charge density of maghemite nanoparticles: Role of electrostatics in the proton exchange. *The Journal of Physical Chemistry C* **111**, 18568-18576 (2007).
89 Lucas, I. T. *et al.* Influence of the volume fraction on the electrokinetic properties of maghemite nanoparticles in suspension. *Molecular Physics* **112**, 1463-1471 (2014).
90 Parks, G. A. & Bruyn, P. D. The Zero Point of Charge of Oxides1. *The Journal of Physical Chemistry* **66**, 967-973 (1962).
91 Kosmulski, M. Ph-dependent surface charging and points of zero charge. IV. Update and new approach. *Journal of Colloid and Interface Science* **337**, 439-448 (2009).
92 Parks, G. A. The isoelectric points of solid oxides, solid hydroxides, and aqueous hydroxo complex systems. *Chemical Reviews* **65**, 177-198 (1965).

93 Damodaran, S. *Amino acids, peptides, and proteins*. Vol. 4 (CRC Press: Boca Raton, FL, 2008).
94 Fritz, G., Schädler, V., Willenbacher, N. & Wagner, N. J. Electrosteric stabilization of colloidal dispersions. *Langmuir* **18**, 6381-6390 (2002).
95 Mudunkotuwa, I. A. & Grassian, V. H. Histidine adsorption on TiO2 nanoparticles: an integrated spectroscopic, thermodynamic, and molecular-based approach toward understanding nano–bio interactions. *Langmuir* **30**, 8751-8760 (2014).
96 Atitar, M. F., Belhadj, H., Dillert, R. & Bahnemann, D. W. in *Emerging Pollutants in the Environment-Current and Further Implications* (InTech, 2015).
97 Papageorgiou, S. K. *et al.* Metal–carboxylate interactions in metal–alginate complexes studied with FTIR spectroscopy. *Carbohydrate Research* **345**, 469-473 (2010).
98 Tackett, J. E. FT-IR characterization of metal acetates in aqueous solution. *Applied Spectroscopy* **43**, 483-489 (1989).
99 Nara, M., Morii, H. & Tanokura, M. Coordination to divalent cations by calcium-binding proteins studied by FTIR spectroscopy. *Biochimica et Biophysica Acta (BBA)-Biomembranes* **1828**, 2319-2327 (2013).
100 Hug, S. J. & Bahnemann, D. Infrared spectra of oxalate, malonate and succinate adsorbed on the aqueous surface of rutile, anatase and lepidocrocite measured with in situ ATR-FTIR. *Journal of electron spectroscopy and related phenomena* **150**, 208-219 (2006).
101 Duckworth, O. W. & Martin, S. T. Surface complexation and dissolution of hematite by C 1-C 6 dicarboxylic acids at Ph= 5.0. *Geochimica et Cosmochimica Acta* **65**, 4289-4301 (2001).
102 Meng, M., Stievano, L. & Lambert, J.-F. Adsorption and thermal condensation mechanisms of amino acids on oxide supports. 1. Glycine on silica. *Langmuir* **20**, 914-923 (2004).
103 Nara, M. *et al.* Infrared studies of interaction between metal ions and Ca2+-binding proteins Marker bands for identifying the types of coordination of the side-chain COO− groups to metal ions in pike parvalbumin (Pi= 4.10). *FEBS letters* **349**, 84-88 (1994).
104 Pouchert, C. (Inc, 1985).
105 Roddick-Lanzilotta, A. D. & McQuillan, A. J. An in situ Infrared Spectroscopic Study of Glutamic Acid and of Aspartic Acid Adsorbed on TiO2: Implications for the Biocompatibility of Titanium. *Journal of Colloid and Interface Science* **227**, 48-54, (2000).
106 Nara, M., Torii, H. & Tasumi, M. Correlation between the Vibrational Frequencies of the Carboxylate Group and the Types of Its Coordination to a Metal Ion: An ab Initio Molecular Orbital Study. *The Journal of Physical Chemistry* **100**, 19812-19817, doi:10.1021/jp9615924 (1996).
107 Parikh, S. J. *et al.* Evaluating glutamate and aspartate binding mechanisms to rutile (α-TiO2) via ATR-FTIR spectroscopy and quantum chemical calculations. *Langmuir* **27**, 1778-1787 (2011).
108 Schwaminger, S. P. *et al.* Nature of interactions of amino acids with bare magnetite nanoparticles. *The Journal of Physical Chemistry C* **119**, 23032-23041 (2015).
109 Vittadini, A., Selloni, A., Rotzinger, F. & Grätzel, M. Formic acid adsorption on dry and hydrated TiO2 anatase (101) surfaces by DFT

calculations. *The Journal of Physical Chemistry B* **104**, 1300-1306 (2000).

110 Sellmann, D., Geck, M. & Moll, M. Transition-metal complexes with sulfur ligands. 62. Hydrogen evolution upon reaction of protons with sulfur-coordinated iron (II) complexes. Investigation of the proton, hydrogen and hydride interactions with iron 1, 2-benzenedithiolate complexes. *Journal of the American Chemical Society* **113**, 5259-5264 (1991).

111 Nesbitt, H., Bancroft, G., Pratt, A. & Scaini, M. Sulfur and iron surface states on fractured pyrite surfaces. *American Mineralogist* **83**, 1067-1076 (1998).

112 Munsch, S., Hartmann, M. & Ernst, S. Adsorption and separation of amino acids from aqueous solutions on zeolites. *Chemical Communications*, 1978-1979 (2001).

113 Harris, L. *et al.* Magnetite nanoparticle dispersions stabilized with triblock copolymers. *Chemistry of Materials* **15**, 1367-1377 (2003).

114 Gambino, G. L., Lombardo, G. M., Grassi, A. & Marletta, G. Molecular modeling of interactions between L-lysine and a hydroxylated quartz surface. *The Journal of Physical Chemistry B* **108**, 2600-2607 (2004).

Chapter 4: Biological Assessment of Aminoacid-modified USPIONs in *in vitro* culture model

4.1 Introduction

This section of the work deals with a preliminary biological assessment of USPIONs in term of their cellular toxicity applying a routine *in vitro* toxicity tests usually described in the literature for other NPs systems [1,2].

Due to their size in the nano-range, USPIONs have potentials to impact on the cells in different ways. A number of studies have demonstrated that exposure to USPIONs of different surface chemistries can cause a significant cytotoxic effect upon mitochondrial function (MTS assay) especially when applied at higher concentrations [3-5]. In addition, and more specifically related to metal oxide USPIONs, it was noticed that the redox active surfaces of USPIONs are implicated in electron flow which in turn acts to influence mitochondrial functionality [6]. As a result, a routine toxicity test measuring the level of mitochondrial dehydrogenases activity cannot provide a sufficient understanding of potential toxic effect of NPs on mitochondria [7]. The studies adopting different toxicity assessments to improve our understanding of USPIONs effects in biological systems demonstrated that USPIONs can cause enhanced interleukin-(IL)-10 production, along with inhibition of tumour necrosis factor-α (TNF-α) [8]. Another study also indicates the presence of a significant signs of inflammation *via* increased expression of IL-1 and -4 in addition to secretion of matrix metalloproteinases [9]. Moreover, detecting the

presence of molecules such as malondialdehyde (MDA), and 4-hydroxynonenal (4-HNE), products of lipid peroxidation, further indicate cytotoxic influence of NPs [10,11].

As indicated in previous chapters, the initial interactions occurring between USPIONs and biological system components dictate and modulate the outcome of cellular response [12]. Depending on the route of entry, these initial interactions will occur with, for example, proteinaceous compounds of systemic circulation if the route of entry is e.g. intravenous injection, or it could be interaction with mucus and cell membrane if the route of entry is e.g. lung of gut [13,14]. The binding of proteins (opsonisation) and creation of corona on the NPs surface was described in the introduction chapter of this thesis.

The current section will focus on investigating the cellular response upon their exposure to USPIONs with distinct surface chemistries – achieved by surface modification with different amino acids, as described in the previous chapter. Experiments described in this chapter aim at provide an initial understanding of effects of USPIONs' surface chemistry on their interactions with, and potential cytotoxic effects on intestinal epithelium Caco-2 cell line – as a biological model reflecting USPIONs possible entry route a human body *via* mouth (oral). The NPs toxicity was assessed using a panel of assays including: cells metabolic activity, cellular membrane integrity and the production of reactive oxygen species (ROS), to reveal a possible toxicity and cell death pathways. The work was also undertaken to visualise the interaction between different USPIONs with cellular surface/ membrane (using TEM microscopy) as well as cellular localization of the USPIONs.

4.2 Materials and Methods

4.2.1 Materials

4.2.1.1 Cells and Cell Culture Consumables

Caco-2 (human intestinal adenocarcinoma) cells were purchased from the American Type Culture Collection (ATCC number; CCL-185) and were used between passages 45-55. Cells were routinely cultured in Eagle's Minimal Essential Medium (EMEM), supplemented with 1% (v/v) antibiotic/antimycotic solution (100 U/ml penicillin, 0.1 mg/ml streptomycin, and 0.25 μg/ml amphotericin B), 1% (v/v) L-glutamine (200 Mm), 1% (v/v) non-essential aminoacids, and 10% (v/v) foetal bovine serum (FBS). All media and supplements were purchased from Sigma-Aldrich (Poole, UK). Trypsin/ethylenediaminetetraacetic acid (EDTA) solution (used to detach adherent cells in the processes of cell 'splitting' or 'passaging') was purchased from Sigma-Aldrich. Phosphate buffered saline (PBS) tablets (pH 7.4) composed of sodium chloride (8.0 g/l), potassium chloride (0.2 g/l), disodium hydrogen phosphate (1.15 g/l) and potassium dihydrogen phosphate (0.2 g/l) were obtained from Oxoid (Basingstoke, UK).

4.2.1.2 Plasticware and Glassware

24-well plates and 75 cm^2 cell culture flasks, and sterile pipettes, which were used for the maintenance of cells, were obtained from Corning Life Sciences (Amsterdam, The Netherlands). Clear, treated tissue culture 96-well plates, clear bottom 96-black well plates (used for luminescence measurements), black 96-well microplates (used for fluorescence measurements), were supplied by Nunc™ (ThermoFisher Scientific, Loughborough, UK). 8-well ibidi® micro–chamber slides used for confocal microscopy were supplied by Thistle Scientific

Ltd (Glasgow, UK). 50 ml and 15 ml volume sterile centrifuge tubes were obtained from Greiner (Stonehouse, UK) and 30 ml and 7 ml universal and bijou tubes were supplied by Sterilin (Newport, UK). Haemocytometer (improved Neubauer, to British Standard 748) was supplied by Scientific Laboratory Supplies (SLS; Nottingham, UK). PD-10 desalting columns and Mr. Frosty™ freezing container were purchased from Fisher scientific. Ultrafiltration centrifugation tubes (Vivaspin®) were obtained from ThermoFisher Scientific. Extruder was purchased from Avanti-polar lipids (Alabama, USA).

4.2.1.3 Chemical and Biological Reagents

3-(4,5-Dimethylthiazol-2-yl)-2,5-Diphenyltetrazolium Bromide is known as MTT cell proliferation assay was obtained from sigma-aldrich. Lactate Dehydrogenase (LDH) assay kit (known commercially as 'In Vitro Toxicology Assay Kit') was supplied by Sigma Aldrich. All assays were performed as per supplier's instructions. The cell-permeant 2',7'-dichlorodihydrofluorescein diacetate (H_2DCFDA) (also known as dichlorofluores *cin* diacetate) was ordered from ThermoFisher scientific. CellEvent™ Caspase-3/7 Green Detection Reagent.

4.2.2 Methods

4.2.2.1 Maintenance of cells

4.2.2.1.1 Routine maintenance and culture of cells

The growth media used for routine cell culture was EMEM supplemented with 10% (v/v) FBS, 0.10 mg/ml streptomycin, 100 units/ml penicillin, 0.25 µg/ml amphotericin and 2 Mm L-glutamine – complete EMEM. Caco-2 cells were cultured in 75 cm^2 flasks at 5% CO_2, 95% relative humidity and at 37°C until confluence (approximately 75-90 % flask coverage by cells).

Cells were fed every other day by aspirating old media from cell flasks and replacing with 15 ml of fresh, pre-warmed (37°C) media. Once confluent, as determined by optical microscopy, cells were passaged. This involved aspirating the culture media from cell flasks and subsequently washing the cells with 5 ml, pre-warmed (37°C) PBS by gently swirling. Following the wash step, PBS was removed by aspiration and replaced with 2.5 ml, pre-warmed (37°C) 0.25 % trypsin/EDTA solution, after which the flask was gently rocked ensuring good coverage over the cells before being transferred to the 37°C incubator. When confluent cell were detached and following cell detachment 5 ml of pre-warmed (37°C) culture media was added to dilute the cell-trypsin/EDTA suspension and deactivate the trypsin. The cell suspension was then transferred from the flask into a sterile 15 ml centrifuge tube and underwent centrifugation at 250 xg for 5 minutes. The supernatant containing trypsin was then aspirated off and the cell pellet re-suspended in 6 ml pre-warmed (37°C) culture media. Fractions of this cell suspension, required to achieve the desired split ration, were then transferred into flasks containing 15 ml of pre-warmed (37°C) culture media. Caco-2 cells were regularly split at ratios of 1:3 and 1:6.

Caco-2 cells were cultured to be confluent in 75 cm^3 flasks at 5% CO2, 37◦C. Once 75-95% of the flask surface covered by cells, they were passaged using the following steps: first, the culture media was aspirated from the flasks and the cells was washed with 6 ml, 37 ◦C pre-warmed PBS. Second, the cells were detached by adding 2.5-3 ml of pre-warmed (37°C) 2.5% trypsin/EDTA solution which was incubated for 10-15 min to ensure complete cell detachment. Following these steps, the deactivated trypsin by approximately 9 ml of pre-warmed (37°C) culture medium was transferred to a sterile centrifuge tube and

the cells centrifuged at 1300 rpm for 5 min. After aspiration of deactivated trypsin-containing supernatant, the pelleted cells was re-suspended by addition of 5-6 ml of fresh pre-warmed 37 ◦C culture media. The 5 ml cell suspension is ready for cell counting to quantify the required cells amount [15].

4.2.2.1.2 Cells Culture of in transwells

For toxicity-assessment studies (MTT and LDH), Caco-2 cells were seeded on 96-well plates at 104 cell density pre well. While for ICP-MS-, TEM- and flow cytometry-intended experiments the cell density was $3*10^5$ cells per each well of 6-well plate. All plates were maintained and incubated at 5% CO2, 37◦C in EMEM supplemented with FBS (10%) and L-glutamine for ≈ 48 hours prior to their use in experiments.

4.2.2.2 Cytotoxicity characterisation of different USPIONs colloidal dispersions

Evaluation the effect of three different dispersion systems (Aspartic acid, Histidine and Phenylalanine stabilised USPIONs) towards cell metabolic activity and cell membrane integrity were performed. In achievement of this aim, a gradient of USPIONs concentrations (40, 80, 150, 250, 350 and 500 µg/ml) were tested for four timeframes (1, 2, 4, 8 and 24 hours). Furthermore, these assays were undertaken in order to identify the nontoxic concentration and cell exposure time of the colloidal dispersions which will be most appropriate for further biological experiments.

4.2.2.2.1 MTT Cell metabolic activity assay

The 96-well plates (sterile, cell culture treated) were prepared according to the conditions mentioned above, unless otherwise stated. Prior to the test, cell medium was removed and replaced by sample dispersions comprising of each

of the above-stated concentrations. Test USPIONs dispersions were freshly obtained by diluting a calculated volume of highly concentrated (previously prepared and stored) stable dispersion in the required EMEM growth media volume (without FBS and L-glutamine supplementation) and thoroughly mixed (vortexed). Triton X-100 (0.2%, v/v in EMEM as received) and EMEM (without FBS and L-glutamine) were used as a positive and negative control, respectively. Cells were incubated (at 37 ◦C, 5% CO2) with samples and controls for the periods specified above. Samples and controls (including both positive and negative) were then removed and cells washed with PBS. The MTT assay was consequently conducted according to the manufacturer's instructions, following which absorbance (560 nm) was measured using a Tecan absorbance multimode microplate reader (Spark™ 10M, Tecan Trading AG, Switzerland). At least mean of five to ten repeats for each sample were statistically considered. The relative cell metabolic activity (%) was calculated using the following equation:

$$\text{Relative Metabolic Activity (\%)} = \frac{(\text{Abs}_\text{S} - \text{Abs}_\text{Tx})}{(\text{Abs}_\text{M} - \text{Abs}_\text{Tx})}$$

Where:

• Abs_S is the absorbance with the tested samples

• Abs_{Tx} is the absorbance with Triton X-100

• Abs_M is the absorbance with incomplete EMEM (as received)

4.2.2.2.2 LDH release assay

The probability of any cell membrane-disruptive effect exhibited by aminoacid-modified USPIONs have been investigated by measuring the extent of LDH released. As mentioned above, the 96-well plates were prepared. The tested

samples (Asp-, His-, and Phe-modified USPOINs colloidal dispersion) and controls were then applied to cells in the same manner (and concentrations) for the same time periods as detailed beforehand. After which and according to the manufacturer's protocol, 50 µl of the supernatants were removed from each well and transferred to a new 96-well plate. 100 µl of the LDH reagent (catalyst) was added to the samples and the plate was incubated at room temperature for 15-30 min. After this period, 50 µl of stop solution was added to these well to stop the reaction and hence color shading. Absorbance (490 nm) was measured using the Tecan absorbance microplate reader.

In order to assess the potential inactivation effect of USPIONs itself on LDH enzyme, a 5 µl of lysis buffer was added to each well of samples dispersion at the beginning of the test. After 8 hours, the aforementioned procedure was followed.

LDH leakage was calculated as the percentage relative to the controls, using the following equation:

$$\text{Relative LDH release (\%)} = \frac{(\text{Abs}_\text{S} - \text{Abs}_\text{M})}{(\text{Abs}_\text{Tx} - \text{Abs}_\text{M})}$$

Where:

• Abs_S is the absorbance obtained with the tested samples

• Abs_M is the absorbance with incomplete EMEM media (as received)

• Abs_Tx is the absorbance with Triton X-100

4.2.2.2.3 Accumulation of ROS measurement

In order to detect the relative amount of reactive species accumulated, the experiment has been proceed over four stages as follow: first, normal cell culturing of Caco-2 cells seeded in 96-well plate at density of $1x10^4$ cells/150µl media/well has been incubated for 48hrs in 37°C, 5% CO_2 environment.

Second, include H_2-DCFDA or (DCFH-DA) (2,7-Dichlorodihydrofluorescein diacetate), the fluorescent probe and hydrogen peroxide solutions preparation: Dissolve 2mg of H_2-DCFDA in 2ml of 99.9% DMSO to prepare a stoke of 2.052 Mm dye concentration. Take 50µl of the stoke and dilute it to 20ml of 1%HEPES (4-(2-hydroxyethyl)-1-piperazineethanesulfonic acid)/HBSS (Hanks' Balanced Salt Solution) buffer solution so that 5µM dye concentration will result and be ready for application to the cells. Dilute 100µl of concentrated 30%w/w H_2O_2 (around 9.8M) with 10ml 1%HEPES/HBSS buffer solution to obtain a stoke H_2O_2 solution of around 100Mm concentration. A second 50µM diluted H_2O_2 solution could be achieved by taking 10ul of 100Mm strength and completed it to be 20ml of incomplete EMEM (without FBS) solution which will be ready to produce stress species as a control for dye efficiency and cell response.

Third include plate preparing for the experiment: 100µl (HEPES/HBSS) of 5µM H_2-DCFDA were added to each well in the plate after old media aspiration. Incubate the plate for 45-60 min for cellular dye uptake. Aspirate the buffer solution and replace it with 200 µl of the following: (i) incomplete EMEM cell culture media without FBS and L-glutamine as negative control. (ii) 50 µM H_2O_2 in incomplete EMEM (as received) as a positive control. (iii) 40, 80, 150, 250, 350 and 500 µg/ml USPIONs in incomplete cell culture media (EMEM as

received). All the target concentrations of USPIONs were prepared from ≈ 6000 µg/ml stock.

The four part of this experiment include data collection using plate reader. The fluorescence intensities were recorded at excitation ʎ 485 and emission of ʎ 535. Two types of experiment timetable were applied. The first was real time measurement which started from 5 min after plate preparation till 60 min in which the plate were inserted in the plate reader and then the data collection was carried out every 5-15 min.

The second timetable was performed by incubating the plates in 5% CO_2 incubator at four time intervals which are 1, 2, 4, and 24 hours.

4.2.2.2.4 Assessment of Caspase-3/7 activation

Conserved events in the execution phases of both intrinsic and extrinsic apoptosis are represented by activation of effector caspases 3 and 7. The activation process of effector caspases could be achieved via cleavage at their DEVD peptide sequence. This step is normally mediated by an initiator caspase [16]. CellEvent® Caspase-3/7 Green ReadyProbes™ Reagent (CellEvent) is a cell permeable probe that includes a nucleic acid-binding dye conjugated to the caspase-3/7 target cleavage sequence (DEVD). The CellEvent reagent is inherently non-fluorescent as the DEVD peptide works to inhibit binding of the dye to DNA. Upon initiation of the effector phase of apoptosis, cleavage of DEVD peptide sequences enables activating caspases-3/7 and the CellEvent reagent which then interact with nucleic acids to generate bright green fluorescence that is labelling apoptotic cells. Detection of caspase-3/7 activation was performed on Caco-2 cells (passages 50-55) that are cultured in 96 well

plates (black) as normal. After that, the treatments with serial dilution (40, 80, 150, 250, 350, 500 µg/ml) of Asp-, His-, Phe-USPIONs are performed similar to previous tests in section 4.2.2.2.2 and 4.2.2.2.3 but in this case only one timeframe has been investigated (24 hours).

In addition to the treatment with serial concentrations of USPIONs in as-received EMEM, cells were also incubated with 0.01-50 µM staurosporine to test the validity of the assay, along with the concentration of the CellEvent probe used. Staurosporine is a well-established inducer of apoptosis and effector caspases [17,18].

CellEvent reagent was obtained as a solution, kept at room temperature in a dark place, and prepared with a 2% (v/v) solution diluted in PBS for application. Following exposure to different aminoacid modified USPIONs, 150 µl 2% (v/v) CellEvent:PBS solution was added directly to every well and left for 30 minutes without removing treatment solutions; thus the final CellEvent reagent concentration in wells was 1% (v/v) as 300µl present. Previous work in our group with staurosporine considered this concentration of reagent applicable to identify the activation of caspases-3/7.

Detection of CellEvent probe cleavage was accomplished by measuring the fluorescence of well solutions following excitation at 502 nm and collecting values of emission at 530 nm.

4.2.2.2.5 Hoechst 33342 / Propidium iodide double staining of nuclei

In order to examine potential apoptotic features of Caco-2 cells after Asp-, His-, and Phe-USPIONs exposure, cell nuclei were co-stained with two DNA binding dyes, Hoechst 33342 (Ho) and propidium iodide (PI) [19]. Ho is cell

permeable and hence can stain the nuclei of viable cells (give an indication of cell number) while PI is cell-impermeable where it can only penetrate the severely injured cells characterised by permeabilised plasma and nuclear membranes.

Stock solutions of PI and Ho were stored protected from light at low temperature (4ºC). They were prepared by dissolving powders in PBS to obtain concentrations of 0.1 and 1 mg/ml, respectively, followed by sonication at 37 kHz for 5 minutes to ensure dissolution. For Ho, further dilution in PBS is required as the working concentration at which the dye could be used is 1 µM (0.6 µg/ml).

With plate preparation, Caco-2 cells (passages 45-55) were seeded at a density of $6x10^4$ cells per well in clear 24 well plates (Corning) and cultured for 48 hours in complete EMEM culture medium. After the removal of culture medium, wells were washed twice with PBS followed by the addition of 0.5 ml USPIONs solution per well.

At this step, three different treatment the cells were exposed to, first, the negative control (as-received EMEM, incomplete media), second, 500µg/ml of Asp-, His-, Phe-USPIONs (dispersed in incomplete EMEM), third, the necrotic control (100% Ethanol) for 240 minutes.

Following exposure, treatments were removed, wells were washed with PBS and dyes sequentially added; initially wells were incubated with 0.5 ml 1 µM Ho for 5 minutes. 10 µl 0.1 mg.ml PI was then added to the dye solution (final PI concentration is 2 µg/ml). The resulting solution was incubated for an additional

5 minutes, after which it was removed, the cells washed twice with PBS, and 0.25 ml PBS returned to the wells prior to imaging.

Stained cell imaging was performed on an inverted EVOS fluorescent microscope. This involved capturing images on the DAPI filter (Excitation 357/44 nm; Emission 447/60nm) for Ho signals and the RFP filter (Excitation 531/40 nm; Emission 593/40 nm) for PI signals. Images were then merged using ImageJ software.

4.2.2.3 Modified USPIONs-cell interaction

4.2.2.3.1 Well plate processing

Basically we have adopted three different standard investigations in order to probe the nature of NPs-cell interaction under different incubation conditions. These are, first, quantification of iron amounts associated with cells using ICP-MS analysis, second, measuring the intensity of light scattering of treated cells as an indication for NPs-cell potential interaction, and third, direct cell imaging using TEM technique to track the location of aminoacid modified-USPIONs in caco-2 cell.

To achieve the above experiments, a common procedure for Caco-2 cells processing was followed. For the three different aminoacids-modified USPIONs, 6-well plates were prepared and cells were cultured as described earlies. Initially, 3 ml of colloidal dispersion of 80 $\mu g ml^{-1}$ aminoacid modified USPIONs in EMEM (with or without serum and L-glutamine supplementation) have been applied to every well after old growth media was aspirated. EMEM (with or without serum and L-glutamine supplementation) was used as background control in all experiments. The plates were incubated under gentle

shaking (at 37 °C, 5% CO_2) for a period of 2 hours. After which, sequence of adequate washing steps were conducted for the purpose of eliminating any loosely attached aggregates of NPs to cell membrane as much as possible.

The cells washing procedure as follow: Aspiration of modified USPIONs-dispersed EMEM from each well and 2-3 cycles of washing were applied. One cycle represent consecutive using 1 ml of both versene and PBS solutions to wash the cells. Next, 2ml 10% FBS supplemented EMEM was added to each well and left under gentle shaking for 5 min to allow particle or aggregate to diffuse into the media protein. Finally, 1 cycle of versene and PBS washing will make cells ready for the next stage of sample processing.

4.2.2.3.2 Iron amount quantification (ICP-MS analysis)

To determine the amount of iron interacted with cell line, the previously washed cells in each well were detached by using 750 µL of trypsin for 5 min which was deactivated by 750 µL of serum supplemented EMEM. The cells thoroughly re-suspended and transferred to 15 ml falcon tubes. 20 µL of cell suspension of each well was mixed with equal amount of trypan blue for cell counting using automatic cell count choice in Tecan microplate reader. The 1.5ml cell suspensions were pelleted after 5 min centrifugation at 1000 xg centrifuge force and the supernatants have been aspirated afterwards. Two principles of cell lysis were combined to make sure maximum iron extraction outcome. This step includes adding of 300 µL of RIPA lysis buffer to each tube with thorough mixing for 30-45 min followed by application of 2 cycles of freeze-thaw. To dissolve the extracted USPIONs 1ml of concentrated HCl solution (37% w/w) were added. After 6 hrs, 5ml of DI water have been used to dilute the concentrated acid. Ultimately, the falcon tubes were centrifuged at 3000 xg to

eliminate any cell debris remaining. Clear samples supernatant were treated with 50-200 µl of antifoaming agent and delivered for ICP-MS analysis. The recorded values are the mean of three measurement ± 1SD.

4.2.2.3.3 Light scattering measurement (Flow cytometry study)

The trypsin-aided detached cells were pelleted at 1000 xg centrifuge force for 5 min as above. The supernatant was replaced by 2ml of serum-free growth media, cells were re-dispersed thoroughly and passed through 40 µm membrane filter to remove cell aggregates. The samples were inserted in ice path and transferred for analysis in flow cytometry suit. The obtained data were triplicate and expressed as mean ± 1SD

4.2.2.3.4 TEM imaging (Samples preparation)

4.2.2.3.4.1 Cell fixation

Double strength of fixative (6% glutaraldehyde in 0.1 M cacodylate buffer, pH 7.2) was added to complete growth media at ratio of 1:1. The previously rinsed cells in 6-wellplate were subjected to glutaraldehyde-media solution at normal growth conditions (37°C, 5% CO_2) as reducing cells temperature below 37°C before fixation may alter the morphological characteristics of them. After 1 hr, the cells in each well were smoothly washed with 1 ml of 0.1 M cacodylate buffer three times. Cautiously, the fixed cell monolayers were scraped, transferred to 1.5 ml Eppendorf tubes and covered with excess of cacodylate buffer then stored in 4°C waiting the next step. The scraped cells will start to form a sediment overnight so that the centrifugation will be avoided to prevent cell smashing.

4.2.2.3.4.2 Embedding resin preparation

Briefly, a total of 100 ml resin were prepared by adding 25ml Araldite CY212 resin, 15ml Agar 100 resin and 55ml DDAS to a 'tripour' beaker (weigh the volumes required on the 2 digit scale instead of direct volume measurement as they are highly viscous). The mixture was efficiently stirred. Then 2ml of Dibutyl phthalate and 1.5 ml of DMP 30 were blended with the resin mix. The intensive stirring should be continued until there are no striations observed in the final combination.

4.2.2.3.4.3 Cell dehydration and resin embedding

Before commencing in dehydrating the cells, Worm 10% gelatine solution has been prepared in order to immerse the pelleted cells in it after aspirating the cacodylate buffer. 100ul of this solution were used in each Eppendorf and then stayed in fridge for 10 min to obtain a relatively hard gelatine blocks. Removing the blocks from the tubes, cutting them into several portions and transferring them to a previously labelled vials have been completed so as to start the dehydration stage. A series of ethanol at gradient concentrations were used as follow: 50%, 70% and 90% ethanol twice for 10min; and 100% ethanol twice for 20 min. For the most effective dehydration process the all vials should be covered tightly to avoid ethanol concentration changing due to evaporation. Next, 100% of propylene oxide (Propox) was used twice for 10 min. The gelatine blocks were pre-embedded with a mixture of resin:Propox at 1:3 v/v ratio for 2hrs, followed by overnight infiltration using 1:1 v/v ratio resin:Propox. In this step the vial lid should be remove to allow propox to escape leaving the resin. Later on in the next day, the resin was completely replaced with fresh resin utilising new vial and left for 3 hrs. Finally, the embedding capsules were used

to polymerise the gelatine blocks-containing resin by exposing them to 60C for 48hrs to make the resin ready for next step of sectioning. The gelatine blocks were pushed by tweezer down to touch the bottom of the capsules.

4.2.2.3.4.4 Resin blocks sectioning

The specimen blocks were tightly held and positioned with their bottom upright. By using razor, the block edges were trimmed leaving an area of 3-5 mm in which the cells in gelatine exist. Then these blocks have been placed in the microtome holder in a certain way to be aligned with diamond knife attached to a boat which is filled with DI water. Lastly, the thickness of cuts were adjusted to be between 70-90 nm. The floated cut sheets were mounted on 3.05 mm carbon coat copper grid of 200 mesh and left overnight in petri dish for air drying. The grids will be ready for TEM imaging thereafter.

4.2.2.4 Statistical analysis

Statistical comparisons were functioned by Prism application using unpaired t-test and one way ANOVA analysis. Values of $p < 0.05$ were considered statistically significant. The asterisk-sign *, **, *** and **** indicate $p < 0.05$, $p < 0.01$, $p < 0.001$ and $p < 0.0001$ respectively. Any other probabilities less than 0.0001 were denoted by ****.

4.3 Results

4.3.1 Colloidal stability of aminoacid modified USPIONs in cell culture media

Figure 4-1 shows differences in particles size of modified USPIONs following dispersion in different cell culture media (with and without serum). It is clearly evident that, in the presence of serum, USPIONs are forming a stable colloidal

dispersion, with particle size of around 120 nm, while in the serum free medium, large particle aggregates, of around 2000-3000 nm, were formed over the experiment timeframe of 90 min, as shown in Figure 4-1.

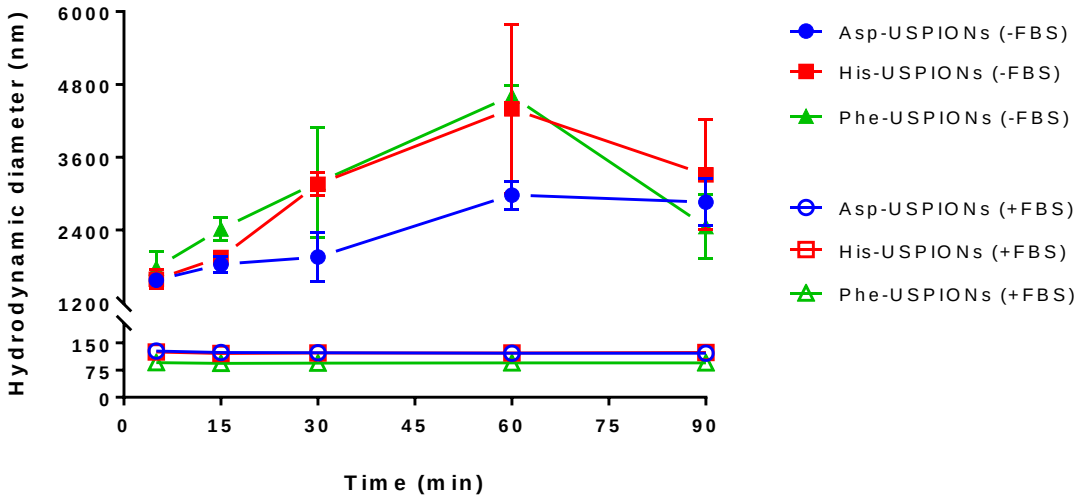


Figure 0-1: Hydrodynamic particle size of amino acid modified USPIONs in EMEM culture media in the presence and absence of FBS as a function of time.

USPIONs concentration is 80ug/ml. error bar represent ± 1SD

4.3.2 Cytotoxicity assessment of aminoacid modified USPIONs

4.3.2.1 Effect on cell metabolic activity

Figure 4-2 reveals that on a short term exposure all aminoacids modified USPIONs tested show no significant reduction in cell metabolic activity over the tested concentration range (40, 80, 150, 250, 350, and 500 µg/ml). In contrast, over a longer period of time (24hrs experiment) a significant concentration dependent reduction ($p < 0.0001$) in cell metabolic activity was

observed. Interestingly, no significant differences in LD_{50} values amongst the three systems tested were obtained – with LD_{50} values of around 400 µg/ml for 24 hours exposure.

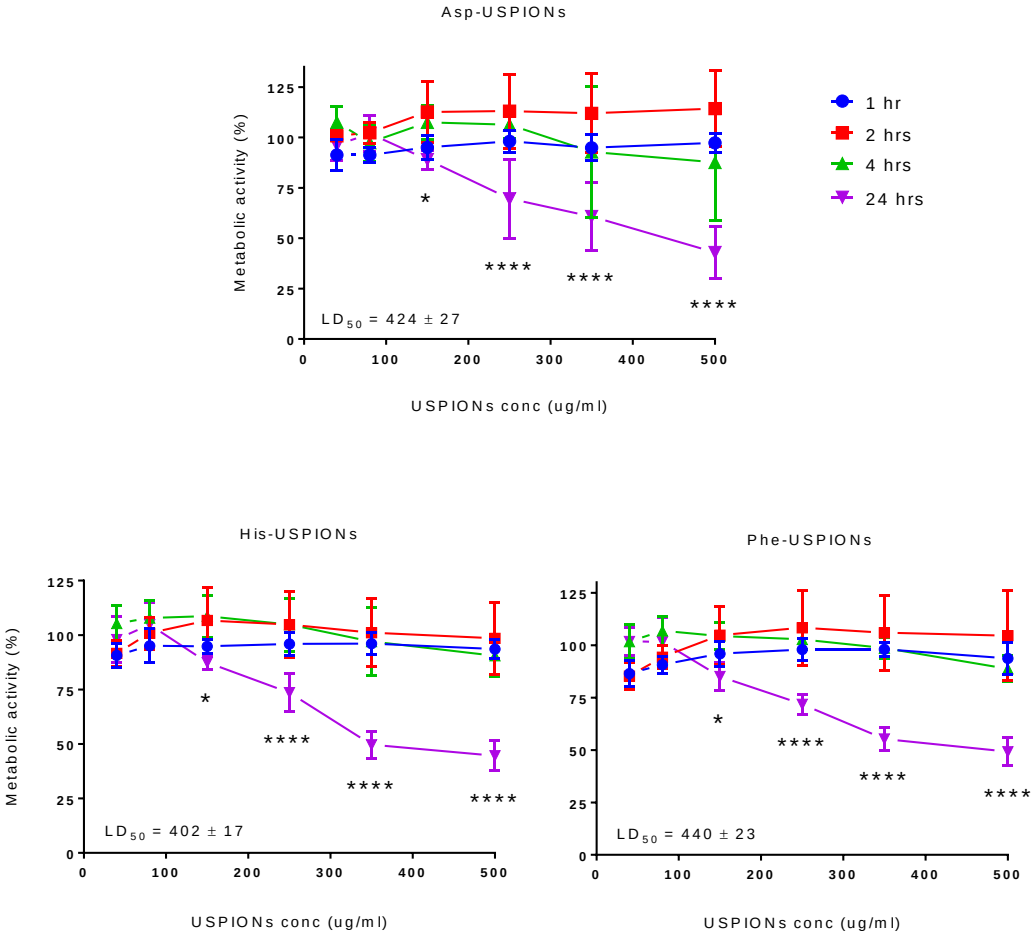


Figure 0-2: Caco-2 cell metabolic activity following exposure to Asp-, His-, and Phe-USPIONs for different time intervals.

*Data represents mean ± 1SD of triplicate measurement from three independent experiments. Lethal dose 50% (LD50) values were calculated using non-linear analysis (GraphPad prism) and are presented as mean ± SD (µg/ml). ANOVA analysis revealed no statistical difference ($p > 0.05$) between LD50 values of the different formulations. Statistical differences (ANOVA followed by Dunnet's multiple comparison test) between treatment values and the negative control are indicated by asterix (formulations at each concentration of significance did not differ in calculated level of significance). *, $P < 0.05$; **, $P < 0.01$; ***, $P < 0.001$; ****, $P < 1x10^{-3}$.*

4.3.2.2 Effect of the modified USPIONs on the cell membrane integrity (LDH assay)

Data summarized in Figure 4-3 illustrate that there was a highly significant effect ($p < 0.01$) on measured LDH activity on exposure to USPIONs in solution. The profile indicates a concentration dependant inhibition, and almost complete inactivation of the enzyme after 8 hours of exposure to higher USPIONs concentrations. This explains a surprising data in Figure 4-4 which show no measurable activity of LDH in the media even for the 8 hours cell exposure to high concentrations of USPIONs.

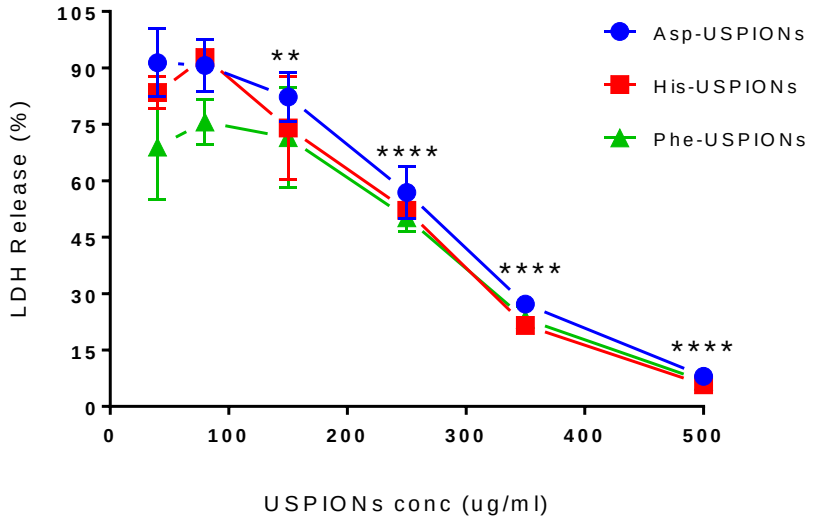


Figure 0-3: Normalised activity of LDH after 8 hours exposure to aminoacid modified USPIONs in solution.

*Data represents mean ± 1SD of triplicate measurement from three independent experiments. Statistical differences (ANOVA followed by Dunnet's multiple comparison test) between treatment values and the negative control are indicated by asterix (formulations at each concentration of significance did not differ in calculated level of significance). *, $P < 0.05$; **, $P < 0.01$; ***, $P < 0.001$; ****, $P < 1x10^{-3}$.*

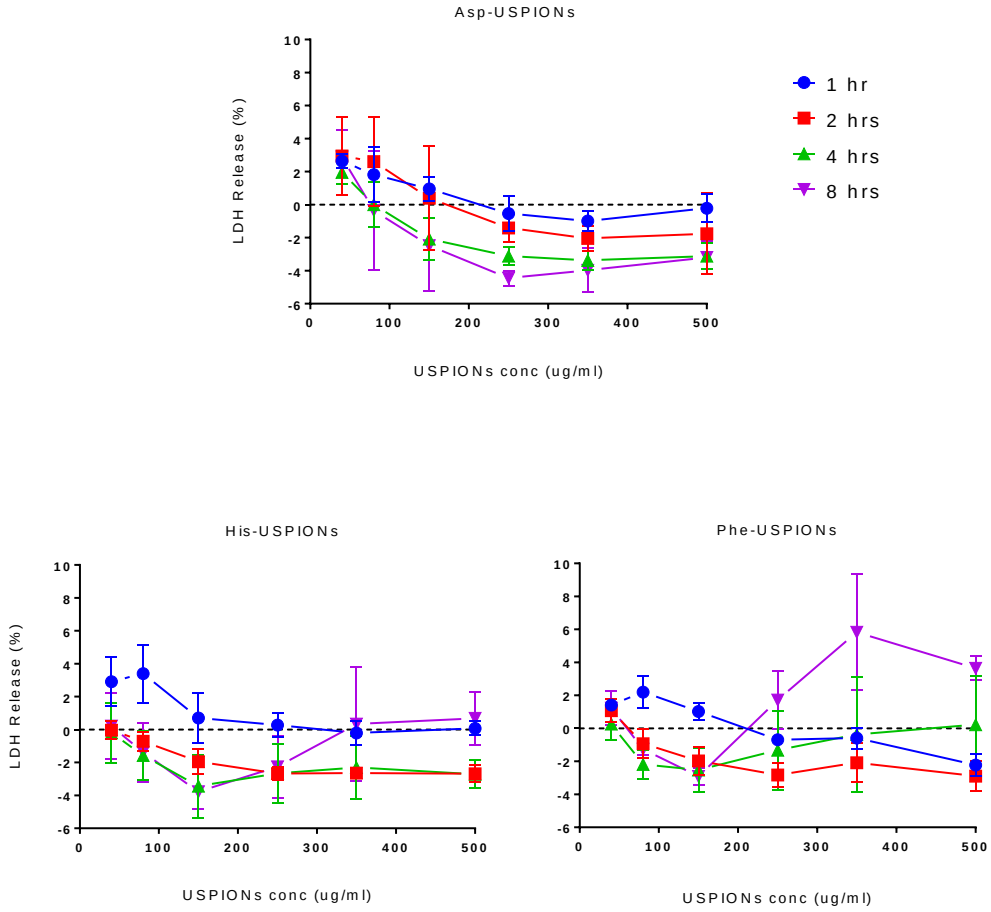


Figure 0-4: Normalised activity of LDH as following Caco-2 exposure to different aminoacids modified USPIONs systems.

Data represents mean ± 1SD of triplicate measurement from three independent experiments. ANOVA analysis revealed no statistical difference ($p > 0.05$) between treatment values and the negative control.

4.3.2.3 Reactive oxidative stress

Effects of short term exposure of Caco-2 cells to increasing concentrations of aminoacid modified USPIONs on ROS production are summarized in Figure 4-5. The data indicate an absence of a significant effect up to ~150 µg/ml concentration, followed by an unexpected reduction in ROS production at higher concentrations. Interestingly there is no clear relationship between effects of either concentration USPIONs used or time of exposure in the latter case. Figure 4-6 summarizes the data for longer term, 1-24 hours, cell exposures. It reveals the presence of strong concentration and time dependant production of ROS for all the systems tested. Interestingly, the effect of Phe-USPIONs seems to be more pronounced, relative to two other systems tested.

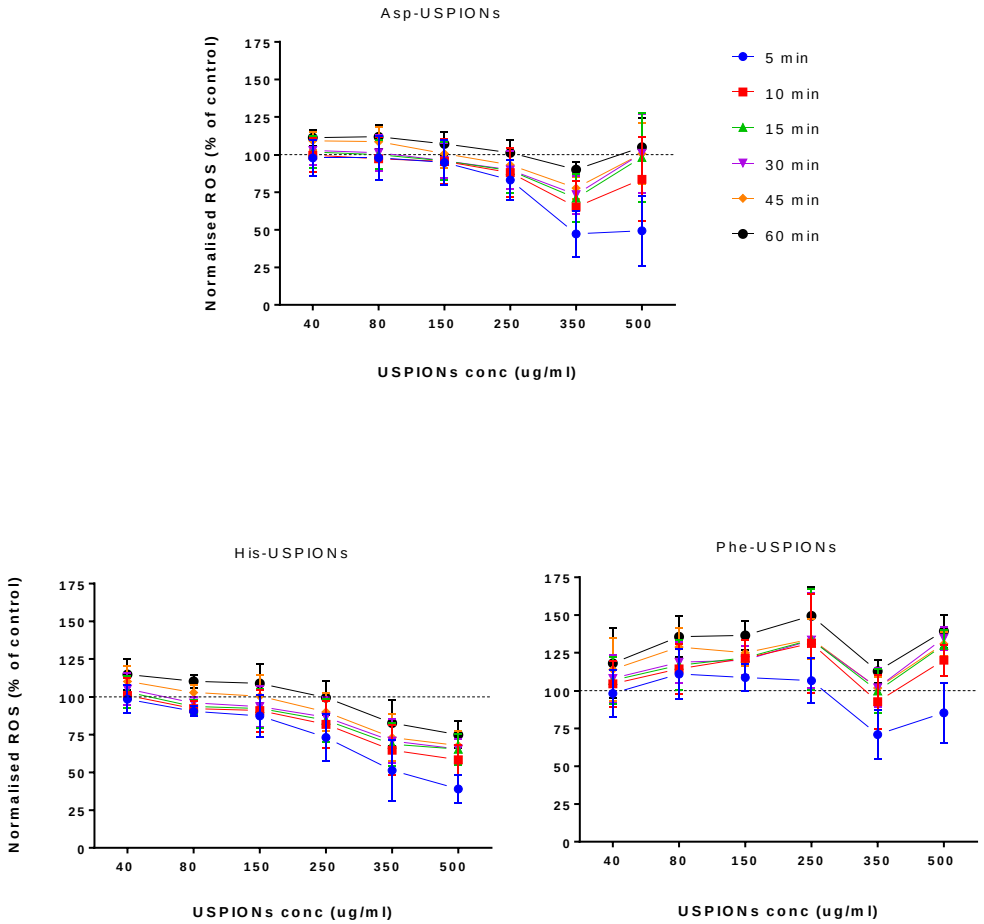


Figure 0-5: Effects of a short term exposure of Caco-2 cells to aminoacid modified USPIONs on ROS production.

A real time experiment was performed by incubating the 96-well plate inside plate reader for around 60 min. the data was recorded every 5-15 min. Data represents mean ± 1SD of triplicate measurement from three independent experiments. Statistical differences (ANOVA followed by Dunnet's multiple comparison test) between treatment values and the negative control are performed.

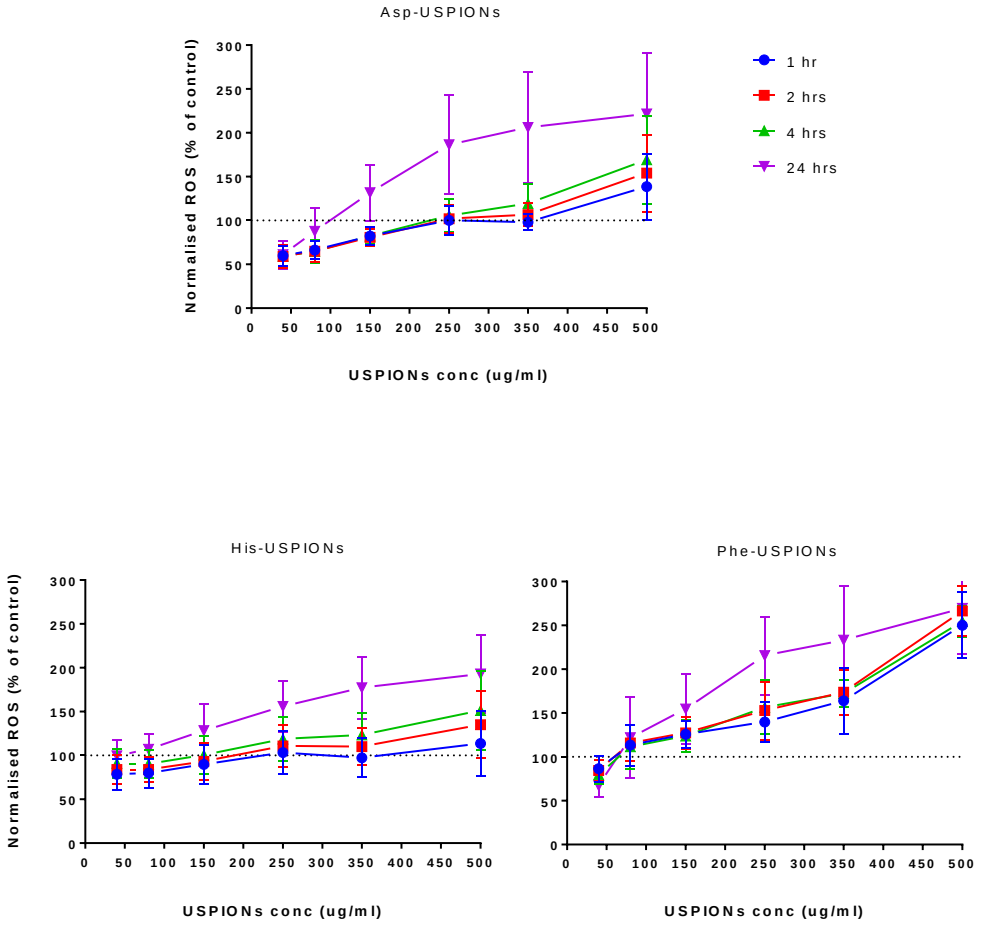


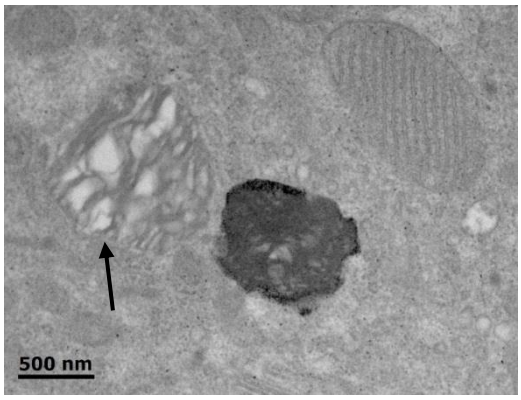
Figure 0-6: Effects of a longer term exposure of Caco-2 cells to aminoacid modified USPIONs on ROS production.

Here, the 96-wellplate was left inside normal incubator for the specified time interval mentioned. Data represents mean ± 1SD of triplicate measurement from three independent experiments.

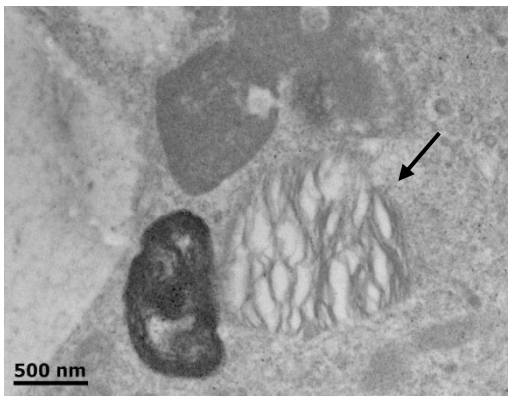
4.3.2.4 Effect of USPIONs on cell mitochondria

TEM images in Figure 4-7 of Caco-2 cells exposed to aminoacid modified USPIONs appear to illustrate the presence of mitochondria with changed, damaged morphology after the 24 hours of exposure. The mitochondria appear distorted, with internal 'disordered' membrane substructure, in addition to the outer irregularly shaped surface – all indicating substantial morphological changes.

Asp-USPIONs



Phe-USPIONs



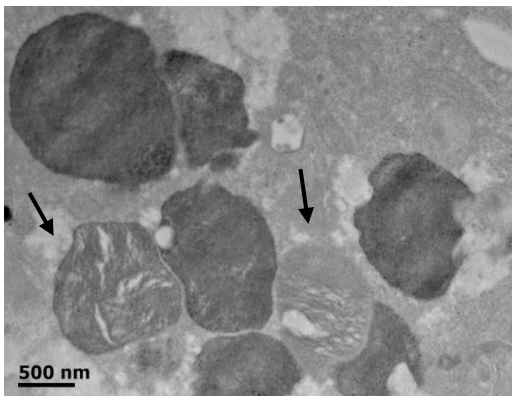


Figure 0-7: TEM micrographs morphology of cell mitochondria after 24 hrs of Caco-2 cells exposure to different USPIONs system

4.3.2.5 Effect on effector caspase activation

The activation of effector caspases-3/7 in Caco-2 cells following 24 h exposure to tested USPIONs was performed to investigate the propensity of these particles to induce cell apoptosis. Figure 4-8 demonstrates that applying Asp-, His- and Phe-modified USPIONs at concentrations ≥ 150 µg/ml elicited significant increases ($p < 0.05$) in caspase-3/7 activation (in a concentration-dependent manner). It can be noted that the maximal (~ 5-fold) increase generated by the tested USPIONs approaches that induced by the apoptotic control (~ 6-fold; 50 µM Staurosporine). Again, effects of Asp- and His-particles are comparable while the trend for Phe-counterparts differ, showing statistically significantly lower values at higher concentrations than the other two systems ($P < 0.01$; ANOVA followed by Turkeys multiple comparison of column means).

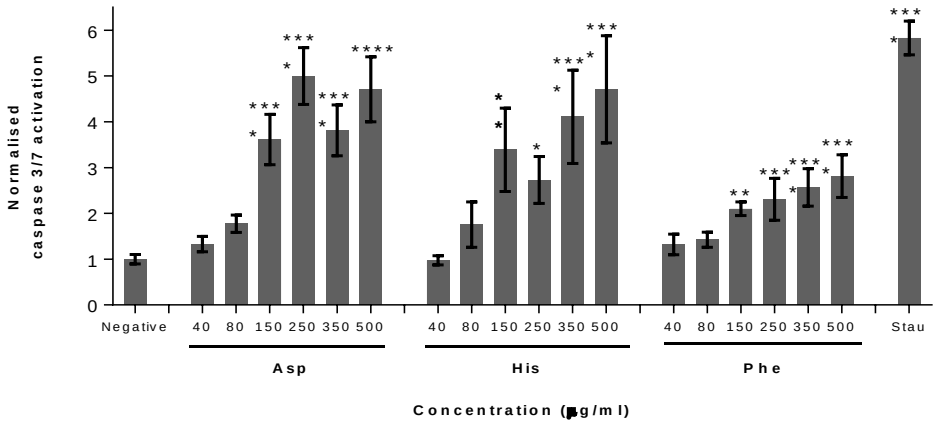


Figure 0-8: ***Effect of aminoacid modified SPIONs on the activation of Caspase-3/7 in Caco-2 cells.***

*Caspase-3/7 activation was assessed using the CellEvent Caspase-3/7 detection reagent following 24h incubation with treatment samples. Staurosporine (50 µM; Stau) was used as a known inducer of apoptosis for comparison. Data represents triplicates from three independent experiments and is presented as mean ± S.E.M. Statistical analysis was performed by ANOVA followed by Dunnet's multiple comparison test (GraphPad prism 7.0). *, P < 0.05; **, P < 0.01; ***, P < 0.001; ****, P < $1x10^{-3}$*

4.3.2.6 Hoechst 33342 / Propidium iodide double staining

To investigate potential apoptotic consequences on Caco-2 cells exposure to aminoacid modified USPIONs, cell nuclei were co-stained with the DNA binding dyes Hoechst 33342 (Ho) and propidium iodide (PI). Hoechst 33342, as a cell membrane permeable dye gives an indication of cell numbers in the sample, while membrane impermeable PI indicates a cell population with permeabilised plasma and nuclear membranes. Figure 4-9 illustrates that cells treated with the negative control (EMEM) display no significant, positive PI staining. On the contrary, application of ethanol, a known inducer of necrosis, shows positive staining in all cell nuclei, as demonstrated by the presence of purple stained nuclei in the merged image. It can be observed that cell treatment with USPIONs solutions (500 μg/ml) resulted in the presence of PI positive staining; however, this staining is shown by a small sub-population of the cells in the field of view. However it should be noticed that the morphology of cell nuclei for His- and Phe- modified USPIONs may be somewhat affected.

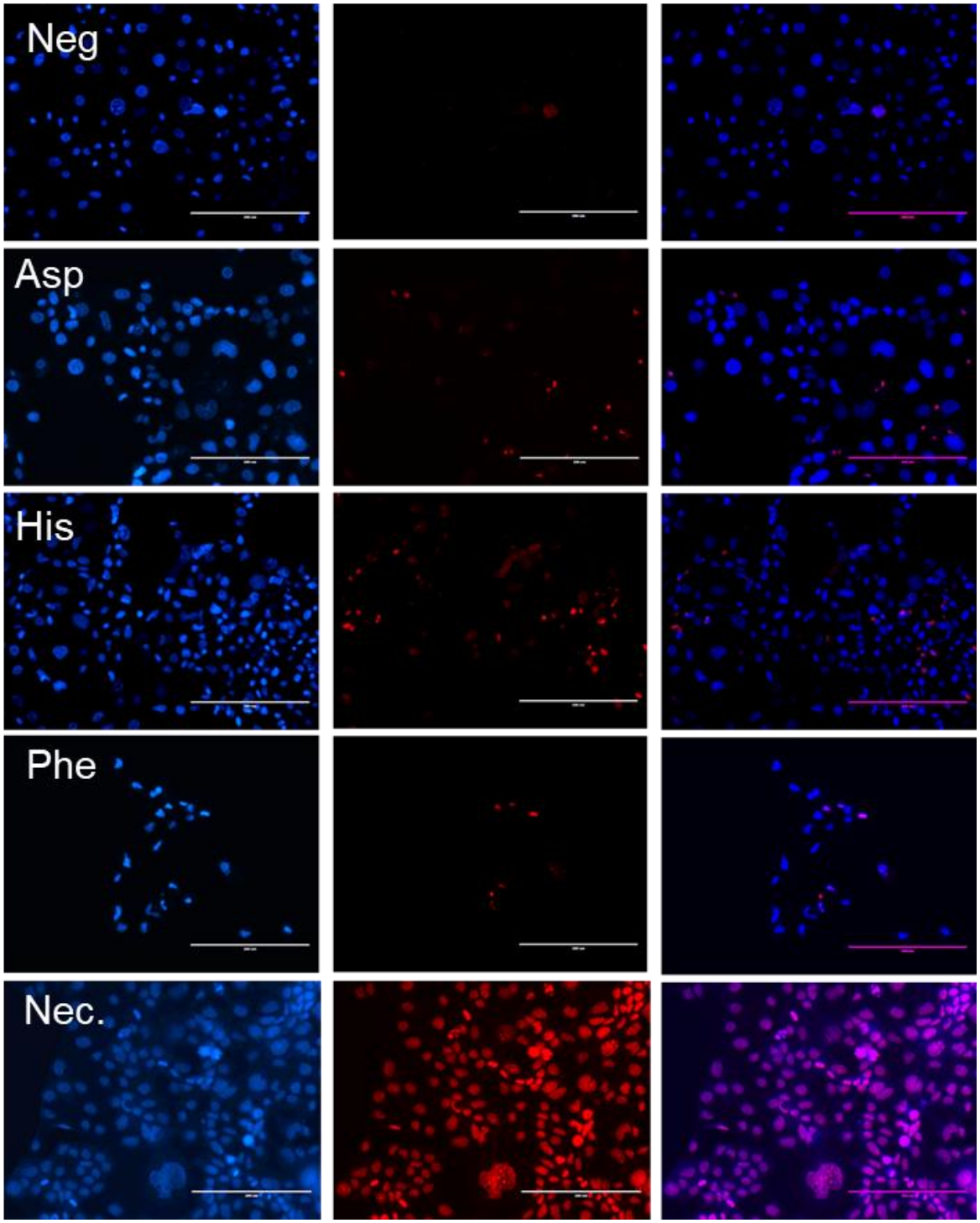


Figure 0-9: Hoechst 33342 / Propridium Iodide (Ho/PI) double staining in Caco-2 cells.

Caco-2 cells were exposed to particle solutions of 500 µg/ml for 24h followed by the incubation with Ho (0.6 µg/ml) and PI (2.0 µg/ml) and imaging on EVOS microscope 20X magnification (scale bar 200 µm). Right hand column shows Ho staining (λex = 357 nm, λem = 447 nm), middle column is PI staining (λex = 531 nm, λem = 593 nm) and left hand column represents merged images (using ImageJ software). Neg; negative control, Nec; necrotic control (100% Ethanol).

4.3.3 Aminoacid modified USPIONs-cell association

4.3.3.1 Quantitative analysis of USPIONs associated with Caco-2 cells

Detection of iron, arising from the USPIONs tested, by using ICP-MS analysis of cell samples is illustrated in Figure 4-10A, B, C and D. The data clearly demonstrate that incubating aminoacid modified USPIONs with Caco-2 cells in culture media lacking FBS resulted in a significant increase ($p < 0.05$) in the amount of cells associated iron, i.e. USPIONs. This occurs at both 37 and 4°C, indicating that the process may not be energy dependent. On the contrary, the presence of FSB in the incubation media resulted in slight increase in cell associated iron, but that was notably smaller than in the FBS absence. It is important to notice the following trend in quantity of cell associated iron: Asp-> His-> Phe, particularly seen in the serum free experiment.

On increasing the concentration of applied USPIONs from 80 (Figure 4-10) to 150 μg/ml (Figure 4-11), an increase in the overall amount of cell-associated iron was seen, without affecting on the general trend (i.e. high amount of iron associated in serum free and a reduction in the presence of serum). The only difference seen, relative to lower concertation applied, are comparable amounts for all three systems at 4°C and serum free conditions (Figure 4-11B).

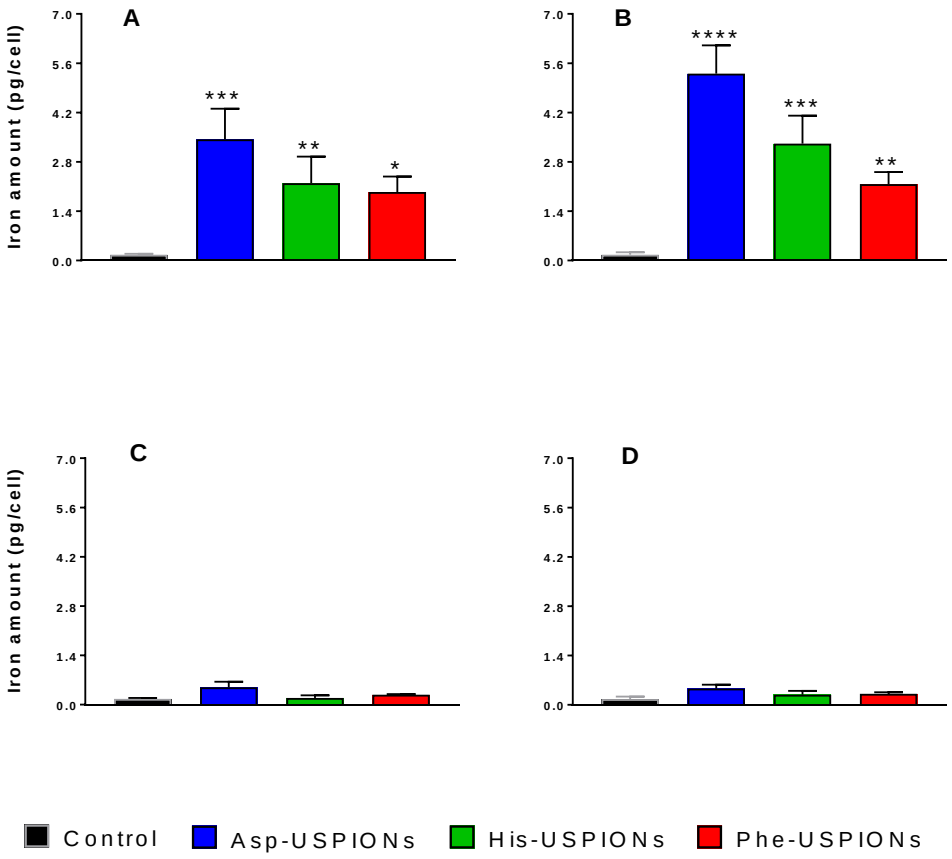


Figure 0-10: Amount of cell associated modified USPIONs (in terms of picogram elemental iron per individual cell).

A)*37°C, serum free conditions* ***B)*** *4°C, serum free,* ***C)*** *37°C media containing serum,* ***D)*** *4°C media plus serum. Concentration of applied USPIONs was 80ug/ml. exposure time is 2 hours. Data represents triplicates from three independent experiments and is presented as mean ± 1SD. Statistical analysis was performed by ANOVA followed by Dunnet's multiple comparison test (GraphPad prism 7.0). *, P < 0.05; **, P < 0.01; ***, P < 0.001; ****, P < 1x10^{-3}*

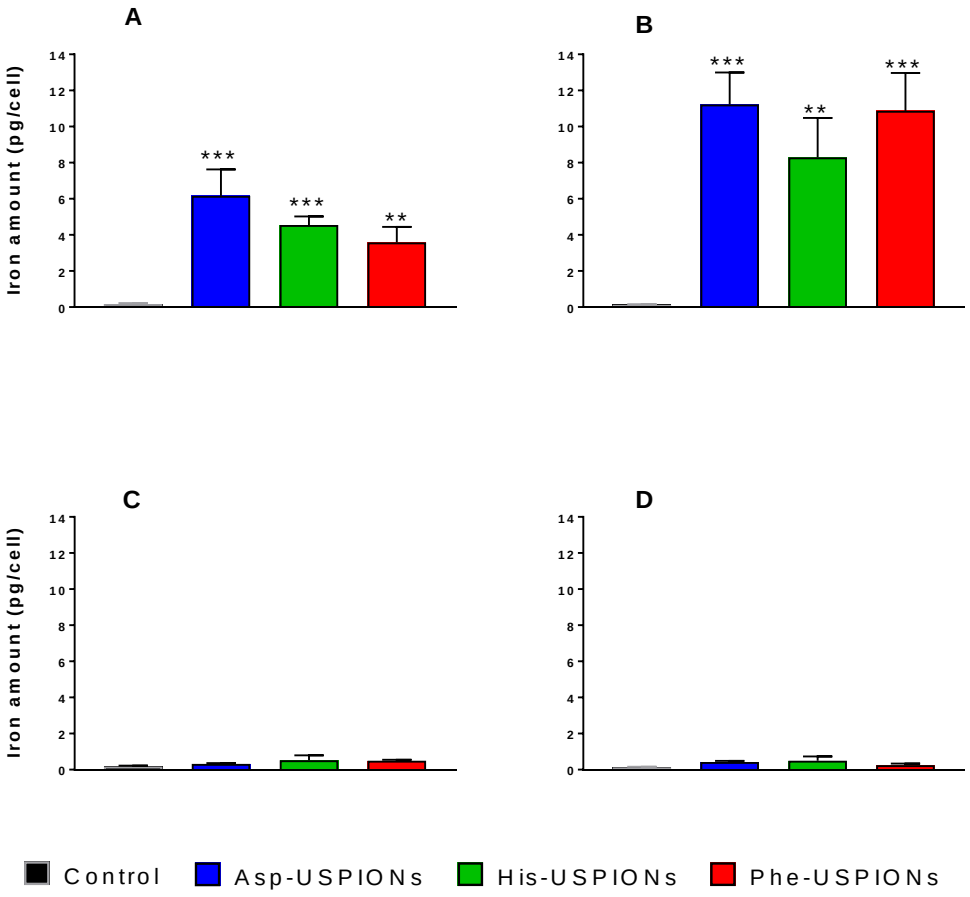


Figure 0-11: Amount of cell associated modified USPIONs (in terms of picogram elemental iron per individual cell).

A)*37°C, serum free* ***B)*** *4°C, serum free* ***C)*** *37°C media plus serum* ***D)*** *4°C, media plus serum****.*** *Concentration of USPIONs is 150 µg/ml. exposure time was 2 hours. Data represents triplicates from three independent experiments and is presented as mean ± SD. Statistical analysis was performed by ANOVA followed by Dunnet's multiple comparison test (GraphPad prism 7.0). *, P < 0.05; **, P < 0.01; ***, P < 0.001; ****, P < 1x10*$^{-3}$

4.3.3.2 Flow cytometry

Figures 4-12 and 4-13 represent the magnitude of side scattering – data collected from flow cytometry analysis for Caco-2 cells exposed to 80 μg/ml and 150 μg/ml USPIONs, respectively. The increase in side scattering values, relative to control cells, indicates association of USPIONs with cells. The data show a statistically significant ($p < 0.05$) cell association for all three systems when tested at 4ºC in serum free media, and for Asp-USPIONs when tested at 37ºC also in the serum free media. In all other experiments, a significant cell association of USPIONs with could not be detected ($p > 0.05$).

Interestingly, and contrary to ICP-MS experiment, levels of side scattering seen for systems tested in absence and in presence of serum are not dramatically different – unlike corresponding ICP-MS data. Furthermore, increasing the concertation of applied USPIONs did not results in an increase in side scattering values (Figure 4-13), unlike in the ICP-MS experiment.

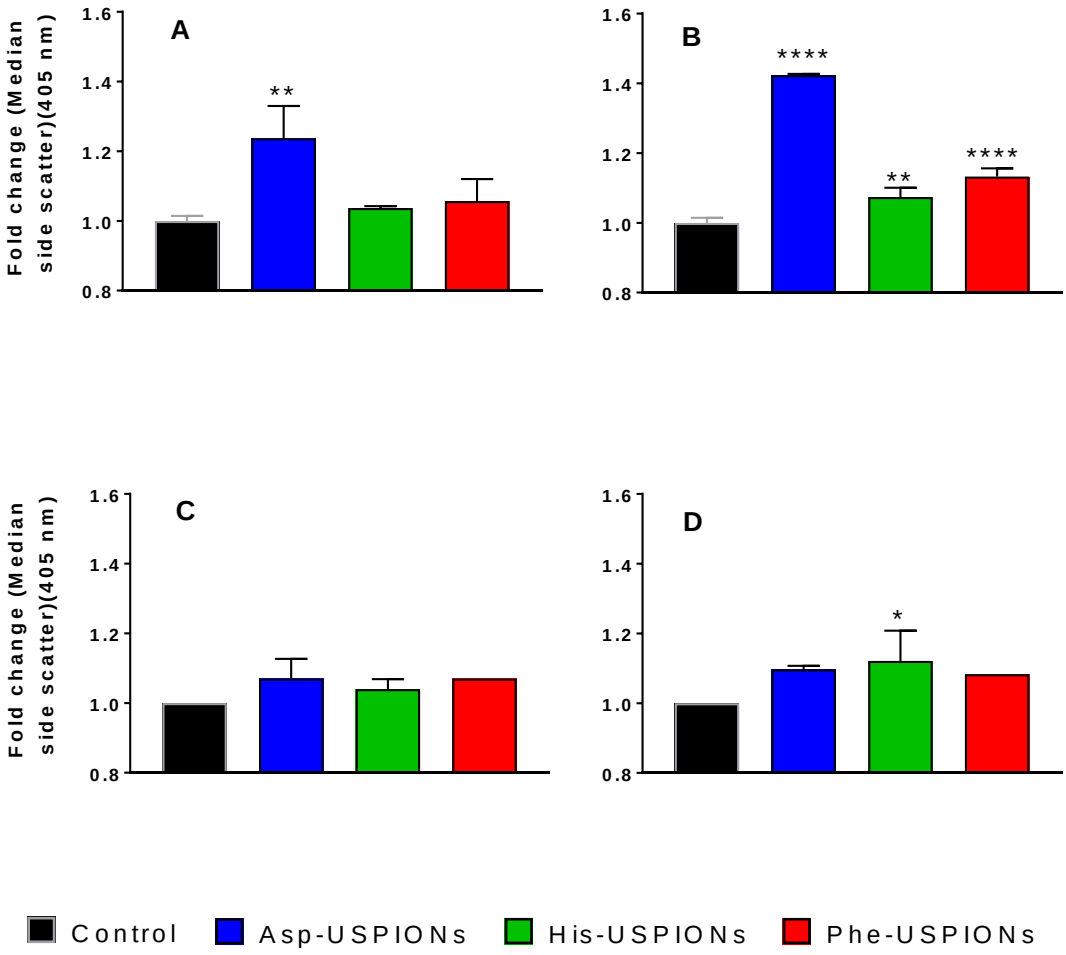


Figure 0-12: Fold change of side scattering in flow cytometry analysis for exposure of Caco-2 cells to modified USPIONs.

A)*37°C, serum free **B)** 4°C, serum free **C)** 37°C media plus serum **D)** 4°C, media plus serum. Concentration of USPIONs is 80ug/ml. Exposure time is 2 hours. Data represents triplicates from three independent experiments and is presented as mean ± SD. Statistical analysis was performed by ANOVA followed by Dunnet's multiple comparison test (GraphPad prism 7.0). *, P < 0.05; **, P < 0.01; ***, P < 0.001; ****, P < $1x10^{-3}$*

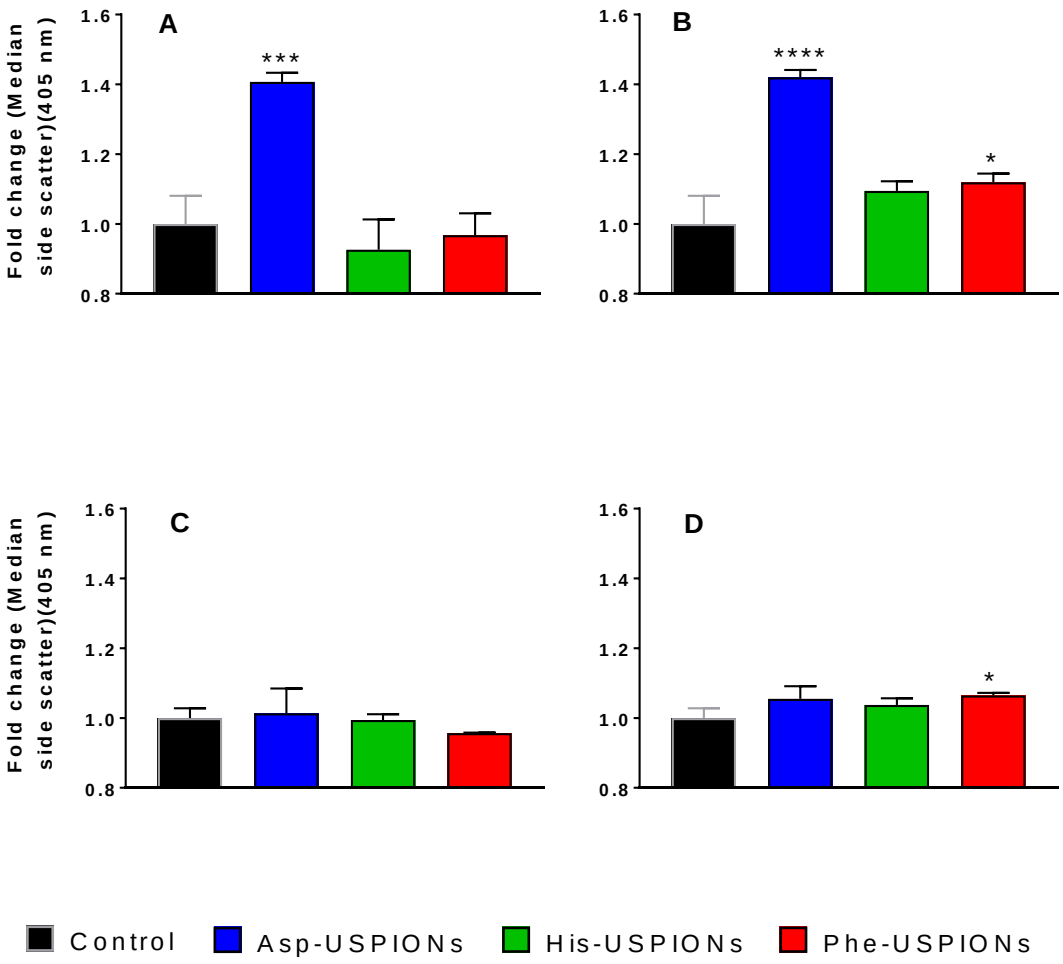


Figure 0-13: Fold change of side scattering in flow cytometry analysis for exposure of Caco-2 cells to modified USPIONs.

A)*37°C, serum free* ***B)*** *4°C, serum free* ***C)*** *37°C media plus serum* ***D)*** *4°C, media plus serum. Concentration of applied USPIONs was 150 µg/ml. Exposure time is 2 hours. Data represents triplicates from three independent experiments and is presented as mean ± SD. Statistical analysis was performed by ANOVA followed by Dunnet's multiple comparison test (GraphPad prism 7.0). *, $P < 0.05$; **, $P < 0.01$; ***, $P < 0.001$; ****, $P < 1x10^{-3}$*

4.3.3.3 TEM analysis

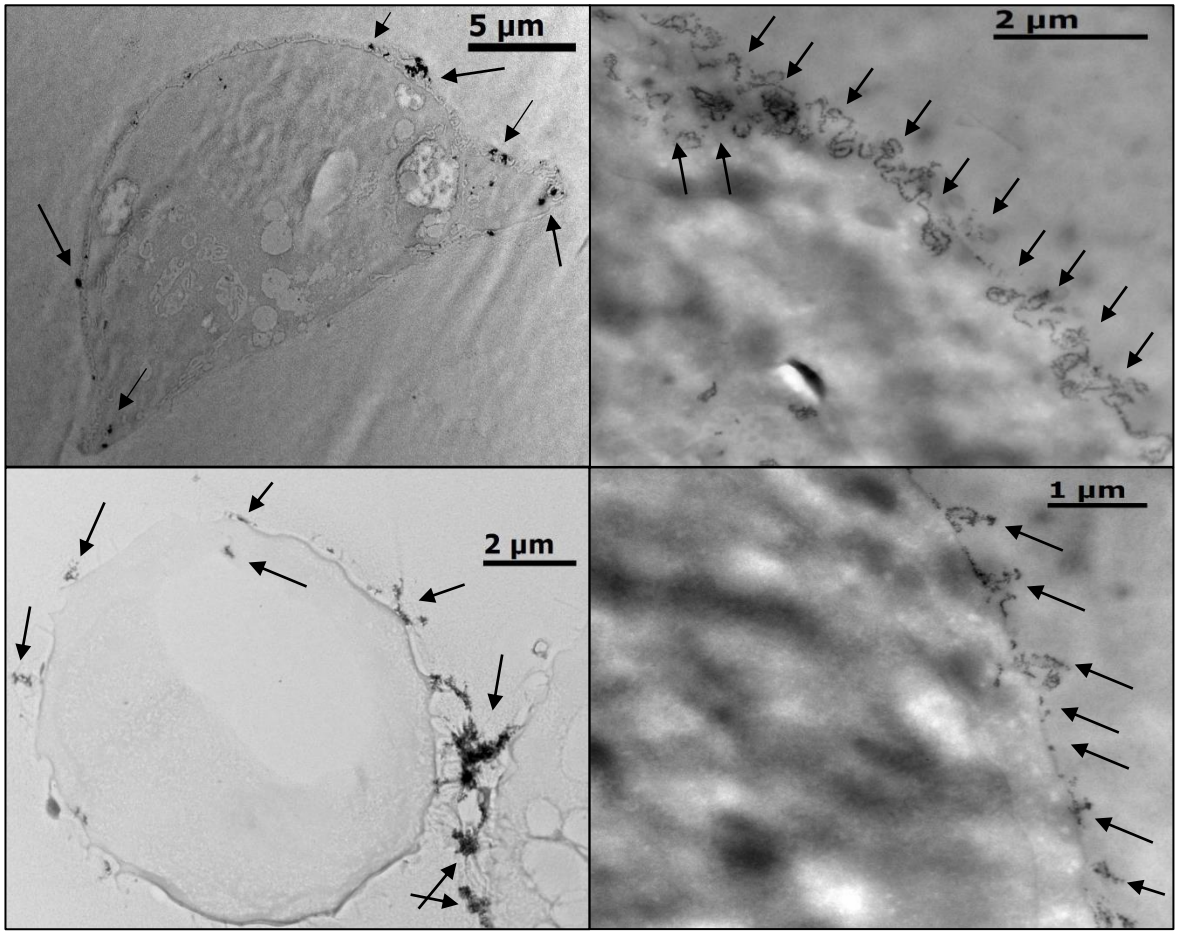
TEM analysis was performed on different USPIONs systems fabricated and applied to cells under different conditions (temperature and serum absence/presence) in order to obtain a high resolution visual analysis of USPIONs – cell interactions. In addition to visualising the location of these particle inside cellular compartment, the interest was also focused on their presence at the cellular membranes, as *per* results described above.

TEM images obtained are summarised in Figure 4-14. They depict that for cells exposures to USPIONs in serum free conditions, an association with cell outer, plasma membrane can be seen. This is especially prominent in the case of Asp-USPIONs. While an almost continuous thin layer of 'individually' adsorbed particles could be seen for Asp-USPIONs, small aggregates of NPs are observed attached to cell plasma membrane in case of Phe-USPIONs. Considering the intracellular presence of USPIONs, Phe-USPIONs show a relatively higher occurrence of particles internalised inside the cellular compartments, whereby much of Phe-USPIONs appear entrapped inside a large 'compartments' within some cells.

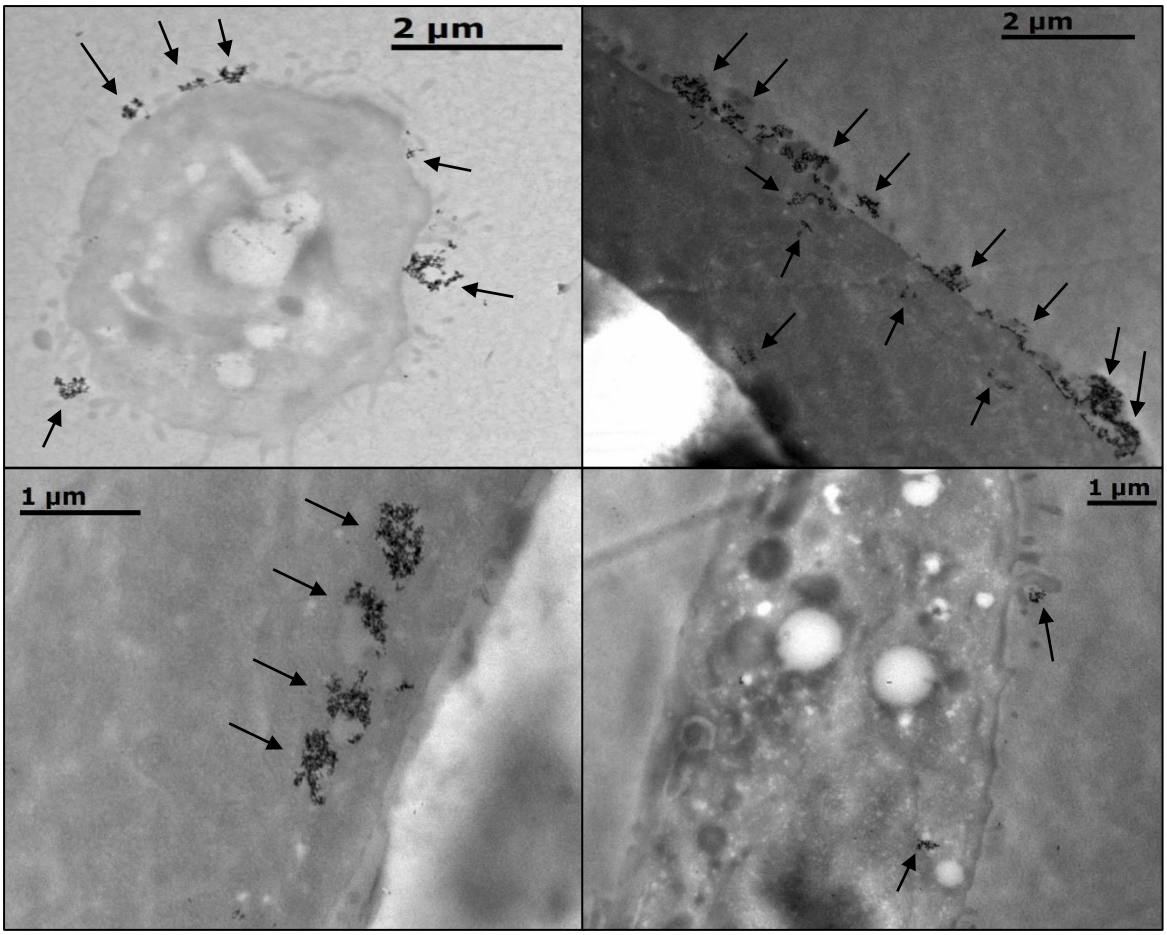
For low exposure temperature ($4^{o}C$), the presence of USPIONs inside cells appears to be absent. This may indicate that (most of) iron detected in ICP-MS experiment to be cell associated could be in fact arising from cell surface associated rather than cell internalised USPIONs.

Upon introduction of serum to culture media (Figure 4-15), surface association of USPIONs with cells could not be observed in TEM analysis, neither at $37^{o}C$ nor at $4^{o}C$. This is observed for all USPIONs tested.

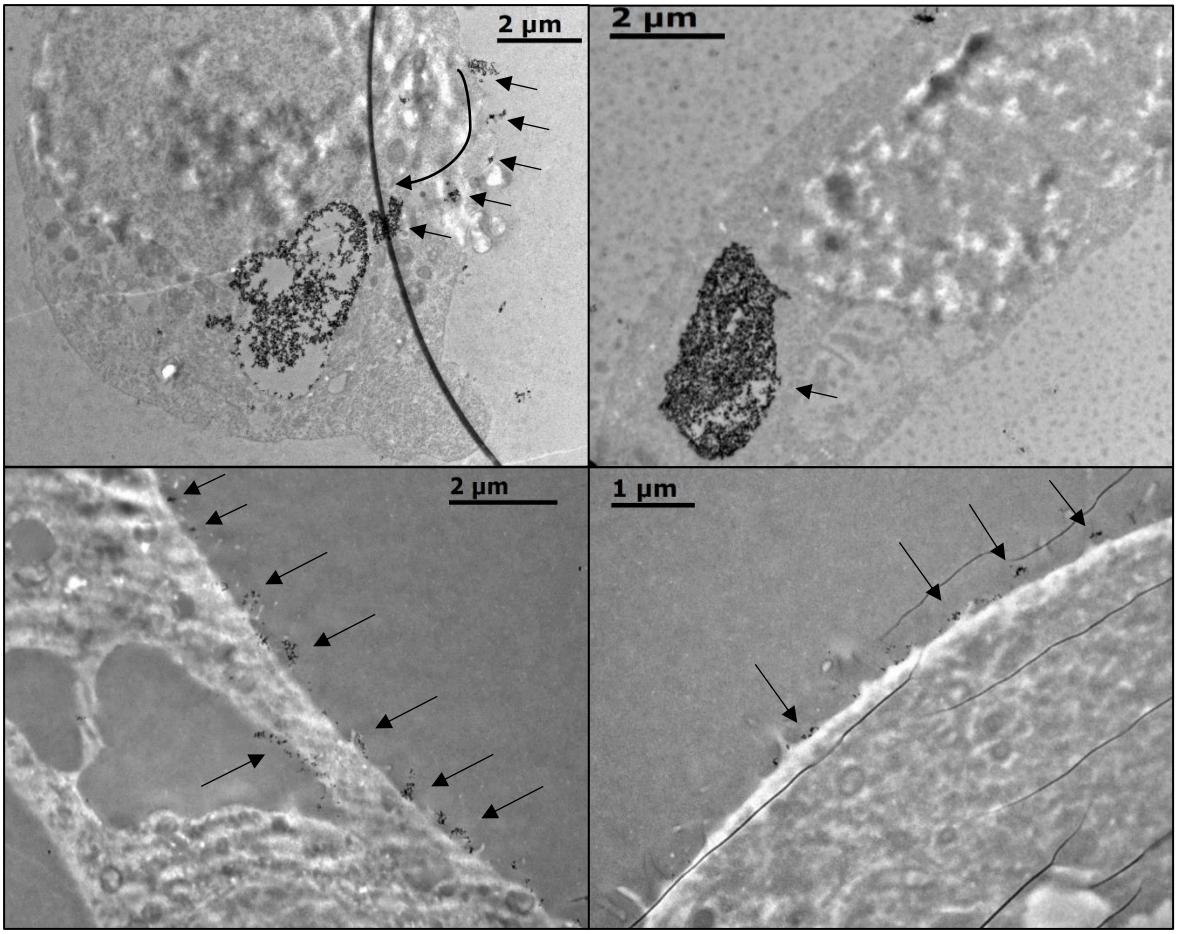
Asp-USPIONs at 37 °C in serum free



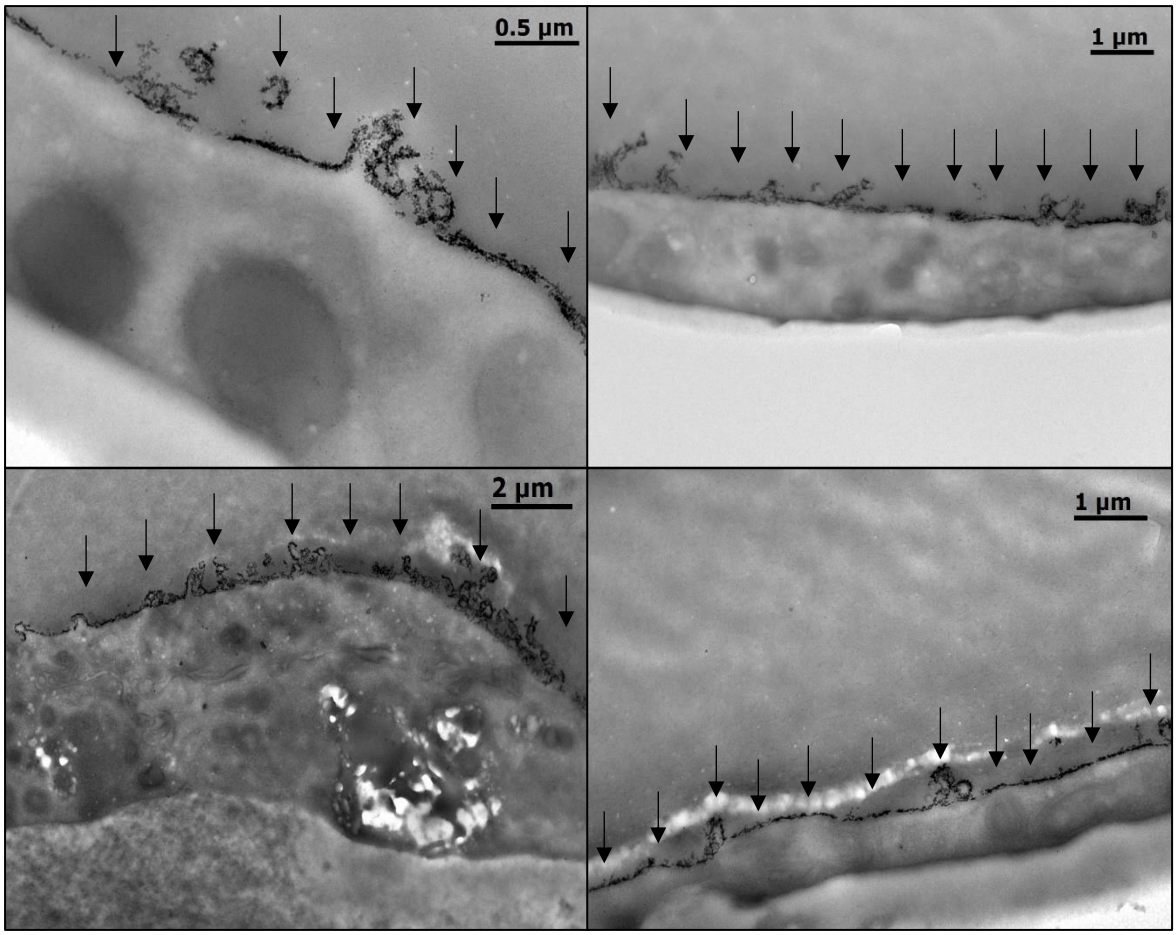
His-USPIONs at 37°C in serum free



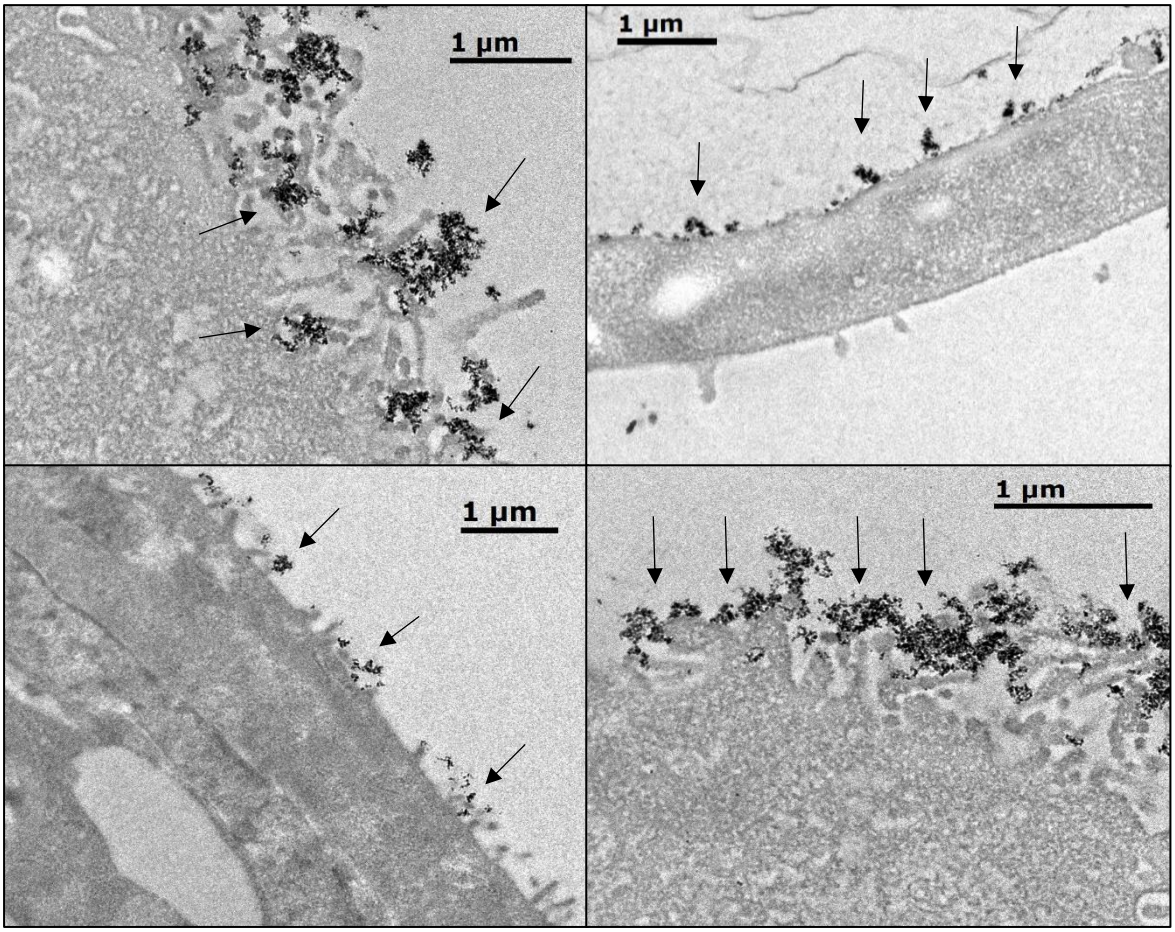
Phe-USPIONs at 37°C in serum-free



Asp-USPIONs at 4°C in serum free



His-USPIONs at 4°C in serum free



Phe-USPIONs at 4°C in serum-free

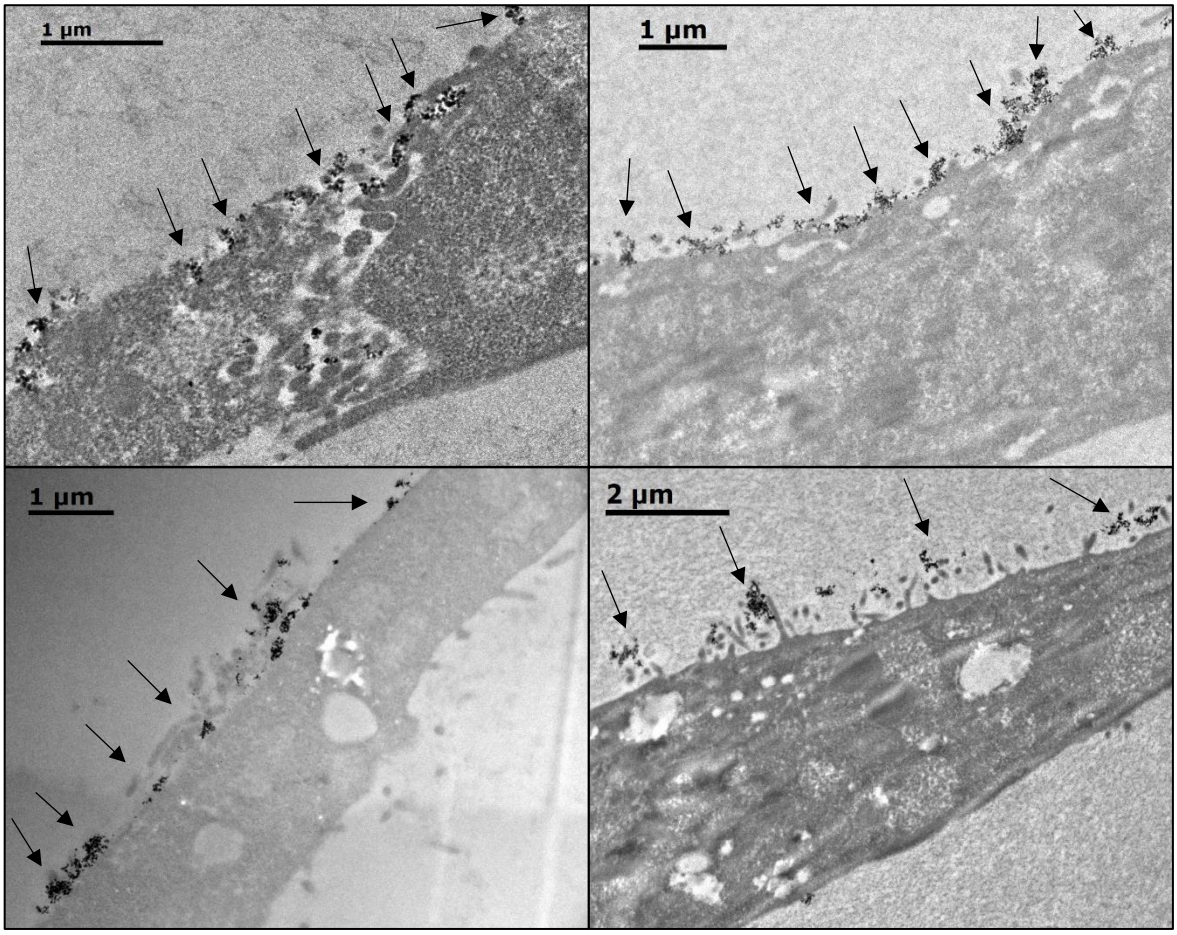
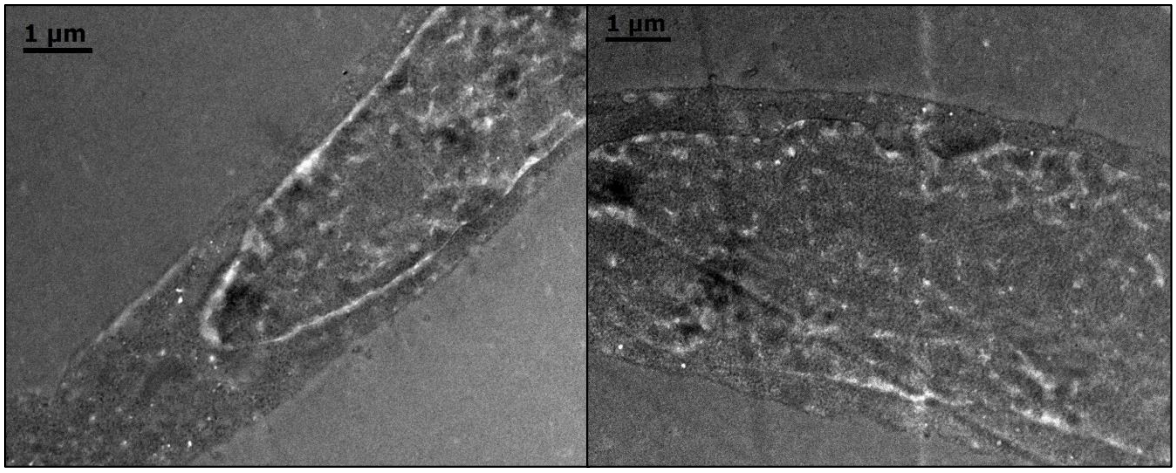
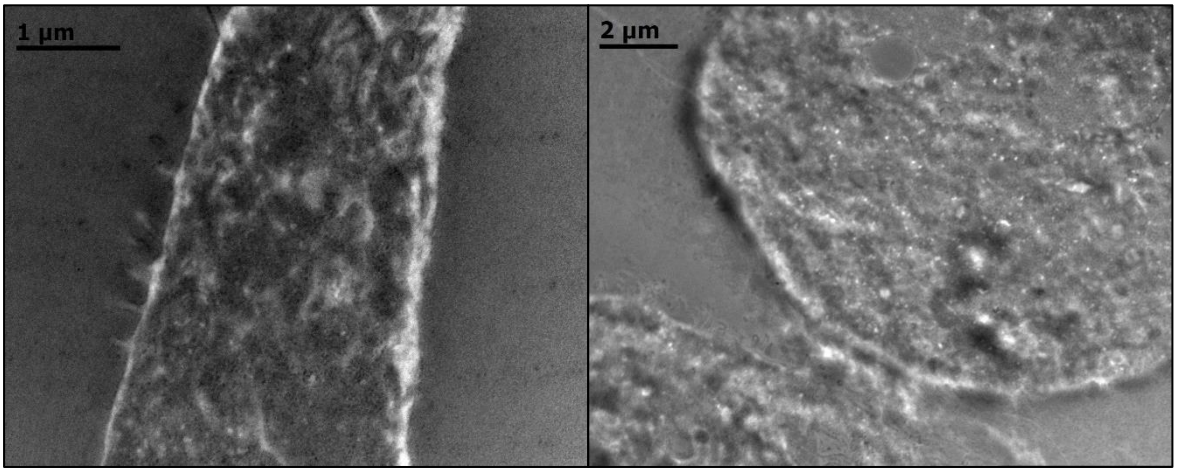


Figure 0-14: TEM micrographs of Caco-2 cells following exposure to modified USPIONs. *The concentration of all amino acid modified USPIONs (Asp-, His, Phe) are 80 µg/ml. exposure time was 2 hours. All TEM micrographs are of cells exposed to serum free media containing USPIONs dispersion*

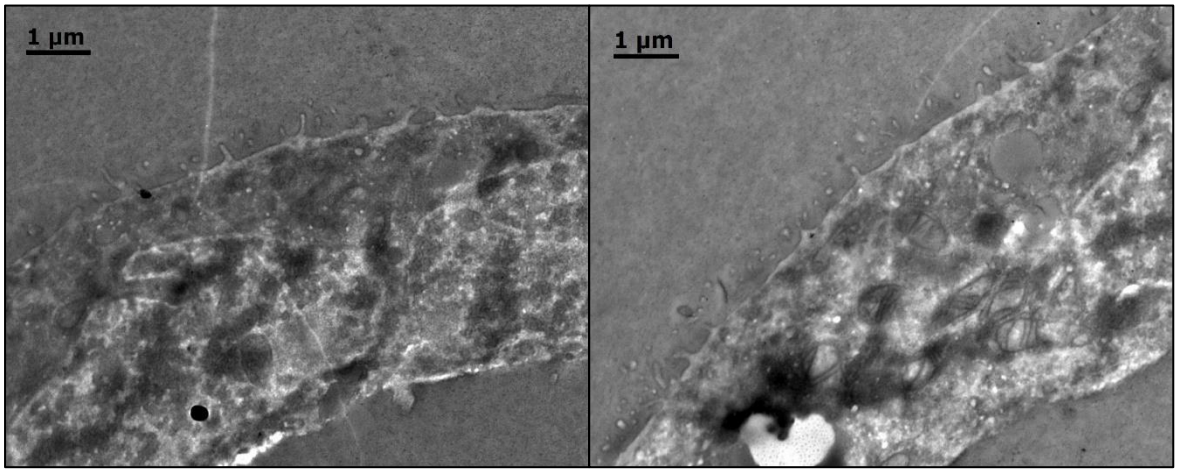
Asp-USPIONs at 37°C in media + serum



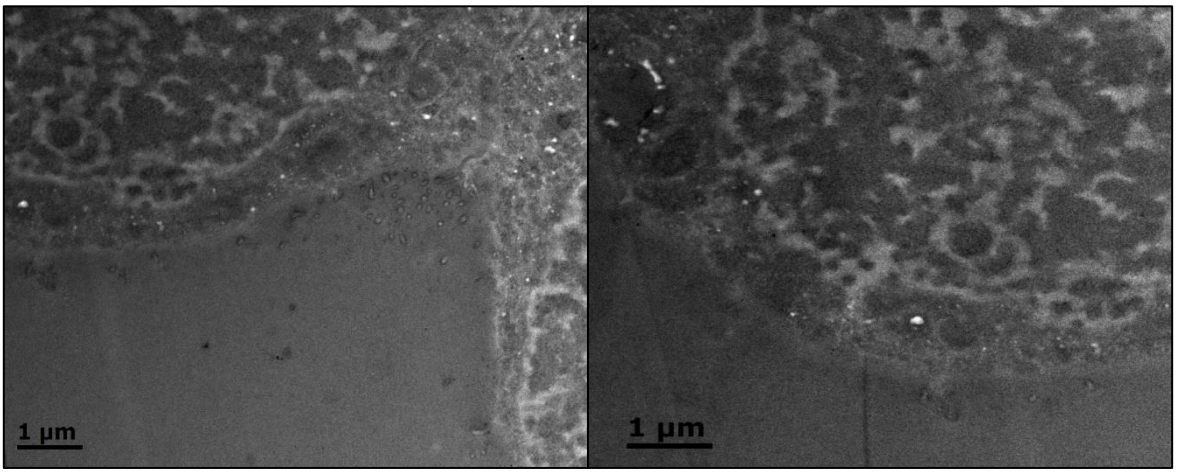
His-USPIONs at 37°C in media + serum



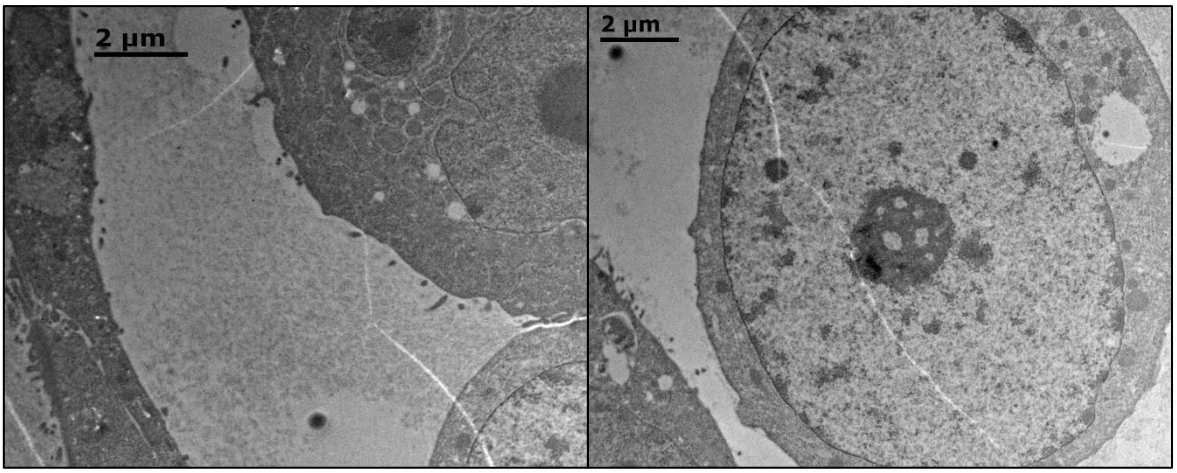
Phe-USPIONs at 37°C in media + serum



Asp-USPIONs at 4°C in media + serum



His-USPIONs at 4°C in media + serum



Phe-USPIONs at 4°C in media + serum

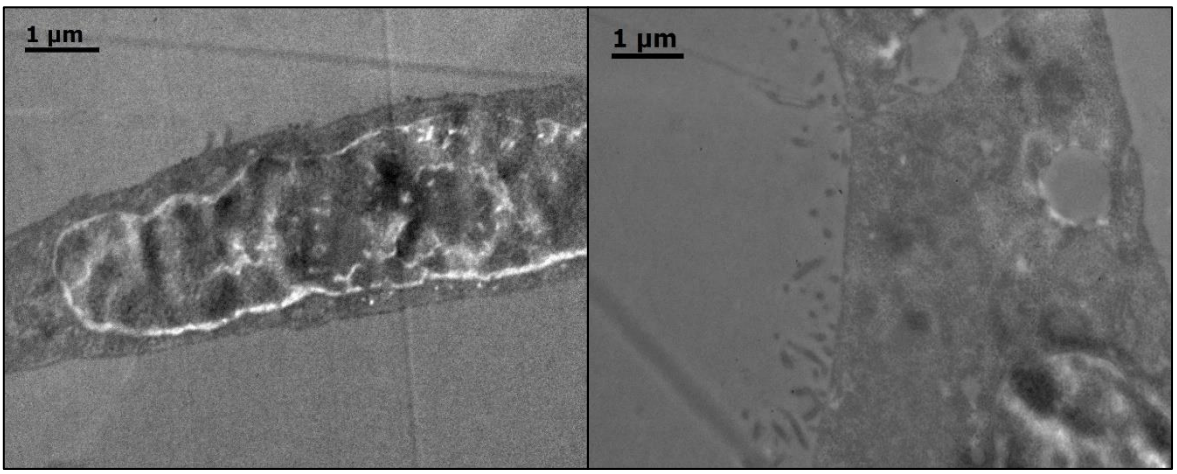


Figure 0-15: TEM micrographs of Caco-2 cells following exposure to modified USPIONs. *The exposure time was 2 hours. USPIONs of all types (Asp-, His-, Phe) have concentration of 80µg/ml. complete EMEM culture media has been used.*

4.4 Discussion

The work presented in this section aimed to assess biological effects on cells in culture upon exposure to aminoacid modified USPIONs. Caco-2 cells were used as a model of gut epithelium. The study contributes to a body of work in the literature directed towards understanding the impact of exposure to metal nanomaterial (with adsorbed organic material) to human respiratory and oral mucosal surfaces [20].

Initially cytotoxicity of USPIONs was assessed by MTT assay, which measures the ability of mitochondrial succinate dehydrogenase enzyme to transform yellow tetrazolium dye into formazan crystal. The amount of formazan crystal accumulation is directly proportional to the cell metabolic activity and, therefore indicates their viability [21]. Accordingly, the reduction in cellular metabolic activity observed gives a preliminary indication that modified USPIONs, at doses higher than 150 $\mu g ml^{-1}$, cause a significant ($p < 0.05$) cytotoxic effect to Caco-2 cells on 24 hours of exposure (Figure 4-2). It should be noted that a reduction in MTT readings should not be directly translated into a reduction in cell survival (viability) as it is in fact a measure of cell metabolic activity [22,23]. Cytotoxicity was also previously reported after incubation of iron oxide NPs with human endothelial cells for prolonged period [24], with a comparable concentration dependent cytotoxicity reported in other literature [3,25]. On the other hand, a long term incubation of L929 (mouse) cell line for more than 24 hours with different functionalised iron oxide NPs (PAA, chitosan and oleic acid) did not show observable toxicity in MTT assay [26-29].

It is important to notice that in the present study, no significant differences ($p > 0.05$) in MTT measured cell metabolic activity were observed amongst the

USPIONs tested. Somewhat unexpected MTT data of 'normal' levels of metabolic activity of cells exposed to high USPIONs concentrations (>250 µg/ml) may be ascribed to the USPIONs aggregation. It is known the nanoparticles aggregation rate is proportional to the concentration of suspended particles [30-32], and may lead to an uncontrolled aggregation to occur fasted at higher concentrations. This in turn may have resulted in a reduced association with / or smaller contact area for association with cells in our case. At low concentrations, 40-150 µg/ml, more individual particles may have remained in the colloidal dispersion for longer time period increasing a probability for particle-cell interactions to occur.

In lactate dehydrogenase assay, a release of the cytosolic enzyme, LDH, from a cellular compartment is taken as a measure of a damage to a cell membrane integrity [33,34]. In the present study, the absence of significant LDH amount ($p > 0.05$) in culture medium may occur due to more than one reason. First, according to the data illustrated in Figure 4-3, there is a significant inactivation ($p < 0.01$) of the enzyme upon prolonged incubation with USPIONs. The reasons for the enzyme deactivation can be briefly discussed by proposing two mechanisms. First, as LDH itself is proteinaceous material, it is expected to form an adsorptive layer around USPIONs in a way similar to 'normal' protein-NPs association process [35,36]. The second reason includes a potentially destructive oxidation of LDH by the action of iron dependent oxidative species that are generated in the media containing USPIONs [37-40]. Therefore, in such a case there would be no benefit of conducting LDH assay studies under prolonged exposure conditions (Figure 4-4). In literature, no sign of LDH release was reported in case of large

hematite NPs [41] however, other articles claimed a presence of LDH leaked from cellular compartment upon exposure to iron oxide NPs [7,42].

Although assays on cellular metabolic activity and LDH have exhibited a considerable cytotoxicity (on prolong exposure to relatively high concentrations) the major mechanism by which USPIONs could mediate cellular toxicity was yet to investigate. The mechanism considered was related to the electron transport properties that transition metals have. Both iron forms (ferrous and ferric) can be effectively involved in a catalytic cycle through which hydrogen peroxide will be transformed into hydroxyl radical, one of most hazardous reactive oxygen species [43,44]. More importantly, the production of such harmful oxidative species is potentiated by overloading the biological system (cell) with iron generating NPs (USPIONs in our case). This results in depletion of antioxidant species (for instance cell present glutathione). Once an imbalance between pro-oxidant and antioxidant material has been shifted in favour of pro-oxidant, a chain of toxic events can be triggered [45,46].

Regarding our results, exposure to Asp-, His-, and Phe-USPIONs in culture media resulted in the generation of oxidative stress in Caco-2 cells, where ROS was normally increased up to 3-fold after 24 hours of exposure to the higher concentrations (500 µg/ml) (Figure 4-6). This strongly indicates the accumulation of toxic species inside the cells, as a result of loss in homeostasis between pro-oxidant and antioxidant materials and thus disruption of cellular 'repair' mechanisms [47]. The data obtained from first 60 minutes (Figure 4-5) support the proposed onset of normal cellular repair mechanisms, whereby one sees a reduction in stress level after the onset for a mild stress at the early exposure tmes [48,49] and where abundant presence of antioxidant materials in the

cells are yet to be depleted. In literature, similar trend of a concentration and time dependant ROS accumulation has been reported after incubating iron oxide NPs with human skin, lung epithelial cells and lymphocytes [50,51].

The accumulation of ROS (especially hydroxyl radical) inside cells functions to trigger a profound and 'long lasting' toxic effect on biological membranes enclosing cell organelles. As a phospholipid bilayer is the main component of these membranes, and a lipid peroxidation process initiated by the action of the free radicals will trigger a series of events that would ultimately terminate in cell death (either apoptosis or necrosis). This situation develops when the oxidative damage overcomes cell repair capacity [52,53]. As a consequence, we believe that the injury to the double-membrane encircling mitochondria may be the initial step in the cell damage as proteins constituting transition pores of mitochondrial membrane are targets for ROS. These experience oxidative modification (damage) and consequently opening of the mitochondrial pores could occur [54,55]. This in turn increases diffusion of mitochondrial ROS that exacerbate the injury effects on mitochondria themselves (as illustrated in Figure 4-7) [55,56]. All these events could culminate in both intrinsic and extrinsic apoptotic mechanisms. In line with our results, previous work by Taha et al reported that iron-ascorbate nanoparticles mediate harmful effect on mitochondrial functions after short incubation with Caco-2 cell line *via* lipid peroxidation [57].

Caspase activation related data in Figure 4-8) unquestionably confirm that aminoacid-(aspartic acid, histidine, and phenylalanine) modified USPIONs possess cytotoxic effects that induce apoptosis-mediated cells death. The detected significant increases ($p < 0.05$) of activated effector caspases occur in a response to pro-apoptotic signals [58,59]. The subsequent release of pro-apoptotic

factor, cytochrome *c*, from the modified and damaged mitochondria plays a key role in triggering the caspase cascade by activation of caspase 9 [60]. This will activate the effector, caspase 3 amounts [56], and which has been detected in our case as significantly increased ($p < 0.05$). Caspase 3 is known to target numerous substrates leading to formation of apoptotic bodies and cell death [61,62].

Taken together, findings that the metabolic activity (Figure 4-2) was not 'totally abolished', absence of positive Ho/PI double staining (an indicator of necrosis [52]) (Figure 4-9), and the caspase activation, may indicate that USPIONs, under the described exposure conditions, induce an apoptotic pathway of cell death in Caco-2 cells. Moreover, a possible indication of the presence of small Ho/PI positive nuclear bodies (apoptotic bodies) in Figure 4-9 could further illustrate that a fraction of cell population may be undergoing late apoptosis.

Interestingly, Phe-USPIONs were observed to induce notably reduced caspase activation, compared to Asp- and His-USPIONs. The reasons for this are not clear. One may suggest that in this case cell death could have been mediated by necrosis in combination with apoptosis. In comparison to Asp- and His-USPIONs under equivalent experimental condition, there is an early high increase of ROS production after short term treatment (1, 2, and 4 hours) with Phe-USPIONs (figure 4-6), which may resulted in cell damage such that a necrotic mode of cell death may not be excluded. Potential cell membrane damage could have been assessed from LDH assay (that may give an indication of necrotic cell death [33]), however this analysis was not helpful in the present study because of the enzyme deactivation by USPIONs noticed (Figure 4-3). In the literature some other studies also propose that iron oxide NPs induce apoptotic mode of cell death [63,64].

Given a demonstrated toxic potentials of aminoacid modified USPIONs, it was decided to investigate their association with cells to help depicting potential risks of human tissue exposure to these objects [20,65,66].

Initially it should be noticed that comparing hydrodynamic size measurements of Asp-, His-, and Phe-USPIONs in different aqueous media – deionised water (Figure 3-5), serum-free culture media, and culture media with 10% FBS (Figure 4-1) evidently reveals a formation of protein adsorptive layer around individual / or group of particles (protein corona) [67,68]. The increase in the average particle size from ~40 nm to ~120 nm has been noticed in FBS presence, with the systems retaining a reasonable colloidal dispersion properties. This can be attributed to the protein adsorbed layer effectively functioning as a steric stabilizing layer that prevents the USPIONs from undergoing aggregation, as observed in the case of serum-free media where hydrodynamic size values higher than 2000 nm have been recorded indicating USPIONs gross aggregation.

To study USPIONs cellular interaction/ uptake, cells associated iron content was measured by ICP-MS, in conjugation with flow cytometry analysis [69]. For ICP-MS, as a preliminary control step, a determination of a metallic element that is naturally present in cells was undertaken [70,71]. The ICP-MS measurements were critical in this study for monitoring label-free USPIONs cellular association and uptake as no normally used approach of encapsulation of fluorescent probe was adopted [72-75]. Experiments were conducted under different cell-USPIONs incubation conditions (serum presence, temperature, and USPIONs concentration) and iron amount determined (Figures 4-10 for 80 µg/ml and 4-11 for 150 µg/ml). The comparisons of data obtained clearly indicate an important role that protein component of serum plays. In this regard, it infers that formation

of protein corona on USPIONs appears to function as a barrier preventing NPs interactions with cell membrane and hence reducing any subsequent processes [76-78].

Considering the effects of incubation temperature, performing experiments at temperature of 4°C is normally considered to drastically inhibits cells membrane trafficking processes (particularly cellular internalisation) [79]. In this case one would expect the amount of cell-associated USPIONs to be lower than at 37°C incubation temperature, if energy dependent active processes are involved [80,81]. Interestingly, incubating Asp-, His-, Phe-USPIONs with cells in serum-free media at 4°C reveals contrary results where the amount of cell-associated iron (detected by ICP-MS) showed significant increase ($p < 0.01$), promoted by using the higher NPs concentration (150 ug/ml) (Figure 4-11). This finding brings about an initial assumption of that the process of physical adsorption of modified USPIONs with cell membrane dominates potential cells internalization processes.

Regarding flow cytometry data, detection was based on side scattering analysis [82-84] and the increase in fold-number of side scattered intensity are correlated to the association of NPs with cells. Similar to ICP-MS experiments, the effects experimental variables (serum presence, temperature, and NPs concentration) were investigated (Figure 4-12 for 80 µg/ml and Figure 4-13 for 150 µg/ml). Data in general indicate not significant increase ($p > 0.05$) in side scattering of the tested samples, with a significant increase ($p < 0.01$) in side-scattered intensity noticed in the case of Asp-USPIONs. Surprisingly there was the lack of significant differences ($p > 0.05$) in the data for His- and Phe-USPIONs

systems following incubation in serum-free conditions or in the presence of serum (for both incubation temperatures), as seen in IPC-MS analysis.

Therefore, it was decided to visualise the USPIONs – cell interactions by TEM study for the different conditions and systems tested. Images for incubation in serum-free culture media (Figure 4-14) evidently illustrate existence of a considerable interaction between cell membrane and aminoacid modified USPIONs in an order of Asp- > His- > Phe-, while an inverse trend may be suggested regarding their cellular internalisation. With incorporating 10% FBS into incubation media, TEM images of all tested samples lack to show either interaction with cell membrane or USIOPNs localisation inside cells. This would be consistent with ICP-MS based results, where very little iron was associated with cells, as well as in agreement with results reported by Zanella et al [85]. This would again indicate that the protein layer formed around modified USPIONs gives rise to a steric hindrance to adsorption to cell surface and subsequent processes of cellular uptake [77,78,86,87].

With serum-free media, the formation of almost continuous adsorbed layer of aminoacid modified USPIONs associated with cell membrane could be mainly attributed to two factors: the nature of core material (USPIONs) and modifying agent (aminoacid molecules) used. In the present case, core material itself may be responsible for USPIONs – cell membrane association noticed. With an assumption that the phosphate functionalities of phospholipids in the cell membrane bilayer could have a higher affinity towards iron, it may be proposed that aminoacid modified USPIONs undergo a 'ligand exchange' by which the surface associated aminoacid molecules are displaced in favour of phosphate groups of phospholipids [88-93]. This 'exchange' mechanism has been successfully

exploited by many protocols to prepare functionalised iron oxide NPs [94-97]. Moreover, there are literature reports on different types of iron oxide NPs to form such a thin adsorbed layer on different biological barriers [64,98].

However, TEM micrographs (Figure 4-14) reveal different behaviour of the three USPIONs tested, depending on the nature of their surface modification. In case of Asp-USPIONs, as demonstrated in the previous chapter, there is more carboxylate functionality in the outer adsorbed layer available for 'bridging interaction' – among themselves and with phospholipids of cell membrane. This kind of interaction is thought to be mediated by calcium ion present in an aqueous medium [86,99]. Therefore, this could lead to a formation of relatively stable NPs-phospholipid molecule(s) complex(es) which may 'fix' the cell membrane and restrict further membrane reorganisations necessary for NPs internalisation [100].

For Phe-USPIONs, the situation is different because of an absence of free carboxylate functionality in favour of the hydrophobic aromatic ring. The likely increased surface hydrophobicity of these USPIONs may have a crucial effect on enhancing nanoparticles engulfment on expense of nanoparticles' 'fixing' the cell membrane [101,102], and result in their observed internalization at 37°C incubation temperature.

4.5 Conclusion and summary

In summary, the data in this chapter indicate that on exposure to coated SPOINs intestinal model Caco-2 cells show signs of toxicity, although relatively high doses and exposure times could be applied to cause a significant toxicity effects ($p < 0.05$), with LD50 of around 400 µg/ml at 24 hours exposure. Future studies

on the coated USPIONs effect on cell membrane integrity, production of reactive oxygen species and mitochondrial damage provides a further insight into possible mechanisms of toxicity. These indicate that, under conditions tested, USPIONs can trigger apoptotic cell death.

Exploiting the unique advantages that fabricated iron oxide USPIONs possess high electron density, TEM was employed, in conjunct to ICP-MS and flow cytometry techniques to study USPIONs interactions with cells in culture. The data obtained indicate the dominant role of the nature of coating aminoacid on the USPIONs interaction with cells – in serum free medium – where high level of Asp-USPIONs adsorption to outer layer of the cell membrane was seen under TEM. This was corroborated with ICP-MS data, but flow cytometry side scattering analysis did not conform the phenomenon. The latter may possibly be connected to the formation of an almost perfect NPs monolayer at the cells membrane rather than a creation of a significantly sized ‘particle’ that would cause side scattering ($p < 0.05$). In the presence of serum – i.e. conditions of organic material adsorption to the USPIONs surface – the effect of aminoacid coating was overruled and steric stabilizing effects of the protein corona appear to dominate the USPIONs behaviour.

4.6 References

1 Sayes, C. M., Reed, K. L. & Warheit, D. B. Assessing toxicity of fine and nanoparticles: comparing in vitro measurements to in vivo pulmonary toxicity profiles. *Toxicological sciences* **97**, 163-180 (2007).

2 Amoabediny, G. *et al.* in *Journal of Physics: Conference Series.* 012037 (IOP Publishing).

3 Jeng, H. A. & Swanson, J. Toxicity of metal oxide nanoparticles in mammalian cells. *Journal of Environmental Science and Health Part A* **41**, 2699-2711 (2006).

4 Au, C. *et al.* Effects of nanoparticles on the adhesion and cell viability on astrocytes. *Biological Trace Element Research* **120**, 248-256 (2007).

5 Pisanic II, T. R., Blackwell, J. D., Shubayev, V. I., Fiñones, R. R. & Jin, S. Nanotoxicity of iron oxide nanoparticle internalization in growing neurons. *Biomaterials* **28**, 2572-2581 (2007).

6 Li, N. *et al.* Ultrafine particulate pollutants induce oxidative stress and mitochondrial damage. *Environmental health perspectives* **111**, 455 (2003).

7 Hussain, S., Hess, K., Gearhart, J., Geiss, K. & Schlager, J. In vitro toxicity of nanoparticles in BRL 3A rat liver cells. *Toxicology in vitro* **19**, 975-983 (2005).

8 Siglienti, I., Bendszus, M., Kleinschnitz, C. & Stoll, G. Cytokine profile of iron-laden macrophages: implications for cellular magnetic resonance imaging. *Journal of neuroimmunology* **173**, 166-173 (2006).

9 Naveau, A. *et al.* Phenotypic study of human gingival fibroblasts labeled with superparamagnetic anionic nanoparticles. *Journal of periodontology* **77**, 238-247 (2006).

10 Radu, M. *et al.* Depletion of intracellular glutathione and increased lipid peroxidation mediate cytotoxicity of hematite nanoparticles in MRC-5 cells. *Acta Biochimica Polonica* **57**, 355 (2010).

11 Sidiropoulou, E. *et al.* Insights into the toxicity of iron oxides nanoparticles in land snails. *Comparative Biochemistry and Physiology Part C: Toxicology & Pharmacology* (2018).

12 Matysiak, M., Kapka-Skrzypczak, L., Brzóska, K., Gutleb, A. C. & Kruszewski, M. Proteomic approach to nanotoxicity. *Journal of proteomics* **137**, 35-44 (2016).

13 Lesniak, A. *et al.* Nanoparticle adhesion to the cell membrane and its effect on nanoparticle uptake efficiency. *Journal of the American Chemical Society* **135**, 1438-1444 (2013).

14 Fleischer, C. C. & Payne, C. K. Nanoparticle–cell interactions: molecular structure of the protein corona and cellular outcomes. *Accounts of chemical research* **47**, 2651-2659 (2014).

15 Vllasaliu, D. *et al.* Tight junction modulation by chitosan nanoparticles: comparison with chitosan solution. *International journal of pharmaceutics* **400**, 183-193 (2010).

16 Bossy-Wetzel, E., Newmeyer, D. D. & Green, D. R. Mitochondrial cytochrome c release in apoptosis occurs upstream of DEVD-specific caspase activation and independently of mitochondrial transmembrane depolarization. *The EMBO journal* **17**, 37-49 (1998).

17 Belmokhtar, C. A., Hillion, J. & Ségal-Bendirdjian, E. Staurosporine induces apoptosis through both caspase-dependent and caspase-independent mechanisms. *Oncogene* **20**, 3354 (2001).
18 Mahajan, S., Thieme, D., Czugala, M., Kruse, F. E. & Fuchsluger, T. A. Lamin Cleavage: A Reliable Marker for Studying Staurosporine-Induced Apoptosis in Corneal Tissue. *Investigative ophthalmology & visual science* **58**, 5802-5809 (2017).
19 Ormerod, M. G., Collins, M. K., Rodriguez-Tarduchy, G. & Robertson, D. Apoptosis in interleukin-3-dependent haemopoietic cells: Quantification by two flow cytometric methods. *Journal of immunological methods* **153**, 57-65 (1992).
20 Kornberg, T. G. *et al.* Potential Toxicity and Underlying Mechanisms Associated with Pulmonary Exposure to Iron Oxide Nanoparticles: Conflicting Literature and Unclear Risk. *Nanomaterials* **7**, 307 (2017).
21 Hussain, R., Nouri, A. & Oliver, R. A new approach for measurement of cytotoxicity using colorimetric assay. *Journal of immunological methods* **160**, 89-96 (1993).
22 Shishatskaya, E. I. *et al.* Short-term culture of monocytes as an in vitro evaluation system for bionanomaterials designated for medical use. *Food and Chemical Toxicology* **96**, 302-308 (2016).
23 Saranya, S., Vijayaranai, K., Pavithra, S., Raihana, N. & Kumanan, K. In vitro cytotoxicity of zinc oxide, iron oxide and copper nanopowders prepared by green synthesis. *Toxicology reports* **4**, 427-430 (2017).
24 Hanini, A. *et al.* Evaluation of iron oxide nanoparticle biocompatibility. *International journal of nanomedicine* **6**, 787 (2011).
25 Naqvi, S. *et al.* Concentration-dependent toxicity of iron oxide nanoparticles mediated by increased oxidative stress. *International journal of nanomedicine* **5**, 983 (2010).
26 Shete, P., Patil, R., Ningthoujam, R., Ghosh, S. & Pawar, S. Magnetic core–shell structures for magnetic fluid hyperthermia therapy application. *New Journal of Chemistry* **37**, 3784-3792 (2013).
27 Shete, P. *et al.* Magnetic chitosan nanocomposite for hyperthermia therapy application: preparation, characterization and in vitro experiments. *Applied Surface Science* **288**, 149-157 (2014).
28 Patil, R. *et al.* Non-aqueous to aqueous phase transfer of oleic acid coated iron oxide nanoparticles for hyperthermia application. *RSC Advances* **4**, 4515-4522 (2014).
29 Patil, R. *et al.* Superparamagnetic iron oxide/chitosan core/shells for hyperthermia application: Improved colloidal stability and biocompatibility. *Journal of Magnetism and Magnetic Materials* **355**, 22-30 (2014).
30 Phenrat, T., Saleh, N., Sirk, K., Tilton, R. D. & Lowry, G. V. Aggregation and sedimentation of aqueous nanoscale zerovalent iron dispersions. *Environmental Science & Technology* **41**, 284-290 (2007).
31 Huang, Y., Yamaguchi, A., Pham, T. D. & Kobayashi, M. Charging and aggregation behavior of silica particles in the presence of lysozymes. *Colloid and Polymer Science*, 1-11 (2018).
32 Kurzhals, S., Gal, N., Zirbs, R. & Reimhult, E. Aggregation of thermoresponsive core-shell nanoparticles: Influence of particle

concentration, dispersant molecular weight and grafting. *Journal of colloid and interface science* **500**, 321-332 (2017).
33 Chan, F. K.-M., Moriwaki, K. & De Rosa, M. J. in *Immune Homeostasis* 65-70 (Springer, 2013).
34 Maes, M. *et al.* Measurement of apoptotic and necrotic cell death in primary hepatocyte cultures. *Protocols in In Vitro Hepatocyte Research*, 349-361 (2015).
35 Raoufi, M. *et al.* Probing fibronectin conformation on a protein corona layer around nanoparticles. *Nanoscale* (2018).
36 Fersht, A. *Structure and mechanism in protein science: A Guide to enzyme catalysis and protein folding*. Vol. 9 (World Scientific, 2017).
37 Donadelli, J. A., Einschlag, F. S. G., Laurenti, E., Magnacca, G. & Carlos, L. Soybean peroxidase immobilized onto silica-coated superparamagnetic iron oxide nanoparticles: Effect of silica layer on the enzymatic activity. *Colloids and Surfaces B: Biointerfaces* **161**, 654-661 (2018).
38 Stadtman, E. R. Metal ion-catalyzed oxidation of proteins: biochemical mechanism and biological consequences. *Free Radical Biology and Medicine* **9**, 315-325 (1990).
39 Stadtman, E. Oxidation of free amino acids and amino acid residues in proteins by radiolysis and by metal-catalyzed reactions. *Annual review of biochemistry* **62**, 797-821 (1993).
40 Stadtman, E. & Levine, R. Free radical-mediated oxidation of free amino acids and amino acid residues in proteins. *Amino acids* **25**, 207-218 (2003).
41 Freyria, F. S. *et al.* Hematite nanoparticles larger than 90 nm show no sign of toxicity in terms of lactate dehydrogenase release, nitric oxide generation, apoptosis, and comet assay in murine alveolar macrophages and human lung epithelial cells. *Chemical research in toxicology* **25**, 850-861 (2012).
42 Malvindi, M. A. *et al.* Toxicity assessment of silica coated iron oxide nanoparticles and biocompatibility improvement by surface engineering. *PloS one* **9**, e85835 (2014).
43 Prousek, J. Fenton chemistry in biology and medicine. *Pure and applied chemistry* **79**, 2325-2338 (2007).
44 Halliwell, B. & Gutteridge, J. M. *Free radicals in biology and medicine*. (Oxford University Press, USA, 2015).
45 Dixon, S. J. & Stockwell, B. R. The role of iron and reactive oxygen species in cell death. *Nature chemical biology* **10**, 9 (2014).
46 Ray, P. D., Huang, B.-W. & Tsuji, Y. Reactive oxygen species (ROS) homeostasis and redox regulation in cellular signaling. *Cellular signalling* **24**, 981-990 (2012).
47 Sharma, P., Jha, A. B., Dubey, R. S. & Pessarakli, M. Reactive oxygen species, oxidative damage, and antioxidative defense mechanism in plants under stressful conditions. *Journal of botany* **2012** (2012).
48 Mittler, R. ROS are good. *Trends in plant science* **22**, 11-19 (2017).
49 Birben, E., Sahiner, U. M., Sackesen, C., Erzurum, S. & Kalayci, O. Oxidative stress and antioxidant defense. *World Allergy Organization Journal* **5**, 9 (2012).

50 Ahamed, M. *et al.* Iron oxide nanoparticle-induced oxidative stress and genotoxicity in human skin epithelial and lung epithelial cell lines. *Current pharmaceutical design* **19**, 6681-6690 (2013).
51 Gaharwar, U. S., Meena, R. & Rajamani, P. Iron oxide nanoparticles induced cytotoxicity, oxidative stress and DNA damage in lymphocytes. *Journal of Applied Toxicology* **37**, 1232-1244 (2017).
52 Lemasters, J. J. in *Molecular Pathology (Second Edition)* 1-24 (Elsevier, 2018).
53 Ayala, A., Muñoz, M. F. & Argüelles, S. Lipid peroxidation: production, metabolism, and signaling mechanisms of malondialdehyde and 4-hydroxy-2-nonenal. *Oxidative medicine and cellular longevity* **2014** (2014).
54 El-Osta, H. & Circu, M. L. in *Mitochondrial Mechanisms of Degeneration and Repair in Parkinson's Disease* 1-23 (Springer, 2016).
55 Circu, M. L. & Aw, T. Y. Glutathione and modulation of cell apoptosis. *Biochimica et Biophysica Acta (BBA)-Molecular Cell Research* **1823**, 1767-1777 (2012).
56 Redza-Dutordoir, M. & Averill-Bates, D. A. Activation of apoptosis signalling pathways by reactive oxygen species. *Biochimica et Biophysica Acta (BBA)-Molecular Cell Research* **1863**, 2977-2992 (2016).
57 Taha, R. *et al.* Oxidative stress and mitochondrial functions in the intestinal Caco-2/15 cell line. *PLoS One* **5**, e11817 (2010).
58 Galluzzi, L. *et al.* Molecular definitions of cell death subroutines: recommendations of the Nomenclature Committee on Cell Death 2012. *Cell death and differentiation* **19**, 107 (2012).
59 Danial, N. N. & Korsmeyer, S. J. Cell death: critical control points. *Cell* **116**, 205-219 (2004).
60 Liu, X., Kim, C. N., Yang, J., Jemmerson, R. & Wang, X. Induction of apoptotic program in cell-free extracts: requirement for Datp and cytochrome c. *Cell* **86**, 147-157 (1996).
61 Muñoz-Pinedo, C. & López-Rivas, A. A role for caspase-8 and TRAIL-R2/DR5 in ER-stress-induced apoptosis. *Cell Death and Differentiation* **25**, 226 (2018).
62 Porter, A. G. & Jänicke, R. U. Emerging roles of caspase-3 in apoptosis. *Cell death and differentiation* **6**, 99 (1999).
63 Zhu, M.-T. *et al.* Oxidative stress and apoptosis induced by iron oxide nanoparticles in cultured human umbilical endothelial cells. *Journal of nanoscience and nanotechnology* **10**, 8584-8590 (2010).
64 Zhu, S., Luo, F., Zhu, B. & Wang, G.-X. Mitochondrial impairment and oxidative stress mediated apoptosis induced by α-Fe 2 O 3 nanoparticles in Saccharomyces cerevisiae. *Toxicology Research* **6**, 719-728 (2017).
65 Englert, N. Fine particles and human health—a review of epidemiological studies. *Toxicology letters* **149**, 235-242 (2004).
66 Solaimani, P., Saffari, A., Sioutas, C., Bondy, S. C. & Campbell, A. Exposure to ambient ultrafine particulate matter alters the expression of genes in primary human neurons. *Neurotoxicology* **58**, 50-57 (2017).

67 Pelaz, B. *et al.* Surface functionalization of nanoparticles with polyethylene glycol: effects on protein adsorption and cellular uptake. *Acs Nano* **9**, 6996-7008 (2015).
68 Treuel, L., Docter, D., Maskos, M. & Stauber, R. H. Protein corona–from molecular adsorption to physiological complexity. *Beilstein journal of nanotechnology* **6**, 857 (2015).
69 Böhme, S. *et al.* Quantification of Al2O3 nanoparticles in human cell lines applying inductively coupled plasma mass spectrometry (neb-ICP-MS, LA-ICP-MS) and flow cytometry-based methods. *Journal of Nanoparticle Research* **16**, 2592 (2014).
70 Dankers, A. C. *et al.* A practical approach to assess inhalation toxicity of metal oxide nanoparticles in vitro. *Journal of Applied Toxicology* **38**, 160-171 (2018).
71 Yin, L. L. *et al.* Determination of the Metals by ICP-MS in Wild Mushrooms from Yunnan, China. *Journal of food science* **77** (2012).
72 Gu, J. *et al.* The internalization pathway, metabolic fate and biological effect of superparamagnetic iron oxide nanoparticles in the macrophage-like RAW264. 7 cell. *Science China Life Sciences* **54**, 793-805 (2011).
73 Sun, R. *et al.* Physical and biological characterization of superparamagnetic iron oxide-and ultrasmall superparamagnetic iron oxide-labeled cells: a comparison. *Investigative radiology* **40**, 504-513 (2005).
74 Kunzmann, A. *et al.* Efficient internalization of silica-coated iron oxide nanoparticles of different sizes by primary human macrophages and dendritic cells. *Toxicology and applied pharmacology* **253**, 81-93 (2011).
75 Bartczak, D., Baradez, M.-O., Goenaga-Infante, H. & Marshall, D. Label-free monitoring of the nanoparticle surface modification effects on cellular uptake, trafficking and toxicity. *Toxicology Research* **4**, 169-176 (2015).
76 Guo, L. *et al.* Effects of a Protein-Corona on the Cellular Uptake of Ferroferric Oxide Nanoparticles. *Journal of Nanoscience and Nanotechnology* **16**, 7125-7128 (2016).
77 Yan, Y. *et al.* Differential roles of the protein corona in the cellular uptake of nanoporous polymer particles by monocyte and macrophage cell lines. *ACS nano* **7**, 10960-10970 (2013).
78 Duan, G. *et al.* Protein corona mitigates the cytotoxicity of graphene oxide by reducing its physical interaction with cell membrane. *Nanoscale* **7**, 15214-15224 (2015).
79 Lauffenburger, D. A. & Linderman, J. J. *Receptors: models for binding, trafficking, and signaling*. (Oxford University Press on Demand, 1996).
80 Cho, E. C., Xie, J., Wurm, P. A. & Xia, Y. Understanding the role of surface charges in cellular adsorption versus internalization by selectively removing gold nanoparticles on the cell surface with a I2/KI etchant. *Nano letters* **9**, 1080-1084 (2009).
81 Iwasa, A. *et al.* Cellular uptake and subsequent intracellular trafficking of R8-liposomes introduced at low temperature. *Biochimica et Biophysica Acta (BBA)-Biomembranes* **1758**, 713-720 (2006).
82 Suzuki, H., Toyooka, T. & Ibuki, Y. Simple and easy method to evaluate uptake potential of nanoparticles in mammalian cells using a flow

cytometric light scatter analysis. *Environmental science & technology* **41**, 3018-3024 (2007).

83 Dhawan, A. & Sharma, V. Toxicity assessment of nanomaterials: methods and challenges. *Analytical and bioanalytical chemistry* **398**, 589-605 (2010).

84 Toduka, Y., Toyooka, T. & Ibuki, Y. Flow cytometric evaluation of nanoparticles using side-scattered light and reactive oxygen species-mediated fluorescence–correlation with genotoxicity. *Environmental science & technology* **46**, 7629-7636 (2012).

85 Zanella, D. *et al.* Iron oxide nanoparticles can cross plasma membranes. *Scientific Reports* **7**, 11413 (2017).

86 Nel, A. E. *et al.* Understanding biophysicochemical interactions at the nano–bio interface. *Nature materials* **8**, 543 (2009).

87 Lesniak, A. *et al.* Effects of the presence or absence of a protein corona on silica nanoparticle uptake and impact on cells. *ACS nano* **6**, 5845-5857 (2012).

88 Reddy, K., Kadlec, R., Flaig, E. & Gale, P. Phosphorus retention in streams and wetlands: a review. *Critical reviews in environmental science and technology* **29**, 83-146 (1999).

89 Torrent, J. Interactions between phosphate and iron oxide. *Advances in Geoecology* **30**, 321-344 (1997).

90 Colombo, C., Barrón, V. & Torrent, J. Phosphate adsorption and desorption in relation to morphology and crystal properties of synthetic hematites. *Geochimica et Cosmochimica acta* **58**, 1261-1269 (1994).

91 Goldberg, S. & Sposito, G. On the mechanism of specific phosphate adsorption by hydroxylated mineral surfaces: A review. *Communications in Soil Science and Plant Analysis* **16**, 801-821 (1985).

92 Parfitt, R. L., Atkinson, R. J. & Smart, R. S. C. The Mechanism of Phosphate Fixation by Iron Oxides 1. *Soil Science Society of America Journal* **39**, 837-841 (1975).

93 Parfitt, R. & Russell, J. Adsorption on hydrous oxides. IV. Mechanisms of adsorption of various ions on goethite. *European Journal of Soil Science* **28**, 297-305 (1977).

94 Hatakeyama, M. *et al.* A two-step ligand exchange reaction generates highly water-dispersed magnetic nanoparticles for biomedical applications. *Journal of Materials Chemistry* **21**, 5959-5966 (2011).

95 Smolensky, E. D., Park, H. Y. E., Berquó, T. S. & Pierre, V. C. Surface functionalization of magnetic iron oxide nanoparticles for MRI applications–effect of anchoring group and ligand exchange protocol. *Contrast media & molecular imaging* **6**, 189-199 (2011).

96 Gogoi, M. *et al.* Direct monophasic replacement of fatty acid by DMSA on SPION surface. *Applied Surface Science* **258**, 9685-9691 (2012).

97 Lam, T. *et al.* Fabricating water dispersible superparamagnetic iron oxide nanoparticles for biomedical applications through ligand exchange and direct conjugation. *Nanomaterials* **6**, 100 (2016).

98 Safi, M., Courtois, J., Seigneuret, M., Conjeaud, H. & Berret, J.-F. The effects of aggregation and protein corona on the cellular internalization of iron oxide nanoparticles. *Biomaterials* **32**, 9353-9363 (2011).

99 Melcrová, A. *et al.* The complex nature of calcium cation interactions with phospholipid bilayers. *Scientific reports* **6**, 38035 (2016).

100 Gao, H., Shi, W. & Freund, L. B. Mechanics of receptor-mediated endocytosis. *Proceedings of the National Academy of Sciences of the United States of America* **102**, 9469-9474 (2005).
101 Chen, H., Langer, R. & Edwards, D. A. A film tension theory of phagocytosis. *Journal of colloid and interface science* **190**, 118-133 (1997).
102 Wong-Ekkabut, J. *et al.* Computer simulation study of fullerene translocation through lipid membranes. *Nature Nanotechnology* **3**, 363 (2008).

Chapter 5: General discussion and future directions

5.1 General discussion

The nano-sized metal oxide NPs are increasing investigated and used in laboratories and diverse industry and they are increasingly present in the environmental cycle dispersed in air, ground, or food and water. In such environments the nano-sized metal oxide NPs interact with organic material present and that consequently influences their properties. With this in mind, the initial part of our work was to apply a novel production method to fabricate 'bare' iron oxide nanoparticles with defined and finely controlled size, morphology and surface properties. The second stage was to control their surface modification with small molecules of different chemistries – to create colloidal stable dispersions of iron oxide nanoparticles and to mimic organic material adsorption to metal oxide particles surface.

The potential toxic effects that metal oxide nanoparticles have on living organism, including humans, once they are brought into the contact with epithelia tissue covering mucosal surface, such as gut, was addressed in the third sectin of our work. Here we investigated the nature of interactions of these nano-particles with biological system and what are the potential consequences.

Regarding iron oxide NPs preparation, a novel SDR-based instrumentation was adopted to investigate its ability for fabricating ultrafine iron oxide NPs (USPIONs). The instrument used was newly designed and a considerable amount of work was devoted to understanding fundamental concepts underlying the fabrication process and how can the process variables be used to fine-tune

the physicochemical properties of the product nanoparticles. Here, we proposed that a physical barrier between NPs nucleation and subsequent growth that the design of instrument creates is of a critical importance for fabricating inorganic NPs having with improved, uniform size distribution.

In general, there are specific requirement should be satisfied for any process to be applicable for preparation of highly uniform size of particles. These include; (i) fast/burst nucleation event, (ii) continuous and homogenous growth stage for a noticeable period of time, and (iii) to ensure the second point, a continuous and regular feed of NPs building blocks (monomer or meso-stable intermediate primary particles). Accordingly our NPs production instrumentation has considered these prerequisite in its design including as follows: (i) a junction set on particular point of reactants stream to force creation a burst nucleation zone which is physically confined, (ii) a horizontally-oriented SDR to function as an area at which the nucleated particles are allowed to grow, and (iii) a continuous process achieved by a smooth injection of precursor materials simultaneously with smooth ejection of fabricated particles so to prevent clogging/congestion of growing particles at any specific instrument point, and thereby inhibit unwanted aggregation or secondary growth.

With respect to the above design, we achieved a fine-tuning in the particle size of fabricated USPIONs within the range of 4-9 nm. The main parameters responsible for the particle size tuning were found to be reactants flowrate and spinning disc rotational speed. It is very important to note that the main reasons for NPs polydispersity and size non-uniformity arising during process of synthesis include the following: (i) relatively long period for nucleation, (ii) immature and secondary unwanted particles growth, and (iii) uncontrolled

Ostwald ripening during main growth stage. Our design aimed to eliminate these factors, whereby the microenvironment for the nucleation event support inhibition of unwanted premature particles by reducing the residence time of the active reactants. This is governed by increasing flowrate thus more uniform nuclei were obtained [1-3].

With respect to uneven growth rate of particles, SDR has provided a perfect platform for maintaining as similar as technically possible at this stage microenvironment in the vicinity of individual growing particles. Therefore, undesirable ripening was minimised. Here, the circular grooves (3D printed) enabled a micro-mixing required for equal rate of particles enlargement within a given timeframe [4,5]. Moreover, according to some scenarios of particles growth, the presence of meso-stable intermediate particles could work as a stable source of building blocks. The number of the intermediate particles is believed to be enhanced during very rapid burst of nucleation, another factor for inhibiting particles ripening. In summary, simultaneous manipulation of production parameters, a good control of NPs size was achieved.

Although at this stage of the instrument development mainly ultrafine NPs could be fabricated, the future work should be conducted for further investigations in its potentials to produce particles with a wide range of sizes.

In the next stage after fabricating USPIONs we modified the surfaces of these particles with small molecular material with different chemistry. Here, we have adopted a new method of dry powder mixing under pressure where surface modifying agent and USPIONs are both in solid, dry form and a mechanical shear force is applied on the mixture [6]. The dry mechanical mixing process

showed superior effectiveness at modifying the surfaces of metal oxide NPs, relative to the process conducted in water suspension, to produce stable colloidal dispersion of USPIONs in aqueous media. Regarding biomedical applications, most of surface modifying materials that are extensively used to functionalise NPs are found to be either heat labile ingredients or unstable upon long term storage in a liquid form. Therefore, the dry conditions of producing modified NPs provides a good opportunity to increase a shelf-life of such products. In addition, this technique is a feasible option for a wide range of biologically active organic materials that could be prepared in a powder form, including vitamins and peptides, which in turn can be used to modify the surfaces of inorganic NPs.

In our case the organic modifying agents tested were aminoacids as HCl salt form. These are selected based on physicochemical diversity of their side chain, to develop a better understanding of how biomolecules or drug-like molecules participate in the interaction with metal oxide NPs with biological barriers and hence living organism's response to exposure [7,8].

Relating to USPIONs surface modification results, it was found that the amount of surface associated molecules increased as the initial quantities of the modifying agent increased, in a direct relationship. Data indicated a formation of multilayer of aminoacid 'monomers' around individual particles. However, this phenomena did not fully prevent amino acid modified USPIONs from aggregation once exposed to physiological media. This may be due to insufficient repulsive forces between particles crated by the aminoacid adsorbed layer.

The results indicate that different aminoacid showed different mechanism of interaction with NPs, which points to the critical role that amino acid side chain may play in the binding with USPIONs' surficial iron ions. Therefore, identifying the nature of this interaction will help in understanding how other small molecules with similar properties could interact with NPs and broaden our knowledge about the best strategy for NPs surface decoration and engineering for more advanced biomedical applications.

Modified USPIONs with different surface chemistry were then brought into interactions with a biological system, represented by Caco-2 cell line as a model for intestinal epithelium. The data demonstrate that for all amino acid modified USPIONs interaction with the cells in culture was dramatically reduced when serum proteins were present in the culture medium. In this case, we believe that formation of an adsorptive layer of plasma protein act as barrier to prevent a direct USPIONs surface contact with cell membrane.

Similarly the literature shows that NPs coated with small molecules interact with cell membrane at faster rate and with higher quantities than corresponding polymer coated NPs [9]. Our study provides an interesting finding that (in serum free media) USPIONs with different surface chemistries (different adsorbed aminoacids) exhibit a different pattern in their interactions with cells. Applying TEM we demonstrate that the more hydrophobic USPIONs (Phe-USPIONs) have increased tendency to accumulate inside cells, whilst Asp-USPIONs displayed higher affinity for binding to the cell membrane forming an interesting 'monolayer'.

These findings provide evidence about importance of the nature of NPs for their cell interactions and hence contribute to our understanding of the effects of surface chemistry of metal oxide pollutants on their potential toxicity. Furthermore, studying the potential toxic effect of aminoacid modified USPIONs clearly show that exposure to these particles, at relatively higher doses and longer exposure times, will cause cell death of exposed cells, which appers to follows an apoptotic pathway. The toxicity of iron oxide USPIONs may be arising from two reasons. First, USPIONs are well-known for their ability to undergo Fenton like reactions and cause a production of high amounts of ROS that results in oxidative stress. The second important reason refers to the direct interaction with phospholipids in cell membrane. This may be contributing to caspase activation – as found for Asp-USPIONs which produced higher level of this enzyme activation in comparison with Phe-USPIONs.

5.2 Future directions

The developed instrument (Figure 2-1) has offered a promising ability to prepare several inorganic NPs rather than USPIONs. In addition, this custom-built system was designed so that further physical modifications could be introduced in order to expand its potential capacity for fabricating NPs with larger size than was already prepared.

Moreover, more advanced investigations might aid to gain an insight regarding the effect of instrument variables on NPs construction (nucleation and growth) crystal lattice formation and magnitude of magnetism. It was believed that increasing reactant flowrate and possibly rotational speed of the SDR would produce different crystal structure and hence magnetism. Also chemical variables (Fe^{+2}/Fe^{+3} ratio and BISS concentration) play a crucial role in changing

the way by which NPs could be built. Therefore overlapping these two kind of parameters (physical and chemical) may lead to an effective control of the whole process.

The influence of additional variables (sampling at different time intervals and disc position and using different disc shape like 'Vase') could also be investigated to determine the more suitable point at which highest degree of size and shape uniformity would be resulted.

In respect of USPIONs surface modification, there are several strategies could be followed to improve the yield of the coated NPs. One of the most promising technique include using cryomilling so that increase the amorphisation of coating monomers and hence more molecules would have a chance to interface NPs surfaces. The advantages of this method were summarised in its usefulness for particular surface modifying agents that are heat labile materials (such as vitamins and some co-enzymes).

Upon exposing NPs to a biological system an instantaneous interaction with its components (such as proteins, cell membrane constituents) would be expected to occur establishing a series of nano-bio interfaces. Numerous technologies are evolving to shape the boundaries of these interactions, for example, atomic force microscopy and surface-enhanced Raman scattering (SERS). SERS is able to distinguish the enhanced Raman scattering of molecules associated with metal NPs surfaces where this technique is sensitive enough to detect every single molecule thereby a reliable bio-image is possible to be built with assistance of radiolabelled NPs.

Furthermore, the interaction of inorganic NPs with biological system could participate in several cellular response via triggering different signalling pathways. In this work a preliminary study was performed to investigate the cytotoxic effect of USPIONs and what is the major route of cell death that the affected cells could follow to terminate their life. However, there are various forms of long term cytotoxic effects represented in genotoxic events in which a series of genetic mutation could be generated in response to the overproduction of ROS. So as to highlight this potential toxic effect, several assays (such as comet, micronucleus (MN), DNA-protein crosslinks assays in addition to ELISA, enzyme-linked immunosorbent assay …. etc) might be used to probe the presence of any sign of genetic modification.

Finally, in order to provide a detailed recommendation, we need to make a comprehensive vision of how toxic are USPIONs modified with thin layer of monomers. This could be achieved by mapping the relationship between the inherent physicochemical properties of a certain modifying agent and core materials along with shape of cellular interaction and potential toxic response they may elicit.

5.3 References

1 Song, Y., Hormes, J. & Kumar, C. S. Microfluidic synthesis of nanomaterials. *Small* **4**, 698-711 (2008).

2 Xu, L. *et al.* Synthesis of copper nanoparticles by a T-shaped microfluidic device. *RSC Advances* **4**, 25155-25159 (2014).

3 Xu, L., Peng, J., Srinivasakannan, C., Chen, G. & Shen, A. Q. Synthesis of copper nanocolloids using a continuous flow based microreactor. *Applied Surface Science* **355**, 1-6 (2015).

4 Chin, S. F., Iyer, K. S., Raston, C. L. & Saunders, M. Size selective synthesis of superparamagnetic nanoparticles in thin fluids under continuous flow conditions. *Advanced Functional Materials* **18**, 922-927 (2008).

5 Mohammadi, S., Harvey, A. & Boodhoo, K. V. Synthesis of TiO 2 nanoparticles in a spinning disc reactor. *Chemical Engineering Journal* **258**, 171-184 (2014).

6 Cave, G. W. V. & Mundell, V. J. (Google Patents, 2015).

7 Schwaminger, S. P. *et al.* Nature of Interactions of Amino Acids with Bare Magnetite Nanoparticles. *Journal of Physical Chemistry C* **119**, 23032-23041, doi:10.1021/acs.jpcc.5b07195 (2015).

8 Mudunkotuwa, I. A. & Grassian, V. H. Histidine Adsorption on TiO2 Nanoparticles: An Integrated Spectroscopic, Thermodynamic, and Molecular-Based Approach toward Understanding Nano–Bio Interactions. *Langmuir* **30**, 8751-8760, doi:10.1021/la500722n (2014).

9 Safi, M., Sarrouj, H., Sandre, O., Mignet, N. & Berret, J.-F. Interactions between sub-10-nm iron and cerium oxide nanoparticles and 3T3 fibroblasts: the role of the coating and aggregation state. *Nanotechnology* **21**, 145103 (2010).